INAUGURAL–DISSERTATION

zur
Erlangung der Doktorwürde
der
Naturwissenschaftlich–Mathematischen
Gesamtfakultät
der
Ruprecht–Karls–Universität
Heidelberg

vorgelegt von
M.Sc. Jasmin Mirjam Link
aus Heidelberg

Tag der mündlichen Prüfung: 22.07.2021

Atlantic Deep Circulation During Marine Isotope Stage 11 and the Last One Million Years Inferred From Neodymium Isotopes

Gutachter:
Prof. Dr. Norbert Frank
Prof. Dr. Oliver Friedrich

Abstract

Paleoceanographic studies are crucial for understanding the role of the ocean and its circulation in the Earth's climate system. The patterns of the circulation can vary widely between different climate states, particularly in the course of the glacial-interglacial cycles of the Quarternary. In deep sea sediments, the isotopic composition of authigenic neodymium (expressed as ε_{Nd}) can be utilized to trace back the provenance of the bottom water mass and therefore to reconstruct past circulation schemes.

In Study I of this thesis, a profile of Nd isotopes at Ocean Drilling Program (ODP) Site 1063 in the Northwestern Atlantic is presented spanning the time period of 150 to 1027 thousand years ago (ka), which corresponds to Marine Isotope Stages (MISs) 6 to 29. Thus, it extends and augments the published record of ε_{Nd} at the Bermuda Rise with a temporal resolution that is unprecedented for that time period in the Atlantic. The overall structure is dominated by the glacial-interglacial cycles, with Northern-Sourced Water masses (NSW) prevailing at the core site most of the time. The circulation experienced a major reorganization at the 900 ka event associated with the Mid-Pleistocene Transition, when for the first time during the past one million years, a higher proportion of Southern-Sourced Water masses (SSW) flooded the deep Northwestern Atlantic. This advance of SSW is also seen during most of the following glacials, however only at glacial maxima. An exception is the mild glacial MIS 14, when NSW was present at the core site.

The circulation pattern in the Atlantic during MISs 12-11 was further explored in Study II. In addition to site ODP 1063, profiles of Nd isotopes were generated for six sites. They range from the Feni and Gardar Drift in the Northeastern Atlantic (ODP 980 and IODP U1304, respectively), to the Cape Verde Plateau (ODP 659) and Ceara Rise (ODP 929) in the tropical North Atlantic to the Walvis Ridge (ODP 1267) and Rio Grande Rise (DSDP 517) in the subtropical South Atlantic. It is thereby the first systematically analysis of Atlantic wide ε_{Nd} patterns for this time period. While a circulation pattern similar to the LGM prevailed during MIS 12, in MIS 11 NSW advanced further to the south compared to the Holocene. Therefore a strong AMOC is attested with active deep water formation even under ongoing freshwater input through melting ice sheets.

Kurzfassung

Paläozeanographische Studien sind unerlässlich für das Verständnis der Rolle des Ozeans und seiner Zirkulation im Klimasystem der Erde. Die Strömumgsmuster können zwischen unterschiedlichen Klimazuständen stark variieren, insbesondere im Verlauf der Glazial-Interglazial-Zyklen des Quartärs. Die Isotopenverteilung von authigenem Neodym in Tiefseesedimenten (ausgedrückt als ε_{Nd}) kann dazu genutzt werden, die Herkunft der Bodenwassermasse zurückzuverfolgen und somit vergangene Zirkulationsschemata zu rekonstruieren.

In der ersten Studie in dieser Arbeit wird eine Zeitreihe von Nd Isotopen der Ocean Drilling Program (ODP) Site 1063 im nordwestlichen Atlantik vorgestellt. Diese deckt den Zeitabschnitt von 150 bis zu 1027 Tausend Jahren vor heute ab, welcher den Marinen Isotopen Stadien (MIS) 6 bis 29 entspricht. Damit wird das bisher veröffentlichte ε_{Nd} Profil am Bermuda Rise verlängert und ergänzt mit einer zeitlichen Auflösung, die für diese Zeitspanne im Atlantik bisher einmalig ist. Der allgemeine Verlauf ist von den Glazial-Interglazialzyklen geprägt, wobei zumeist aus dem Norden stammende Wassermassen (Northern-Sourced Water, NSW) an der Kernlokation vorherrschten. Die Zirkulation wurde während des 900 ka Events, welches mit der Mid-Pleistocene Transition assoziiert ist, neu angeordnet, sodass zum ersten mal in den vergangenen eine Million Jahren ein größerer Anteil an Wassermassen, die aus dem Süden stammen (Southern-Sourced Water, SSW) den tiefen nordwestlichen Atlantik fluteten. Dieses Vordringen von SSW fand auch während der meisten folgenden Glazialen statt, allerdings nur innerhalb der Glazialen Maxima. Eine Ausnahme stellt das relativ milde Glazial MIS 14 dar, während dessen NSW an der Kernlokation vorherrschte.

Studie II rekonstruiert die Atlantik-weiten Zirkulationsmuster in der Zeitspanne von MIS 12 bis MIS 11. Zusätzlich zu ODP 1063, wurden Profile von Nd Isotopen an insgesamt sechs weiteren Lokationen erstellt. Diese erstrecken sich von der Feni und Gardar Drift im Nordostatlantik (ODP 980 bzw. IODP U1304), über das Kapverden Plateau (ODP 659) und den Ceara Rücken (ODP 929) im tropischen Nordatlantik, bis hin zum Walfisch- und Rio Grande-Rücken (ODP 1267 bzw. DSDP 517) im subtropischen Südatlantik. Damit ist dies die erste systematische Analyse Atlantik-weiter ε_{Nd} Muster für diesen Zeitabschnitt. Während im MIS 12 ein ähnliches Zirkulationsschema wie während des LGM vorherrschte, drang NSW im MIS 11 weiter nach Süden vor relativ zum Holozän. Daher ist eine starke AMOC nachgewiesen mit einer aktiven Tiefenwasserbildung selbst unter anhaltendem Schmelzwasserbeitrag der Eisschilde.

Contents

List of Figures

List of Tables

List of Abbreviations

AABW	Antarctic Bottom Water
AAIW	Antarctic Intermediate Water
amcd	adjusted meter composite depth
AMOC	Atlantic Meridional Overturning Circulation
ARM	anhysteretic remanent magnetization
CHUR	Chondritic Uniform Reservoir
CMIP	Coupled Model Intercomparison Project
DSDP	Deep Sea Drilling Project
DSOW	Denmark Strait Overflow Water
DWBC	Deep Western Boundary Current
GNABW	Glacial North Atlantic Bottom Water
GNADW	Glacial North Atlantic Deep Water
GNAIW	Glacial North Atlantic Intermediate Water
GRAPE	Gamma Ray Attenuation Porosity Evaluator
ICP-Q-MS	inductively coupled plasma quadrupol mass spectrometer
IODP	Integrated Ocean Drilling Program (2003-2013), International Ocean Discovery Program (2013–present)
IRD	ice-rafted debris
IRM	isothermal remanent magnetization
IRMS	isotope ratio mass spectrometer
ISOW	Iceland-Scotland Overflow Water
ka	thousand years
LDW	Lower Deep Water
LGM	Last Glacial Maximum

LSW	Labrador Sea Water
Ma	million years
MBE	Mid-Brunhes Event
mbsf	meter below sea floor
MC ICP-MS	multi-collector inductively coupled mass spectrometer
mcd	meter composite depth
MIS	Marine Isotope Stage
MOW	Mediterranean Outflow Water
MPT	Mid-Pleistocene Transition
NADW	North Atlantic Deep Water
Nps	Neogloboquadrina pachyderma (sinistral)
NSW	Northern-Sourced Water
ODP	Ocean Drilling Program
PMIP	Paleoclimate Modeling Intercomparison Project
RPI	relative paleointensity
s.l.e.	sea level equivalent
SPMW	Subpolar Mode Water
SST	sea surface temperature
SSW	Southern-Sourced Water
T	glacial Termination
VPDB	Vienna Pee Dee Belemnite
VSMOW	Vienna Standard Mean Ocean Water
WTROW	Wyville-Thomson Ridge Overflow Water

1 Introduction

The reconstruction of past ocean circulation and the understanding of the underlying processes are challenging tasks. However, it is important to address these challenges since the ocean is a vital player in the climate system of the Earth. It redistributes salt and heat across latitudes, stores carbon into and releases it from the deep sea. In times of current anthropogenic global warming, the thermohaline circulation was identified as one of the tipping elements, that may cross a tipping point in the future [Lenton *et al.*, 2008]. Several studies indicate that the meridional overturning circulation in the Atlantic (AMOC) has already started to weaken [e.g. Caesar *et al.*, 2018; Thornalley *et al.*, 2018].

The modern ocean circulation can be studied by in situ measurements. The strength of the AMOC is monitored at arrays at several latitudes, where the variability of the meridional volume transport is measured [Frajka-Williams *et al.*, 2019]. In addition, the number and spatial coverage of observations of physical parameters like temperature and salinity have markedly increased in the past decades also due to the establishment of the Argo array [Abraham *et al.*, 2013; Riser *et al.*, 2016]. To better understand the modern biochemical cycles of trace elements and their isotopes, another major international effort is currently underway, the GEOTRACES program [SCOR Working Group, 2007; Anderson, 2020]. One of those key elements is neodymium (Nd), as the ratio of its isotopes ^{143}Nd to ^{144}Nd is used as a tracer for the provenance of a water mass [van de Flierdt *et al.*, 2016; Tachikawa *et al.*, 2017].

To put the current AMOC weakening into context and to determine its natural background conditions prior to anthropogenic influences, one has to look into the past, for which no direct instrumental measurements are available. Thereby one can address the question of how the AMOC is modulated throughout different climate states. Cores of deep sea sediment serve as excellent archives to reconstruct the past overturning circulation. Its components like the remnants of past organisms or the lithogenic particles themselves carry information about the past environmental conditions during which those have been transferred into the sediment. Here again, an international program enables the recovery of long and high-quality sediment cores, which provides

the basis for paleoceanographic studies since many decades. It began in 1966 with the *Deep Sea Drilling Project* (DSDP, until 1983) and was followed up by the *Ocean Drilling Program* (ODP, 1985–2003), *Integrated Ocean Drilling Program* (IODP, 2003–2013), and *International Ocean Discovery Program* (2013–recent). Sediment cores from a total of seven sites drilled in the framework of these programs were analyzed in this thesis.

Since the establishment of Nd isotopes as a water mass provenance and mixing tracer in seawater in the late 1970s [Piepgras *et al.*, 1979], many studies have made use of this potential in paleoceanographic reconstructions using ferromanganese crusts and nodules, fish teeth, planktic foraminifera, corals and authigenic coatings [e.g. Burton *et al.*, 1997; Martin and Haley, 2000; Rutberg *et al.*, 2000; van de Flierdt *et al.*, 2006]. Even though the details of the global fluxes are still a matter of debate [e.g. Jeandel, 2016; Haley *et al.*, 2017], more and more temporally highly resolved studies show climate driven changes in the past dynamic Atlantic deep circulation. Hence, apart from further studies of the Nd cycle, it is most crucial to advance our understanding of the link between climate and ocean circulation. This requires high-resolution records of the past Nd isotopic composition of the seawater, which are similar in resolution to other tracers such as stable oxygen isotopes of benthic foraminifera, to further improve on the timing and scale of the variability through time. Most of the (sub-)millennial records of Nd isotopes in the Atlantic focus only on the last deglaciation [e.g. Lippold *et al.*, 2016; Howe *et al.*, 2017] or the last glacial cycle [e.g. Piotrowski *et al.*, 2008; Böhm *et al.*, 2015; Hu *et al.*, 2016]. In contrast, solely few studies cover older time periods in the Pleistocene, but mostly only on orbital time scales [e.g. Khélifi and Frank, 2014; Pena and Goldstein, 2014; Dausmann *et al.*, 2017; Farmer *et al.*, 2019]. An exception is the record of the equatorial deep Ceara Rise with a sub-orbital resolution of the Nd isotopic composition of the past 800 thousand years [Howe and Piotrowski, 2017].

After the description of the fundamentals about the climate of the past one million years (Section 2.1), the present and past ocean circulation patterns (Section 2.2), and Nd isotopes as a water mass tracer (Section 2.3), two main studies are introduced.

In Study I (Chapters 3 to 6), a record of Nd isotopes at ODP Site 1063 in the deep Northwestern Atlantic for the past one million years is presented. The climate during this time period was characterized by several glacial-interglacial cycles. Their period changed from 41 to 100 thousand years in the course of the Mid-Pleistocene Transition. But also the character of the glacials and interglacials themselves differed widely. Hence, the past one million years are a suitable time window to study the behavior of the past overturning circulation under different background conditions.

For this purpose, the Nd isotopic composition of authigenic coatings is analyzed to reconstruct the past prevailing bottom water masses and therefore the water mass competition in the deep Northwest Atlantic. The data presented here, expand and augment the previous published records [Roberts *et al.*, 2010; Gutjahr and Lippold, 2011; Böhm *et al.*, 2015; Deaney *et al.*, 2017; Lippold *et al.*, 2019; Jaume-Seguí *et al.*, 2020] at the Bermuda Rise back to 1026 thousand years with an unprecedented millennial scale temporal resolution.

The second study (Chapters 7 to 10) is based on findings in the Nd isotope record of ODP 1063 during Marine Isotope Stage 11, about 400 thousand years ago. For a time span of nearly 30 thousand years a constant extreme Nd isotopic composition was detected at the Bermuda Rise. Moreover, this time interval is very fascinating as one can (possibly) consider it as a close analogue to the recent and near future time period at least in terms of orbital configurations [e.g. Loutre and Berger, 2003]. The Greenland Ice Sheet was partly melted [de Vernal and Hillaire-Marcel, 2008; Reyes *et al.*, 2014] and the sea level higher than today [Dutton *et al.*, 2015]. Therefore the conditions during this stage resembles the ones projected for the future [Aschwanden *et al.*, 2019] although different forcing mechanisms and time scales are involved. To reconstruct the state of the AMOC during this time interval, the deep water flow pattern was reconstructed using Nd isotopes of in total seven sites. They are distributed all over the Atlantic starting close to the formation regions of deepwater in the North Atlantic and following the flowpaths south to the subtropical South Atlantic. They were chosen to answer the questions, whether the extreme Nd values found at the Bermuda Rise spread out over the Atlantic or whether they correspond to a more regional signal, as well as how the flow patterns of water masses changed from the preceding glacial to and within this warm stage and how this affected the overturning circulation.

2 Background

2.1 Climate of the past one million years

The climate of the Earth has changed dramatically over the course of time (see Figure 2.1). During the Cenozoic (the past 66 million years [Ma]) it experienced the transition from greenhouse conditions with high greenhouse gas concentrations, high temperatures, and ice-free poles to icehouse conditions, which was characterized by markedly lower greenhouse gas concentrations, and both poles glaciated [Zachos *et al.*, 2001]. After the Early Eocene Climatic Optimum (about 52 to 50 Ma ago), a long-term increase in the oxygen isotope ratio of deep-sea benthic foraminifera commenced. This ratio is given in δ^{18}O, which expresses the ratio of ^{18}O to ^{16}O compared to a standard[1]. In first order, variations of this value correspond to changes in the temperature of the deep sea and in the volume of continental ice sheets. For the first time in the Cenozoic, continental-scale ice sheets were found in Antarctica during the earliest Oligocene [e.g. Miller *et al.*, 1991; Ivany *et al.*, 2006]. On the Northern Hemisphere, large-scale glaciation started and intensified in the Pliocene/early Pleistocene, at around 3.6 to 2.4 Ma [Mudelsee and Raymo, 2005]. The following time period is characterized by the waxing and waning of ice sheets on the Northern Hemisphere, which is orbitally paced. However, the dominant frequency of this glacial-interglacial cycles changed from an obliquity-driven period of about 41 thousand years (the so-called "*41 kyr-world*") to a quasi-100 thousand years long period ("*100 kyr-world*"). This change is called the *Mid-Pleistocene Transition* (MPT) by most authors [e.g. Clark *et al.*, 2006; Elderfield *et al.*, 2012]. However, due to the redefinition of base the Pleistocene from 1.8 Ma to 2.58 Ma [Gibbard *et al.*, 2010], the term *Early–Middle Pleistocene Transition* was introduced [Head and Gibbard, 2015]. In order to be consistent with most of the literature, the term MPT will be used throughout this thesis.

The MPT is characterized not only by a change in pacing of glacial-interglacial

[1] $\delta^{18}O = \left[\left(\frac{(^{18}O/^{16}O)_{Sample}}{(^{18}O/^{16}O)_{Reference}} \right) - 1 \right] \cdot 1000$. For δ^{18}O values measured in calcite the Vienna Pee Dee Belemnite (VPDB) standard is used and Vienna Standard Mean Ocean Water (VSMOW) for water, respectively [Ravelo and Hillaire-Marcel, 2007].

cycles, but also in a transformation of the waveform of climate records. Before the MPT, climate cycles are expressed by low amplitudes and relatively symmetrical waveforms, while afterwards they are characterized by high amplitudes and a typical sawtooth pattern [Head and Gibbard, 2015]. This also indicates a shift from a linear forcing of the climate system to a strong non-linear one [Head and Gibbard, 2015]. The ice volume increases during the MPT [Clark *et al.*, 2006] and both deep and surface ocean temperatures decreased, especially during the glacials [McClymont *et al.*, 2013; Bates *et al.*, 2014]. However, the exact timing of these transitions is controversial. While Head and Gibbard [2015] report a broader time range of 1.4 to 0.4 Ma, Clark *et al.* [2006] for example define the MPT more narrow, happening between 1.25 to 0.70 Ma.

In addition, the cause of the MPT is highly debated. Orbital forcing itself induces the climate oscillations, but is not sufficient to explain the shift in the periodicity from 41 to 100 thousand years, as variations in the insolation show no evidence of a change in the state [Ruddiman *et al.*, 1986; Head and Gibbard, 2015]. Therefore, several hypotheses have been postulated to explain the abovementioned alterations in the climate records.

A global cooling trend [Zachos *et al.*, 2001; McClymont *et al.*, 2013] is hold responsible for the MPT, that may have led the Earth cross a threshold, where ice-sheets were able to survive 41 thousand years cycles of high summer insolation [Clark *et al.*, 2006; Head and Gibbard, 2015]. A long-term decrease in atmospheric CO_2 has been invoked as a possible mechanism [e.g. Raymo *et al.*, 1997; Berger *et al.*, 1999]. Reconstructed pCO_2 shows only a slight decline in primarily glacial values [Hönisch *et al.*, 2009; Tripati *et al.*, 2011; Chalk *et al.*, 2017], however data are still scarce. CO_2 extracted from Antarctic ice cores [Petit *et al.*, 1999; Monnin *et al.*, 2001; Pépin *et al.*, 2001; Raynaud *et al.*, 2005; Siegenthaler *et al.*, 2005; Lüthi *et al.*, 2008] does not show a decreasing trend for the past 800 thousand years (ka), instead it shows higher interglacial values for the most recent climate cycles compared to lower values during the so-called *Lukewarm Inter-*

Figure 2.1 ***(following page)*:** Climate evolution of the Cenozoic with the studied time interval highlighted in light blue. (A) Record of benthic $\delta^{18}O$ for the past 66 Ma [Zachos *et al.*, 2001, 2008, 5pt-running mean]. (B) Global benthic $\delta^{18}O$ stack LR04 for the past 5 Ma [Lisiecki and Raymo, 2005]. (C) LR04, sea-level reconstruction [Elderfield *et al.*, 2012], CO_2 extracted from Antarctic ice cores [Petit *et al.*, 1999; Monnin *et al.*, 2001; Pépin *et al.*, 2001; Raynaud *et al.*, 2005; Siegenthaler *et al.*, 2005; Lüthi *et al.*, 2008], and June insolation at 65°N [Laskar *et al.*, 2004] during the studied time interval. Numbers in boxes indicate MISs after Railsback *et al.* [2015], periods and epochs are based on Cohen *et al.* [2013; updated]. Note that in (A) and (B) the Holocene is too short to be displayed.

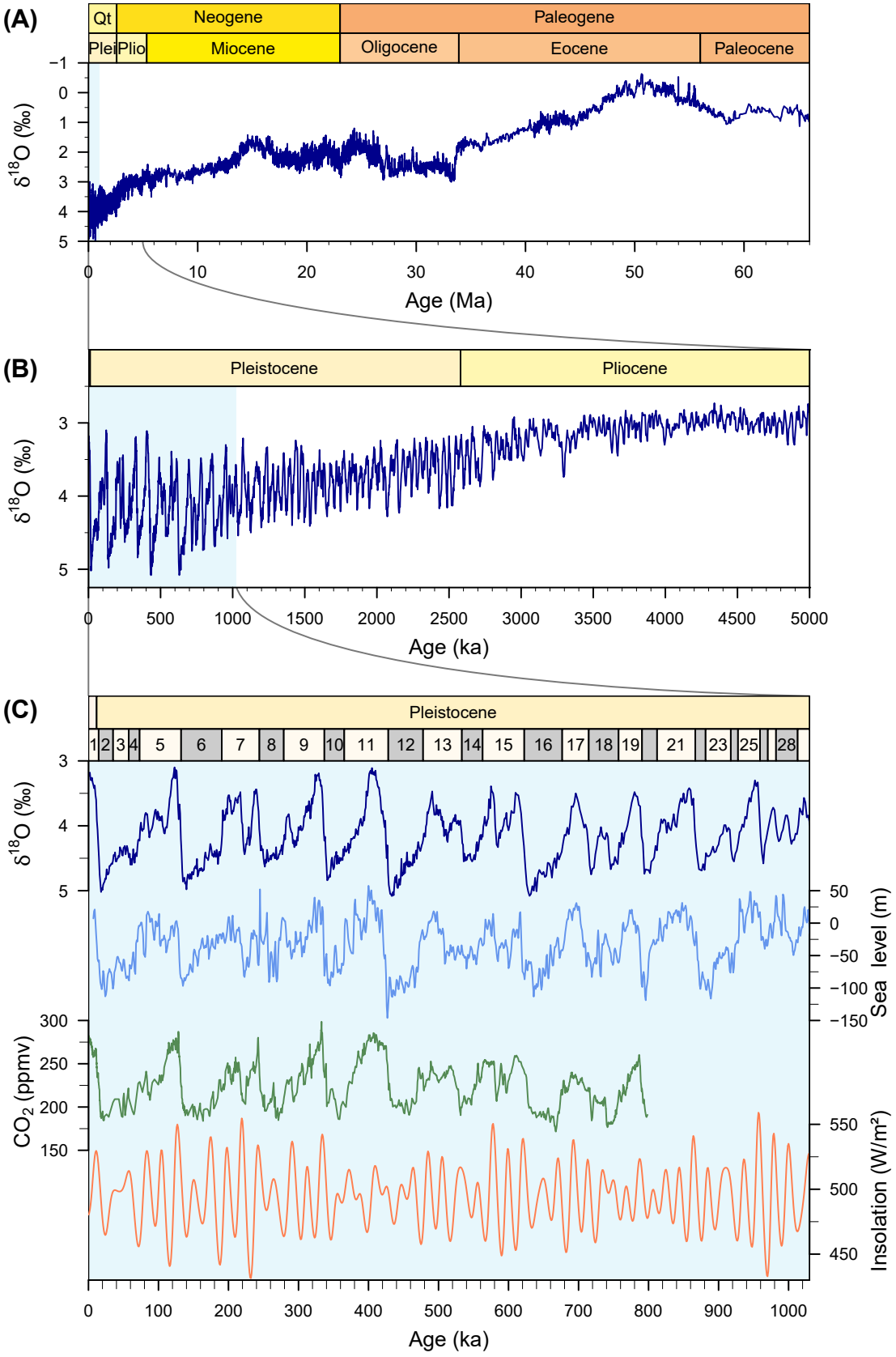
(A)
Qt
Neogene
Paleogene
Plei
Plio
Miocene
Oligocene
Eocene
Paleocene
δ18O (‰)
Age (Ma)
(B)
Pleistocene
Pliocene
δ18O (‰)
Age (ka)
(C)
Pleistocene
1 2 3 4 5 6 7 8 9 10 11 12 13 14 15 16 17 18 19 21 23 25 28
δ18O (‰)
Sea level (m)
CO2 (ppmv)
Insolation (W/m²)
Age (ka)

glacials. Therefore, a declining trend of this greenhouse gas must have reversed [Clark *et al.*, 2006]. A possible sink for CO_2 is silicate weathering [Tripati *et al.*, 2011]. It is assumed to have increased due to the provision of fine ground sediment by the erosion of basement rocks as a result of the glaciations [Vance *et al.*, 2009; Head and Gibbard, 2015] on the one hand and to the uplift of the Himalaya/Tibetan Plateau [Raymo *et al.*, 1988] on the other hand. Together with the uplift of the Sierra Nevada Mountains and the Transverse Ranges in Western North America, these mountain ranges also led to a rearrangement of the atmospheric circulation to more meridional circulation patterns. Hence, more cold Arctic air during summer months would decrease the ablation of ice sheets and therefore favor the ice growth [Ruddiman *et al.*, 1986]. The *Regolith Hypothesis* by Clark and Pollard [1998] and Clark *et al.* [2006] explains the increase in global ice volume. The early ice sheets on the Northern Hemisphere were sitting on a thick layer of regolith, which is a low-friction substrate. Therefore, only thin, but mobile ice sheets could develop. During their waxing and waning of the 41 thousand years cycles, they gradually eroded the regolith and exposed the underlying crystalline bedrock. Now sitting on a high-friction substrate, ice sheets could grow in thickness and therefore survive a 41 thousand years cycle. In a modelling study, Willeit *et al.* [2019] stated that the combination of both the regolith removal and the decline of CO_2 is necessary to control the timing of the MPT. Other hypotheses include the shift in the northern deep-water formation area from the Arctic to the Nordic Seas as a result of the uplift of the Greenland-Scotland submarine ridge [Denton, 2000], the closure of the Bering Strait [Kender *et al.*, 2018], and the *Clathrate Gun Hypothesis*, where high amounts of methane get released into the atmosphere [Kenneth *et al.*, 2003]. The expansion of both the East Antarctic Ice Sheet [Raymo *et al.*, 2006] and the West Antarctic Ice Sheet [Lawrence *et al.*, 2010] have also been invoked as possible mechanisms, the latter increasing the incursions of Antarctic Bottom Water to the North Atlantic. In addition, the climate system was analyzed for its chaotic nature during the MPT [Huybers, 2009; Maslin and Brierley, 2015], as well as for its role as a natural oscillator [Rial *et al.*, 2013].

One prominent event during the MPT is the so-called *900 ka event*, which can be found in many climate records and spans the Marine Isotope Stages[2] (MISs) 24–22 [Clark *et al.*, 2006; Head and Gibbard, 2015]. It is assumed to represent the first long glaciation of the Northern Hemisphere and is accompanied by an abrupt drop in glacial sea level [Elderfield *et al.*, 2012] and a nearly global minimum of sea surface temper-

[2]In this thesis, the definition of the MIS and the corresponing substages expressed as lowercase letters is following the nomenclature of Railsback *et al.* [2015].

atures (SST) [McClymont *et al.*, 2013]. Stable carbon isotopes of benthic foraminifera (expressed as δ^{13}C [3]) are commonly used as a proxy for the distribution of water masses [Lynch-Stieglitz, 2003]. They show very depleted values during the *900 ka event* [e.g. Raymo *et al.*, 1997; Hodell *et al.*, 2003], indicative of a change in the global partitioning of inorganic and organic carbon as well as a reduction of the deep-ocean circulation [Clark *et al.*, 2006; Head and Gibbard, 2015]. A disruption of the thermohaline circulation is also documented by Pena and Goldstein [2014] using neodymium isotopes (see Section 2.3 for more details). The authors infer a shift in the vigor of the circulation from an active mode during glacials before this event to a reduced glacial mode afterwards.

The glacial cycles of the past 800 ka are characterized by fluctuations in the sea level record of more than 100 m, are roughly 100 ka long and show a typical sawtooth pattern [Past Interglacials Working Group of PAGES, 2016]. This shape is caused by a rapid transition from a glacial maximum to interglacial values, called glacial Termination [Broecker and van Donk, 1970][4], that usually takes 4–9 ka [Past Interglacials Working Group of PAGES, 2016] and is characterized by a sharp sea level rise [Elderfield *et al.*, 2012]. Here, the definition of an interglacial from Past Interglacials Working Group of PAGES [2016] is followed, who determine an interglacial as a period with only little ice on the Northern Hemisphere continents outside Greenland, with periods of significantly greater ice volume before and after the respective interglacial. Therefore, for the past 800 ka the following MIS substages are classified as an interglacial: MIS 1, 5e, 7a–c, 7e, 9e, 11c, 13a, 15a, 15e, 17c, and 19c [Past Interglacials Working Group of PAGES, 2016]. The interglacials themselves do not show any coherent pattern regarding their length, their shape, amplitude, and spatial pattern of the climate records [Lang and Wolff, 2011; Past Interglacials Working Group of PAGES, 2016]. Interglacials end with a glacial inception and are followed by a long-term trend of ice build-up [e.g. Elderfield *et al.*, 2012], a decline in greenhouse gases [e.g. Lüthi *et al.*, 2008] and an increase in dust flux [e.g. Winckler *et al.*, 2008]. In contrast to the rather invariable interglacials, the transition to and the full glacial conditions themselves are characterized by an enhanced millennial-scale variability, which can be found in sediment cores throughout the North

[3] $\delta^{13}C = \left[\left(\frac{(^{13}C/^{12}C)_{Sample}}{(^{13}C/^{12}C)_{Reference}} \right) - 1 \right] \cdot 1000.$

[4] Glacial Terminations (T) are numbered using Roman numerals for Terminations at the change from even- to odd-numbered MIS, while for T happening within an odd-numbered MIS an uppercase letter is additionally added. Note that the nomenclature of Railsback *et al.* [2015] is used, which includes a Termination at the shift from MIS 24 to 23 (T-XI). However, not all other studies mark it as a Termination and therefore refer to T-XII at the change from MIS 26 to 25 as T-XI.

Atlantic [e.g. McManus *et al.*, 1999; Hodell and Channell, 2016; Past Interglacials Working Group of PAGES, 2016].

The interglacials of 800 to 450 ka are often referred to as *Lukewarm Interglacials* as a step change after 450 ka for atmospheric CO_2 [Lüthi *et al.*, 2008], Antarctic temperatures [EPICA Community Members, 2004], and deepwater temperatures [Elderfield *et al.*, 2012] is seen [Past Interglacials Working Group of PAGES, 2016]. However, not all climate records show a change toward more intense interglacials at this so-called *Mid-Brunhes Event* (MBE). Lang and Wolff [2011] and Past Interglacials Working Group of PAGES [2016] analyzed the strength of the individual glacial and interglacials and found that even if there is a prevalence of stronger interglacials after the MBE in some records, the interglacials during MIS 7a–c and 7e are far weaker and resemble the interglacials before the MBE. Another striking feature of their analyses is that strong interglacials were preceded by strong glacials and weak glacials were followed by weak interglacials.

The time period of MISs 15–13 is also characterized by weakly expressed glacials and interglacials with only low amplitudes in many records. MIS 14 is barely more prominent than the time period between the interglacials of MIS 15e and 15a [Lang and Wolff, 2011]. The weakest interglacial of the past 800 ka is MIS 13 in most of the records [Lang and Wolff, 2011; Past Interglacials Working Group of PAGES, 2016]. However, it is surprising that the Greenland Ice Sheet must have been smaller compared to most other interglacials, as pollen are found in a sediment core south of Greenland, indicating a forest vegetation on southern Greenland [de Vernal and Hillaire-Marcel, 2008].

Besides MIS 5e, MIS 11c is one of the strongest interglacials [Lang and Wolff, 2011; Past Interglacials Working Group of PAGES, 2016] and also stands out in many other terms. It is the longest interglacial with nearly 30 ka duration [Cheng *et al.*, 2016]. The orbital configuration was similar to MIS 1 as well as the upcoming future due to a weak precessional forcing [Ruddiman, 2006] and has therefore been invoked as a potential analog for the Holocene [Howard, 1997; Berger and Loutre, 2002; Loutre and Berger, 2003]. However, comparison with modern climate remains debated [Candy *et al.*, 2014, and references therein]. Despite this, MIS 11 is of strong interest for many studies, because of its extreme characteristics for which it earned the nickname “super-interglacial" [Lauritzen and Lundberg, 2004; Melles *et al.*, 2012]. Extreme warmth was detected in the Arctic Lake El’gygytgyn [Melles *et al.*, 2012] and in Scandinavia [Lauritzen and Lundberg, 2004]. Sea level was up to +13 m higher than present [Dutton *et al.*, 2015], corresponding to a significant loss of the Greenland Ice Sheet [Reyes *et al.*,

2014]. These ice-free conditions on at least southern Greenland are also in line with a potential forest vegetation there [de Vernal and Hillaire-Marcel, 2008] and are attributed to an overall strong AMOC [Rachmayani *et al.*, 2017]. Looking at the sea surface temperatures, an opposing pattern prevailed on the North Atlantic with warmer than present SSTs in the mid-latitudes [Kandiano *et al.*, 2012; Milker *et al.*, 2015] compared to a surface cooling in the Nordic Seas [Bauch *et al.*, 2000]. This cold and fresh surface layer recently even provoked the question where and under which circumstances the deep water formation in the Nordic Seas could have occurred [Kandiano *et al.*, 2016].

2.2 Ocean Circulation

2.2.1 Modern ocean circulation

The motion of the water masses of the world's oceans is globally connected via the so-called *great ocean conveyor belt* [Broecker, 1987], which can be seen in Figure 2.2. It is primarily driven by wind stress as well as heat and freshwater fluxes [Rahmstorf, 2006]. The latter form the concept of the thermohaline circulation. Differences in the salt and heat content of water masses lead to distinct densities and small changes in these properties therefore lead to vertical mixing. Strong westerly winds across Antarctica induce a northward flow of water masses as a result of the Coriolis force. Hence, the so-called Ekman transport leads to a divergence and in turn upwelling of deep waters [Kuhlbrodt *et al.*, 2007].

In the ocean, these processes drive the meridional overturning circulation. The density of water masses increases as the water masses get cooled down as well as when salt gets rejected through sea ice formation. Thus, they sink down and form deep waters. Currently, this solely happens in restricted regions of the world: the Nordic Seas and the Labrador Sea in the Northern Hemisphere, together with the Weddell and Ross Seas on the Southern Hemisphere. These deep waters spread across the ocean basins mostly as Deep Western Boundary Currents (DWBC), before they ultimately get upwelled – either through mixing-driven upwelling in the lower- to mid-latitudes or through wind-driven upwelling in the region of the Antarctic Circumpolar Current [Rahmstorf, 2006; Stewart, 2008].

The Atlantic part of the meridional overturning circulation consists of two cells – an upper and a lower cell [Marshall and Speer, 2012]. The upper cell consists of the northward transport of near-surface waters, starting in the Southeastern Atlantic with

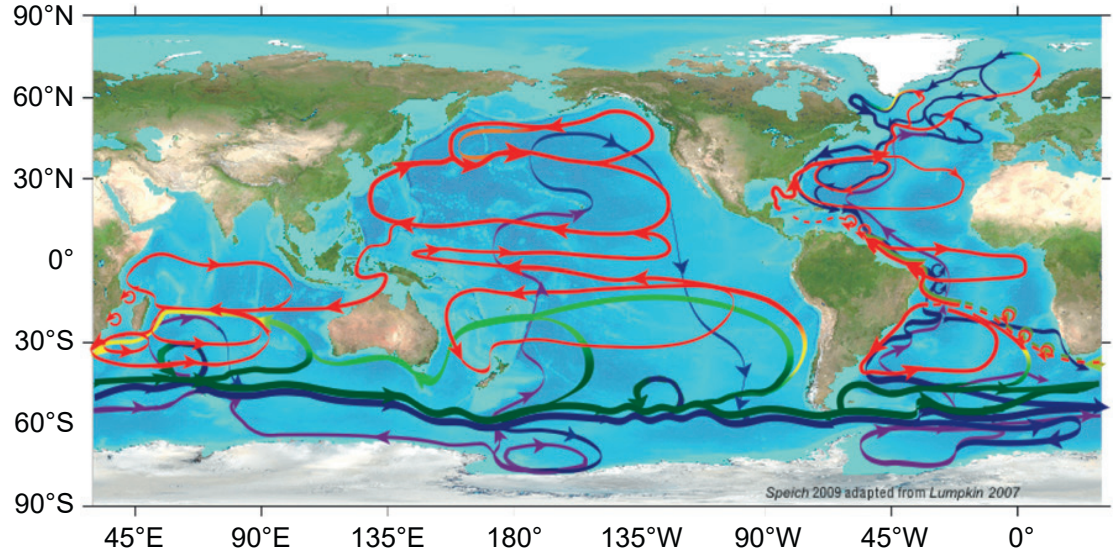

Figure 2.2: Schematic view of the global ocean circulation. Red corresponds to surface flow, blue and purple to deep flows, and yellow and green to the transitions between the depths. Figure taken from Garzoli and Matano [2011, p.1838], based on S. Speich following Lumpkin and Speer [2007] and Speich *et al.* [2007].

the Benguela Current, which turns partly to the west to the Southern Equatorial Current, crosses the equator as the North Brazil Current travels further to the north as the Gulf Stream and eventually the North Atlantic Current. It looses buoyancy and becomes denser until it eventually sinks to greater depths in the Labrador and the Nordic Seas, where it forms North Atlantic Deep Water (NADW) [Buckley and Marshall, 2016]. It can be separated based on its properties and the respective formation region into the overflow waters that cross the Greenland-Iceland-Scotland Ridge east and west of Iceland (Iceland-Scotland Overflow Water, ISOW, and Denmark Strait Overflow Water, DSOW, respectively) and the Labrador Sea Water (LSW).

NADW travels southward, primarily as the DWBC along the American margin but also within complex interior pathways [Rhein *et al.*, 2015; Buckley and Marshall, 2016]. At 5°S, after crossing the equator, the exported NADW can solely be found in a narrow DWBC, which breaks up into eddies south of 8°S [Garzoli *et al.*, 2015]. At the Trindade Ridge at about 20°S, about 22% of the NADW flows eastwards toward the interior of the basins, while the remainder continues its journey southwards [Garzoli *et al.*, 2015]. The upwelling due to the Ekman transport happens in the Southern Ocean along tilted isopycnals [Marshall and Speer, 2012]. The lower cell gets supplied with Antarctic Bottom Water (AABW) that is formed in the Ross and Weddell Seas and flows northwards into the Atlantic Basin [Marshall and Speer, 2012].

2.2.2 Past ocean circulation

During the glacial-interglacial cycles, the geometry of the AMOC was subject of reorganizations. Conceptual models exist, which divide the state of the overturning circulation into three different modes [Sarnthein *et al.*, 1994; Alley and Clark, 1999; Rahmstorf, 2002]. In the modern warm (or interstadial) state the deepwater formation takes place in the Nordic Seas and the Labrador Sea, and the NADW travels south at great depths.

During the cold (stadial) mode, it is believed that the region of the deepwater formation moved to the subpolar open ocean, i.e. south of Iceland [e.g. Labeyrie *et al.*, 1992; Oppo and Lehman, 1993; Rahmstorf, 2002] with a shallow to intermediate deep convection in the Nordic Seas, which contributed to the shallow Glacial North Atlantic Intermediate Water (GNAIW) [e.g. Meland *et al.*, 2008; Thornalley *et al.*, 2015]. This northern-sourced water mass (NSW) is assumed to be the glacial counterpart to the NADW. Reconstructions for the Last Glacial Maximum (LGM) based on δ^{13}C and Cd/Ca show a significant shoaling of this NSW, and a concomitant significant northward and volumetric advance of southern-sourced water (SSW) in the deep Atlantic [Curry and Oppo, 2005; Marchitto and Broecker, 2006]. However, most simulations from the recent Palaeoclimate Modelling Intercomparison Project contribution to the Coupled Model Intercomparison Project (PMIP4-CMIP6) do not show a change in the depth of the NSW from preindustrial to LGM conditions, of which two show a deep reaching NADW cell down to the sea floor while four simulate the presence of some AABW in the North Atlantic [Kageyama *et al.*, 2020].

Gebbie [2014] performed a water mass decomposition for the LGM and found that albeit the core of the NSW shoaled and SSW extended into the deep Atlantic in greater quantities, the depth of the deep interface of NSW was not that different than the modern one. In a reconstruction based on Nd isotopes, Howe *et al.* [2016a] concluded that there was a greater influence of SSW in the deep Atlantic during the LGM. However, beside GNAIW, there was also a second NSW present, namely Glacial North Atlantic Deep Water (GNADW) which mixed with SSW in the deep North Atlantic.

Another form of NSW to the deep glacial Atlantic was attested by Keigwin and Swift [2017], who postulated the presence of Glacial North Atlantic Bottom Water (GNABW, see Figure 2.3). This relatively young, nutrient depleted and very dense water mass is assumed to form in the Labrador Sea by brine rejection and to underlie the SSW in the

deep Northwestern Atlantic. Nd isotopes corroborate that theory [Pöppelmeier *et al.*, 2018].

The third state of the AMOC is associated with Heinrich Events (off mode). Due to the large inputs of freshwater originating of catastrophic iceberg discharges, the deepwater formation is considered to cease and the AMOC to reduce substantially [Rahmstorf, 2002; Böhm *et al.*, 2015; Henry *et al.*, 2016].

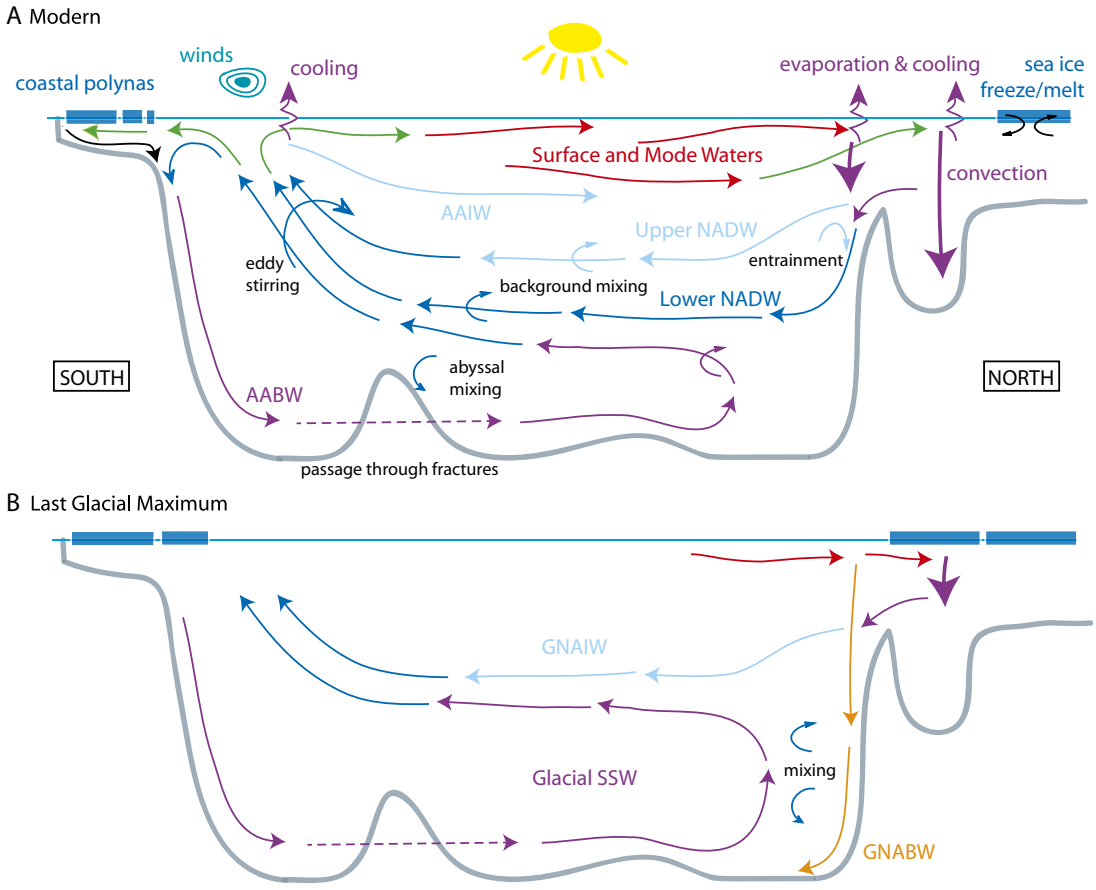

Figure 2.3: Schematics of the AMOC during (A) modern and (B) LGM state. See text for details regarding GNAIW and GNABW during the glacial circulation state. Modified after Matsumoto [2017, p. 2795].

Last glacial cycle at the Bermuda Rise

The Bermuda Rise in the northwestern Atlantic is a well-studied region of past AMOC variability during the last glacial cycle. Besides classical nutrient-type tracers, the ratio $^{231}Pa/^{230}Th$ as an indicator of the strength of the AMOC as well as Nd isotopes as tracer for the water mass provenance were covered in several studies (see Figure 2.4) [McManus *et al.*, 2004; Lippold *et al.*, 2009; Roberts *et al.*, 2010; Gutjahr and Lippold,

2011; Böhm *et al.*, 2015; Henry *et al.*, 2016; Deaney *et al.*, 2017; Lippold *et al.*, 2019].
During both the LGM and the penultimate glacial maximum, the Bermuda Rise was bathed by a higher proportion of SSW and the cold mode prevailed. Not only during the Heinrich Stadials associated with the deglaciations, but also during other Heinrich Events that were associated with iceberg discharges from the Hudson Strait, the AMOC considerably reduced in accordance with the off mode. However, the presence of SSW was rapidly replaced by NSW during Termination II and I, of which the latter was characterized by a short setback during the Younger Dryas. The interglacials were characterized by an active and deep overturning circulation (warm mode), which also lasted for most of the last glacial cycle, even after the actual interglacial came to an end.

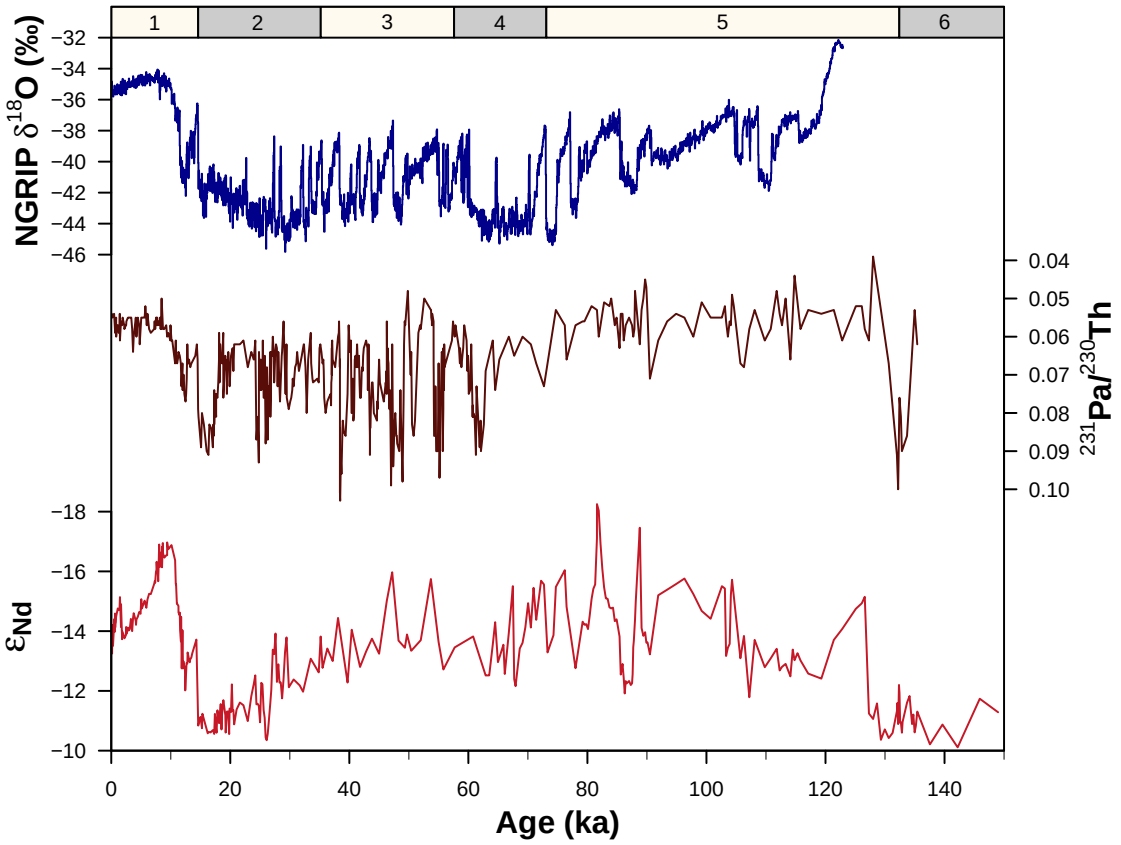

Figure 2.4: Paleoclimatic and -oceanographic records of the past 150 ka. (Top): Stable oxygen isotopes from the NGRIP ice core [North Greenland Ice Core Project members, 2004]. (Middle) $^{231}Pa/^{230}Th$ ratio as indicator of AMOC strength [McManus *et al.*, 2004; Böhm *et al.*, 2015; Henry *et al.*, 2016; Lippold *et al.*, 2019] and (bottom) Nd isotopes as water mass provenance tracer [Roberts *et al.*, 2010; Gutjahr and Lippold, 2011; Böhm *et al.*, 2015; Lippold *et al.*, 2019] at the Bermuda Rise.

2.3 Neodymium isotopes

Neodymium is one of the lanthanoids, which belong to the group of Rare Earth Elements (REE). It has seven natural isotopes with masses ranging from 142 to 150 u [Böhlke *et al.*, 2005], that are all stable or quasi-stable on geological timescales [O'Nions *et al.*, 1979]. Three of the isotopes – ^{143}Nd, ^{144}Nd, and ^{145}Nd – are radiogenic, meaning they are a decay-product of their mother isotope ^{147}Sm, ^{148}Sm, and ^{149}Sm, respectively. However, due to the long half-lives in the order of 10^{16} a, the decay of the latter two isotopes doesn't lead to an enrichment of their daughter isotopes on geological timescales. In contrast, ^{147}Sm decays with a half-life of only about $1.06 \cdot 10^{11}$ a [Lugmair and Marti, 1978], which leads to a slight accumulation of ^{143}Nd.

2.3.1 From the continents to the ocean

Despite both Sm and Nd being REEs and therefore having similar chemical properties, they have different ionic radii and thus are heterogeneously compatible with the structure of various minerals. During the formation of crust these elements fractionate as Sm tends to stay in the mantle while Nd gets enriched in the partial melt. The resulting crust formed from that partial melt has therefore a lower ratio of Sm/Nd in contrast to the mantle which has a higher Sm/Nd ratio [e.g. Goldstein and Hemming, 2003]. As ^{143}Nd is a decay product of ^{147}Sm, the continental ratio of ^{143}Nd/^{144}Nd therefore varies according to the initial Sm/Nd ratio and the age of the crust [Frank, 2002]. Old cratons like the Canadian Shield have very low ^{143}Nd/^{144}Nd ratios while on the opposite young mantle derived crust, like it is found in Iceland, has a high ratio. However, as the differences in the ratios are small, the ratio is expressed in ε-notation [DePaolo and Wasserburg, 1976]:

$$\varepsilon_{Nd} = \left[\frac{\left(^{143}Nd/^{144}Nd\right)_{sample}}{\left(^{143}Nd/^{144}Nd\right)_{CHUR}} - 1 \right] \cdot 10^4 \tag{2.1}$$

As a reference, the *Chondritic Uniform Reservoir* (CHUR) is used as it is assumed that the bulk Earth has the same Sm/Nd ratio as it is found in chondritic meteorites. The present-day value for $(^{143}\mathrm{Nd}/^{144}\mathrm{Nd})_{\mathrm{CHUR}}$ is 0.512638 [Jacobsen and Wasserburg, 1980]. Hence old continental crust has low, negative $\varepsilon_{\mathrm{Nd}}$ values as low as -56, which are called unradiogenic, in contrast to younger crust, which has higher – so called radiogenic – $\varepsilon_{\mathrm{Nd}}$ values up to +12 at recent mid-oceanic ridges [Jeandel *et al.*, 2007]. An overview of

the recent Nd isotopic composition of the continents is shown in Figure 2.5.

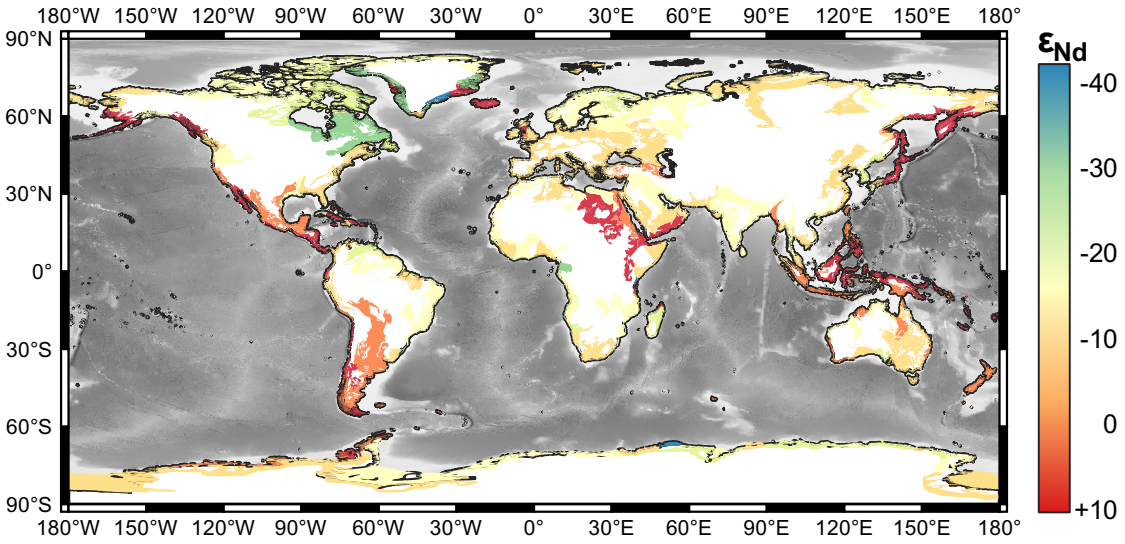

Figure 2.5: Nd isotopic composition on the continents. Adapted after Robinson *et al.* [2021] with bathymetry based on the ETOPO1 Global Relief Model [Amante and Eakins, 2009].

The continental signal of Nd isotopes gets imprinted into the ocean. There, the trivalent element Nd hydrolyses easily and is therefore very particle-reactive [Bau and Koschinsky, 2006]. In dissolved form in seawater at a pH of 8, it forms monocarbonate ($NdCO_3^+$) and dicarbonate ($Nd(CO_3)_2^-$) complexes, whereby the former slightly predominates [Byrne, 2002; Bau and Koschinsky, 2006]. In general, the concentration of Nd increases with depth in most regions with the exceptions of marginal seas and areas with modified particle-seawater dynamics and/or strong convection [van de Flierdt *et al.*, 2016]. For example, NADW has a Nd concentration of (20.3 ± 3.2) pmol/kg, whereas close to continental inputs an enhancement in the Nd concentration of up to 150 pmol/kg is found in surface waters [Tachikawa *et al.*, 2017]. Different processes with geographically varying importance are responsible for how the seawater gains its Nd isotopic composition. An overview of these processes is given in Figure 2.6 and they are described in detail in the following.

Riverine input is thought to be one of the most important sources of Nd to the oceans [Rousseau *et al.*, 2015; Jeandel, 2016]. Continental crust and soils get physically as well as chemically weathered and eroded, and transported to the ocean by rivers either in dissolved, colloidal or particulate form [Frank, 2002; Jeandel and Oelkers, 2015; Jeandel, 2016]. The latter can again be divided into the bed load, which accounts to a global flux of annually 1.6–10 Pg released to the oceans [Walling, 2006], and the

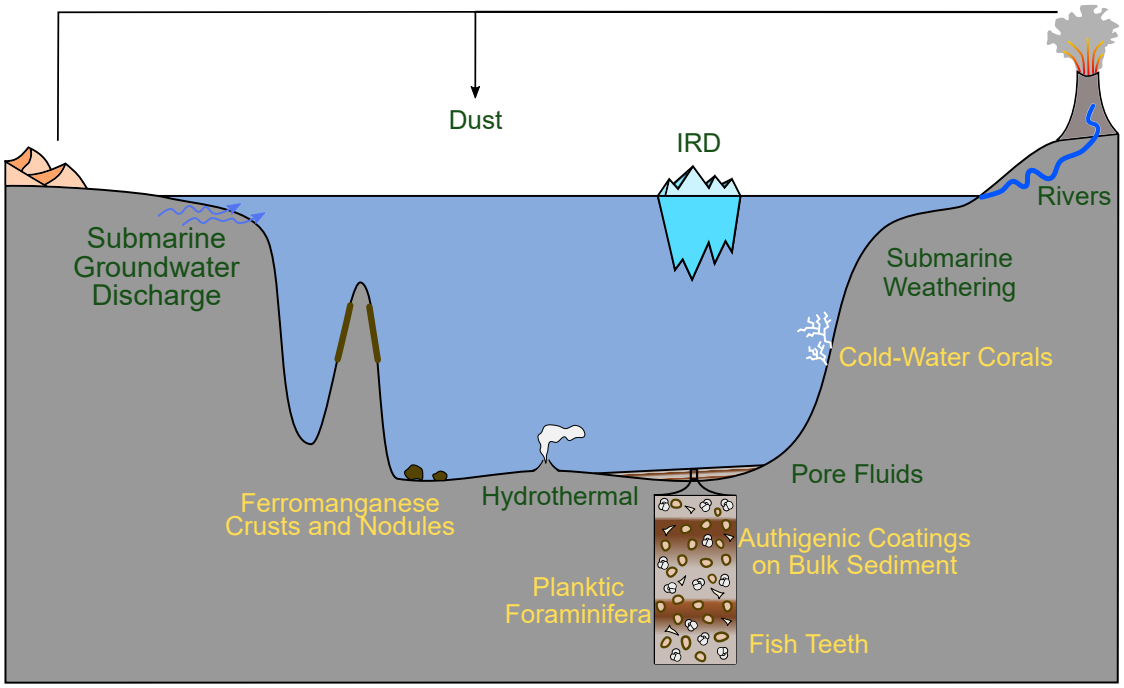

Figure 2.6: Schematic sketch of sources of Nd to the ocean (in green) and archives which can be used to reconstruct the past seawater Nd isotopic composition (in yellow). See text for detailed information about the significance of the individual sources (Section 2.3.1) and the assets and drawbacks of the various archives (Section 2.3.3).

suspended flux, which is in the order of 18.5 Pg per year [Peucker-Ehrenbrink, 2009]. In contrast, the global dissolved riverine flux is about one order of magnitude smaller ($\sim$1 Pg per year [Jeandel and Oelkers, 2015, and references therein]), whereof Nd makes up 1.7 Gg per year [Goldstein and Jacobsen, 1987]. However, about 70% of the dissolved Nd gets removed inside the estuaries, so that eventually approximately 500 Mg per year of dissolved Nd end up in the oceans [e.g. Goldstein and Jacobsen, 1987; Rousseau *et al.*, 2015]. That is about one order of magnitude smaller than the estimate for the Nd component released by suspended particulate matter of about 5700 ± 2600 Mg per year [Rousseau *et al.*, 2015].

Not only is material directly deposited at the mouth of rivers a dominant source of Nd, but also the sediments deposited at the margins of the continents. Through submarine weathering, a portion of the lithogenic particles gets dissolved and supplies Nd to the seawater [e.g. Arsouze *et al.*, 2009; Pearce *et al.*, 2013; Jeandel, 2016]. The influence of this process decreases with increasing distance from the continental margin [Pearce *et al.*, 2013].

In addition, submarine groundwater discharge was proposed as another source for Nd to the oceans [Johannesson and Burdige, 2007]. In subterranean estuaries, fresh

terrestrial groundwater and salty seawater get mixed and discharge as undersea springs and seeps across the seafloor [Kim and Kim, 2014]. It was shown that this formerly underestimated source can have an impact both on the concentration as well as on the isotopy of Nd in coastal and surface seawater [e.g. Kim and Kim, 2014; Chevis *et al.*, 2015; Fröllje *et al.*, 2016; Johannesson *et al.*, 2017]. However, data is still scarce and further studies are needed to better understand the role of submarine groundwater discharge on the global Nd budget [Jeandel, 2016].

Wind-transported particles are another source of Nd. They either originate from the erosion of continental crust and subsequent aeolian transport or stem from volcanic activity [Frank, 2002]. Annually a total of about 450 Tg of dust is transported globally to the oceans of which about 43 % are deposited solely in the North Atlantic [Jickells *et al.*, 2005]. However, its role regarding the Nd budget of the oceans is still under debate [Fröllje *et al.*, 2016; van de Flierdt *et al.*, 2016], as on the one hand some studies show no or only little influence of dust [van de Flierdt *et al.*, 2004; Hongo *et al.*, 2006]. On the other hand, an impact on the surface waters Nd isotopy and concentration was traced back to dust particles at least under high input conditions [Stichel *et al.*, 2015; Fröllje *et al.*, 2016].

Recently, sediment pore fluids were proposed as a source for Nd to the oceans [Haley *et al.*, 2004, 2014; Abbott *et al.*, 2015a,b, 2016; Haley *et al.*, 2017]. During diagenesis, REE are suggested to be released into the pore fluids and finally influence the bottom water ε_{Nd} signatures. However, this process seems to be regionally restricted, as no impact has been detected in other studies [Fröllje *et al.*, 2016; Laukert *et al.*, 2017; Grasse *et al.*, 2017; Blaser *et al.*, 2019]. It was suggested that an influence of pore fluids may be masked by high ventilation rates of water masses, as their exposure times to the benthic flux of Nd are low [Haley *et al.*, 2017].

Hydrothermal activity, however, does not play an important role as a source for Nd on a global scale. In fact, despite hydrothermal fluids having a Nd concentration two to three orders of magnitude higher than typical seawater [e.g. Michard *et al.*, 1983; James *et al.*, 1995], Nd concentrations inside the hydrothermal plume itself are even depleted [Stichel *et al.*, 2018]. This points to an enhanced removal of Nd by scavenging and emphasizes hydrothermal activity to be a net sink for Nd [German *et al.*, 1990; Halliday *et al.*, 1992; Stichel *et al.*, 2018], which can account to a removal of 6–8 % of the global Nd flux added to the oceans [Stichel *et al.*, 2018]. The neodymium isotopic composition of the water changes from highly radiogenic values directly at the vent towards more unradiogenic values inside the hydrothermal plume due to admixture

of ambient seawater after the initial Nd removal [Chavagnac *et al.*, 2018]. In another study, Stichel *et al.* [2018] found only slightly more radiogenic ε_{Nd} values inside the hydrothermal plume compared to the surrounding seawater and attribute this increase to the exchange of hydrothermal particles with seawater. Outside the plume, no impact on the Nd isotopic composition was detected [Stichel *et al.*, 2018], supporting the view that hydrothermal activity has only a local impact on Nd isotopes.

For glacial time periods, ice-rafted debris (IRD) was proposed as another source for Nd [Roberts and Piotrowski, 2015; Blaser *et al.*, 2019]. Icebergs deliver freshly eroded material to the open ocean as they melt. While sinking through the water column, both fine grained glacial flour and volcanic IRD alter the Nd isotopic composition and therefore re-label the water mass. However, the spread of this signal over long distances along the flowpaths still needs to be further tested [Roberts and Piotrowski, 2015]. A modeling study [Vogt-Vincent *et al.*, 2020] confirmed the possibility of IRD causing a non-conservative behavior in ε_{Nd} through changes in the scavenging intensity.

The processes happening on the continent-ocean interface, i.e. submarine weathering and groundwater discharge, pore fluids, and dissolution of solid river discharge, are often compiled in the term *boundary exchange* [Jeandel, 2016]. This term was introduced by Lacan and Jeandel [2005b] to address the so called *Nd paradox* [Tachikawa *et al.*, 2003; Goldstein and Hemming, 2003]. It describes the discrepancy between altering the Nd isotopic composition but not changing the concentration of Nd while a water mass flows along a continental margin. Together with boundary scavenging as a sink term, the abovementioned processes illustrate a pathway to resolve this conundrum [Arsouze *et al.*, 2009; Jeandel, 2016].

2.3.2 Nd in the Atlantic Ocean

Nd isotopes are considered a quasi-conservative tracer of water masses [e.g. Frank, 2002]. The continental signal is imprinted into the oceans and water masses acquire their typical ε_{Nd} signature. The most unradiogenic waters with ε_{Nd} values of -26.6 are found in the Baffin Bay [Stordal and Wasserburg, 1986], while on the other extreme, the most positive values were measured in the Eastern Equatorial Pacific with ε_{Nd} of +4.3 [Grasse *et al.*, 2017]. As the residence time of Nd is smaller than the global mixing time of the oceans (360–700 a vs. $\sim$1500 a; Tachikawa *et al.* [2003], Siddall *et al.* [2008], Rempfer *et al.* [2011], Broecker and Peng [1982]), there is not sufficient time to globally homogenize the signal and hence, water masses can be distinguished regarding

their provenance. The Nd isotopic composition of water masses deeper than 1500 m generally reflects water mass mixing, however local to regional effects can alter this concept, especially along continental margins [Tachikawa *et al.*, 2017].

A latitudinal cross section through the Atlantic can be seen in Figure 2.7. Unradiogenic ε_{Nd} values are found in the Labrador Sea Water (upperLSW: -14.34 ± 0.13, classical LSW: -14.15 ± 0.13), which form the upper NADW [Lambelet *et al.*, 2016]. The overflows from the Greenland-Iceland-Scotland Ridge are originally radiogenic (ISOW: -8.2 ± 1.8, DSOW: -8.3 ± 0.2), but become more unradiogenic as they get exported from the subpolar region and form the middle and lower layers of NADW [Lambelet *et al.*, 2016; van de Flierdt *et al.*, 2016]. In the subtropical North Atlantic, seawater values of -13.2 ± 1.0 for upperNADW and -12.4 ± 0.4 for lowerNADW are recorded [Lambelet *et al.*, 2016], which is in line with a mean value for NADW of -12.3 ± 0.9 found by [Tachikawa *et al.*, 2017]. Opposing those southwards flowing northern-sourced water masses, more radiogenic water masses travel northwards and thereby overlie (Antarctic Intermediate Water, AAIW: -8.6 ± 1.4) and underlie (AABW: -8.6 ± 0.6) the NADW respectively.

However, as mentioned in Section 2.3.1, the way how the water masses exactly gain

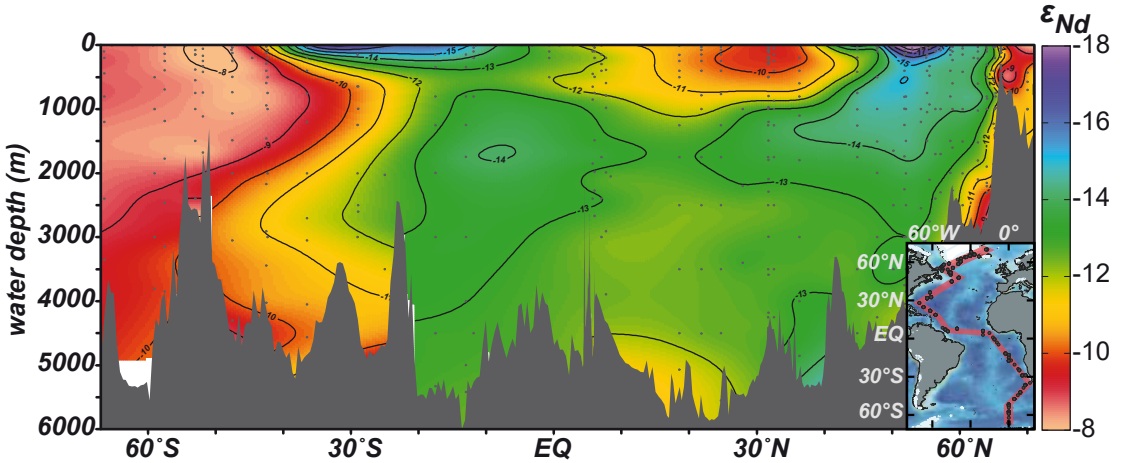

Figure 2.7: Nd isotopic composition of modern seawater along a latitudinal cross section through the Atlantic. Due to the lack of data in the southwestern Atlantic, the cross section switches between ocean basins from the northwestern to the southeastern Atlantic. Data from Piepgras and Wasserburg [1980, 1987]; Lacan and Jeandel [2004a,c, 2005a]; Rickli *et al.* [2009, 2010]; Stichel *et al.* [2012]; Garcia-Solsona *et al.* [2014]; Huang *et al.* [2014]; Rousseau *et al.* [2015]; Lambelet *et al.* [2016]; Filippova *et al.* [2017]; Stichel *et al.* [2018]; Rahlf *et al.* [2020]; Zieringer *et al.* [2019] and visualized with ODV software [Schlitzer, 2019]. Insert map based on the ETOPO1 Global Relief Model [Amante and Eakins, 2009].

their Nd isotopic composition is not understood in all details. The question remains, whether the recent picture of Nd endmembers changed through time as the former view of constant endmembers [van de Flierdt *et al.*, 2006; Foster *et al.*, 2007] got challenged [e.g. Wilson *et al.*, 2014; Struve *et al.*, 2019] (see e.g. Section 5.1).

2.3.3 Archives of the past Nd seawater signal

The past seawater Nd isotopic composition can be reconstructed using different types of archives. Since the end of the 1990s several studies were published which focused on the long-term evolution of Nd isotopes in the ocean basins using ferromanganese crusts and nodules [Abouchami *et al.*, 1997; Burton *et al.*, 1997; Ling *et al.*, 1997; O'Nions *et al.*, 1998; Abouchami *et al.*, 1999; Reynolds *et al.*, 1999; Frank *et al.*, 1999]. The seawater Nd and other trace metals are coprecipitated during the genesis of the crusts and nodules. Koschinsky and Halbach [1995] describe this process in a two-stage colloid-chemical model. First, Mn and Fe from the seawater form mixed colloids in the water column thereby scavenging trace metals by surface adsorption. Heavy REE, which preferentially occur as dicarbonate complexes in seawater, preferentially associate with Fe oxyhydroxides, while light REE in the preferential form of monocarbonate, associate with Mn oxides. Therefore, Nd is associated both with Fe and Mn oxyhydroxides [Bau and Koschinsky, 2006]. During the scavenging process, an exchange equilibrium is established between the Nd complexes and the surface complexes of the Fe and Mn oxides, whereby the concentration of Nd on the Fe and Mn oxides stays constant as long as the concentration and the speciation of dissolved Nd stays the same. However, the isotopic composition of Nd is still changing, as there is still continous ad- and desorption of Nd. This implies that the Nd isotopic composition of the oxide surfaces will represent the local ambient seawater, even when the initial Fe and Mn colloids formed far away from the current location [Bau and Koschinsky, 2006]. In a second step, these colloids precipitate and form amorphous oxide or oxyhydroxide encrustations. The sorbed trace metals either get incorporated by coprecipitation or by solid solution formation into the mineral lattice [Koschinsky and Halbach, 1995]. However, as the ferromanganese crusts grow very slowly, with only 1–15 mm per million years, only studies of low temporal resolution can be conducted as each individual sample from a ferromanganese crust would at least integrate over 10^4–10^5 years [Frank, 2002].

Another authigenic archive for the Nd isotopic composition of past sea water are fossil fish teeth and fish debris, which are assumed to record past Nd isotopes robustly

[e.g. Staudigel *et al.*, 1985; Thomas *et al.*, 2008; Huck *et al.*, 2016]. They consist of hydroxylfluorapatite and contain high amounts of Nd [10^2–>10^3 ppm, Shaw and Wasserburg, 1985; Staudigel *et al.*, 1985]. This is three to six orders of magnitude greater than the concentration found in living fish teeth, which are made of hydroxyapatite [Martin and Haley, 2000]. Hence, they acquire their Nd post-mortem during early diagenesis at the sediment-water interface, while REE exchange with the Ca in the apatite matrix [Arrhenius *et al.*, 1957; Martin and Haley, 2000; Huck *et al.*, 2016]. Thus, Nd isotopes of fossil fish teeth reflect past bottom water instead of the water column value of the fish's habitat depth [Martin and Haley, 2000]. Huck *et al.* [2016] have also shown that the Nd isotopic composition of fossil fish teeth is not affected by changing redox conditions at the core site. However, although fish teeth and debris are widely found in sediment cores, they are not present in every sample and therefore only provide discontinuous records of Nd isotopes.

Fossil foraminifera found in sediment cores do also serve as an recorder for past bottom water Nd. A first down-core record for the past 60 Ma was published in 1986 [Palmer and Elderfield, 1986], though further studies using this archive were only published more than a decade later [Vance and Burton, 1999; Burton and Vance, 2000; Vance *et al.*, 2004; Klevenz *et al.*, 2008]. However, while some studies have suggested the usability of cleaned planktic foraminifera to record the past seawater signal at calcification depth [Vance *et al.*, 2004; Pena *et al.*, 2013], other studies highlighted that even cleaned planktic foraminifera archive the past bottom/pore water Nd signature [Roberts *et al.*, 2012; Tachikawa *et al.*, 2013]. This is based on the fact that only 10–20 % of the Nd is found in the calcite lattice itself [Palmer, 1985; Palmer and Elderfield, 1986; Roberts *et al.*, 2012]. The other 80–90 % of Nd is associated with Nd carrier phases that are acquired by post-mortem processes. Those phases are Fe-Mn oxides attached to the surface of the calcite tests, Fe oxide and oxyhydroxides within the pores and chambers of the foraminifera, which formed by oxidation of Fe sulphides, organic-rich layers in inner tests, and Mn-carbonate precipitates [Roberts *et al.*, 2012; Tachikawa *et al.*, 2013, 2014]. This leads to the conclusion that the ε_{Nd} signature extracted from planktic foraminifera also represent the past bottom/pore water signature [Roberts *et al.*, 2012; Tachikawa *et al.*, 2013, 2014] as already suggested by Palmer [1985]. Therefore, several reconstructions of the past bottom water signal are based on only mechanically cleaned planktic foraminifera, where detrital particles are removed but no further oxidative or reductive cleaning is executed [e.g. Roberts *et al.*, 2010; Elderfield *et al.*, 2012; Pena and Goldstein, 2014; Osborne *et al.*, 2014].

The past seawater signal can also be extracted from deep-sea corals [van de Flierdt *et al.*, 2006; Copard *et al.*, 2010; Colin *et al.*, 2010; Wilson *et al.*, 2014]. An advantage for this archive is that they can be precisely dated by U/Th-dating [Wefing *et al.*, 2017]. However, they do not grow continuously, which often leads to hiatuses in the climatic record. It was shown that scleractinian cold-water corals do robustly record the past seawater signal [van de Flierdt *et al.*, 2010; Struve *et al.*, 2017]. A prerequisite for that is that the fossil samples are thoroughly cleaned and the contaminating phases like ferromanganese coatings or detrital particles are removed. Only the aragonitic skeleton (Nd concentration of only less than 50 ppb [Struve *et al.*, 2017]) is analyzed for its neodymium signature, where inclusions of apatite were recently suggested as an important Nd carrier phase [Struve *et al.*, 2017].

The archives mentioned above all have their advantages and drawbacks. For example, while FeMn crusts on the one hand do have a high Nd content and record the seawater directly, they lack a sufficient high growth rate on the other hand to create suborbital-resolved records. In contrast, corals, which have only a relatively low concentration of Nd, allow for temporally highly resolved reconstructions, however, only for time periods when the corals were actually growing. Fish teeth and foraminifera also have in common that the manually picking of the individual tests is quite a tedious work and they might be not ubiquitous in the sediment column. So to encompass the scarcity of individual specimens and to generate temporal highly resolved reconstructions of the neodymium isotopic signature of the past seawater, another approach is to perform acid-reductive leaching of the bulk sediment itself. First studies which extracted the Fe-Mn oxyhydroxide component of the sediment were published at the beginning of the century [Rutberg *et al.*, 2000; Bayon *et al.*, 2002; Piotrowski *et al.*, 2004] and were based on Chester and Hughes [1967]. As seen at the FeMn crusts, FeMn oxides precipitate from the water column and form either coatings on detrital or biogenic phases (e.g. foraminifera) or form small FeMn-particles themselves [Rutberg *et al.*, 2000]. The goal of the leaching procedure is to extract those coatings while not attacking any detrital phase itself. This is a challenging task, especially in regions, where a lot of easily leachable material is abundant [e.g. Elmore *et al.*, 2011; Wilson *et al.*, 2013; Blaser *et al.*, 2016]. That applies to regions near volcanic islands, like Iceland or the Azores, with positive ε_{Nd} values for material derived from there [Cohen and O'Nions, 1982; França *et al.*, 2006], or regions with fine-grained glacial flour or detrital carbonates originating from the Canadian Shield [Elmore *et al.*, 2011; Blaser *et al.*, 2016]. They can be found near the continental margin and in IRD belts and can have very negative ε_{Nd}

signatures [Grousset *et al.*, 2001]. To deal with the problem of potentially attacking the detrital phases while leaching, recent studies suggested to skip the traditional step of prior sediment decarbonation (as used e.g. by Piotrowski *et al.* [2004] and Gutjahr *et al.* [2007]) and to use only a mild acid [Wilson *et al.*, 2013; Blaser *et al.*, 2016]. Additionally, Blaser *et al.* [2016] recommend to measure the Al/Nd and Sr/Ca ratios in the leachate itself as an indicator for contributions of volcanogenic or other detrital contaminant phases, and of detrital or authigenic carbonate respectively.

—— STUDY I ——

One million years of Nd isotope variability in the deep Northwest Atlantic

3 Material and methods

3.1 Site description

The Bermuda Rise is a height located in the Sargasso Sea in the subtropical western North Atlantic. On its northeastern part, a sediment drift with laminated sediments can be found [Laine and Hollister, 1981]. It is build up by sediment particles from eastern Canadian sources, that are delivered to the Bermuda Rise via the westward directed Gulf Stream Return Flow [Laine and Hollister, 1981]. Here, ODP Site 1063 was drilled at 33°41′N and 57°37′W in 4584 m water depth [Shipboard Scientific Party, 1998] (see Figure 3.1 and Table 3.1 for further details). Hence, it is situated more than 1300 km away from the American continental margin and 680 km east-northeasterly off the Bermuda Islands.

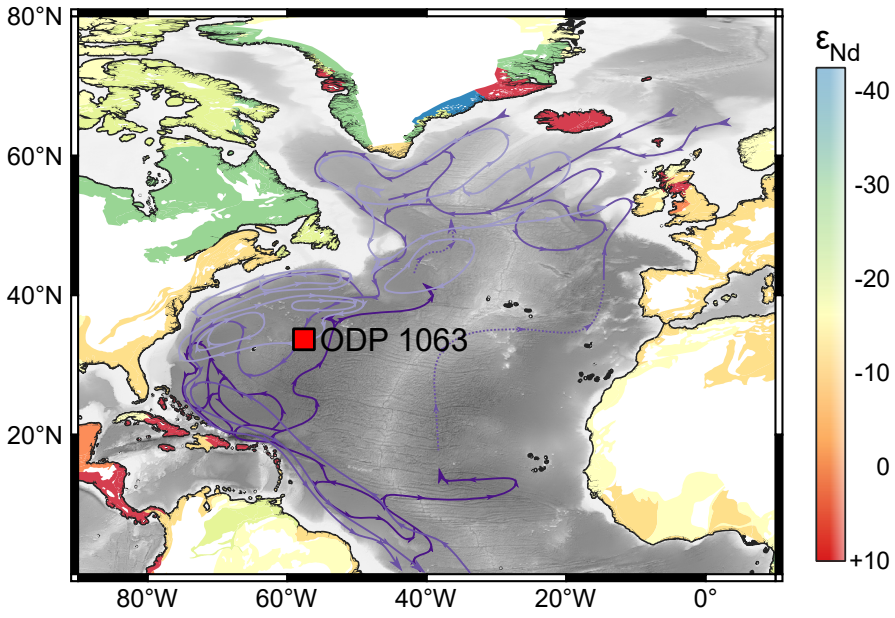

Figure 3.1: Location ODP Site 1063 (red square) together with the Nd isotopic composition of the continents [Robinson *et al.*, 2021]. The modern flow paths of the main intermediate (light purple), lower (purple) and bottom (dark purple) water masses are shown after Schmitz and McCartney [1993]. Bathymetry is based on the ETOPO1 Grid [Amante and Eakins, 2009].

Currently, the core site is situated near the interface of AABW and NADW [Shipboard Scientific Party, 1998] (see Figure 3.2), but is thought to be bathed by SSW during glacial maxima [Keigwin and Jones, 1994; Roberts *et al.*, 2010; Böhm *et al.*, 2015]. High sedimentation rates are recorded at ODP 1063 especially during glacial periods [e.g. Grützner *et al.*, 2002; Channell *et al.*, 2012a]. Therefore, the location is ideally suited to record fluctuations between the mentioned water masses at a high temporal resolution.

The analyzed sediment here in this study (44.89–194.21 mcd[1]), belongs to the lithostratigraphic Subunits IA (down to 182.22 mcd) and IB. The first is characterized by medium light olive gray to greenish gray clay with varying amounts of silt and carbonate- and siliceous-bearing nannofossils. Also the variable presence of dark grayish brown to greenish gray clay with biogenic silica was noted, as well as the appearance of red lutite beds [Shipboard Scientific Party, 1998]. The latter is mainly present in glacial–deglacial intervals and is thought to originate from the Canadian Maritime Provinces, especially from the region of the Gulf of St. Lawrence [Giosan *et al.*, 2002]. Subunit IB is distinguished from IA due to the lower number and lesser extent of the red lutite beds, and the disappearance of biogenic silica [Shipboard Scientific Party, 1998].

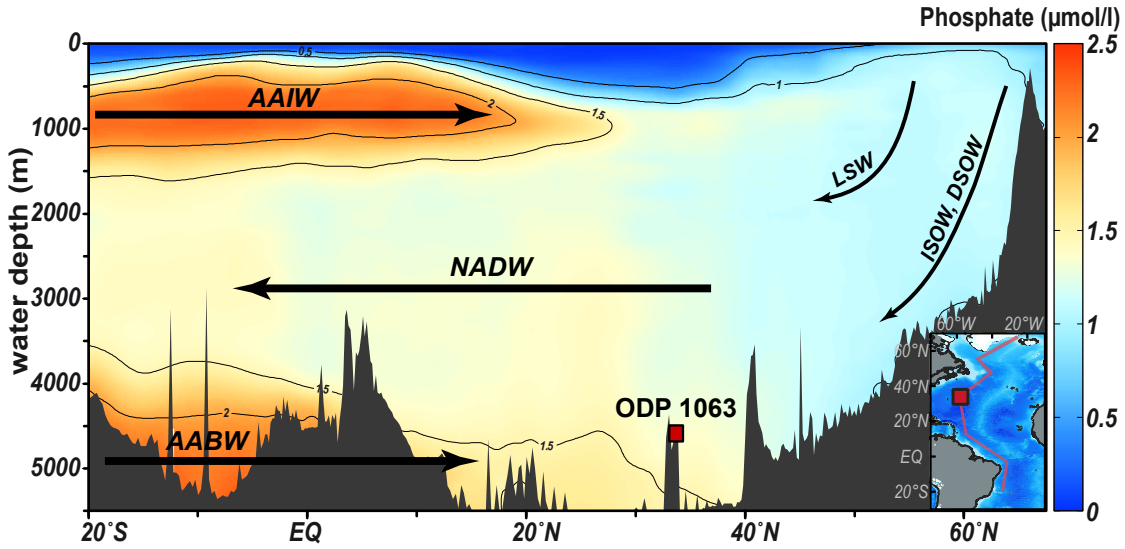

Figure 3.2: Hydrography at ODP 1063 shown as a latitudinal cross section through the Atlantic using annually averaged World Ocean Database phosphate data [Boyer *et al.*, 2013]. Data visualized with ODV software [Schlitzer, 2019]. Insert map based on the ETOPO1 Global Relief Model [Amante and Eakins, 2009].

[1]mcd: meter composite depth.

Table 3.1: Coordinates of the holes drilled at ODP Site 1063 [Shipboard Scientific Party, 1998]. As the individual holes are 18–61 m apart from each other, differences in the thickness of individual sediment packages could appear.

Site	Hole	Latitude	Longitude	Water depth (m)
ODP 1063	A	33°41.204′N	57°36.898′W	4583.5
	B	33°41.189′N	57°36.898′W	4583.0
	C	33°41.181′N	57°36.903′W	4584.1
	D	33°41.172′N	57°36.907′W	4584.3

3.2 Age model

ODP 1063 is a well studied site for which different age models are already published. Grützner *et al.* [2002], for example, established their age model for the past 900 ka by using the color reflectance data of the sediment and thereby the predicted $CaCO_3$ content. Both the raw, and the band-pass filtered carbonate content was correlated to the ones of the reference site ODP 1062east, which in turn was correlated to the obliquity and precession signal of La90 [Laskar, 1990].

Channell *et al.* [2012a] used a tandem fitting of planktic $\delta^{18}O$ values, and relative paleointensity (RPI) of the ancient magnetizing field to the reference curves LR04 [Lisiecki and Raymo, 2005] and PISO [Channell *et al.*, 2009]. However, this age model also reaches back only to 900 ka.

The age model of Poirier and Billups [2014] covers the time interval 247–1027 ka. It uses a composite record of benthic $\delta^{18}O$ data [Poli *et al.*, 2000; Ferretti *et al.*, 2005; Billups *et al.*, 2011; Poirier and Billups, 2014], which was aligned to the LR04 [Lisiecki and Raymo, 2005].

Since it is common in the recent literature to use the LR04 [Lisiecki and Raymo, 2005] as a reference stack for the benthic $\delta^{18}O$ records of the individual cores, this strategy was chosen for the age model in this thesis. Therefore, the age model of Poirier and Billups [2014] was applied for the sediment deeper than 63.88 mcd, corresponding to 263.1 ka. For the sediment interval 44.69–63.69 mcd, new benthic $\delta^{18}O$ data (see Section 3.2.1 for further details and Table C.3 for data) produced here was combined with the published data of Billups *et al.* [2011]. The combined $\delta^{18}O$ record was tuned to the LR04 [Lisiecki and Raymo, 2005] with minima, maxima and rapid transitions as tie points using the *R* package *Astrochron* [Meyers, 2014] which is based on Paillard *et al.*

[1996]. Hence, a consistent and continuous age model was created for the time interval studied in this thesis.

3.2.1 Benthic foraminiferal stable oxygen isotopes

Between 44.69 and 63.69 mcd, benthic foraminifera of the species *Cibicidoides wuellerstorfi* and *Oridorsalis umbonatus* were handpicked for stable oxygen isotope analysis. They were measured at the Institute of Earth Sciences, Heidelberg University, using the isotope ratio mass spectrometer (IRMS) Thermo Fisher MAT 253plus with a Kiel IV device. Isotopic ratios are given in ‰ relative to VPDB.

In cases where tests of *C. wuellerstorfi* were present, this species was used for the δ^{18}O record. The disequilibrium between the foraminiferal calcite and the seawater was accounted for by applying a correction of +0.64 ‰ [Shackleton and Hall, 1984]. In some cases, where only *O. umbonatus* was available, the δ^{18}O values were first corrected to *C. wuellerstorfi* by -0.43 ‰ (mean of the differences of 45 paired measurements of both species) and afterwards corrected by +0.64 ‰ [Shackleton and Hall, 1984].

3.2.2 Depth alignment of the sampled cores to the splice

At most of the ODP/IODP sites, several holes are drilled in order to recover the full sediment column. In order to compare the sediments recovered from the individual holes, a common depth scale has to be established, expressed here as meter composite depth (mcd). At ODP Site 1063, this was done through inter-hole correlation using the color reflectance data (Lightness, L*, as well as chromaticity, a* and b*), the magnetic susceptibility and the gamma ray attenuation porosity evaluator (GRAPE) density (the latter only down to a depth of $\sim$180 mcd) [Shipboard Scientific Party, 1998]. In doing so, a constant depth offset is added to the individual cores. To get a stratigraphically continuous record, a splice is created, which uses tranches of different holes.

The published δ^{18}O records [Poli *et al.*, 2000; Poirier and Billups, 2014; Ferretti *et al.*, 2005; Billups *et al.*, 2011] rely on samples which were taken from the splice. Unfortunately, not all samples processed for ε_{Nd} in this thesis are from the splice. Therefore the individual core sections need to be aligned to the splice to compensate for expansion and compression during for example the drilling process or differences in the thickness of individual sediment layers. For this purpose, the lightness or magnetic susceptibility data of the individual cores were tuned to the ones of the splice. This was done using the *R* package *Astrochron* [Meyers, 2014], which is based on Paillard

et al. [1996]. The depth of those aligned samples is given as adjusted mcd (amcd). The shift of the sample depths ranges from −28 cm (D8H6W 8-10 cm) to +42 cm (D9H1W 8-10 cm) and the most extreme age shifts result in −4.5 ka (D8H7W 38-40 cm) and +6.1 ka (D9H1W 8-10 cm). A detailed listing of these aligned cores and the used tie points is given in Appendix A.1.

3.3 Benthic foraminiferal stable carbon isotopes

In the course of the measurement of stable oxygen isotopes of benthic foraminifera for refining the age model (see Section 3.2.1), stable carbon isotopes were also determined on the same samples. In analogous procedure to $\delta^{18}O$, $\delta^{13}C$ values of *C. wuellerstorfi* were used, where this species was present. As *C. wuellerstorfi* precipitates its shell close to $\delta^{13}C$ equilibrium, no adjustment factor needs to be applied [Mackensen *et al.*, 1993]. In cases where only *O. umbonatus* tests were available, the $\delta^{13}C$ values were corrected to *C. wuellerstorfi* by +1.42 ‰, which corresponds to the mean of the differences of 45 paired measurements of both species.

3.4 Sample treatment for Nd isotopes

ODP 1063 was sampled 510 times beginning from 44.89 mcd (B5H4W 55-57 cm) down to 194.21 mcd (B20H3W 89-91 cm) in 1 or 2 cm thick sediment slices.

3.4.1 Bulk sediment leaches

To extract the past seawater ε_{Nd} signal, the bulk sediment leaching technique following Blaser *et al.* [2016] was applied to the sediment samples. In short, 0.25–0.30 g of freeze-dried and ground bulk sediment gets rinsed with high purity water (MilliQ 18.2 MΩ). Afterwards the acid-reductive leaching solution is added, which consists of 0.26 M acedic acid, 0.005 M hydroxylamine hydrochloride, and 0.003 M Na-EDTA buffered to pH4. However, in contrast to Blaser *et al.* [2016], ammonia instead of sodium hydroxide was used to buffer the leaching solution, thereby bypassing the addition of excess Na [see Pöppelmeier *et al.*, 2018; Blaser *et al.*, 2019]. After one hour of gentle shaking and rotating, the samples get centrifuged and the supernatant decanted into Teflon vials. In a clean-lab environment, Nd was purified from the other leached elements via a two-step ion exchange column chromatography following standard procedures [Cohen *et al.*, 1988]. First, REEs got separated using DOWEX 50WX8 (200-400 mesh)

resin. The purification of Nd was achieved with TRISKEM LN-B50A resin (100-150 µm) [Pin *et al.*, 1994]. The processing of the sediment samples by bulk sediment leaching was performed at the *Institute of Environmental Physics* and the *Institute of Earth Sciences*, Heidelberg University, Germany.

3.4.2 Foraminifera analyses

In addition, at 8 selected depths mixed planktic foraminifers were hand picked. In some cases, where the amount of foraminifera would have been too small for ε_{Nd} analysis, samples from the same depth range but different holes were combined. A maximum distance of 8 cm (corresponding to 0.6 ka for those samples) was accepted, as this is still in the range of a typical bioturbation length [Trauth *et al.*, 1997]. The samples were afterwards treated following Osborne *et al.* [2014]. In summary, the foraminifera tests were cracked between glass plates to open all chambers. Afterwards, the samples were washed at least five times with high purity water (MilliQ) and once with methanol to get rid of any lithogenic particles. Any contaminating remains were removed under a microscope. Subsequently, the foraminifera fragments were dissolved in 0.3 M HNO_3 and transfered to a clean-lab environment. During a two-step column chromatography, the REE were separated using AG 50WX12 (200-400 mesh) resin [Barrat *et al.*, 1996] and Nd got purified using Ln Spec (50-100 µm) [Le Fèvre and Pin, 2005]. All foraminifera samples were processed at *GEOMAR Helmholtz Centre for Ocean Research Kiel*, Germany.

3.4.3 Measurements of Nd isotopes

Before the measurement of the abundance of the different Nd isotopes, the samples were checked for their concentration of Ca, Ba, Ce, Pr, Nd, and Sm on an inductively coupled plasma quadrupol mass spectrometer (ICP-Q-MS, Thermo Fisher iCap Q) at the *Institute of Environmental Physics*, Heidelberg University. Thus, matrix elements were monitored and the Nd concentration could be adjusted to a target value of typically 50 ppb.

The measurements of the neodymium isotopic composition were performed on three different multi-collector inductively coupled mass spectrometers (MC ICP-MS), one at the *Institute of Environmental Physics*, Heidelberg University (Thermo Fisher Neptune Plus), and two at the *GEOMAR Helmholtz Centre for Ocean Research Kiel*, Germany (Thermo Fisher Neptune Plus and Nu Instruments). The raw data was corrected to $^{146}Nd/^{144}Nd = 0.7219$ using an exponential mass bias law to account for

instrument-induced mass fractionation. Subsequently, the corrected data was normalized to $^{143}Nd/^{144}Nd = 0.512115$ of the bracketing JNdi-1 standard solutions [Tanaka *et al.*, 2000]. The samples were corrected for the influence of Ce hydride formation on the $^{143}Nd/^{144}Nd$ ratio, which was assessed during each measurement session by a series of Ce spiked standards. The results are reported in the ε-notation (see Equation (2.1)). For each sample, the internal error is given as 2 SEM of the respective measurement. Additionally, the external reproducibility for each measurement session was assessed by repeated measurements of secondary standard solutions (2 SD).

4 Results

In total, 576 samples were measured for the Nd isotopic composition in the depth interval 44.89–194.21 mcd including 48 samples already produced in Link [2015]. The samples originate from 510 different depths, from which 45 depths were replicated (see Section 4.1.1). The reconstructed Nd isotopic composition spans a range from ε_{Nd} values of -10.07 ± 0.11 (D18H2W 68–70 cm) to -21.46 ± 0.11 (D12H3W 84–86 cm), with a mean of -14.11 ± 1.93 (1 SD) (see Figure 4.1). Total procedural blanks were always smaller than 148 pg (n=30), which corresponds to a blank contribution of 0.1% to a typical sample, and are therefore negligible. The external reproducibility of different measurement sessions varied between 0.09 and 0.37 ε-units.

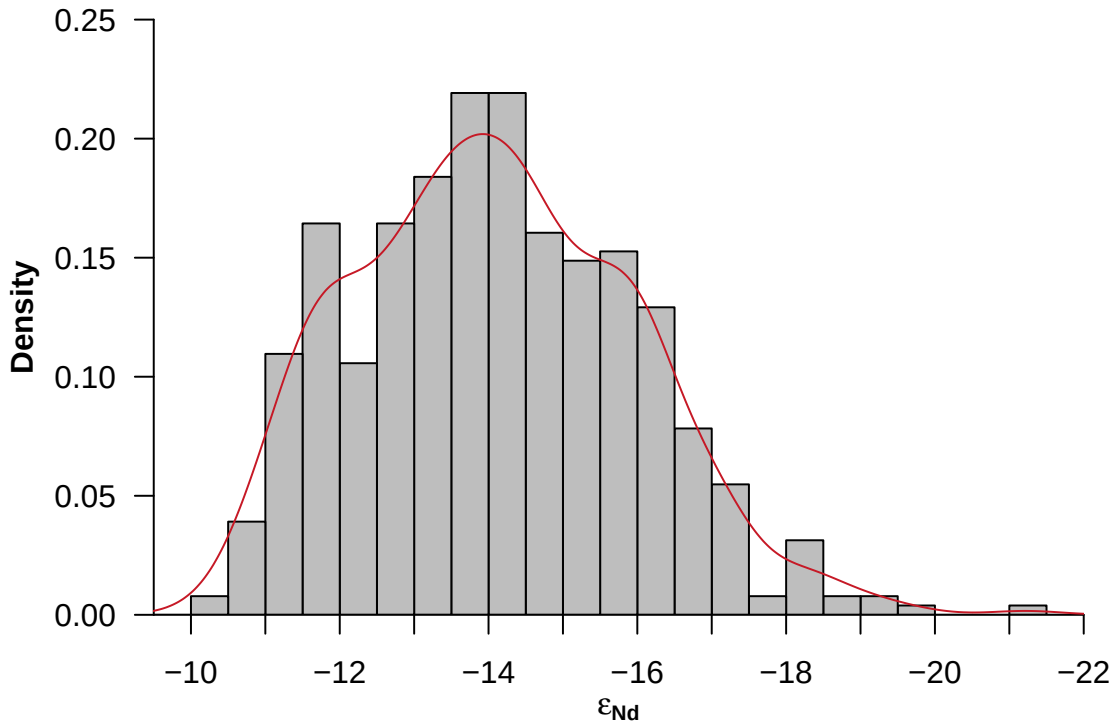

Figure 4.1: Histogram of the ε_{Nd} values recorded at ODP 1063 for the time period older than 149 ka.

4.1 Quality control

In order to reconstruct the Nd isotopic composition at the Bermuda Rise reliably, the quality and comparability of the measured data needs to be examined. For this purpose, on the one hand, sediment samples were repeatedly processed (see Section 4.1.1) to address the reproducibility of the data measured from ODP 1063. On the other hand, the international standard material Nod-A-1 was processed as a quality control and for a comparison with other laboratories (see Section 4.1.2). The reliability of the leaching method is often challenged due to a discrepancy between the Nd isotopic composition of mixed planktic foraminifera and leachates [e.g. Elmore *et al.*, 2011; Crocker *et al.*, 2016]. However, the method used here [after Blaser *et al.*, 2016] is based on a weaker leaching solution, in order to minimize the attack of detrital material, and has provided matching foraminiferal and leachate data [Blaser *et al.*, 2016, 2019; Lippold *et al.*, 2019]. To test whether this is also true for ODP 1063, mixed planktic foraminifera were analyzed and compared to data derived from bulk sediment leaching (see Section 4.1.3). Concluding, to test the comparability with the already published records, selected samples from Böhm *et al.* [2015] and Jaume-Seguí *et al.* [2020] were reproduced (see Section 4.1.4).

4.1.1 Total procedural replicates

The reproducibility of the chosen method for ODP 1063 was tested. Therefore, total procedural replicates of samples from 45 different depths were produced, off which 38 were dublicated, six were triplicated and one target depth was reproduced 17 times (see Figure 4.2). The replicates show an excellent agreement. The individual data points scatter around their respective weighted mean with a two-sigma standard deviation of 0.24 ε-units. Hence, differences between ε_{Nd} values greater than this value can be considered significant.

For some samples, the external reproducibility of a measurement session is bigger than the reproducibility of the total procedural replicates and therefore seems overestimated. Hence, for individual ε_{Nd} values, only the analytical error is reported in this study.

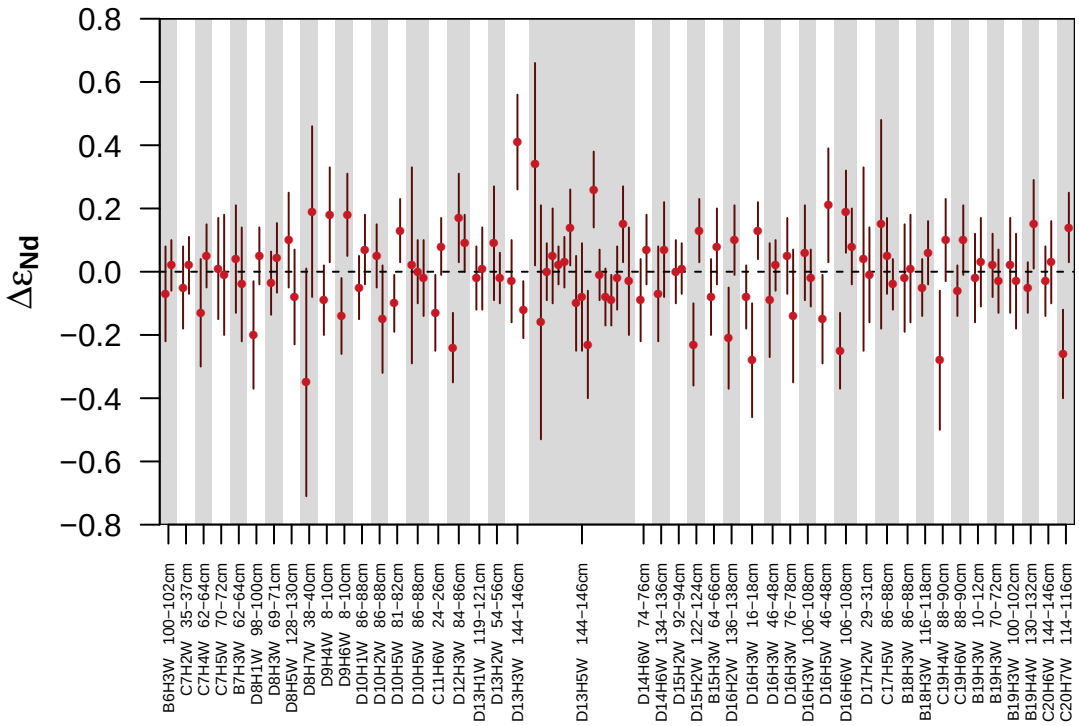

Figure 4.2: Total procedural replicates of ODP 1063. The deviation from the respective weighted mean (dashed line) is given for the data points with their individual analytical errors (2 SEM).

4.1.2 Nod-A-1

To monitor the quality of the sample treatment and measurement, the USGS standard Nod-A-1 [Flanagan and Gottfried, 1980] was processed 9 times. This powder originates from manganese nodules from the Blake Plateau in the Atlantic ocean. The weighted mean Nd isotopic composition of the processed samples was $\varepsilon_{Nd} = -9.50 \pm 0.04$ (for individual data see Table C.4). This is in line with published values of -9.68 ± 0.12 (bulk sediment leaching, Gutjahr *et al.* [2010]), -9.56 ± 0.16 (digestions) and -9.91 ± 0.47 (laser ablation, both Foster and Vance [2006]), and -9.62 ± 2.11 (laser ablation, Xu *et al.* [2018a]) (see Figure 4.3).

4.1.3 Comparison with foraminifera

In order to test the robustness of the leaching technique, the leached values were compared to $\varepsilon_{\mathrm{Nd}}$ values from foraminifera (see Figure 4.4), which are often considered as more reliable for the reconstruction of the Nd isotopic composition of bottom water [e.g. Elmore *et al.*, 2011]. In total, mixed planktic foraminifera from 8 different depths were analyzed for their Nd isotopic signatures. They span $\varepsilon_{\mathrm{Nd}}$ values from -13.90 ± 0.12

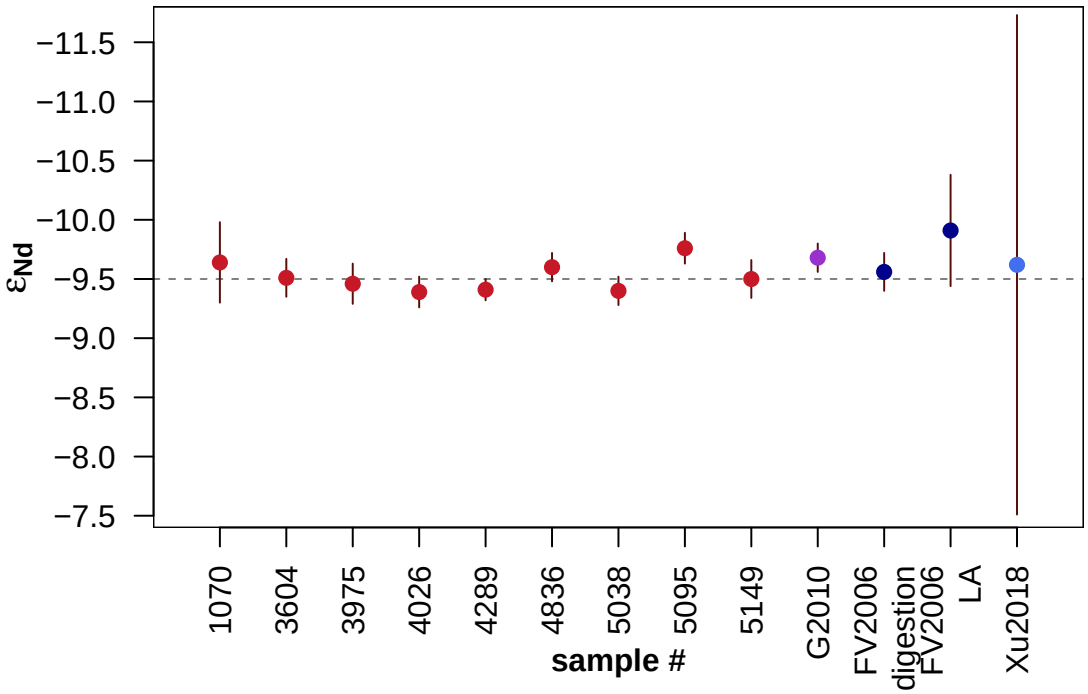

Figure 4.3: Nd isotopic composition of the USGS standard Nod-A-1 for repeatedly processed samples with their analytical errors (2 SEM). The weighted mean of the processed samples (gray dashed line) fits well into the range of the published values of Gutjahr *et al.* [2010] (G2010), Foster and Vance [2006] (FV2006 digestion and FV2006 LA) and Xu *et al.* [2018a] (Xu2018).

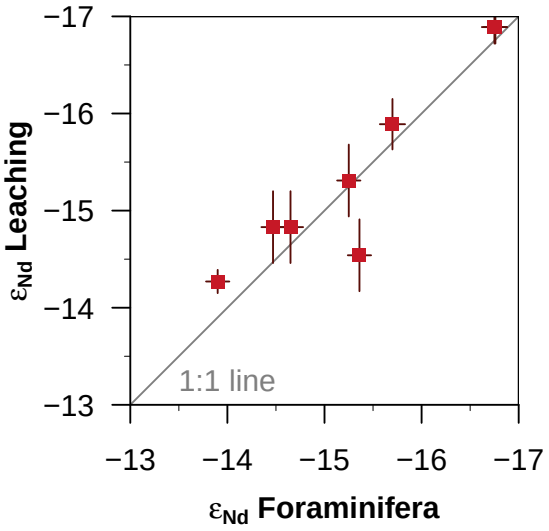

Figure 4.4: Comparison between the Nd isotopic signatures derived from foraminifera and bulk sediment leaching for ODP 1063. Note that the two values near $\varepsilon_{Nd} \approx -17$ are nearly identical and therefore overlap in this plot.

to -16.76 ± 0.12. The total procedural blank was 46 pg and is therefore negligible.

The comparison of the Nd isotopic composition of the foraminifera and from the leaching method, shows a very good agreement. Most data fall on the 1:1–line within their errors. Hence, the data are correlated with a Pearson's r value of 0.93 [0.66; 0.99] (95 % confidence interval). Therefore one can conclude that both methods create consistent results.

4.1.4 Comparison with previous studies

For the Bermuda Rise, there are already records of ε_{Nd} published for the past 150 ka [Roberts *et al.*, 2010; Gutjahr and Lippold, 2011; Böhm *et al.*, 2015; Deaney *et al.*, 2017; Lippold *et al.*, 2019] and very recently for 250-1024 ka by Jaume-Seguí *et al.* [2020]. In order to check the comparability of those records with the data produced in this study, four samples from the study of Böhm *et al.* [2015] and one of Jaume-Seguí *et al.* [2020] were reproduced. Those samples span the full range of typical glacial to interglacial Nd isotopic compositions found in ODP 1063 (see Figure 4.5 and Table C.5 for data). Böhm *et al.* [2015] used a slightly different leaching method with higher concentrated acid and longer leaching time. However, despite the discrepancy in the method, three of the ε_{Nd} values produced here, agree to the ones published in Böhm *et al.* [2015] within their errors. One sample (C4H4W 140–141 cm) shows a very small disagreement between both leached samples (-18.62 ± 0.34, this study vs. -18.03 ± 0.20, Böhm *et al.* [2015]), but a very good agreement with the Nd isotopic composition of planktic foraminifera (-18.58 ± 0.57, Böhm *et al.* [2015]). The Nd isotopic composition of the leached sample and the one of fish debris [Jaume-Seguí *et al.*, 2020] are also in accordance within errors. Therefore, the data produced here, can be directly connected and integrated to the previous published records.

4.2 Nd isotopes of the past one million years

Based on the positive results from the quality control, the existing record of the Nd isotopic composition at the Bermuda Rise [Roberts *et al.*, 2010; Gutjahr and Lippold, 2011; Böhm *et al.*, 2015; Deaney *et al.*, 2017; Lippold *et al.*, 2019] was extended back from 149.1 to 1026.2 ka with an average temporal resolution of 1.7 ka for the new data. Together with the recently published data by Jaume-Seguí *et al.* [2020] for 250-1024 ka, the temporal resolution of the whole one million year record increases to 1.0 ka. It now covers also MISs 6–29 and therefore interesting features of the past climate as

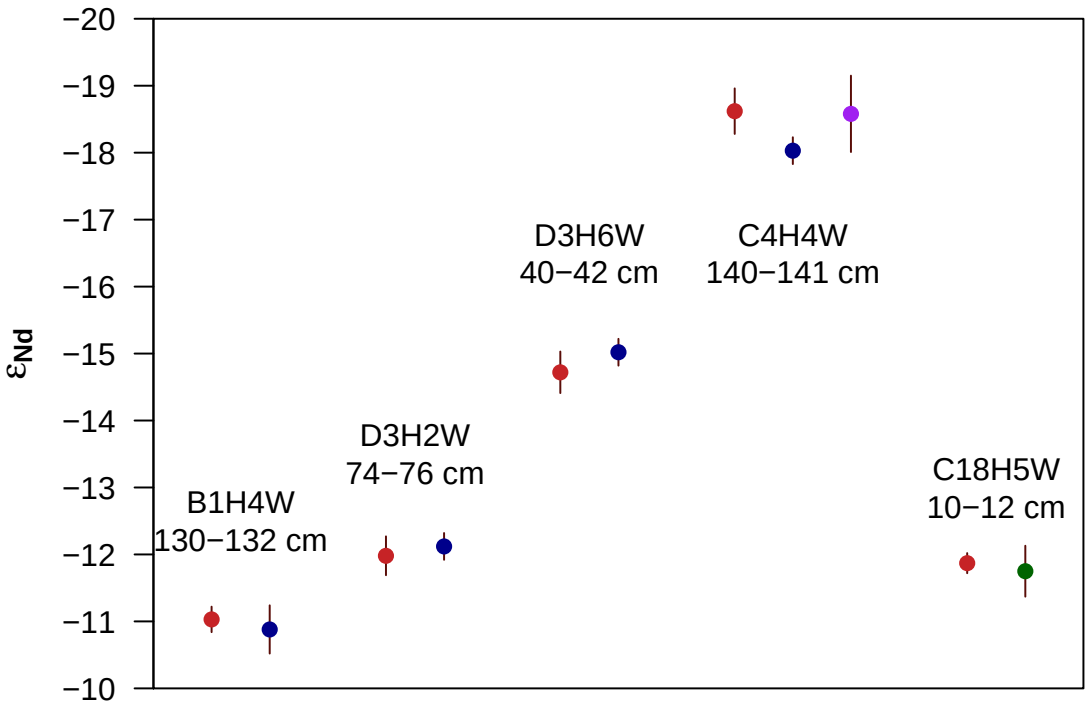

Figure 4.5: Comparison of the Nd isotopic composition produced in this thesis (red) and Böhm *et al.* [2015] (blue: leached; purple: foraminifera) as well as Jaume-Seguí *et al.* [2020] (green: fish debris). The replicates show an excellent agreement.

MIS 11, the lukewarm interglacials and part of the MPT including the 900 ka event (see Section 2.1, Chapter 5, and Figure 4.6).

In the following, the temporal progression of the new data will be described. Starting in MIS 29, the values start with a peak in ε_{Nd} of -19.30 ± 0.18, while afterwards they vary highly temporally with amplitudes of 3–4 ε-units. However, during the more glacial like periods of MISs 28c, 28a and 26, they reach similar values of around -14. After the glacial Termination XII, the Nd isotopic composition at the Bermuda Rise shows a pronounced and prolonged peak with the most extreme values of -19.66 ± 0.10 at 953.3 ka. During the course of MIS 25, they increase to -13.22 ± 0.11 ε_{Nd}, whereas at the end of MIS 25, a short excursion to values of about -16.1 occurs. MIS 24 starts again with values of around -13.21 ± 0.09, however, they again shortly vary with amplitudes

Figure 4.6 ***(following page)*:** (Top) Global benthic $\delta^{18}O$ stack LR04 [Lisiecki and Raymo, 2005] for comparison. Numbers in the boxes indicate the MISs, letters at the curve the substages and roman numbers the glacial Terminations [after Railsback *et al.*, 2015]. (Bottom) Nd isotopic composition at ODP 1063 generated in this thesis for the time period of 150 ka to 1026 ka.

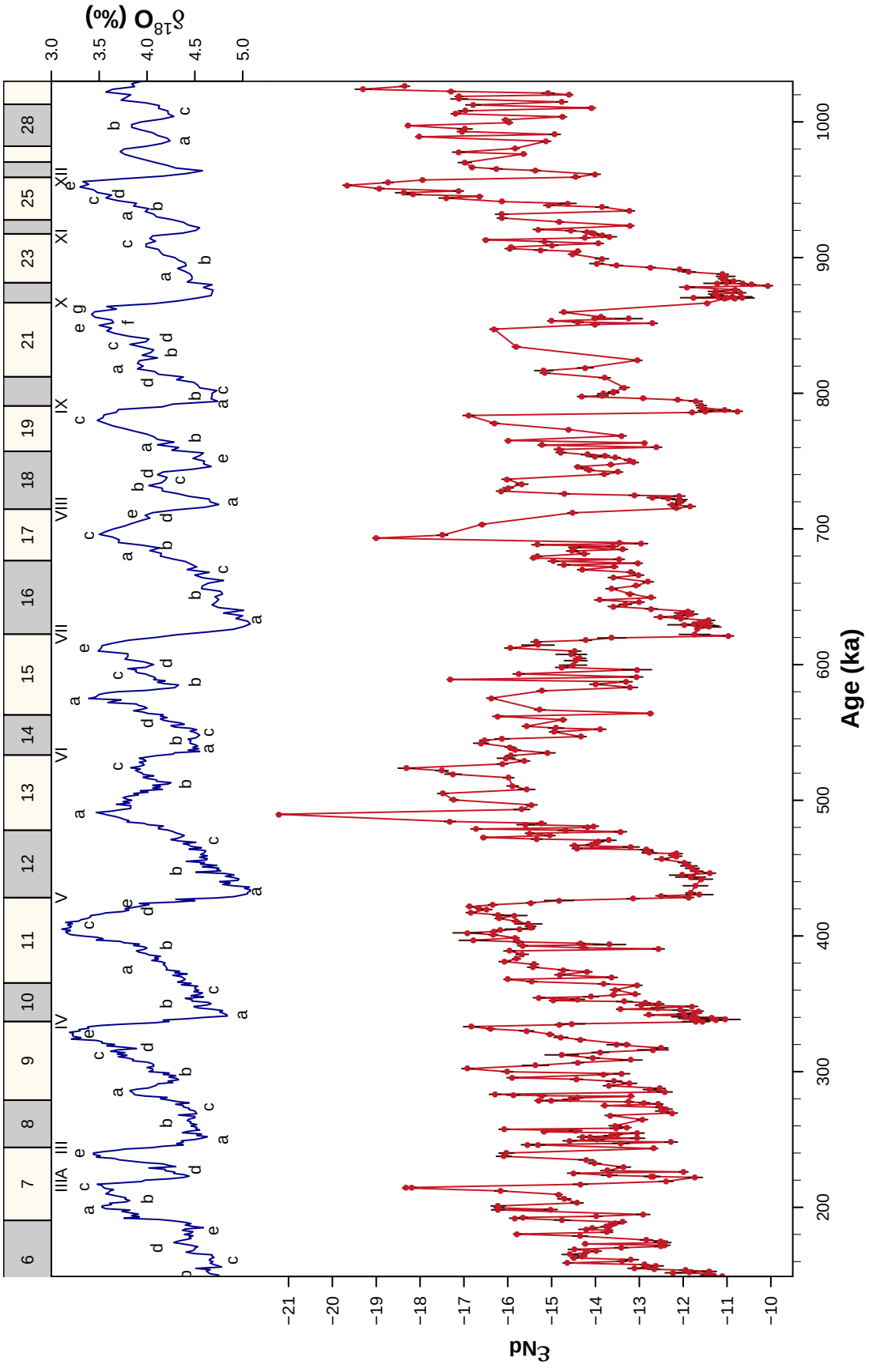
$\delta^{18}O$ (‰)
3.0
3.5
4.0
4.5
5.0
6
7
8
9
10
11
12
13
14
15
16
17
18
19
21
23
25
28
IIIA
III
IV
V
VI
VII
VIII
IX
X
XI
XII
εNd
−21
−20
−19
−18
−17
−16
−15
−14
−13
−12
−11
−10
Age (ka)
200
300
400
500
600
700
800
900
1000

of 2–3 ε-units until including MIS 23c. Hence, the T-XI is not as pronounced as seen at other Terminations. During MIS 23b the Nd isotopic composition increases toward values greater than -13 for the first time. They peak in a long lasting time period with fairly constant ε_{Nd} values around -11 during MISs 23a–22.

Termination X is characterized by an abrupt shift to an ε_{Nd} value of -14.72 ± 0.10. However, there is a second shift in the Nd isotopic composition from -12.70 ± 0.11 to -16.31 ± 0.10 at the transition from MIS 21f to MIS 21e. A third but short peak is occurring during MIS 21a. Afterwards during MIS 20, there is again a transition to more radiogenic values, only shortly interrupted at around 798 ka. At T-IX, the Nd isotopic composition jumps from ε_{Nd} values of -10.76 ± 0.11 to -16.89 ± 0.13 and increases again toward the end of MIS 19c. The rest of MIS 19 is characterized by high frequent short term variations. In the glacial-like substage MIS 18e, an ε_{Nd} value of -13.13 ± 0.13 is reached, which shifts abruptly to ~ -16 during MIS 18b–d. Just as abrupt as the values decreased, they increase again and reach fairly constant radiogenic values of about -12 during MIS 18a.

The following T-VIII turns out to be a gradual decrease in ε_{Nd} until the peak value of -19.00 ± 0.08 is reached during MIS 17c. Then a sharp increase to -12.96 ± 0.15 occurs, which is followed by varying Nd isotopic compositions between -13.0 and -15.4. MIS 16 shows a two-step increase in ε_{Nd} with only slightly fluctuating values around -13.2 and then a gradual increase from -12.0 to-10.97 ± 0.12 during MIS 16a.

This increase ends abruptly at T-VII, where a shift to an unradiogenic Nd isotopic composition happens, that peaks in -15.94 ± 0.13 ε_{Nd} during MIS 15e. After a time period of 12 ka with nearly constant ε_{Nd} values of -14.5, short term fluctuations with amplitudes up to 4 ε-units (-13 to -17) occur. During MIS 15a, the Nd isotopic composition first decreases from -13.21 ± 0.17 to-16.37 ± 0.11 and increases again to -12.75 ± 0.07. In contrast to the other glacials, the increase toward more radiogenic values does not continue. Instead, during MIS 14, the values are more unradiogenic an vary between -13.89 ± 0.13 and -16.61 ± 0.17. The actual T-VI is not apparent in the Bermuda Rise ε_{Nd} record as the starting value essentially lies at -15.09 ± 0.17. During the whole MIS 13, no ε_{Nd} value higher than -15.46 ± 0.13 is recorded. In contrast, three peaks with extreme unradiogenic values of -18.31 ± 0.19, -17.48 ± 0.12, and -21.22 ± 0.06 are occuring. In fact, the latter is by far the most negative ε_{Nd} value that is recorded in ODP 1063.

The first part of MIS 12 is characterized by a gradual transition to radiogenic values, with only three short-term unradiogenic derivations. This trend culminates in

a long-lasting period with only slight variations from -11.39 ± 0.13 to -12.50 ± 0.12. Termination V interrupts this stable period. The ε_{Nd} values abruptly shift again toward -16.87 ± 0.08 during MIS 11c. This substage is described by two pronounced peaks, which are only separated by a small dip of values around -15.5. But apart from that, MIS 11c shows relatively constant values over a long period of time. During MIS 11b excursions toward radiogenic values occur, but which return to values of around -16 during MIS 11a. During the later part of that substage, a gradual increase towards more positive ε_{Nd} values starts, which lasts until the complete MIS 10. This trend is only interrupted by two short more unradiogenic anomalies.

Termination IV ends this trend. The ε_{Nd} values change again abruptly from -11.56 ± 0.07 to -16.83 ± 0.18. In the course of MIS 9e, they increase monotonically until they reach their maximum at -12.50 ± 0.15 during MIS 9d. During the rest of MIS 9, the Nd isotopic composition is again highly variable and fluctuates frequently between values of -12.42 ± 0.17 to -16.92 ± 0.13. The first half of MIS 8 records a slight increase of ε_{Nd} values to -12.25 ± 0.12. In the latter half, however, this trend does not continue as expected from the other glacials, but instead shows again highly variable values between -12.93 ± 0.12 and -16.08 ± 0.12. Thus, T-III itself is not recognizable as the other Terminations, as only one radiogenic data point of -12.67 ± 0.09 is preceding. Regardless of the small number of data, there is a switch to unradiogenic values of -16.03 ± 0.17, which increase again toward MIS 7d, where values of -11.73 ± 0.17 are recorded. T-IIIA is clearly apparent and a Nd isotopic composition of -18.32 ± 0.08 is reached during MIS 7c. Afterwards, the values fluctuate between -12.91 ± 0.15 and -16.22 ± 0.16 until they reach values of -12.43 ± 0.15 during MIS 6d. The values shift to fairly constant values of about -14.5 until 159 ka. Then, the Nd isotopic composition increases toward the Penultimate Glacial Maximum, where values as high as -10.21 ± 0.20 are reported by Böhm *et al.* [2015].

Looking at the overall picture of the past 1 Ma (see also Figure 5.1), the record of the neodymium isotopic signature of the bottom water at ODP 1063 shows long-term variations on orbital time scales. Most glacial maxima are characterized by more radiogenic ε_{Nd} values compared to their following interglacial, which is often characterized with the most unradiogenic values at their respective beginning. The following intermediate climate and glacial inceptions are often modulated by short-term fluctuations with a high amplitude, which resemble in their pattern the Dansgaard/Oeschger events recorded in the last glacial cycle [Böhm *et al.*, 2015].

5 Discussion

5.1 Origin of the unradiogenic Nd isotopic signatures

Over the past one million years, ε_{Nd} values were often more unradiogenic than the modern seawater value for NADW near the core site of ODP 1063 of about -13 [Lambelet *et al.*, 2016; Piepgras and Wasserburg, 1987]. It can be excluded that those values represent an artifact from the leaching method, as ε_{Nd} values extracted from foraminifera and leaching show a very good agreement (see Section 4.1.3). Thus, the recorded values reflect past bottom water Nd signatures. This phenomenon of a more unradiogenic Nd isotopic signature as modern is also known from locations nearby [Pöppelmeier *et al.*, 2018] as well as at other North Atlantic regions [e.g. Lippold *et al.*, 2016; Howe and Piotrowski, 2017] and a number of different reasons were put forward to explain this.

Roberts *et al.* [2010], Böhm *et al.* [2015], and Lippold *et al.* [2016] explain those more negative ε_{Nd} values with an increased contribution of LSW to NADW, as LSW is the most unradiogenic water mass constituting the NADW today (see Section 2.3.2). A shift in the convection centers of LSW itself was speculated by Deaney *et al.* [2017], where more unradiogenic surface waters could have been transported to depth.

Deaney and co-authors also proposed the dominance of water masses formed in NW Atlantic at the Bermuda Rise, which requires lower densities and/or diminishing of the other prevailing deep water masses. A formation of dense brines for example at polynyas in the Baffin Bay, which could transport very negative Nd signatures, also must be considered. However, this contradicts the good preservation state of carbonate at ODP 1063 as dense brines are often associated with a low carbonate saturation state [Deaney *et al.*, 2017].

Furthermore, it is possible that water cascading at the shelves is contributing to the very negative Nd isotopic signatures. Near-surface waters (50 m water depth) on the shelf northeast of Newfoundland (Belle Isle line, Filippova *et al.* [2017]) show twice as high Nd concentrations than their open-sea counterparts in the Labrador Sea, which also decrease with increasing distance from shore. A similar pattern is found for the Nd isotopic signatures. With ε_{Nd} values of -25.4 to -23.3, they are very unradiogenic

and clearly exhibit the terrestrial input from the hinterland [Filippova *et al.*, 2017]. If those waters end up in the deep sea and mix with the ambient sea water, they have the potential to shift the Nd isotopic composition to more negative values. Dense shelf-water cascading is happening today in many regions of the world [Ivanov *et al.*, 2004], among them the southern coast of Newfoundland [Puig *et al.*, 2013b]. One of the possible mechanisms that drive the formation of dense waters is the response of local temperature to winter cooling, especially if the convection depth is greater than the depth of the shelf [Shapiro *et al.*, 2003]. When those waters propagate down the slope, they can cause the erosion and resuspension of sediments. Thus, the water-particle mixture can sink even deeper and eventually form nepheloid layers at intermediate depths or benthic nepheloid layers that spread out at the bottom of the deep basins, as it is seen for example in the Mediterranean Sea today [Puig *et al.*, 2013a].

Besides these hydrographical explanations, there are effects that are related to the way how a water mass acquires its Nd signature (see also Section 2.3.1). Howe *et al.* [2016b] postulated for the early Holocene a re-labeling of the bottom water through a pulse of poorly chemically weathered detrital material, that was deposited into the Labrador Sea following the retreat of the Laurentide Ice Sheet. As this type of sediment is reactive for boundary exchange processes, unradiogenic Nd is released into the bottom water and further advected to the south. A combination of this effect and a gradual end member change of lower NADW (their NWABW) was proposed by Pöppelmeier *et al.* [2018] for the Corner Rise during the early Holocene. This end member change upstream of the Corner Rise could originate from a continuously decreasing portion of poorly weathered material prone to boundary exchange throughout the Holocene. Pöppelmeier *et al.* [2019a] suggested additionally that a combination of the processes of an end member change induced at the Labrador Sea, and the influence of benthic nepheloid layers is important for the alteration of the bottom water masses in the northwestern Atlantic. In addition to the processes discussed above, benthic nepheloid layers form in the northwestern Atlantic due to the high sea-surface eddy kinetic energy of the Gulf Stream and can reach considerable loads of particulate matter [Gardner *et al.*, 2017]. They can either transport preformed authigenic phases and/or might release unradiogenic Nd due to the dissolution of particles and therefore alter the bottom water signal [van de Flierdt *et al.*, 2016; Pöppelmeier *et al.*, 2019a]. Jaume-Seguí *et al.* [2020] propose that these benthic nepheloid layers are the reason for the extreme unradiogenic values at the Bermuda Rise during both deglaciations and the transitions to interstadials.

Nevertheless, what should be kept in mind is that, regardless of the exact mechanism that provokes the unradiogenic values at the Bermuda Rise, all processes described above reflect the presence of water masses from the North(-west) Atlantic, during times when those unradiogenic isotopic signatures are recorded. They can be clearly distinguished from water masses with a southern origin.

5.2 Glacial-interglacial evolution of water mass changes

The record of the Nd isotopic composition of the bottom water at the Bermuda Rise nicely follows the glacial-interglacial cycles of the past one million years. This can be seen in Figure 5.1 and Figure 5.2, where the ε_{Nd} values are compared to the benthic stable carbon and oxygen isotopes of the same core [this study and Poli *et al.*, 2000; Ferretti *et al.*, 2005; Billups *et al.*, 2011; Poirier and Billups, 2014] or a sediment core nearby (KNR191-CDH19, 33°41.194′N, 57°36.907′W, 4579 m water depth, Henry *et al.* [2016]). As the data for neodymium and stable isotopes do not originate from the same sediment samples, for every 1 ka time step an average value was calculated using a 3 ka gaussian kernel in Figure 5.2. This allows the determination of the correlation coefficients which results in an Pearson's r value of -0.46 [-0.51; -0.40] (95% confidence interval) for ε_{Nd} and $\delta^{13}C$, and +0.49 [0.43; 0.54] (95% confidence interval), for ε_{Nd} and $\delta^{18}O$ respectively. Hence, the neodymium signature at the Bermuda Rise varies in first order concordantly with the global ice volume (as one of the main factors determining $\delta^{18}O$ values in benthic foraminifera) and with the ocean circulation as expressed in $\delta^{13}C$. In times of high ice volume the most positive ε_{Nd} signatures are found and vice versa.

A reoccurring feature along most of record is the change in circulation pattern

Figure 5.1 ***(following page)*:** (Top) Nd isotopic composition at the Bermuda Rise for the past 1030 ka. Data points from previous studies [Roberts *et al.*, 2010; Gutjahr and Lippold, 2011; Böhm *et al.*, 2015; Lippold *et al.*, 2019; Jaume-Seguí *et al.*, 2020] are depicted in open squares, in contrast to the new data in circles. Data of Deaney *et al.* [2017] is left out due to differences in the age models. For better visual presentation, error bars are omitted, but are typically in the order of 0.19 ε-units and can be seen in Figure 4.6 for the new data. (Middle) Stable carbon isotopes and (bottom) stable oxygen isotopes from benthic foraminifera for ODP 1063 [this study and Poli *et al.*, 2000; Ferretti *et al.*, 2005; Billups *et al.*, 2011; Poirier and Billups, 2014]. Data for the first 150 ka are from nearby core KNR191-CDH19 also from the Bermuda Rise [Henry *et al.*, 2016]. Solid lines represent a 3 ka-gaussian running mean. The dark gray line in the lower panel shows the global benthic $\delta^{18}O$ stack LR04 [Lisiecki and Raymo, 2005].

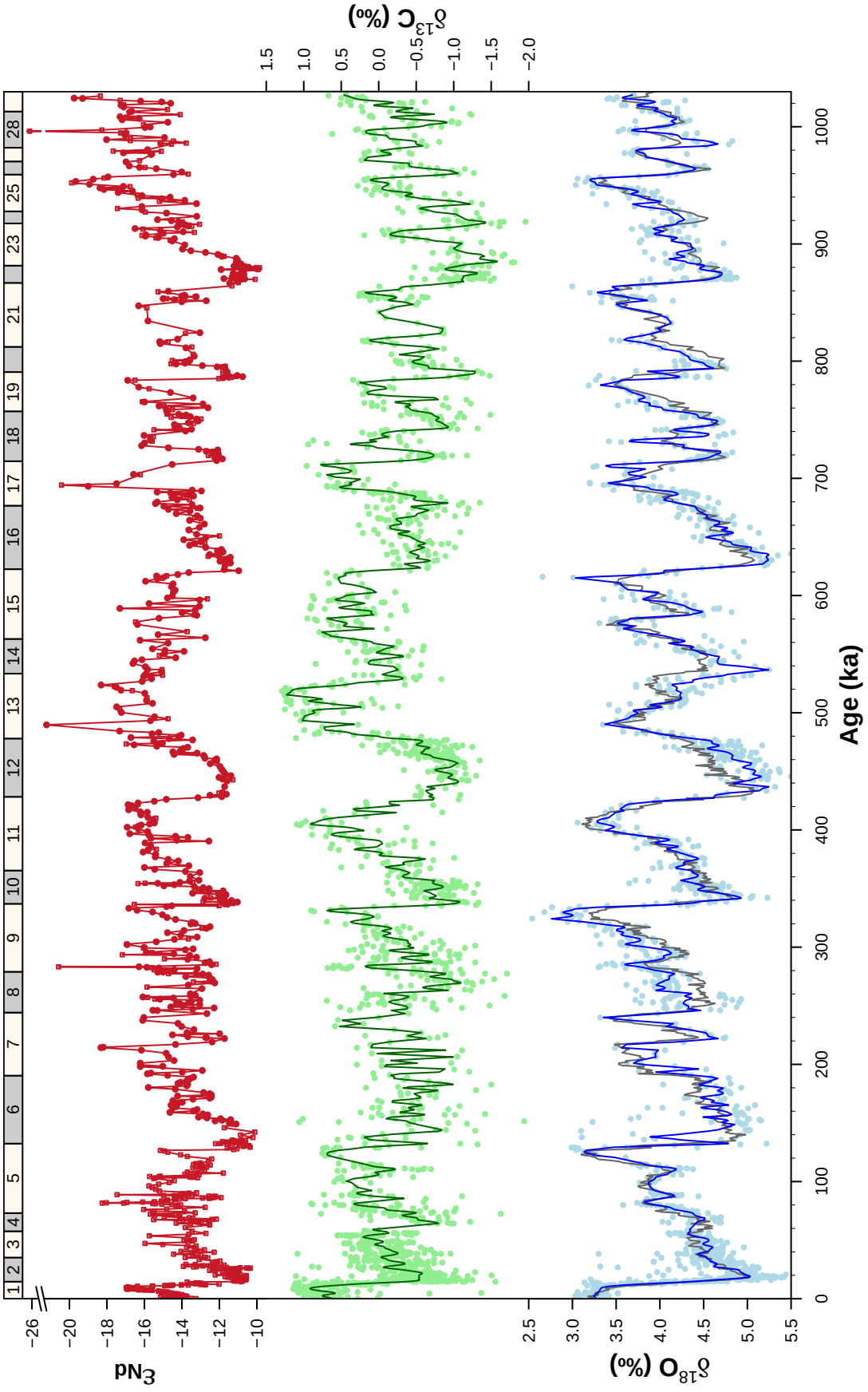
εNd
δ18O (‰)
δ13C (‰)
Age (ka)

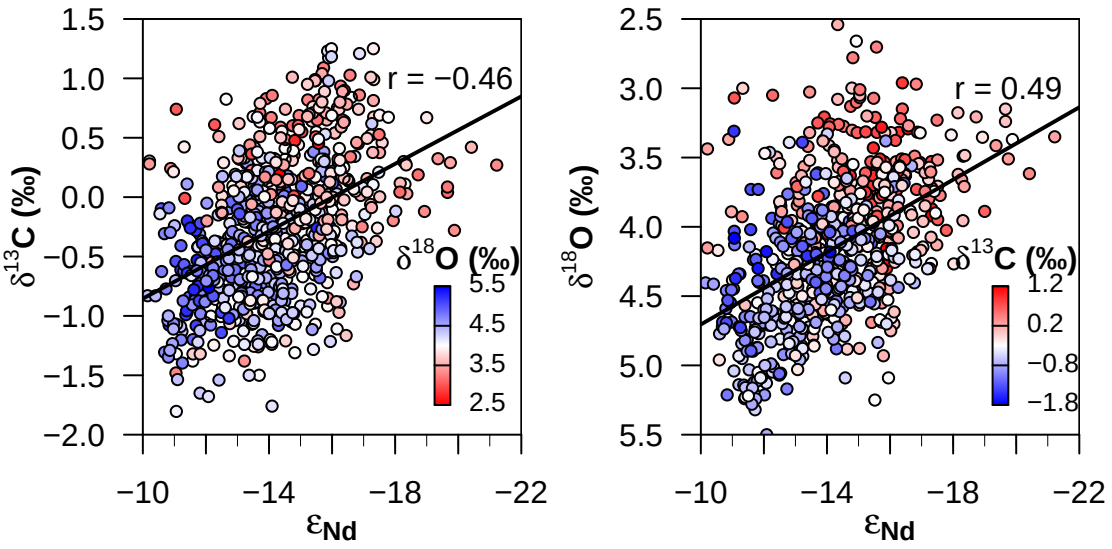

Figure 5.2: Correlation of Nd isotopes with stable carbon (left) and oxygen (right) isotopes of benthic foraminifera. Data is the same as in Figure 5.1, but smoothed beforehand with a 3 ka gaussian kernel for every 1 ka-time step. The color of the dots represent their respective δ^{18}O (left) or δ^{13}C (right) value. The linear regression line is depicted in black and Pearson's r value is given. For better visualization, the extreme ε_{Nd} value of -26.12 is omitted in this plot, but included in the calculations.

across glacial Terminations. These sharp decreases in ε_{Nd} values often exceed 4 ε-units (see Figure 5.3). However, as mentioned earlier, Terminations III, VI, and XI are not fully expressed, as the precedent glacial maximum was not markedly visible (see Section 5.4 for a further discussion on T-VI and MIS 14). The earliest Termination XI and XII are also characterized with more negative starting values during the glacials compared to the following Terminations. Those unradiogenic values during the glacials are indicative of an absence of influence from southern-sourced water masses. In contrast, the following glacial maxima are characterized by water masses with a higher fraction of southern-sourced water that shifted to northern-sourced-dominated water masses during the Terminations and following interglacials.

At the start of the interglacials often the most unradiogenic values are found, which in the course of time increase to more modern like ε_{Nd} values. This typical pattern suggests a common process, which is inherent to the evolution of Nd isotopes in interglacials. At least for the Holocene, this trend is also present in a number of sediment cores and is a (North) Atlantic wide feature [e.g. Howe *et al.*, 2016b; Lippold *et al.*, 2016; Howe *et al.*, 2017; Pöppelmeier *et al.*, 2019a]. For other interglacials, no such highly resolved data is available yet from other Atlantic sites.

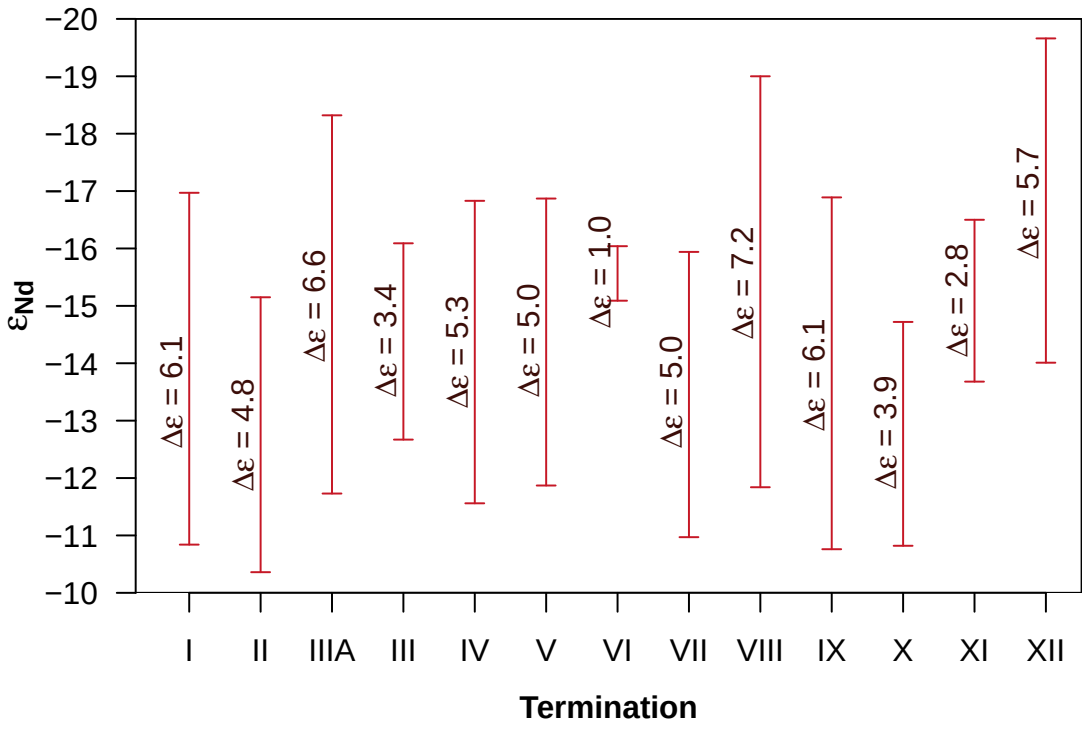

Figure 5.3: Amplitude of ε_{Nd} at Glacial Terminations at the Bermuda Rise.

Assuming that unradiogenic values ($\lessapprox -13$) at the Bermuda Rise represent water masses with a northern provenance, i.e. northern-sourced water (NSW), despite not knowing the exact mechanisms on how they gained these signatures (see Section 5.1 for further discussion on this topic), the ε_{Nd} record can be interpreted as a water mass competition between northern- and southern-sourced water masses. It is striking, that radiogenic ε_{Nd} values, that are indicative of a higher ratio of SSW, are only present during times of pronounced glacial maxima and potential Heinrich Events, especially in MISs 2, 6ab, 10a, 12ab, 16a, 18a, 20ab, 22, and 23a. This feature was also recognized in Böhm *et al.* [2015], where the authors compared the ε_{Nd} and Pa/Th record of the first 150 ka at the Bermuda Rise. They concluded that during most of the last glacial cycle, a vigorous and deep overturning mode persisted. Following that logic and despite no available Pa/Th record (due to the short half-lives of the isotopes), one can speculate that this is also true for most of the past one million years with the exception of the time periods stated above with pronounced glacials. However, during the glacials before the 900 ka event, no presence of SSW can be attested at the Bermuda Rise (for an in-depth discussion of this topic, see Section 5.6).

However, even during those times of more positive ε_{Nd} values, the water mass at the Bermuda Rise did not consist of 100% of SSW as the southern end member was more

radiogenic than the values recorded at the Bermuda Rise. This is indicated by more positive ε_{Nd} values recorded at locations further south like at ODP 929 at the Ceara Rise (6°N, Howe and Piotrowski [2017]), as well as at ODP 1267 (28°S, Farmer *et al.* [2019]) and ODP 1090 (43°S, Pena and Goldstein [2014]) in the southeastern Atlantic (see Section 5.5). Hence, the water mass bathing the Bermuda Rise must have consisted of a proportion of NSW even in times of glacial maxima. Howe *et al.* [2016a] calculated this amount to be 72% for the LGM, but by all means at least 44% using different end member values, and therefore claimed the presence of GNADW in the deep North Atlantic below 2500 m water depth during the LGM. Unfortunately, such computations could not been made for other time intervals of the past one million years, as the current knowledge about the end members needed for the calculations is too limited (see Chapter 11). Recently, Keigwin and Swift [2017] called for a presence of an even denser young water mass that underlay the SSW at depths deeper than 4200 m based on $\delta^{13}C$ and $^{14}C_{B\text{-}P}$ ages at a sediment core at the Corner Rise (KNR197/10 17GGC, 36°24.3′N, 48°32.4′W, 5010 m water depth). The authors speculated that the water mass could have originated from brine rejection around the margins of the Labrador Sea. In a follow-up study, Pöppelmeier *et al.* [2018] provided further evidence for a northern-sourced water mass at the Corner Rise during the LGM based on Nd isotopes. Using a simple binary mixing model, they calculated a presence of 70% NSW, with a lower limit of 30%.

With the exception of the pronounced glacials, NSW bathed the Bermuda Rise during most of the past one million years. As also seen in the ε_{Nd} record at the Ceara Rise [Howe and Piotrowski, 2017], no difference can be identified between the lukewarm interglacials (800–430 ka) and the warm periods thereafter in the Bermuda Rise record. This strengthens the observations of Howe and Piotrowski [2017] that there was no significant difference in the proportions of NSW during and after the lukewarm interglacials, and that the upper and lower circulation cell of the AMOC must have been decoupled to explain the drop of interglacial CO_2 levels during the lukewarm interglacials. Barth *et al.* [2018] also concluded based on $\delta^{13}C$ data that during the lukewarm interglacials AABW occupied more volume compared to the later interglacials, but that this change happened south of the equator and was therefore not detectable at the Bermuda Rise.

5.3 Water mass evolution during MIS 11

One of the most interesting marine isotope stages of the past one million years is MIS 11. It hosts one of the longest interglacials of nearly 30 thousand years [Cheng *et al.*, 2016], during which great parts of the Greenland Ice Sheet melted [de Vernal and Hillaire-Marcel, 2008; Reyes *et al.*, 2014; Rachmayani *et al.*, 2017] and a higher-than-present global mean sea level prevailed [e.g. Dutton *et al.*, 2015] (see Section 2.1 for further details).

In the record of neodymium isotopes at the Bermuda Rise, this time intervals also catches attention, as for a long period of time, unradiogenic ε_{Nd} values between -16 and -17 were recorded. While most other interglacials (like the Holocene, MISs 5e, 9e, 15e, and 19c), record their most unradiogenic peak right at their beginning and show increasing ε_{Nd} values toward modern like conditions at their ends, the Nd isotopic composition of MIS 11c does not exhibit such increase. Only a minor dip in the middle of the interglacial is apparent. Therefore, the Nd isotopic composition stays very unradiogenic for the whole duration of that interglacial.

The question arises, why the ε_{Nd} values stayed on this unradiogenic level. As the first peak is similar to other glacial terminations, it may be interpreted in the same way, as for example a pulse of freshly eroded material into the Labrador Sea and therefore overprinting the Nd isotopic signal of deep water masses [Howe *et al.*, 2016b]. Also, a transport of unradiogenic particles inside a benthic nepheloid layer from the Labrador Sea to the south and thereby continuously releasing an unradiogenic signature to the bottom water [Pöppelmeier *et al.*, 2019a] is possible. However to explain the nearly constant level of Nd, these mechanisms would have been more long-lasting than during the other interglacials. One possible explanation is the marked retreat of the Greenland Ice Sheet, whereby unradiogenic bedrock could get exposed. Sea-level reconstructions indicate an extended deglaciation and a minimum in ice volume in the latter half of MIS 11c [Raymo and Mitrovica, 2012; Elderfield *et al.*, 2012; Spratt and Lisiecki, 2016]. The retreat of the ice sheet is not only supported by modeling studies [e.g. Rachmayani *et al.*, 2017], but also by proxy evidence. Pollen found in a sediment core in the Labrador Sea suggest that at least southern Greenland was covered by a forest-type vegetation [de Vernal and Hillaire-Marcel, 2008] and the provenance analysis of terrigenous material of a close-by sediment core also second the ice-free conditions on Southern Greenland [Reyes *et al.*, 2014]. As a consequence, both a greater area and amount of freshly physically eroded material from glacial tills get exposed. This

phase is more prone to chemical weathering and can influence the oceanic Nd isotopic composition [von Blanckenburg and Nägler, 2001]. This can happen either directly by dissolved input via the meltwaters, possibly setting the Nd isotopic signature within the Baffin Bay and Labrador Sea toward more unradiogenic values or indirectly as mentioned above [Howe *et al.*, 2016b; Pöppelmeier *et al.*, 2019a], when the sediment load gets transported into the ocean. Hyperpycnal flows would have facilitated the transport of unradiogenic Nd into the deep Labrador Sea and thus influencing the deeper part of NADW.

Alternatively, oceanographic changes may be an explanation (see also Section 5.1). A shift of the deep water convection center in the Labrador Sea to locations with more unradiogenic surface waters [Deaney *et al.*, 2017] is an alternative, as well as NW water masses being denser than the ones originating in the NE Atlantic and therefore bathing the abyssal water column at the Bermuda Rise [Deaney *et al.*, 2017]. Another possibility is that the deep waters present in the NE Atlantic were still dense, but did not flow into the western basin through the Charlie-Gibbs Fracture Zone, which would also lead to the situation that the water masses from the NW Atlantic can reach deeper depths (see Section 9.1.2 for further details).

Looking at the ε_{Nd} record of ODP 929 at the Ceara Rise [Howe and Piotrowski, 2017], it does not show significantly more unradiogenic values during MIS 11c, in fact even more unradiogenic values are recorded during other interglacials. However, whether this is because of a lower temporal resolution compared to ODP 1063 needs to be further investigated (see Section 8.5).

The persistent unradiogenic Nd isotopic composition at the Bermuda Rise speaks for a long-lasting active AMOC during MIS 11c, especially in its latter half. Inferred from carbon isotopes, Dickson *et al.* [2009] detected a strong ventilation of the deep Atlantic during the early part of the interglacial, followed by a slight weakening and a re-strenghtening during mid-MIS 11c. This progression is very similar to the shape of the Nd isotope record, where after the first peak, an increasing trend is reversed to more negative ε_{Nd} values half-way through the interglacial. From this, one can conclude that deep northwesterly water masses dominated the Bermuda Rise and the circulation within MIS 11c.

In order to see, how the flow patterns in other parts of the Atlantic behaved, and whether the recorded Nd isotopic values at ODP 1063 were unique, or whether such extremely unradiogenic ε_{Nd} values can be found at more locations in the Atlantic, a detailed study of sediment cores spanning from the far North to the South Atlantic will

be presented in Study II of this thesis.

5.4 MIS 14 – a "failed" glacial?

Compared to the other glacial time periods of the past 900 ka, the glacial during MIS 14 stands out in the ε_{Nd} record, as it does not show the typical glacial increase to more radiogenic values. On the contrary - during this time period, connecting MIS 15 and MIS 13, the ε_{Nd} values stay on a very unradiogenic level. A possible hiatus or another distortion of this part of the sediment column can be excluded, as the typical glacial increase can be seen in benthic $\delta^{18}O$ values for MIS 14 [Poirier and Billups, 2014] (see Figure 5.1). As the thickness of the sediment layer corresponding to MIS 14 amounts to about 4 m, a diffusion of the Nd signal from the layers above or below via pore water and/or bioturbation can be ruled out as well.

Therefore, one can confidently assume that the ε_{Nd} values represent the signature of the past bottom water. This means that the greater proportion of southern-sourced water masses typically filling the whole deep Northwestern Atlantic does not reach the core site. The stable carbon isotopes [Poirier and Billups, 2014] further support this view, as they are only slightly decreased and do not reach glacial-like values. Another hint to the absence of SSW at the Bermuda Rise provides the predicted carbonate content [Giosan *et al.*, 2001] that does not collapse during MIS 14, which would have indicated the presence of a corrosive water mass, i.e. SSW. Likewise, the carbonate content further to the north on the western flank of the Mid-Atlantic Ridge (DSDP Site 607, 41°0.1′N, 32°57.5′W, 3427 m water depth) usually decreases during the glacials of the past 900 ka [Ruddiman *et al.*, 1989]. However, this is not the case during MIS 14, as the percentage of carbonate stays high during the whole time interval of MISs 15–13 (see Figure 5.4). In contrast, Giosan *et al.* [2001] also reports the predicted carbonate content for ODP 1062 (28°14.8′N, 74°24.4′W, 4763 m water depth) at the deep Bahama Outer Ridge. Here, a relatively short, but pronounced reduction is seen, indicating that SSW might still have underlain the NSW in the very deep North Atlantic. However, the percentage of carbonate in the sediment is only an indirect indicator of the water mass bathing the site. Beside the dissolution by corrosive water masses, also the dilution of the sediment by terrigenous particles and/or a reduced production of carbonate may play a role [e.g. Keigwin and Jones, 1989].

Other records of Nd isotopes in the deep Atlantic are sparse. A singular data point from sediment core MD03-2705 (18°6′N, 21°9′W, 3085 m water depth) [Tachikawa *et al.*,

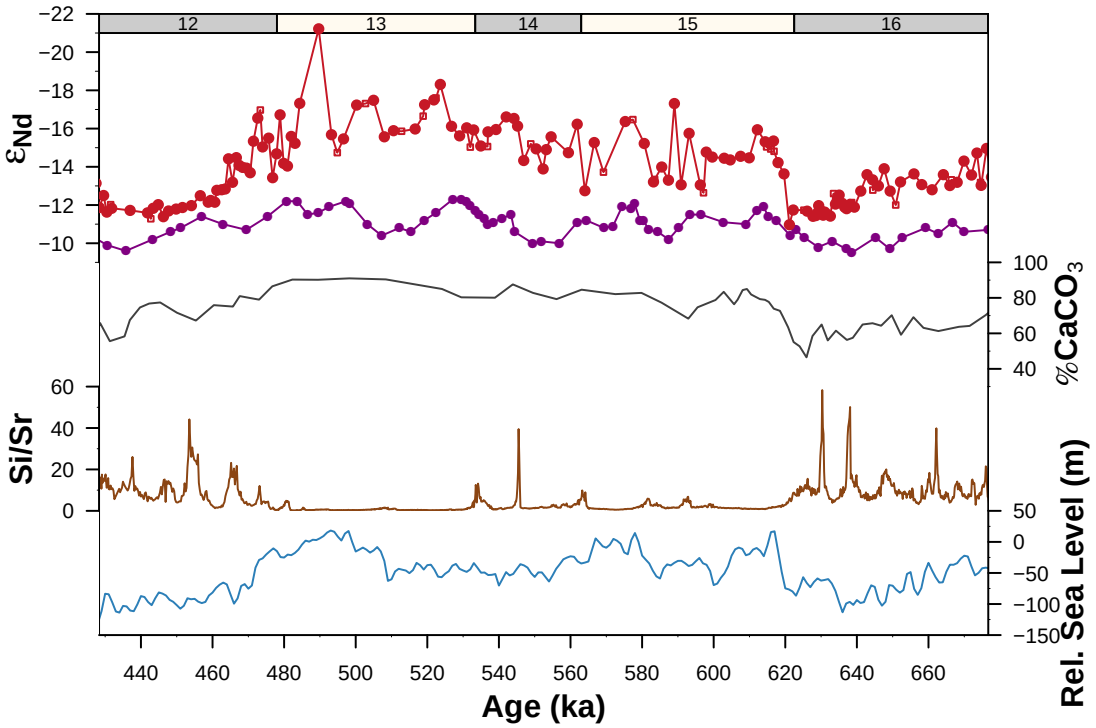

Figure 5.4: Nd isotopic composition (top) at the Bermuda Rise (red) and the Ceara Rise (purple, Howe and Piotrowski [2017]) spanning MISs 16–12 and therefore highlighting the weak glacial MIS 14. The calcium carbonate content of DSDP 607 [Ruddiman *et al.*, 1989] is shown in gray. The Si/Sr ratio of IODP U1308 [Hodell *et al.*, 2008] is indicative of detrital silicate delivered to the site via ice-rafting and shows a reduction during MIS 14 compared to the previous and following glacial. The relative sea-level [Elderfield *et al.*, 2012] is shown in blue.

2021] corroborates the absence of SSW in the North Atlantic. In contrast, the Ceara Rise further south (ODP 929, 5°58.57′N, 43°44.39′W, 4356 m water depth) [Howe and Piotrowski, 2017] is bathed by a more radiogenic water mass during MIS 14 with similar values compared to other glacials. This implies that the influence of SSW was still present in the deep equatorial Atlantic, but not anymore about 27 degrees of latitude further to the north. The interface between NSW and SSW must have shifted further to the south and may also have deepened compared to the common glacial periods. Whether this is due to a stronger production and export of NSW or a reduction in SSW cannot be answered based solely on those few records.

Looking at the overall climate that prevailed during MIS 14, several other climatic records show that this glacial was one of the weakest during the past 800 ka [Lang and Wolff, 2011], especially on the Northern Hemisphere, where it was not as pronounced as in its southern counterpart [Hao *et al.*, 2015]. A record of the Chinese Loess Plateau

also clearly hints for a very weak glacial with only restricted ice shields on the Northern Hemisphere [Hao *et al.*, 2015]. This is supported by less IRD transported to the North Atlantic region compared to other glacial periods [Hodell *et al.*, 2008; Channell *et al.*, 2012b] and only a halfway drop in sea level to about −60 m RSL [Elderfield *et al.*, 2012; Spratt and Lisiecki, 2016]. Subsuming, this hints to a stronger, but still not fully pronounced AMOC compared to other glacial periods, which presumably is responsible for sustaining the – for a glacial – mild climate on the Northern Hemisphere.

5.5 Comparison with other Atlantic records of Nd isotopes

Only few data sets exist for Nd isotopes in the Atlantic Ocean beyond the last glacial cycle. Ferromanganese crusts are not considered in this analysis, as due to their slow growth rates of 1–15 mm per million years they integrate over 10^4–10^5 ka per sample [Frank, 2002] and therefore do not resolve the glacial-interglacial shifts and millennial variability as seen in the Bermuda Rise ε_{Nd} record. Therefore, only reconstructions with lower temporal resolution of Nd isotopes of six sediment cores in the Atlantic are evaluated here (see Figure 5.5 and Figure 5.6).

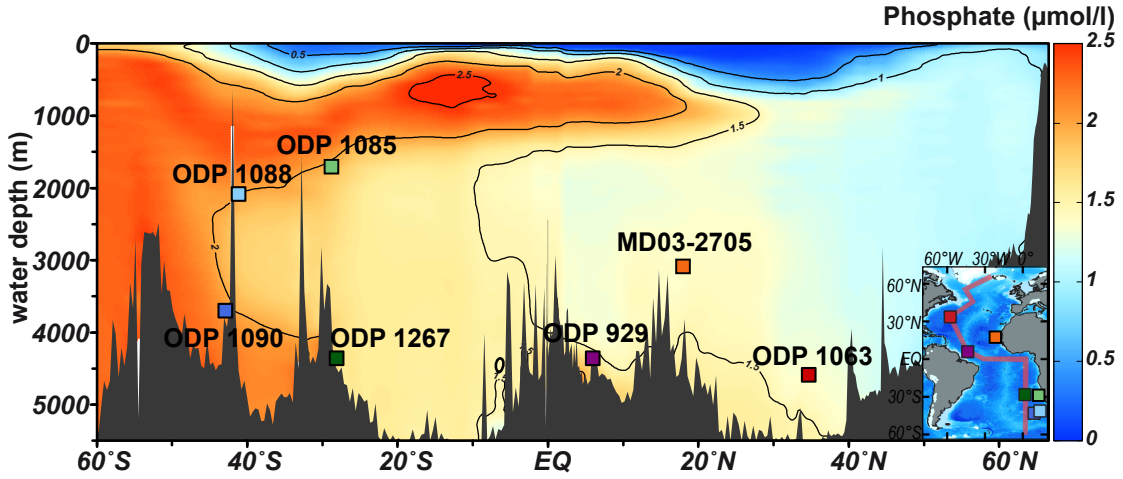

Figure 5.5: Location of sediment cores in the Atlantic with ε_{Nd} records spanning older time periods than the last glacial cycle. The cross section shows the annual mean phosphate concentration [Boyer *et al.*, 2013]. Data visualized with ODV software [Schlitzer, 2019]. Insert map based on the ETOPO1 Global Relief Model [Amante and Eakins, 2009].

In the eastern tropical Atlantic, Tachikawa *et al.* [2021] provide a low resolution record of MD03-2705 ((18°6′N, 21°9′W) in 3085 m water depth on the Cape Verde

Plateau. For the past 800 ka, Howe and Piotrowski [2017] present an ε_{Nd} record for ODP 929 at the Ceara Rise (5°58.57′N, 43°44.39′W, 4356 m water depth). The age model published in this study was generated by tuning the $\delta^{18}O$ record of benthic foraminifera [Bickert *et al.*, 1997; Howe and Piotrowski, 2017] to the LR04 [Lisiecki and Raymo, 2005]. However, the core was an original constituent of the LR04 itself [Lisiecki and Raymo, 2005], whereby an additional tuning results in a less good agreement between the actual and the target record. Therefore, here the age model by Lisiecki and Raymo [2005] was used for the ε_{Nd} record of ODP 929, except for the time span of 240–367 ka, where there was a data gap in the underlying $\delta^{18}O$ record [Bickert *et al.*, 1997] at the time of creation of the LR04, that was afterwards closed by Howe and Piotrowski [2017]. For this time period, the data was aligned again to the LR04 using the R package *Astrochron* [Meyers, 2014].

Data for the South Atlantic is even more scarce. Farmer *et al.* [2019] report punctual ε_{Nd} data for ODP 1267 (28°5.88′S, 1°42.66′E, 4355 m water depth) at the northern flank of the Walvis Ridge. Peak glacial-interglacial values are given by Tachikawa *et al.* [2021] for ODP 1085 in the shallow Cape Basin (29°22′S, 13°59′E, 1713 m water depth). Further to the south at the Agulhas Ridge, data is available for the shallower site ODP 1088 (41°8.16′S, 13°33.77′E, 2082 m water depth) [Pena and Goldstein, 2014; Hu *et al.*, 2016; Dausmann *et al.*, 2017] and the deeper ODP 1090 (42°54.82′S, 8°53.98′E, 3701 m water depth) [Pena and Goldstein, 2014].

At all core sites, glacial-interglacial cycles can be distinguished with more radiogenic values found during glacial maxima and more unradiogenic values during the rest of the time, with the most unradiogenic values especially at start of the interglacials,

Figure 5.6 ***(following page)*****:** Nd isotope records in the Atlantic for the past 1030 ka. Only records with data beyond the last glacial cycle are considered. Most unradiogenic ε_{Nd} values are found in the northern most core ODP 1063 (red) at the Bermuda Rise [this study and Roberts *et al.*, 2010; Gutjahr and Lippold, 2011; Böhm *et al.*, 2015; Lippold *et al.*, 2019; Jaume-Seguí *et al.*, 2020]. The East Atlantic site MD03-2705 (orange) [Tachikawa *et al.*, 2021] records similar glacial values during the past 900 ka, while generally more radiogenic signatures are found in the equatorial core ODP 929 (purple) [Howe and Piotrowski, 2017]. Sediment cores from the South Atlantic show the most positive ε_{Nd} values starting at the Walvis Ridge at ODP 1267 (dark green) [Farmer *et al.*, 2019], and becoming most radiogenic in the Cape Basin (ODP 1085; light green; Tachikawa *et al.* [2021]) and at the Agulhas Ridge at the shallower ODP 1088 (light blue) [Dausmann *et al.*, 2017; Hu *et al.*, 2016; Pena and Goldstein, 2014] and the deep ODP 1090 (dark blue) [Pena and Goldstein, 2014]. The data of Hu *et al.* [2016] and Pena and Goldstein [2014] for ODP 1088 was integrated into the record of Dausmann *et al.* [2017] and highlighted by no filling and a black border around the symbols, respectively.

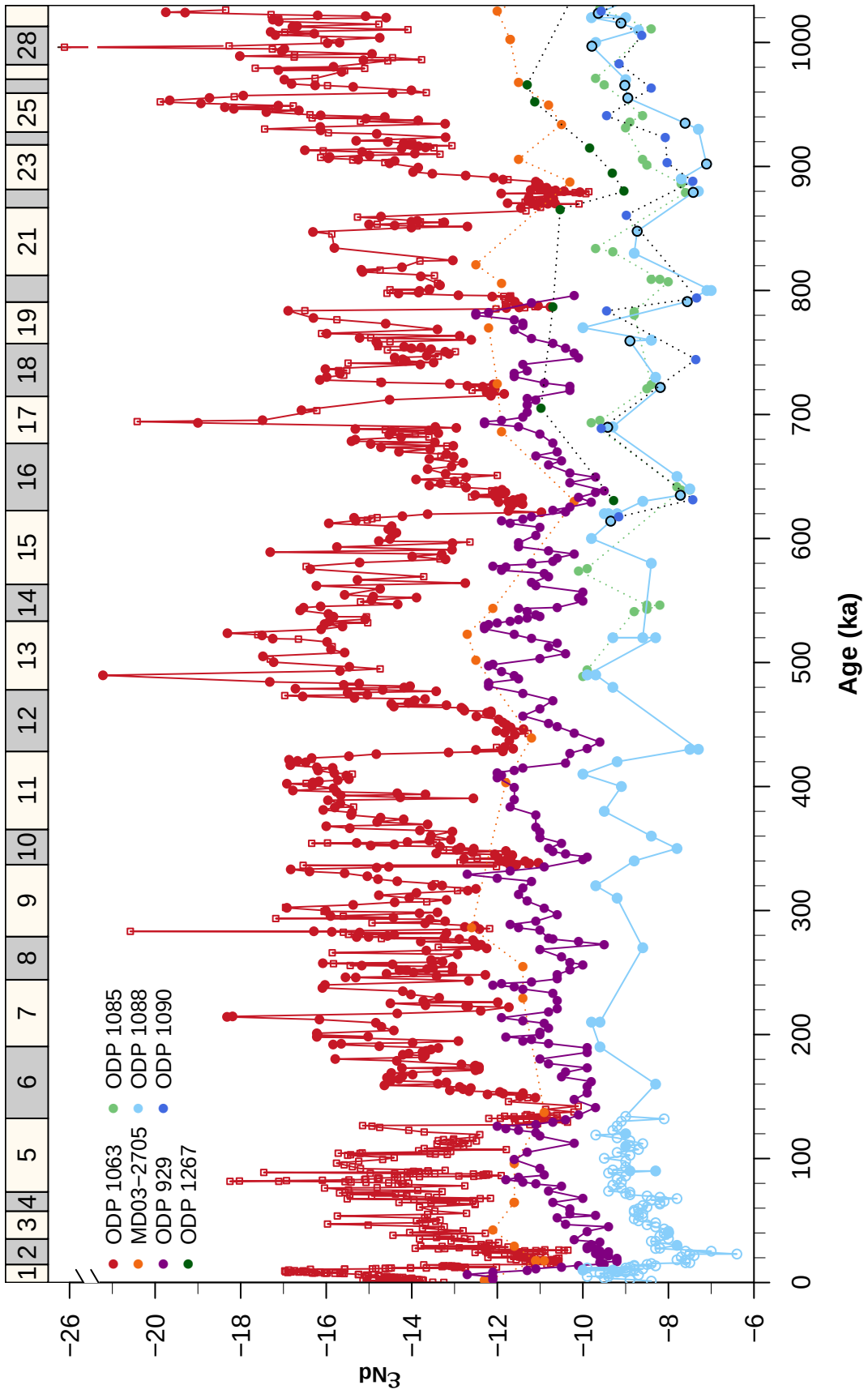
ODP 1063
MD03−2705
ODP 929
ODP 1267
ODP 1085
ODP 1088
ODP 1090
εNd
Age (ka)

resembling the pattern found in ODP 1063 despite the lower temporal resolution of the other records. The amplitude of the records is greatest at ODP 1063, which can be explained by the proximity to the source of unradiogenic Nd to the oceans and therefore the greater sensitivity. As one goes from north to south, the ε_{Nd} values are getting more and more radiogenic. This is indicative of a decreasing proportion of NSW and a greater dominance of SSW at the respective core sites.

5.5.1 Comparison with the Ceara Rise

Because the ε_{Nd} data of ODP 929 [Howe and Piotrowski, 2017] is the only record, which reaches an almost similar temporal resolution as achieved in ODP 1063, both reconstructions are compared in more detail. The Bermuda Rise record is always more unradiogenic compared to the values found at the Ceara Rise about 27 degrees of latitude further to the south and therefore also further away both from the source of unradiogenic Nd, i.e. the northeastern American continent and Greenland and from the deepwater formation sites. However, the variations in both records are quite synchronous.

But first, to directly compare these records, one must account for the different temporal resolutions of both time series. Hence, the Bermuda Rise ε_{Nd} record was recalculated to fit to the lower resolved record of ODP 929 (see Figure 5.7, top panel). Therefore, a Gaussian kernel with a bandwidth of 1.7 ka was applied for every time-stamp in ODP 929 [Howe and Piotrowski, 2017, using the new age model as described above]. Rehfeld *et al.* [2011] showed that this method is more robust compared to the traditionally used linear interpolation when comparing irregularly sampled time series. In a next step a gedankenexperiment was performed: How would the Ceara Rise record would look like, if it would have been recorded at the Bermuda Rise? For this purpose, the ε_{Nd} values of ODP 929 were adjusted to fit the ε_{Nd} values found in ODP 1063 to consider both the overall more unradiogenic Nd isotopic composition and the higher amplitude at the more northern site. In order to do this, ε_{Nd} values of ODP 929 were linearly scaled with $\varepsilon_{Nd\_rescaled} = 1.83 * \varepsilon_{Nd\_original} + 6.29$. As reference points served the peak values of the early Holocene and the LGM. Now, by removing the differences in absolute values as well as in amplitudes, one can compare the temporal variations directly (see Figure 5.7, middle panel). Strikingly, both records show an exceptional agreement. Both the temporal variations are nearly the same (considering slight differences in the individual age models) and the now reached ε_{Nd} values themselves.

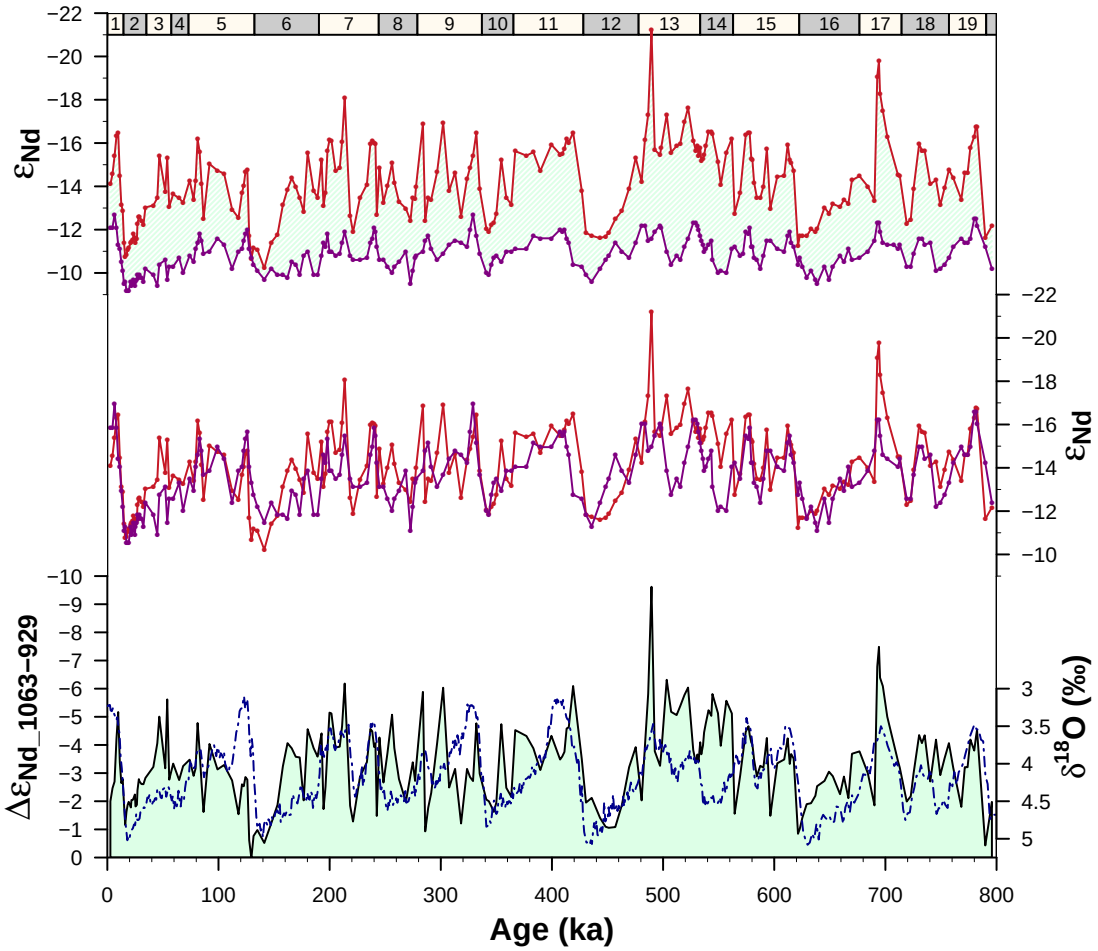

Figure 5.7: Comparison of North Atlantic Nd isotope records of the past 800 ka. (Top) ε_{Nd} records of the Bermuda Rise (red) [this study and Roberts *et al.*, 2010; Gutjahr and Lippold, 2011; Böhm *et al.*, 2015; Lippold *et al.*, 2019; Jaume-Seguí *et al.*, 2020] and ODP 929 (purple) [Howe and Piotrowski, 2017]. To account for the different temporal resolution, the Bermuda Rise record got recalculated at the time-stamps of ODP 929 (see text for details). The area hatched in mint green shows the differences of both records, which is displayed in the bottom panel. (Middle) The recalculated Bermuda Rise record (red, same as in the top panel) and the Ceara Rise record (purple) linearly scaled to the amplitude of the Bermuda Rise record ($\varepsilon_{Nd\_rescaled} = 1.83 * \varepsilon_{Nd\_original} + 6.29$). For this, the peak values of the early Holocene and the LGM serve as reference points. (Bottom) The calculated $\Delta\varepsilon_{Nd\_1063-929}$ record (mint green) compared to the LR04 (dotted blue line) [Lisiecki and Raymo, 2005] as a climatic reference.

Therefore one can conclude that the Nd isotopic composition which is recorded at the Bermuda Rise is not only a local signal, that was for example influenced by pore waters at the specific site, but that this signal rather is representing an actual water mass signal which gets also transported further to the south. Along the flow path the signal becomes more radiogenic and dampened as a greater proportion of SSW gets admixed.

If the very same water mass, with the same mixing proportions would bath both the Bermuda Rise and the Ceara Rise, the difference between both $\varepsilon_{\mathrm{Nd}}$ records would equal zero, regardless whether the water mass originates from the north or the south. To test this, the difference between both records was calculated as $\Delta\varepsilon_{Nd\_1063-929}$, where the $\varepsilon_{\mathrm{Nd}}$ values from ODP 929 were subtracted from the Gaussian smoothed values of ODP 1063 (see Figure 5.7, bottom panel). As already seen, this is never the case during the past 800 ka. During times of glacial maxima, when a higher proportion of SSW bathed the deep North Atlantic, the difference gets smaller. In contrast, during the other time periods, especially when the most unradiogenic values are recorded at the Bermuda Rise, the $\Delta\varepsilon_{Nd}$ gets greater. That means that this gradient is mainly driven by the NSW component, i.e. its proportion and the processes that influence its Nd isotopic signature, and reacts sensitively to changes that happen in the North Atlantic.

5.6 900 ka event within the Mid-Pleistocene Transition

As described in Section 2.1, a prominent shift in the period of the glacial-interglacial cycles happened, changing from the *41 kyr-world* to the *100 kyr-world*, which is called the Mid-Pleistocene Transition. One prominent event within the MPT is the 900 ka event which encompasses MISs 24–22. Associated with this event is a drastic drop in sea-level commencing in MIS 24 and finally culminating in MIS 22, where for the first time a sea-level low-stand comparable to the one of the LGM was reached [Elderfield *et al.*, 2012] (see Figure 5.8). A strong growth of the Antarctic Ice Sheet was also attested [Sutter *et al.*, 2019], as well as an enhanced volume of the ice sheets on the Northern Hemisphere [Clark and Pollard, 1998]. The ratio of quartz to calcite in the sediments of IODP Site U1313 shows intensified ice-rafting in the North Atlantic especially during MIS 22, which is in line with the enhanced modelled calving of the Laurentide Ice Sheet [Willeit *et al.*, 2019]. It is hypothesized that the increase in ice volume of the northern hemispheric ice sheets is due to the gradual removal of regolith and therefore a change from a soft-bedded ice sheet to a hard-bedded which allows for the volumetric increase

[Clark and Pollard, 1998; Clark *et al.*, 2006]. A recent study by Willeit *et al.* [2019] suggests that in addition to the regolith removal also the proposed gradual decline of CO_2 [e.g. Raymo *et al.*, 1997; Berger *et al.*, 1999] was necessary to reproduce the evolution of climate variability over the course of the Pleistocene.

Pena and Goldstein [2014] had a look on the ocean circulation during this time period by analyzing sediment cores from the Agulhas Ridge in the South Atlantic for their authigenic Nd isotope composition (see Figure 5.9). The authors concluded that the vigor of the thermohaline circulation was substantially weakened and underwent a 'crisis' during the 900 ka event. This statement is based on unradiogenic values found in both the shallower (ODP 1088, 2082 m water depth) and the deeper core (ODP 1090, 3702 m water depth) earlier than 950 ka indicating that the southeastern Atlantic was bathed by a high proportion of NSW during both glacials and interglacials. The ε_{Nd} record of ODP 1063 fits into this scheme, as also only unradiogenic values are recorded, which hints to an absence of SSW during both glacial and interglacial cycles in the northwestern Atlantic.

During MIS 24, this pattern of an active export of NSW to the south started to collapse. MD03-2705 and ODP 1088 both record ε_{Nd} values that are markedly more radiogenic than previously and argue for a higher proportion of SSW at mid-depths in the tropical eastern Atlantic and southeastern Atlantic. At greater depth, the Nd isotopic composition gets slightly more radiogenic compared to the previous glacials, however not as pronounced as in shallower depth [Pena and Goldstein, 2014]. At the Bermuda Rise, though, nothing hints to an advance of SSW to the deep NW Atlantic.

At the beginning of MIS 23, the ε_{Nd} values at the Bermuda Rise are still unradiogenic, arguing for NSW at that site as well as at the Cape Verde Plateau. In contrast, in the deep southeastern Atlantic the proportion of NSW gets smaller as ODP 1267 starts recording a more positive Nd signature [Farmer *et al.*, 2019]. In the further course of MIS 23, the most southern sites are bathed by nearly the same NSW proportion as already seen in MIS 24, or even less for the shallower ODP 1088 [Pena and Goldstein, 2014]. This presence of SSW during a, technically seen, interglacial led Pena and

Figure 5.8 ***(following page)*:** The Nd isotopic signature at the Bermuda Rise (top) [this study (circles) and Roberts *et al.*, 2010; Gutjahr and Lippold, 2011; Böhm *et al.*, 2015; Lippold *et al.*, 2019; Jaume-Seguí *et al.*, 2020, (squares)] for the past 1030 ka compared with (middle) the percentage of NSW at DSDP 607 in the North Atlantic (41°0.068′N, 32°57.438′W, 3427 m water depth, see text for details) [Lang *et al.*, 2016]. (Bottom) Relative sea level [Elderfield *et al.*, 2012].

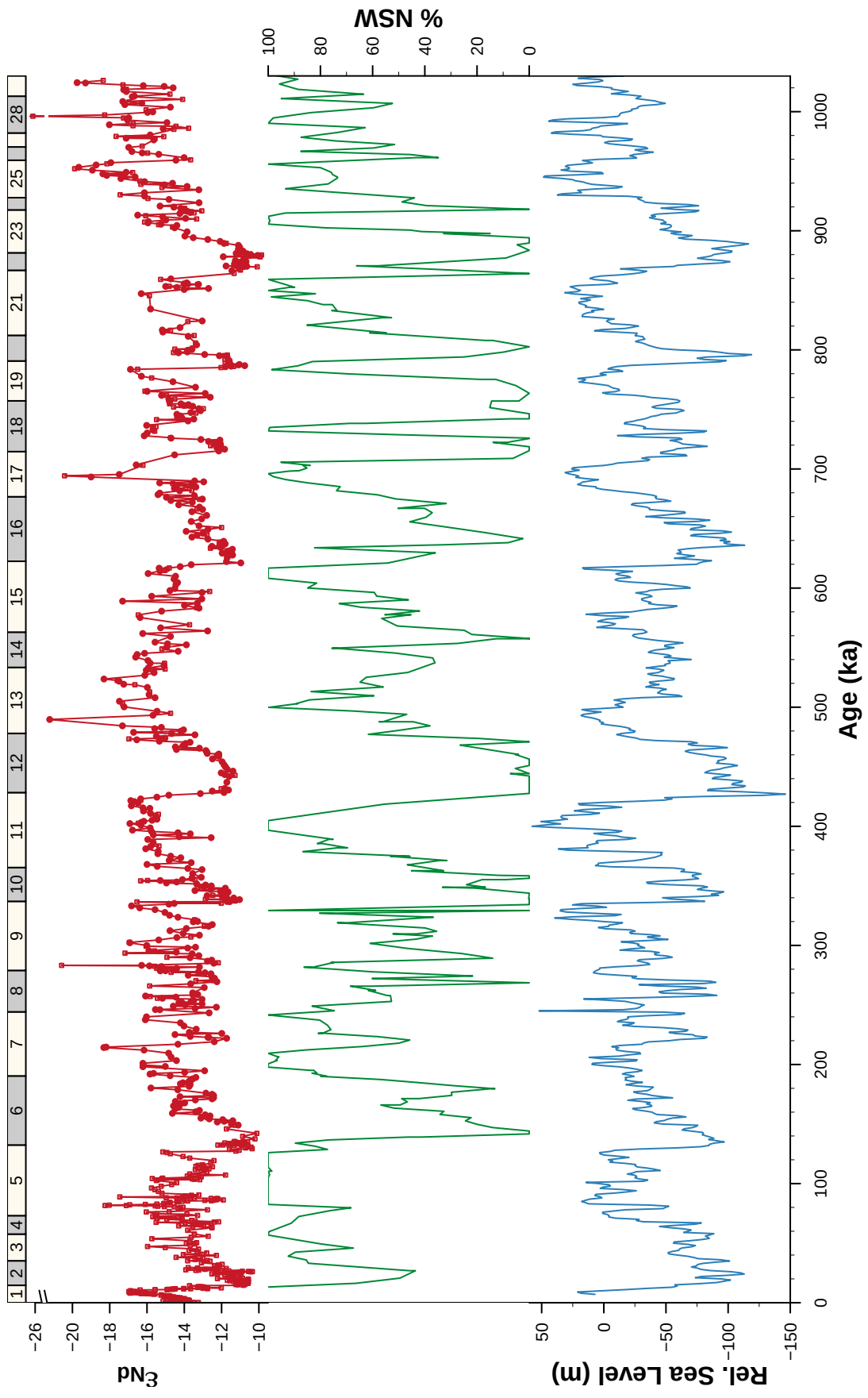
MSN %
100
80
60
40
20
0
1
2
3
4
5
6
7
8
9
10
11
12
13
14
15
16
17
18
19
21
23
25
28
εNd
−26
−20
−18
−16
−14
−12
−10
Rel. Sea Level (m)
50
0
−50
−100
−150
Age (ka)
0
100
200
300
400
500
600
700
800
900
1000

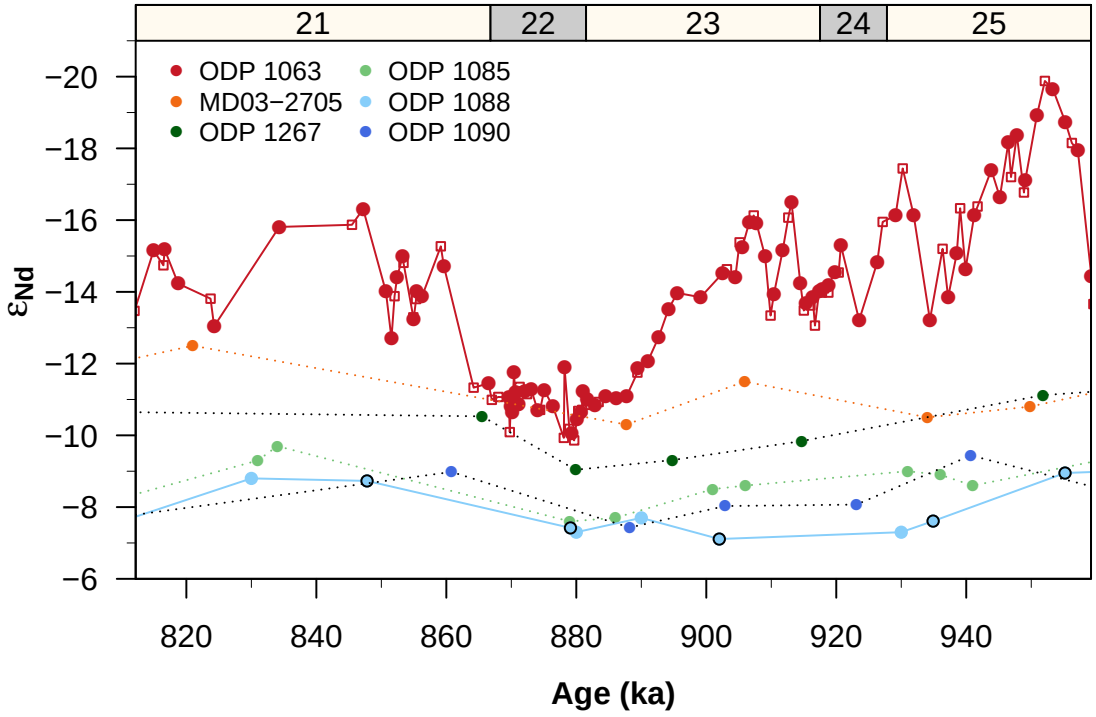

Figure 5.9: Neodymium isotopic composition during MISs 21–25 and therefore spanning the 900 ka event. Data and colors are the same as in Figure 5.6.

Goldstein [2014] to call MIS 23 a 'transglacial' – a glacial-like interglacial. However, as seen at the Bermuda Rise, the Cape Verde Plateau, and the Walvis Ridge, at least at the beginning of this MIS a significant proportion of NSW bathed the deep Atlantic and therefore does not show 'glacial-like' conditions.

Not until the end of MIS 23b the ε_{Nd} values at the Bermuda Rise start to get more radiogenic and show an increased influence of SSW in the deep NW Atlantic for the first time. These radiogenic values are, however, one of the most radiogenic ones of the entire one million year record at ODP 1063. They are also very persistent and last from the end of MIS 23 through the whole MIS 22 for at least 18 ka. In combination with the singular data points from the tropical northeastern Atlantic and South Atlantic cores, which also show one of their respective most radiogenic values, one can conclude that large parts of the Atlantic were bathed by a higher proportion of SSW and the presence of NSW was reduced in the deep Atlantic. However, NSW did not disappear completely, as still a north-south gradient can be seen in the records with more unradiogenic values the further north you go (see Section 5.2).

After this long time period, at T-X in all cores the values shifted again to typical interglacial values as seen before the 900 ka event and the higher proportion of NSW

at the different sites. However during the following glacials, all cores show radiogenic values comparable to MIS 22, indicating a lesser amount of NSW at the respective sites. However, at least for ODP 1063, the long-lasting period with constant reduced NSW export as sees in MISs 23a–22 was only reached again in MIS 12, while all other glacials were considerably shorter.

However, one must note that these comparisons with the other neodymium studies [Pena and Goldstein, 2014; Dausmann *et al.*, 2017; Farmer *et al.*, 2019; Tachikawa *et al.*, 2021] must be treated with caution, as the records have a low temporal resolution and only report single data points for each glacial/interglacial maximum. Therefore, it is possible that for example the presence of NSW at the Bermuda Rise at the beginning of MIS 23 was just not captured in the South Atlantic records. A higher resolution of these cores as well as more data from the Northern Atlantic would definitely increase the knowledge and understanding of the actual progression of the 900 ka event and its role in the Mid-Pleistocene Transition.

An alternative interpretation for the shift in ε_{Nd} values from unradiogenic during glacials before the 900 ka event to radiogenic values afterwards, could be a drastic endmember-shift in the Nd isotopic composition. However, Nd isotope data of ferromanganese crusts from the Southern Ocean [Frank *et al.*, 2002] do not support such a change in the southern endmember, strengthening the interpretation of a decreased export of NSW during the glacials after the 900 ka event. Tachikawa *et al.* [2021] performed sensitivity studies and found that an increased supply of radiogenic Nd by the Eurasian Ice Sheets to the North Atlantic and a decreased AMOC provoked that shift at the 900 ka event.

Further evidence for a change in water masses comes from benthic stable carbon isotopes. Lang *et al.* [2016] calculated the percentage of NSW at DSDP 607 at the Mid-Atlantic Ridge (41°0.068′N, 32°57.438′W, 3427 m water depth) based on benthic $\delta^{13}C$ records. This site is more than thousand meters shallower than ODP 1063 and lies further to the north. For the computation served the records of ODP 982 on the Rockall Plateau and ODP 849 in the equatorial Pacific as northern and southern end members respectively. The calculations for % NSW based on carbon isotopes support the finding that the deep North Atlantic was filled with a higher percentage of NSW during the glacials before the 900 ka event compared to afterwards (see Figure 5.8). In contrast to no SSW during MIS 24 at the Bermuda Rise, DSDP 607 sees a short reduction of NSW. Admittedly, whether this is a singular outlier in the benthic isotope record or whether this excursion was just not sampled in ODP 1063, cannot be ultimately determined yet.

A possible mechanism to explain this difference might be the production of GNABW during MIS 24, which might have bathed the Bermuda Rise but not the shallower located DSDP 607. In contrast to the South Atlantic, where no NSW was recorded during MIS 23 [Pena and Goldstein, 2014], also DSDP 607 reveals the presence of 100% NSW in the North Atlantic site as already seen in ODP 1063. Toward the end of the stage, also at DSDP 607 the presence of NSW collapsed and was displaced by SSW. The time period of MISs 23a–22 was characterized by the presence of 'pure' SSW in the North Atlantic, which happened in such a prolonged form for the first time in the past 3.5 million years [Lang *et al.*, 2016] as the glacial time periods before saw still a mixture between NSW and SSW waters, while the interglacials were bathed by 100% NSW.

6 Conclusions

The record presented here in this thesis is the first reconstruction of the Nd isotopic signatures for the past one million years with a high temporal resolution, that allows resolving circulation changes on time scales shorter than orbital cycles. Although the extremely unradiogenic ε_{Nd} values at the Bermuda Rise present a challenge to explain the exact underlying processes, the record highlights the history of deepwater circulation in the Northwest Atlantic. On orbital time scales, the proportion of NSW vs. SSW changed. A greater fraction of SSW is present during glacial maxima compared to the other time periods of interglacial and intermediate climates, similar as seen in Böhm *et al.* [2015] were a strong and active overturning circulation was attested for most of the last glacial cycle. The Nd isotopic signature at the Bermuda Rise is not only a local signal, but also gets transported further to the south along the flowpath of NADW. However, as the Bermuda Rise is located closer to the source area of the rocks with the most unradiogenic ε_{Nd} values, it records more sensitively changes in ε_{Nd}.

Looking at the paleoceanographic variations recorded in the one million year time-series, several major time intervals stand out. In course of the Mid-Pleistocene-Transition a substantial change in water mass configuration of the glacials occurred. The North Atlantic was not bathed by SSW during the glacials before the 900 ka event (MISs 24–22). While in the South Atlantic, the presence of SSW started during MIS 24 and prevailed until MIS 22 [Pena and Goldstein, 2014; Farmer *et al.*, 2019], the advance of SSW toward the North Atlantic began during late MIS 23. This glacial advance of a higher proportion of SSW at the Bermuda Rise is a common feature of the following glacial maxima.

However, MIS 14 is an exception, as no SSW reached the core site. This is in line with a couple of other climate records and hints towards an eased northward advance of SSW during this weak glacial. The water mass structure was different compared to the other post-900 ka event glacials, as presumably the interface of NSW and SSW was situated further to the south and maybe also deeper.

MIS 11 is also prominent in the record, as a long lasting interglacial with continuous unradiogenic ε_{Nd} values. Various theories may explain this unradiogenic Nd isotopic

composition, but all do agree that there was a strong overturning circulation prevailing during that time, with NSW covering the core site. Whether these values are local feature or are also seen at different locations in the Atlantic will be investigated in the second study of this thesis.

STUDY II

Water mass dynamics in the Atlantic during MISs 12–11

7 Material and methods

7.1 Site selection

For the time period spanning mid-MIS 12 and MIS 11 several sediment cores throughout the Atlantic were analyzed. An overview of the exact locations is given in Table 7.1 and Figure 7.1. The sites were chosen to follow the flow path of NSW as it travels from the subpolar North Atlantic into the western and eastern subtropical South Atlantic.

Table 7.1: The locations of sediment cores used for an Atlantic-wide reconstruction of Nd isotopes during MIS 11.

Leg/Expedition	Site	Latitude	Longitude	Water depth (m)
ODP Leg 162	980	55°29.09′N	14°42.13′W	2180
IODP Exp. 303	U1304	53°3.39′N	33°31.76′W	3065
ODP Leg 108	659	18°4.63′N	21°1.57′W	3070
ODP Leg 154	929	5°58.57′N	43°44.39′W	4356
ODP Leg 204	1267	28°5.88′S	1°42.66′E	4356
DSDP Leg 72	517	30°56.81′S	38°2.47′W	2963

7.1.1 ODP Site 980

The shallowest sediment core used in this study, ODP Site 980, is located at about 2180 m water depth in the northeastern Atlantic. It was drilled in 1995 on the Feni Drift, a sediment drift deposited along the northwestern flank of the Rockall Trough downstream of the Wyville-Thomson Ridge [Shipboard Scientific Party, 1996]. A high accumulation rate allows for high temporally resolved climate records from this approximately 570 km long pelagic sediment structure [Jones *et al.*, 1970; Jansen and Raymo, 1996]. The core sections used here belong to the lithostratigraphic Unit I, which is characterized by variable amounts of calcareous nannofossils, clay, and smaller amounts of silt and foraminifera [Shipboard Scientific Party, 1996].

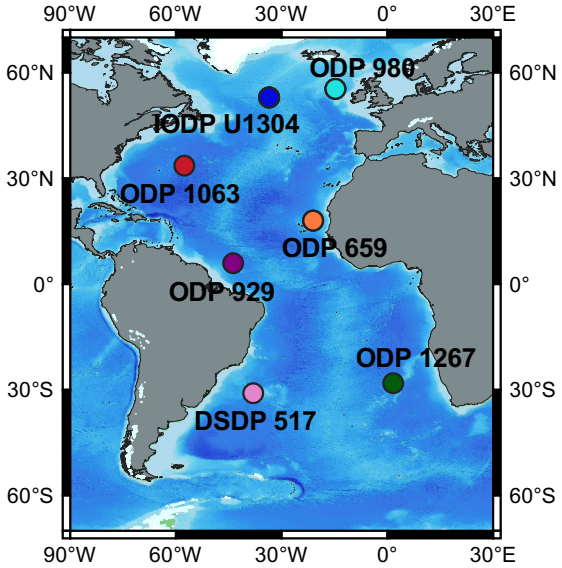

Figure 7.1: Map of the location of all sites studied for the Atlantic-wide reconstruction of Nd isotopes during MIS 11. Bathymetry based on the ETOPO1 Global Relief Model [Amante and Eakins, 2009].

Age Model

The benthic stable oxygen isotopes record of ODP 980 [Oppo *et al.*, 1998] is part of the LR04 stack [Lisiecki and Raymo, 2005]. Hence, the age-depth relationship composed by Lisiecki and Raymo [2005] is used here. An average sedimentation rate of 17.7 cm/ka prevailed during the analyzed time interval. The samples for ε_{Nd} analysis are from the identical core sections as the benthic $\delta^{18}O$ samples [Oppo *et al.*, 1998].

Hydrography

Today, the hydrography of the Rockall Trough (see Figure 7.2) is characterized by several different water masses. For this study, only the mid-depth to deep ones are of importance, which will be described here following New and Smythe-Wright [2001]. In a water depth of about 1600 to 1900 m LSW can be found which enters the Rockall Trough from the south and forms a cyclonic gyre in the central Rockall Trough. Below, there is a small contribution of dense overflow waters of the Wyville-Thomson Ridge. This Wyville-Thomson Ridge Overflow Water (WTROW) flows southwestwards along the local topography in the western part of the basin. However, Johnson *et al.* [2010] only suspect an event-like presence of this water mass. NEADW is also found in the Rockall Trough at water depths of 2000 to 2500 m, which again forms a cyclonic gyre in the center of the trough. In greater depths, this water mass is mixed with the

underlying Lower Deep Water (LDW, which is derived from AABW). This water mass can be found in a purer form at depths below 3300 m [New and Smythe-Wright, 2001]. Therefore, ODP 980 is situated in a zone of water mass competition of LSW, WTROW, and NEADW.

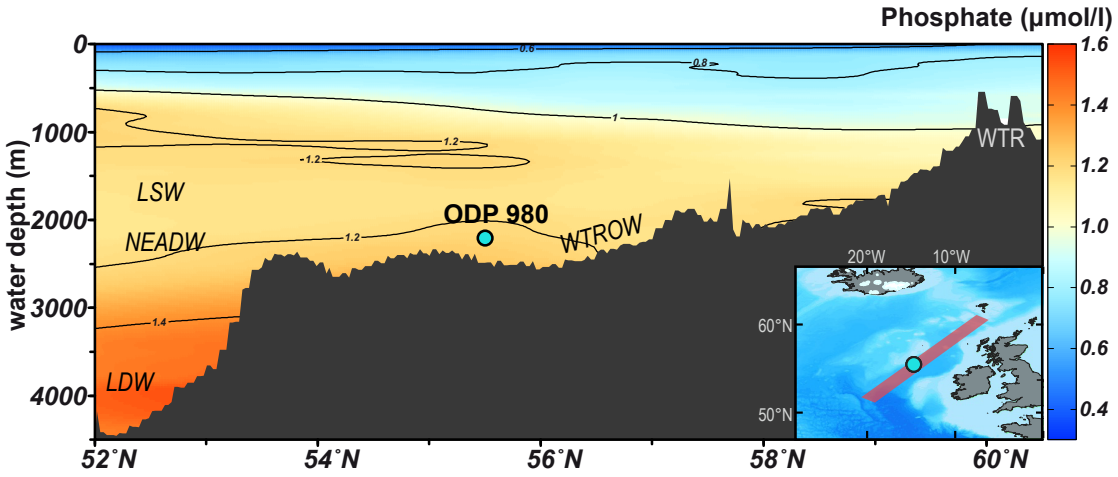

Figure 7.2: Hydrography at Rockall Trough represented by the phosphate concentration [Boyer *et al.*, 2013]. Data visualized with ODV software [Schlitzer, 2019]. Insert map based on the ETOPO1 Global Relief Model [Amante and Eakins, 2009].

7.1.2 IODP Site U1304

IODP Site U1304 was drilled during IODP Expedition 303 in 2004 on the southern tip of the Gardar Drift, close to the Charlie-Gibbs Fracture Zone [Expedition 303 Scientists, 2006]. The contourite drift deposit itself is approximately 1100 km long and reaches from the relatively shallow northeastern part with about 1400 m water depth to the deeper southwestern part in about 3000 m water depth [Bianchi and McCave, 2000]. An excellent recovery and a good core quality as well as a high sedimentation rate enables high-resolution profiles of past paleoceanography [Channell *et al.*, 2010]. The latter fluctuates during the past 1.5 Ma and ranges between ~ 5 cm/ka while cold stages and > 45 cm/ka during the warm counterparts mainly due to the fluctuating abundance of diatoms [Xuan *et al.*, 2016]. Analyzed core sections are part of the lithostratigraphic Unit I, which consists of interbedded nannofossil ooze and diatom ooze [Expedition 303 Scientists, 2006].

Age Model

The age model for the used core sections is based on the alignment of the benthic δ^{18}O record [Xuan *et al.*, 2016] to the LR04 stack [Lisiecki and Raymo, 2005], which was provided by Hodell and Channell [2016]. The average sedimentation rate for the analyzed part of MIS 12 is 6.0 cm/ka and increases to on average 36.1 cm/ka in MIS 11. Both samples for ε_{Nd} and δ^{18}O originate from the same core sections.

Hydrography

The core site is currently bathed by overflow waters of the Iceland-Faroe Ridge. While Norwegian Sea Deep Water is formed by winter convection north of the Ridge, it is mixed with Subpolar Mode Water (SPMW) and LSW as it travels through the ridge system. The overflow waters now have homogeneous characteristics as they flow southwestwards as ISOW and are distinct from other water masses. It then follows the bathymetric contours and flows parallel to the Reykjanes Ridge before it eventually turns west at the southern end of the Gardar Drift and enters the western North Atlantic though the Charlie-Gibbs Fracture Zone [van Aken and de Boer, 1995; Bianchi and McCave, 2000].

7.1.3 ODP Site 659

ODP Site 659 was drilled on the Cape Verde Plateau approximately 500 km offshore the northwestern African coast [Shipboard Scientific Party, 1988]. It is located under the Saharan Dust Plume and therefore under the influence of the aeolian supply of dust particles from the Saharan Desert during recent times as well as during the Last Glacial Maximum [Sarnthein *et al.*, 1981; Grousset *et al.*, 1998]. The sediment cover on the core site is characterized by finely laminated, pelagic and hemipelagic sediments. The core sections used in this thesis are part of the lithological Subunit IA, which is expressed by interbedded nannofossil ooze and foraminifer-nannofossil ooze [Shipboard Scientific Party, 1988].

Age Model

The shipboard splice for ODP 659 [Shipboard Scientific Party, 1988] was revised by Tiedemann [1991]. Therefore the shipboard and revised depth scales differ. Here, I report the depths from the shipboard splice as “mcd” (meter composite depth) and

the adjusted depths by Tiedemann [1991] as "amcd" (adjusted meter composite depth). The depths reported in the available benthic δ^{18}O records [Tiedemann *et al.*, 1994] correspond to the amcd depth scale. This record is also part of the LR04 [Lisiecki and Raymo, 2005] and therefore the published age model is used. Sampling for neodymium isotopes took place on the splice of Tiedemann [1991], whereby both δ^{18}O and ε_{Nd} samples were from the same core sections. For the time period between 378 and 450 ka the average sedimentation rate adds up to only 4.2 cm/ka.

Hydrography

Currently, the dominant water mass at ODP 659 is UNADW. It originates from the DWBC, where it bifurcates and flows eastwards. It has essentially the same temperature and salinity properties as found in the western Atlantic basin [Zieringer *et al.*, 2019]. Nd isotope signatures, however, show slightly more radiogenic values than found in the western basin, which was interpreted as an influence of the boundary exchange of the Canary and Cape Verde islands (see Figure 7.3) [Zieringer *et al.*, 2019].

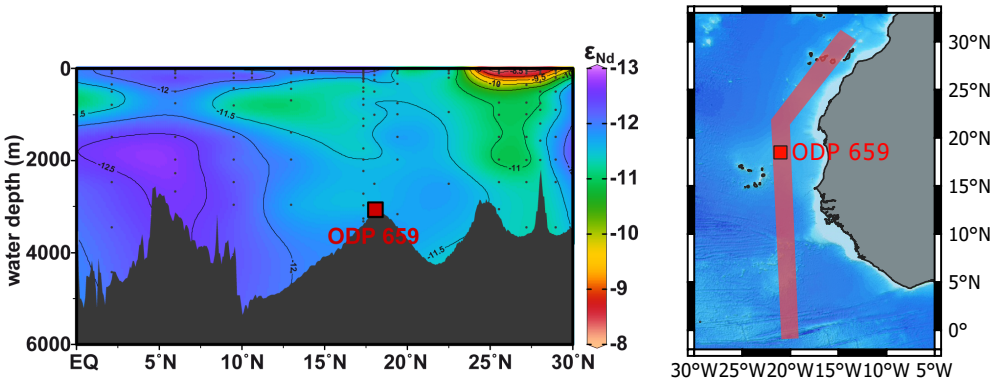

(a) Section of Nd isotopes.

(b) Location of section shown in Figure 7.3a.

Figure 7.3: Neodymium isotopic composition of seawater in the (sub)tropical North Atlantic [Tachikawa *et al.*, 1999; Rickli *et al.*, 2009, 2010; Stichel *et al.*, 2015; Zieringer *et al.*, 2019]. Data visualized with ODV software [Schlitzer, 2019]. Figure 7.3b based on the ETOPO1 Global Relief Model [Amante and Eakins, 2009].

7.1.4 ODP Site 929

In 1994 during ODP Leg 154 several core sites were drilled on the Ceara Rise, which is located close to the Brazilian Margin, about 900 km northeast of the Amazon delta. ODP Site 929 is located on the northern flank of the Rise on a small local plateau [Shipboard Scientific Party, 1995]. Analyzed samples belong to the lithological Subunit

IA, which is characterized by an alternating sequence of clay with nannofossils and nannofossil clay with foraminifers [Shipboard Scientific Party, 1995].

Age Model

The benthic δ^{18}O record of Bickert *et al.* [1997] is part of the LR04 [Lisiecki and Raymo, 2005] and therefore this age model is used (see also Appendix B.1 for a more detailed annotation). However, there is a gap in the δ^{18}O data between 278 and 367 ka, which was filled by Howe and Piotrowski [2017]. Therefore, I tuned the extended δ^{18}O record to the LR04 for the time period of 240 to 367 ka using the *R* package *Astrochron* [Meyers, 2014]. The sampling of the core sections for the higher resolved MIS 11 ε_{Nd} record was conducted along the shipboard splice and therefore on the same core sections as the benthic δ^{18}O [Bickert *et al.*, 1997] and ε_{Nd} [Howe and Piotrowski, 2017] samples. The average sedimentation rate for the analyzed time span is about 3.0 cm/ka.

Hydrography

The Ceara Rise is located directly under the core of the southward flowing DWBC. ODP 929 on the foot of the rise, is located in the mixing zone of NADW and AABW today [Shipboard Scientific Party, 1995] and therefore reacts sensitive to changes in the mixing proportions of these two water masses [Howe and Piotrowski, 2017] (see Figure 7.4).

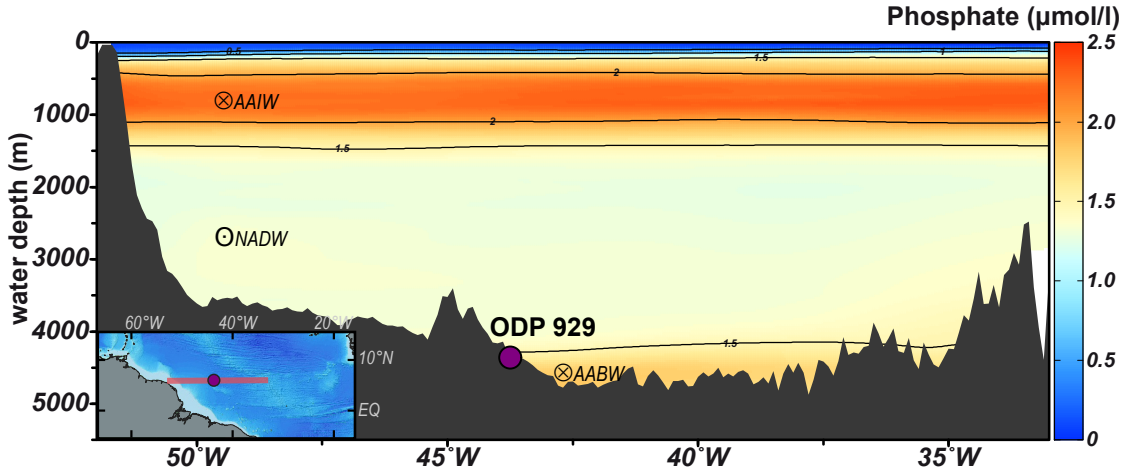

Figure 7.4: Hydrography at ODP 929 represented by the phosphate concentration at 6°N [Boyer *et al.*, 2013]. Data visualized with ODV software [Schlitzer, 2019]. Insert map based on the ETOPO1 Global Relief Model [Amante and Eakins, 2009].

7.1.5 ODP Site 1267

In the eastern South Atlantic, the Walvis Ridge separates the Cape Basin to the South from the Angola Basin to the North. ODP Site 1267 was drilled during Leg 204 on the northwestern flank of this ridge in a water depth of 4356 m. The sampled core sections are part of the lithostratigraphic Unit I, which is characterized by dominantly nannofossil ooze [Shipboard Scientific Party, 2004]. The visual core description states an extensive bioturbation with a bioturbation length exceeding 10 cm [Shipboard Scientific Party, 2004], which is higher than the global average of about 6 cm [Teal *et al.*, 2008]. The sampling strategy followed the shipboard splice [Shipboard Scientific Party, 2004], so that both $\delta^{18}O$ [Bell *et al.*, 2014] and ε_{Nd} samples originate from the same core sections.

Age Model

For ODP 1267 the age model published by Bell *et al.* [2014] was used. These authors first aligned the composite depth scales of ODP 1267 and nearby ODP 1264 primarily via the benthic $\delta^{18}O$ records and supported by the records of magnetic susceptibility and lightness. Afterwards the combined benthic $\delta^{18}O$ records (the 'Walvis stack') was visually linked to the LR04 [Lisiecki and Raymo, 2005]. The sedimentation rate in the analyzed sediment segment ranges between 1 and 2 cm/ka and is therefore markedly lower compared to the other sediment cores studied in this thesis.

Hydrography

The hydrography of the eastern South Atlantic (see Figure 7.5) is influenced by the bathymetric barrier of the Walvis Ridge. It hinders AABW to flow from the Cape Basin into the Angola Basin. The only exceptions where AABW is found in the Angola Basin are close to the two passages in the southwestern part of the ridge, which are deeper than 4000 m, though this spread of AABW is tightly confined and does not reach the core site of ODP 1267 [Connary and Ewing, 1974]. Instead, deep water masses enter the Angola Basin either through the Romanche Fracture Zone near the equator or via the so-called Namib Col Current through the Rio de Janeiro Fracture Zone near 22°S [Stramma and England, 1999; Mercier *et al.*, 2000]. As lower NADW and AABW are forced to flow through the fracture zones of the Mid-Atlantic-Ridge, they mix and form a relatively uniform deep water mass. This water mass flows first southwards along the African continental rise, and subsequently the deepest part turns southwestwards and flows along the northern flank of the Walvis Ridge [Arhan *et al.*, 2003] and baths

ODP 1267. Nd isotopes measured in seawater samples from the southern Angola Basin indicate that the measured Nd isotopic composition reflects conservative water mass mixing and that reconstructed authigenic sedimentary Nd isotopes reliably measure paleo water mass compositions [Rahlf *et al.*, 2020].

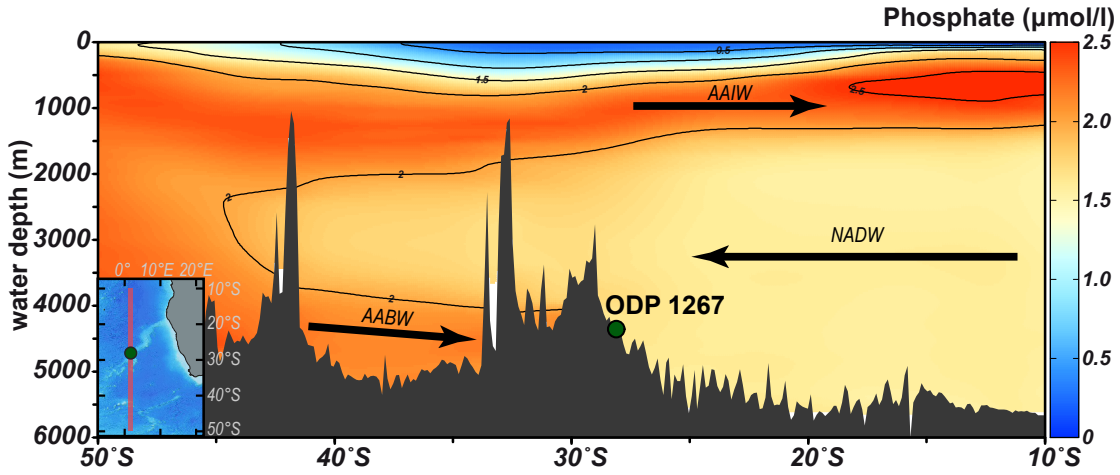

Figure 7.5: Hydrography at ODP 1267 represented by the phosphate concentration [Boyer *et al.*, 2013]. Data visualized with ODV software [Schlitzer, 2019]. Insert map based on the ETOPO1 Global Relief Model [Amante and Eakins, 2009].

7.1.6 DSDP Site 517

The southwestern subtropical Atlantic is an area in which very few expeditions of the Deep Sea Drilling Project (and none of the follow-up programs ODP, and IODP) were conducted, and of those few sites drilled, only one is suited for this study. Site 517 was drilled in 1980 during DSDP Leg 72 on the western flank of the Rio Grande Rise, which is gently sloping toward the Vema Channel. The recovered sediments form one lithostratigraphic unit, which consists of foraminiferal-nannofossil ooze with scattered pteropods and aragonite needles. No evidence of slumping or reworking of older sediment was detected [Shipboard Scientific Party, 1983]. However, the sediments are poorly consolidated and drilling disturbances are apparent [Shipboard Scientific Party, 1983]. Notwithstanding the quality of this sediment core, this thesis provides first valuable insight into the water mass structure in the southwestern Atlantic.

Age model

Initial age control was provided by Vergnaud Grazzini *et al.* [1983], who present a low resolution record of benthic $\delta^{18}O$ for DSDP 517. However, these data points are

too scarce to confidently align the stable oxygen isotope record to the LR04 stack by Lisiecki and Raymo [2005]. Thus, due to the similarity of the ε_{Nd} record during MIS 12 to the one of ODP 1267, the age model for DSDP 517 was created by correlating those two records presuming synchronous water mass change. Therefore, the oldest six data points of DSDP 517 were aligned to the MIS 12 part of ODP 1267. This results in a sedimentation rate of 2 cm/ka, which is propagated and kept constant for the younger part of the sediment column.

Hydrography

Today, DSDP 517 is sitting amidst the core of the southward flowing NADW (see Figure 7.6). It is sandwiched by northward flowing shallower Antarctic Intermediate Water and Upper Circumpolar Water with their respective cores in 900–1000 m and 1300–1550 m water depth and the deeper Antarctic Bottom Water, which is found approximately below 3600 m in the Vema Channel [Johnson, 1983]. This channel is the main passage with a significant deep sill depth of about 4500 m, through which AABW can propagate northward from the Argentine into the Brazil Basin [ibid.].

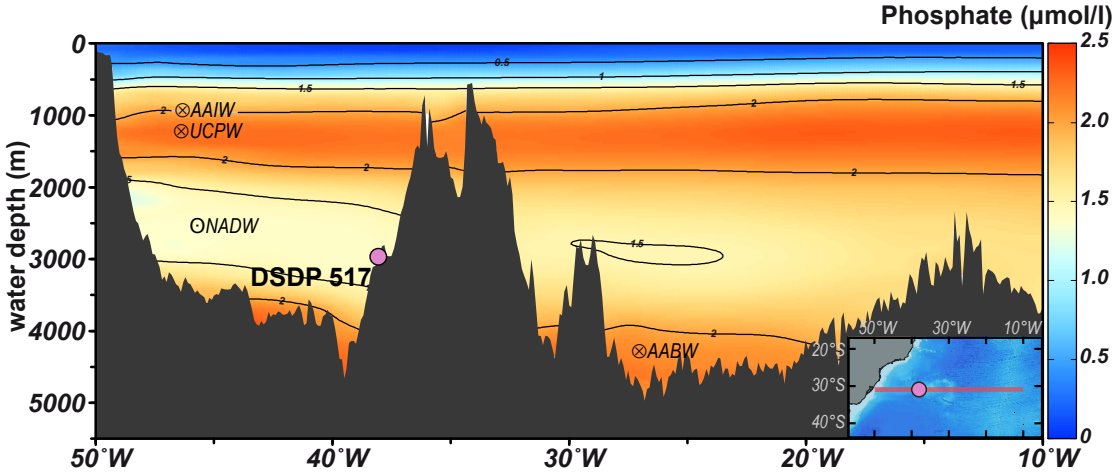

Figure 7.6: Hydrography at DSDP 517 represented by the phosphate concentration [Boyer *et al.*, 2013]. Data visualized with ODV software [Schlitzer, 2019]. Insert map based on the ETOPO1 Global Relief Model [Amante and Eakins, 2009].

7.2 Sample treatment for Nd isotopes

Additional to the ε_{Nd} record of ODP 1063 (see Section 5.3), temporal highly resolved reconstructions for other core sites were produced spanning full MIS 11 and MIS 12a.

For this purpose, ODP 980 was sampled 34 times in 1 cm thick slices along the shipboard splice from 50.02 to 59.90 mcd (B6H2W 67-68 cm to B7H1W 142-143 cm) resulting in an average temporal resolution of 1.8 ka. Additionally three total procedural replicates were carried out. Site IODP U1304 was sampled in 1 cm thick slices from 54.11 to 74.48 mcd (B6H3W 2-3 cm to A7H4W 122-123 cm) 69 times along the shipboard splice of which five samples were replicated. Thereby a temporal resolution of 0.8 ka for MIS 11 and 5.0 ka for MIS 12 was achieved. ODP 659 was sampled along the adjusted splice from Tiedemann [1991] 26 times in the depth interval 12.68–15.38 amcd (C2H2W 11-120 cm to C2H4W 88-90 cm). The 2 cm thick samples result in an average temporal resolution of 3.0 ka and two samples were replicated. The resolution of the ε_{Nd} profile of ODP 929 by Howe and Piotrowski [2017] was increased from 4.9 ka to 2.0 ka in the age range 374-451 ka. Hereto, 22 new 1 to 2 cm thick samples were taken from the shipboard splice from 16.84 to 18.57 mcd (B2H5W 72-74 cm to B2H6W 95-96 cm). One of them was also replicated. ODP 1267 was sampled in 1 cm slices along the shipboard splice 24 times from 3.38 to 4.65 mcd (A1H3W 35-36 cm to A1H4W 12-13 cm), which resulted in an average temporal resolution of 3.9 ka. A total procedural replicate of one sample was processed. The southernmost site DSDP 517 was sampled 26 times in 2 cm thick slices from 3.18 to 4.97 mbsf[1] (Z2H1W 68-70 cm to Z2H2W 97-99 cm). The sampling results in an average temporal resolution of 3.0 ka using the preliminary age model (see Section 7.1.6) and one sample was also replicated. The ε_{Nd} profiles of ODP 1267 and DSDP 517 were analyzed in Müller [2019].

7.2.1 Bulk sediment leaches

The sample processing was performed analogously to the method described in Section 3.4.1. However, for all sediment samples from sites DSDP 517 and ODP 1267 as well as for some samples from ODP 929, AG 50W-X8 (200-400 mesh) resin was used to seperate the REE from the other leached elements.

7.2.2 Measurement of Nd isotopes

The measurement of Nd isotopes followed the procedure described in Section 3.4.3. Isotopic measurements were entirely conducted on the MC ICP-MS at the *Institute of Environmental Physics*, Heidelberg University (Thermo Fisher Neptune Plus).

[1] mbsf: meter below sea floor.

8 Results

In addition to the data from ODP 1063 (see Section 5.3), sediment cores from six further sites were analyzed for their respective Nd isotopic composition spanning the time period of mid MIS 12 to MIS 11. In total, 214 samples were processed originating from 201 different depths. Total procedural blanks were always lower than 73 pg (n=22) and therefore neglectable. The measured values span from -6.88 ± 0.13 at IODP U1304 (394 ka) to -13.52 ± 0.12 at ODP 980 (409 ka). This range of values reflects seawater data observed within the modern Atlantic [van de Flierdt *et al.*, 2016; Tachikawa *et al.*, 2017] and compares to the past climate cycle [e.g. Crocker *et al.*, 2016].

8.1 Quality control

Spanning the six sediment cores, a total of 13 sediment samples were processed twice as total procedural replicates. All replicates overlap within their analytical 2σ errors (see Figure 8.1) and show an excellent agreement. The twofold standard-deviation of the deviation from their respective weighted means adds up to 0.14 ε-units and is therefore in the range of the external reproducibility of the measurements (2 SD of 0.12–0.18, and one measurement session with 0.27). Therefore, the error for each data point reported in this study is the external reproducibility of the respective measurement session.

8.1.1 Laboratory and method intercomparison

Sediment samples from ODP 929 were analyzed in this thesis to generate a better resolved record of MIS 11 in combination with the published one of Howe and Piotrowski [2017]. In this process, six samples were analyzed that differ only by 2 cm from one another, which is equivalent to a maximum age difference of 780 a. They can be used to compare the different methods (bulk sediment leaching vs. mixed planktic foraminifera) including possible laboratory biases. As seen in Figure 8.2, the values of both studies are in agreement within their analytical uncertainty. Hence, the new data points generated here can be included into the previous ε_{Nd} record of Howe and Piotrowski [2017].

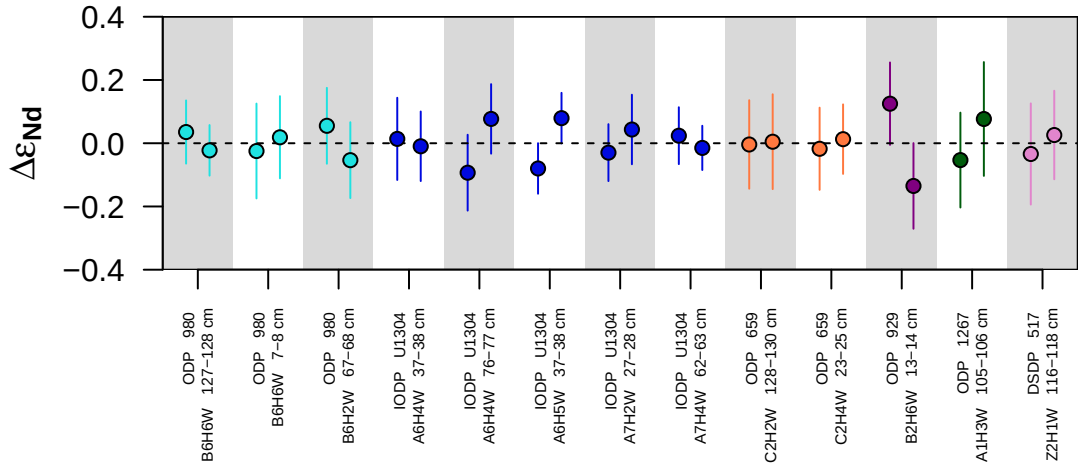

Figure 8.1: Total procedural replicates of ODP 980, IODP 1304, ODP 659, ODP 929, ODP 1267, and DSDP 517. The deviation from the respective weighted mean (dashed line) is given for the data points with their individual analytical errors (2 SEM).

8.2 ODP 980

The Nd isotopic composition at the Feni Drift at Rockall Trough is reconstructed with an average temporal resolution of 1.8 ka (see Figure 8.3). It reveals an ε_{Nd} range from

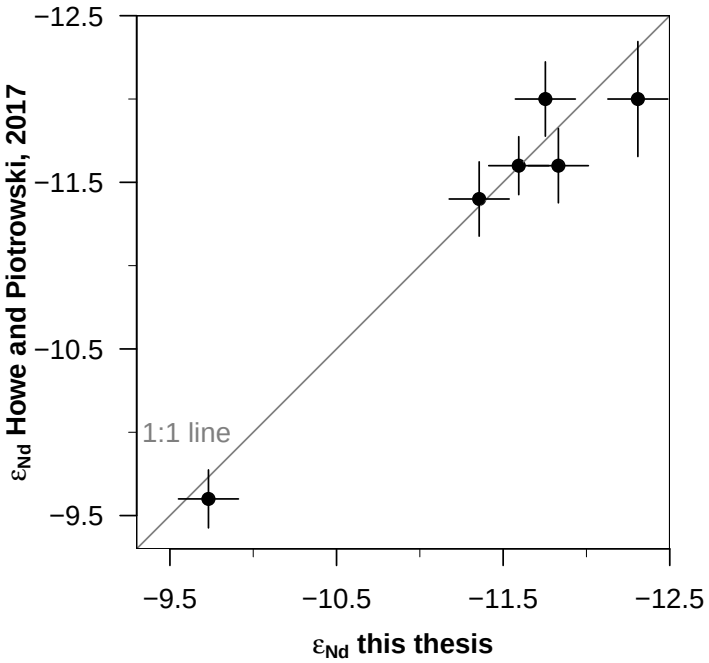

Figure 8.2: Comparison between the Nd isotopic signatures published in Howe and Piotrowski [2017] using mixed planktic foraminifera and analyzed here using bulk sediment leaching. The sample depths differ by 2 cm and can be considered coeval.

−7.20 to −13.52 and thus spans more than 6 ε-units. The most radiogenic values are found during MIS 12, while during MIS 11 they are more unradiogenic.

The records starts at 444.6 ka with an ε_{Nd} value of -10.62 ± 0.17. It is followed by a short spike towards a more radiogenic value of -7.55 ± 0.12 and returns to relatively constant values of around −9.3. A second excursion with more radiogenic values peaking at 432.6 ka with an ε_{Nd} value of -7.20 ± 0.17 last for at least 6 ka, until it returns to a constant Nd isotopic composition of −9.7 from 425.6 to 423.2 ka. After another short excursion at 421.9 ka with an ε_{Nd} value of -8.48 ± 0.17, a gradual decrease starts at 420.7 ka with -10.19 ± 0.12 and ends at 415.3 ka with -11.17 ± 0.12. A sharp drop to ε_{Nd} values of −13.2 follows. After the minimum of ε_{Nd} values is reached at 409.3 ka with -13.52 ± 0.12 a monotonic gradual increase starts and continues until 388.7 ka when an ε_{Nd} value of -10.36 ± 0.12 is reached. The last two data points of the record at 386.7 and 384.8 ka are marked by a Nd isotopic composition of −11.4.

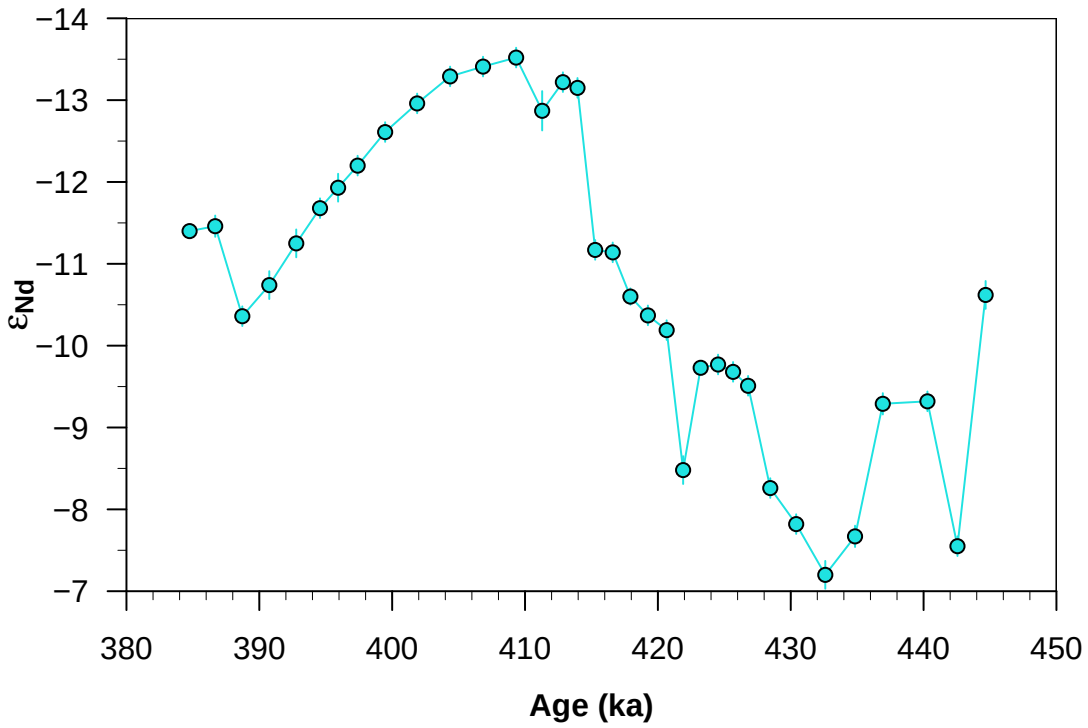

Figure 8.3: Nd isotopic composition at ODP 980 spanning mid-MIS 12 to MIS 11.

8.3 IODP U1304

At the Gardar Drift at IODP U1304 the Nd isotopic composition spans nearly 6 ε-units ranging from −6.88 to −12.67 (see Figure 8.4), whereby in contrast to the typical glacial-

interglacial pattern found at the other sites, the most radiogenic values occur during MIS 11 and the most unradiogenic ones during the glacial.

MIS 12 is characterized by ε_{Nd} values fluctuating between -10.25 ± 0.18 and -12.67 ± 0.18 but centered at around -11.5. After 422.5 ka ε_{Nd} increases reaching -8.42 ± 0.07 at 420.0 ka. The ε_{Nd} values form a double peak, separated by a slight decrease with ε_{Nd} values of ~ -9.2. After these peaks, at 414.7 ka a short excursion toward more unradiogenic values with -10.16 ± 0.13 occurs. The following time period until 399.6 ka is characterized by an exceptionally stable Nd isotopic composition of around -9.3 ε_{Nd}. Thereafter, a gradual increase toward the most radiogenic values sets in until 394.0 ka when an ε_{Nd} value of -6.88 ± 0.13 is recorded. A sharp decrease to a Nd isotopic composition of -11.50 ± 0.18 at 391.7 ka follows. However, this excursion does not last long and from 389.9 to 387.2 ka values of -9.6 ε_{Nd} are reached. The time period of 386.2–377.1 ka is characterized by a Nd isotopic composition fluctuating between -9.15 ± 0.18 and -7.71 ± 0.18 and is terminated by an again glacial-like ε_{Nd} value of -11.53 ± 0.18.

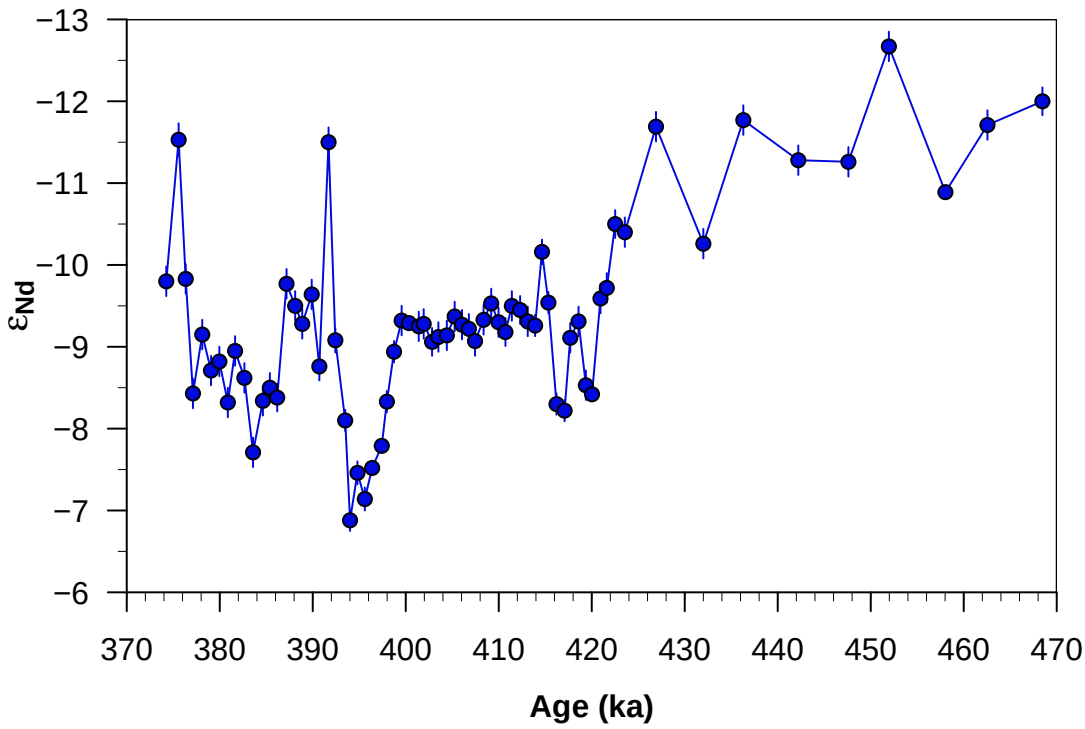

Figure 8.4: Nd isotopic composition at IODP U1304 spanning mid-MIS 12 to MIS 11.

8.4 ODP 659

The profile of Nd isotopes at ODP 659 (see Figure 8.5) varies only slightly around a mean of -11.6 ± 0.6 (1 SD), whereof the most radiogenic values are found during MIS 12a. The record starts at 460.3 ka with an ε_{Nd} value of -12.14 ± 0.13. During the course of MIS 12, the values increase to -10.44 ± 0.13 at 442.1 ka. After a slight decrease of about 0.3 ε-units, the values increase again towards -10.01 ± 0.13 at 432.0 ka and represent the most radiogenic Nd isotopic signature recorded at ODP 659. Subsequently, a sharp decrease to -11.77 ± 0.13 takes place. Until 423.3 ka the ε_{Nd} values increase again. However, they decrease again to -12.1 recorded between 418.7 and 415.9 ka. An excursion to an ε_{Nd} of -10.80 ± 0.15 is happening at 412.6 ka, but the Nd isotopic composition returns to values between -11.66 ± 0.14 and -12.12 ± 0.13 until 380.7 ka. The record ends with an increase in ε_{Nd} toward -11.20 ± 0.18 at 378.0 ka.

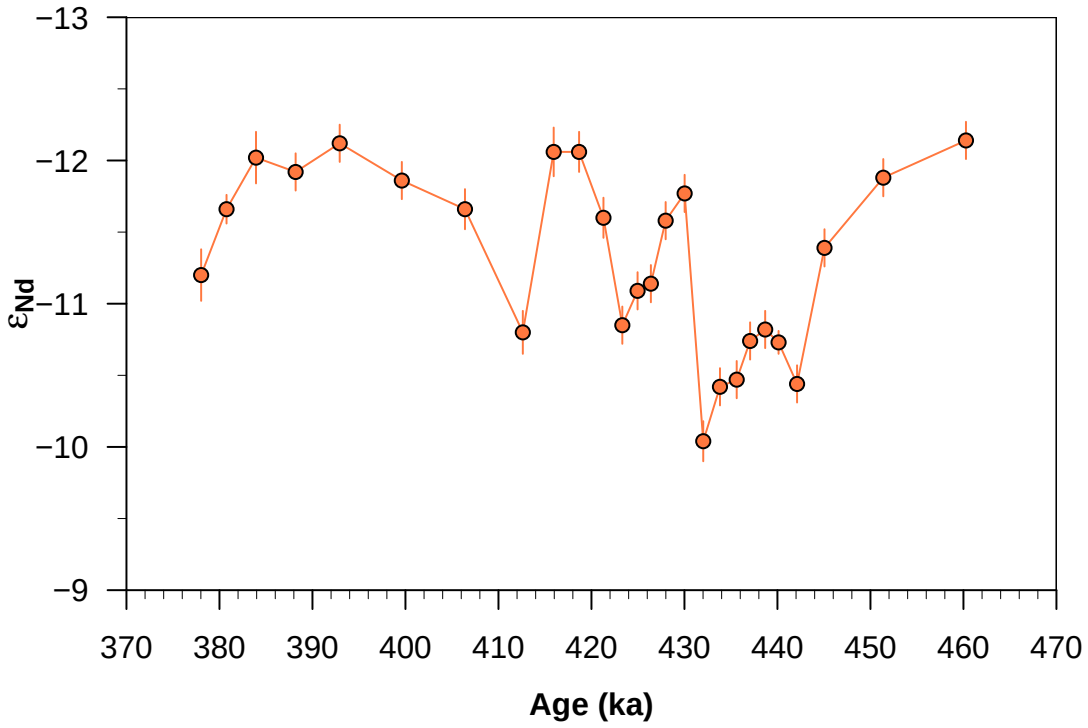

Figure 8.5: Nd isotopic composition at ODP 659 spanning mid-MIS 12 to MIS 11.

8.5 ODP 929

The published record of Nd isotopic composition at the Ceara Rise [Howe and Piotrowski, 2017] was complemented by new measurements in order to increase the

temporal resolution. For the time span of 450 to 370 ka, the Nd isotope values range from -9.29 to -12.38 with more radiogenic values recorded during MIS 12 compared to MIS 11.

The new composite record (see Figure 8.6) shows an increase in ε_{Nd} to -9.29 ± 0.18 at 433.3 ka. Afterwards, the values decrease gradually with a slight stagnation between 423.7 and 419.0 ka of around -10.5. The peak values are reached at 408.1 ka with a Nd isotopic composition of -12.31 ± 0.18 and is kept for the next four thousand years. Thereafter, the ε_{Nd} increase again toward -10.88 ± 0.18 at 395.5 ka. A second decrease in MIS 11 takes places and reaches similar values like the first peak of -12.38 ± 0.18 at 385.8 ka. However, the younger one is not as pronounced as the first one and the ε_{Nd} values promptly increase again. At 377.1 ka an ε_{Nd} value of -11.10 ± 0.36 is reached.

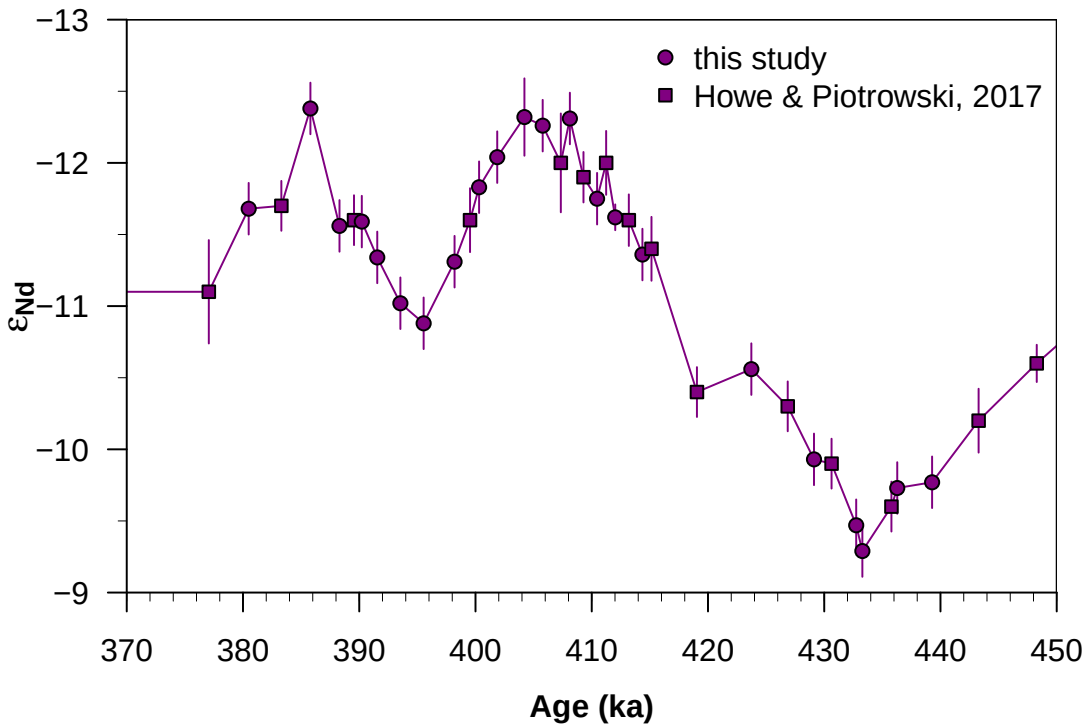

Figure 8.6: Nd isotopic composition at ODP 929 spanning mid-MIS 12 to MIS 11. Data points from Howe and Piotrowski [2017] are depicted as squares.

8.6 ODP 1267

At ODP 1267, the record of Nd isotopic composition is very smooth (see Figure 8.7). The record begins at 464.5 ka with an ε_{Nd} value of -10.95 ± 0.27. It increases gradually until 438.6 ka, when for a period of 8 thousand years relatively constant values of

~ -9.0 are recorded. As gentle as the values increased, they become constantly more unradiogenic. At 398.1 ka, the minimum value is reached with ε_{Nd} of -12.26 ± 0.27. Afterwards, the values increase again until the end of the record at 374.3 ka with a Nd isotopic composition of -11.00 ± 0.27.

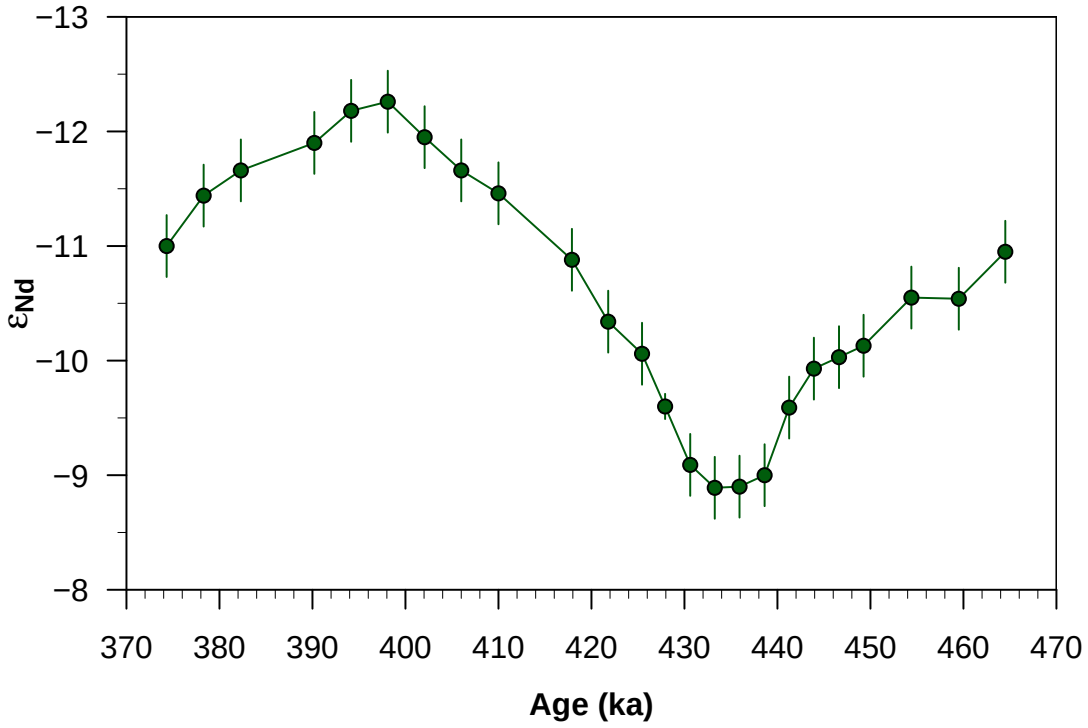

Figure 8.7: Nd isotopic composition at ODP 1267 spanning mid-MIS 12 to MIS 11.

8.7 DSDP 517

The Nd isotopic composition at the Rio Grande Rise recorded at DSDP 517 (see Figure 8.8) is characterized by ε_{Nd} values of about -10 during MIS 12. It rises toward the most radiogenic value recorded at that site with -8.44 ± 0.27. Afterwards, the signature of Nd isotopes decreases again first smoothly until a value of -9.83 ± 0.27 is reached. Then it drops by more than two ε-units to an ε_{Nd} value of -12.18 ± 0.27. However, this is just a singular peak and the neodymium values increase again towards a Nd isotopic composition of -9.88 ± 0.27. The following time period is marked by about 0.4 ε-units more unradiogenic values, centered at around -10.3. It gently evolves to a fairly constant Nd isotopic composition of an ε_{Nd} value of -9.7, which prevails from 380.9 to 356.9 ka according to the current age model.

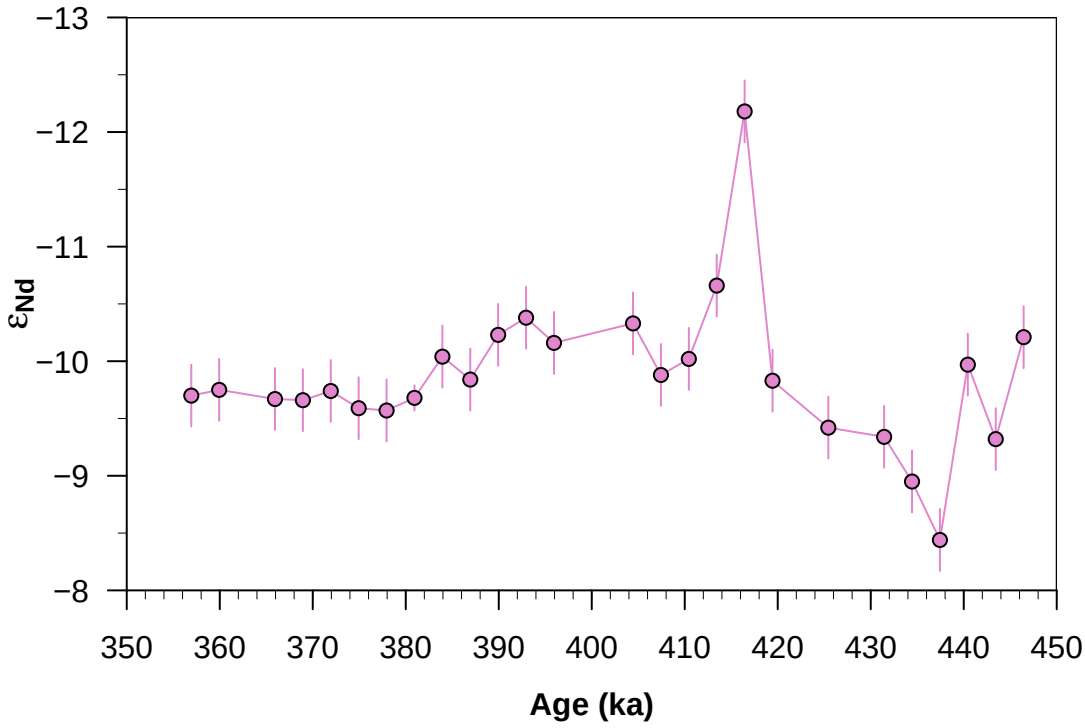

Figure 8.8: Nd isotopic composition at DSDP 517 spanning mid-MIS 12 to early MIS 10.

9 Discussion

9.1 Regional water mass changes

9.1.1 ODP 980

Reliability of the data

Two studies have reconstructed the Nd isotopes at ODP 980 for the past 44 ka. Crocket *et al.* [2011] used bulk sediment leaching following the method of Gutjahr *et al.* [2007], and Crocker *et al.* [2016] analyzed mixed species of planktic foraminifera and fish debris. While the data for planktic foraminifera and fish debris agree with each other, they differ to the leachate data toward less radiogenic values during the Holocene [Crocker *et al.*, 2016], and are therefore better in line with expected seawater values. The authors state that this offset is most likely due to the increased influence of silt-sized titanomagnetite grains in the sediment column of ODP 980, which are transported by bottom currents likely from the Nordic Basaltic Province, thus are radiogenic and susceptible to leaching. Also the leaching method itself might contribute to the offset [Crocker *et al.*, 2016], as it uses a prior decarbonation step, which was shown to be unfavorable for the reliable extraction of ε_{Nd} values as the carbonate of the sediment acts as a buffer against attacking the detrital fraction and therefore a possible shift toward more radiogenic values [Wilson *et al.*, 2013; Blaser *et al.*, 2016].

Here in this study, the leaching method of Blaser *et al.* [2016] was used, which skips the decarbonation step and has shown to reliably extract bottom water signatures in accordance with foraminiferal ε_{Nd} values. The reconstructed ε_{Nd} values for mid-MIS 12–MIS 11 span the same range as the values recorded during the past 44 ka by Crocker *et al.* [2016], and are similar during glacial and interglacial states respectively (see Figure 9.1). Additionally, during MIS 11, the magnetic susceptibility [Shipboard Scientific Party, 1996] (see Figure 9.2) as well as isothermal and anhysteretic remanent magnetization (IRM, and ARM respectively) [Channell and Raymo, 2003] are close to zero, which point to a very low concentration of magnetic minerals [Channell and Raymo, 2003] and only a minor content of titanomagnetites (which usually have a high magnetic susceptibility

[Robinson, 1986; Robinson and McCave, 1994]) in the sediment column. Therefore, the possibility of a shift toward more radiogenic ε_{Nd} values is minimized during this warm period compared to the Holocene, during which the magnetic susceptibility is higher [Shipboard Scientific Party, 1996]. Thus, there is high confidence that the chosen method to extract the Nd isotopic signature at ODP 980 was the right choice and that the ε_{Nd} values represent the bottom water signature at the Feni Drift.

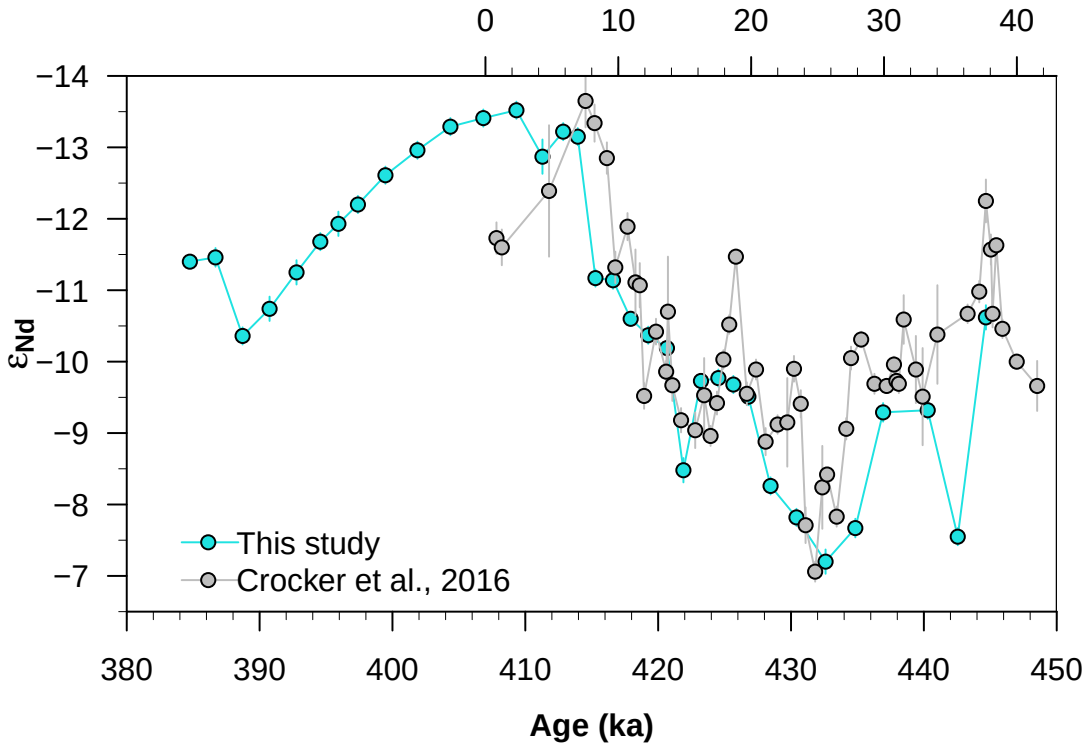

Figure 9.1: Comparison of the Nd isotope records at ODP 980 from the past 44 ka (gray, top x-axis) [Crocker *et al.*, 2016] and from MISs 12–11 (blue, bottom x-axis). The alignment of both records is based on the obliquity signal following the approach by Masson-Delmotte *et al.* [2006].

Modern seawater data

In the close vicinity to ODP 980, a seawater profile of Nd isotopes was taken at station ICE-CTD3 (55°56′N, 14°24′W, see Figures 9.3 and 9.4) in 2012 [Dubois-Dauphin *et al.*, 2017]. In about 1500 m water depth LSW is found, which is characterized by a Nd isotopic signature of -13.7 ± 0.2. Below, the ε_{Nd} values become slightly more radiogenic with -12.8 ± 0.2 at the bottom in 1750 m water depth. Unfortunately, no modern seawater data from the central Rockall Trough covering deeper depths are available so far. Just north of the Wyville-Thomson Ridge in the Faroe-Shetland Channel, a

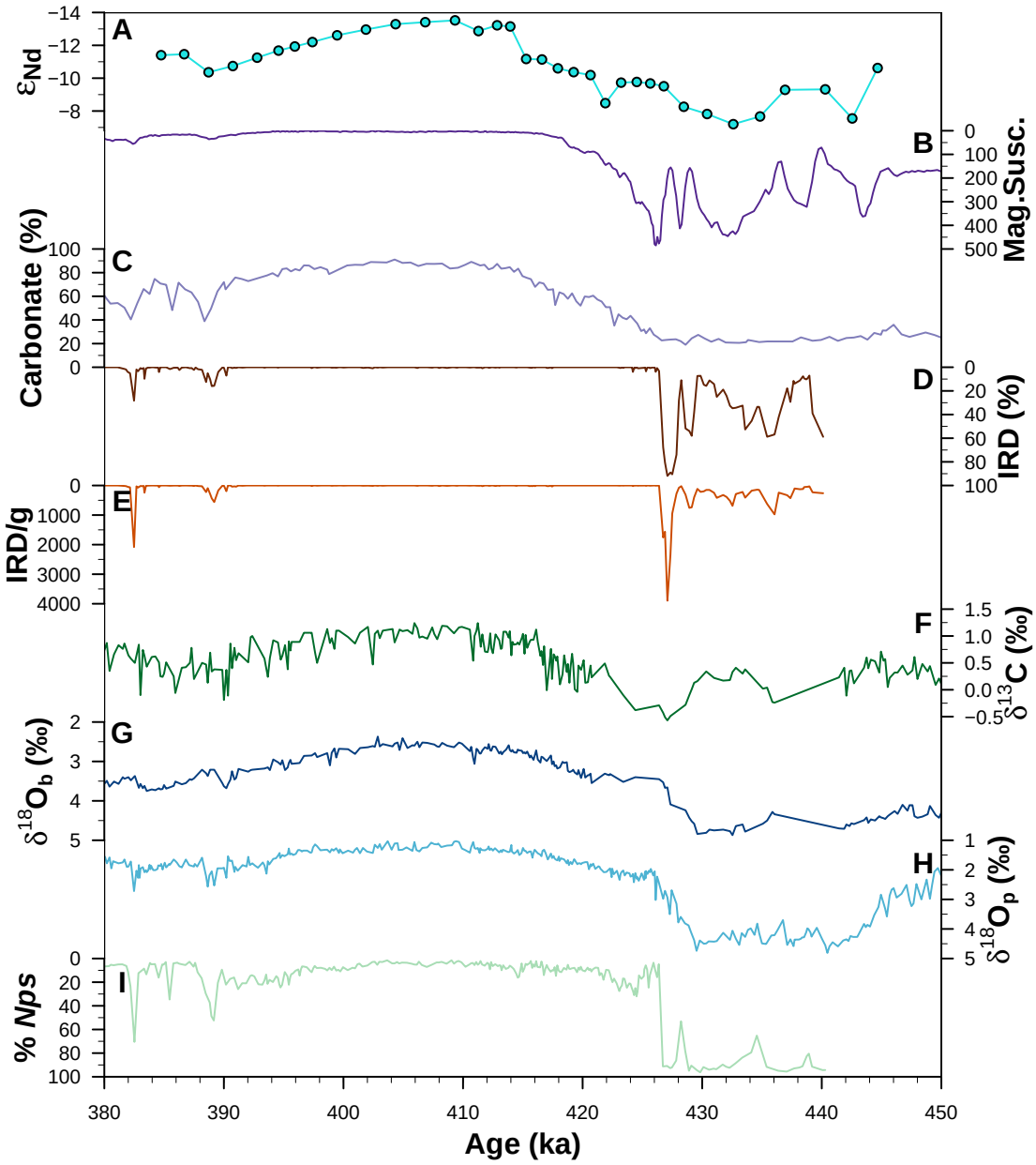

Figure 9.2: Climate records of ODP 980. (A) Nd isotopic composition. Note that most error bars are smaller than the symbols. (B) Magnetic Susceptibility of the sediment [Shipboard Scientific Party, 1996]. (C) Carbonate content derived from diffuse spectral reflectance [Ortiz *et al.*, 1999]. Ice-rafted debris as (D) percentage relative to total entities and as (E) ratio relative to dry bulk sediment weight [Oppo *et al.*, 1998]. Stable carbon (F) and oxygen (G) of the benthic foraminifera *C. wuellerstorfi* [Oppo *et al.*, 1998]. (H) Stable oxygen isotopes of the polar planktic foraminifera *N. pachyderma* (right-coiling) and (I) the percentage of *N. pachyderma* (left-coiling) [Oppo *et al.*, 1998]. Note that in (A,B,D,E,G,H,I) y-axes are reversed.

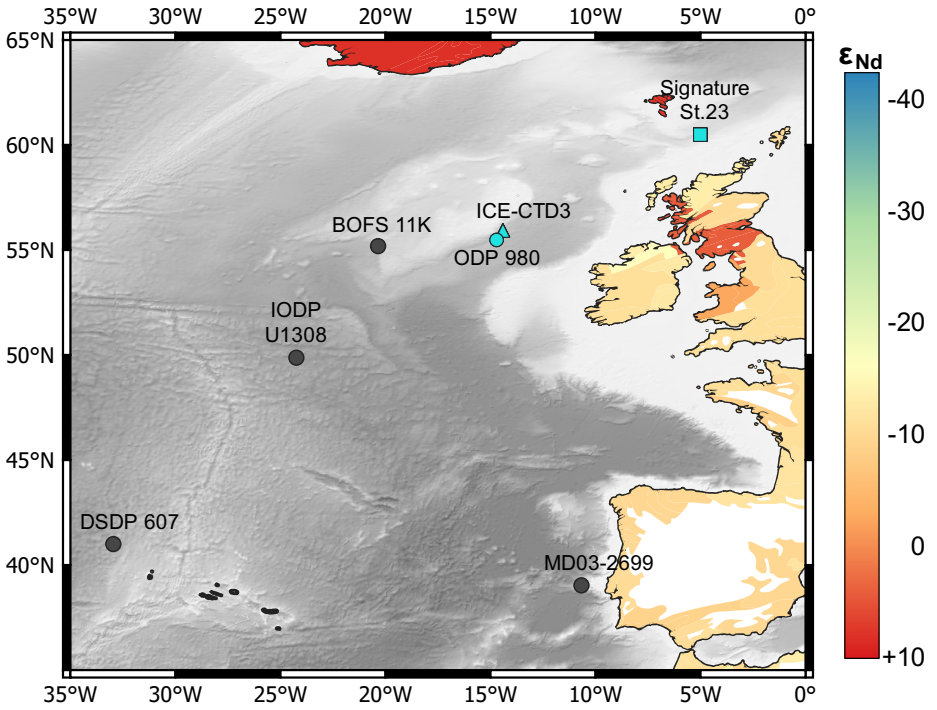

Figure 9.3: Location of ODP 980 and of other sediment cores and seawater stations discussed in the text. Color on the continents represents their Nd isotopic composition [Robinson *et al.*, 2021]. Bathymetry based on the ETOPO1 Global Relief Model [Amante and Eakins, 2009].

seawater profile was taken during the Signature Cruise at station 23 in 1999 (60°30′N, 5°0′E) [Lacan and Jeandel, 2004b]. The deeper water samples were described by the authors as pure ISOW (before it flows into the Iceland Basin and thereby gets entrained with Atlantic waters and Labrador Sea Water). Its Nd isotopic signature is marked by a radiogenic ε_{Nd} value of -8.2 ± 0.6, which shows the imprint of basaltic material along the western and southern margins of the Norwegian Basin [Lacan and Jeandel, 2004b].

Radiogenic peaks

Two peaks toward radiogenic values are recorded during MIS 12. A shorter peak at 442.6 ka with a Nd isotopic composition of -7.55 ± 0.12 is followed by a six thousand years long peak with a maximum value of -7.20 ± 0.17. Such radiogenic peaks are also present during the last glacial at ODP 980 [Crocket *et al.*, 2011; Crocker *et al.*, 2016] and at sediment cores atop and on the southern flanks of the Rockall Plateau nearby [Roberts and Piotrowski, 2015]. The latter study investigated sediment cores along a depth transect from 1150 m to 4045 m water depth and found in all cores elevated ε_{Nd} values, which reached up to -4.2 in BOFS 11K (55°12′N, 20°21′W, 2004 m water depth).

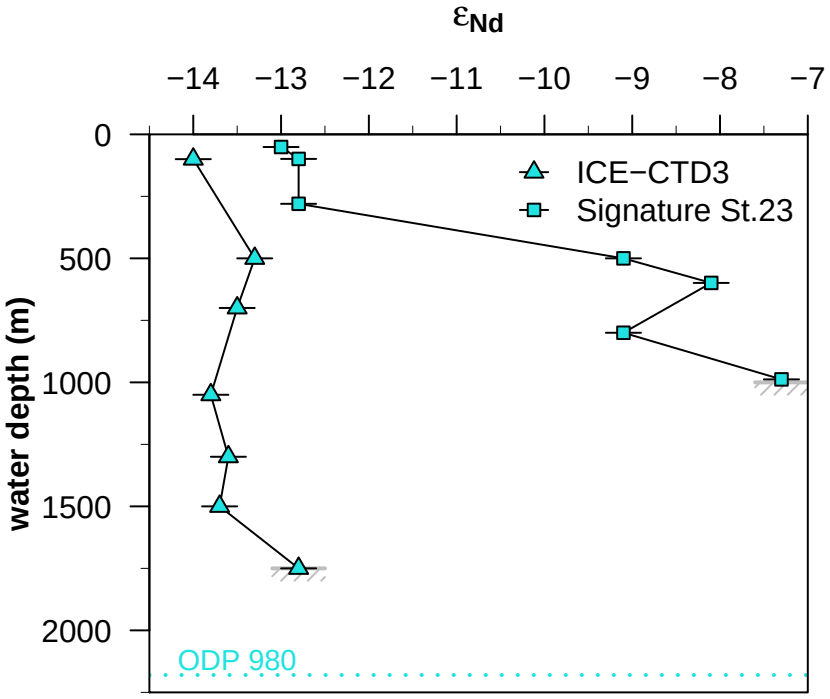

Figure 9.4: Nd isotopic composition of seawater at Station ICE-CTD3 (triangles) at the Rockall Trough [Dubois-Dauphin *et al.*, 2017] and at Signature Station 23 (squares) in the Faroe-Shetland Channel [Lacan and Jeandel, 2004b]. The former is located roughly 50 km and the latter 800 km to the northeast of ODP 980, for which its depth is depicted by the dotted line.

As this trend is recorded in all sediment cores, the authors argue for a re-labeling of the overlying seawater by IRD particles that rain through the water column. However, Crocker *et al.* [2016] rule out this process as a dominant control on the ε_{Nd} signature at ODP 980 during Heinrich Events. This is because they do not record ε_{Nd} values higher than -8, and despite similar IRD assemblages during Heinrich Events 2 and 4 the Nd isotopic signatures point into opposite directions. Furthermore, the amount of IRD per g sediment is smaller than at the BOFS sites which the authors interpret as a reduced potential for a re-labeling due to less material sinking through the water column.

For MIS 12, the process of re-labeling as a cause of the radiogenic peaks can also be considered as unlikely. The shapes of the peaks do not agree with the IRD recorded [Oppo *et al.*, 1998]. While a high percentage of IRD is present at about 435 ka and decreases afterwards, the ε_{Nd} profile shows a bell shape. Additionally, the terminal ice rafting event at around 427 ka, is not traced in the ε_{Nd}.

For Heinrich Event 2, Crocker *et al.* [2016] found that an increased presence of over-

flow waters originating from the Nordic Seas are most likely to generate the observed radiogenic peak. Today, the deepest seawater value of Signature Station 23 [Lacan and Jeandel, 2004b] reaches an ε_{Nd} value of -7.3 ± 0.2, which can be seen as a precursor for the overflow waters that eventually reach the core site of ODP 980. Therefore, the Nd isotopic signature recorded during MIS 12 might resemble a pure signal of Wyville-Thompson Ridge overflow water (under the assumption that the Nd isotopic signature of this water mass was identical to today). Another explanation, which also hints to an increased influence of a water mass coming from the Nordic Seas, is an increased transport of (titano)magnetites to the core site. The magnetic susceptibility [Shipboard Scientific Party, 1996] shows a good agreement with the ε_{Nd} record during MIS 12. A higher magnetic susceptibility suggests a higher amount of magnetites, which likely originate from the Nordic basaltic province [Kissel *et al.*, 1999; Ballini *et al.*, 2006]. During the transport, these particles might release their Nd isotopic signature in the ambient seawater and thus influence the seawater toward more radiogenic values. A similar process was proposed for the benthic nepheloid layers found in the Northwestern Atlantic [Pöppelmeier *et al.*, 2019a]. However, the last peak in the magnetic susceptibility at 426 ka does not seem to have a counterpart in the Nd isotope record. Nevertheless, the radiogenic signatures recorded during the two peaks at ODP 980, seem to hint to an increased influence of overflow waters from the Nordic Seas.

A common explanation for radiogenic ε_{Nd} during glacials in Atlantic sediment cores, is an increased contribution of SSW to the core site. In this case for ODP 980 though, there is evidence that contradict that reasoning. To record such radiogenic ε_{Nd} values of -7.2, a water mass originating from the southern ocean must have arrived in the very far North Atlantic in a rather undiluted form. This is unfeasable, especially as the sediment cores along the northward flow path display more unradiogenic values (see Chapter 8). Admittedly, most sediment cores have a lower sedimentation rate than ODP 980 and hence may not resolve the radiogenic excursions. Furthermore, the benthic stable carbon isotope record of ODP 980 still shows positive $\delta^{13}C$ values especially during the long-lasting radiogenic ε_{Nd} peak, which are suggestive of a northern source for the water mass.

Water mass changes

Irrespective of the radiogenic peaks, there is no clear change evident in the Nd isotope record at Termination V, where typically an alteration in ε_{Nd} values is expected

associated with a modification of circulation patterns, when the climate shifts from a cold into a warm state. However, this is not because the sediment section is missing or because the bioturbation is too pronounced to smear out a clear transition, since other proxies like both benthic and planktic stable oxygen isotopes and the percentage of *N. pachyderma* (left-coiling) [Oppo *et al.*, 1998] shift sharply and clearly capture the glacial termination (see Figure 9.2). The relatively constant and similar ε_{Nd} values are indicative that either the same water mass, or different water masses with the same Nd isotopic signature, bathed ODP 980 both during MIS 12 and during the beginning of MIS 11, when already peak interglacial conditions were established.

Several lines of evidence argue against the presence of SSW at ODP 980. For the time period of 440–437 ka only Nd isotopes can point to the provenance of the water mass, as benthic stable carbon isotopes are scarce. Looking only at the Nd isotopic signature of -9.3 at ODP 980, one cannot rule out a presence of SSW in the Rockall Trough. But if one considers the Nd isotopic signature at ODP 659, which would be located upstream of a SSW mass, more unradiogenic ε_{Nd} values with a minimum value of -10 are recorded and therefore are even more negative than the ones detected at ODP 980. The beginning of MIS 11 from 426 to 424 ka, a Nd isotopic composition of about -9.7 is recorded. While the few stable carbon isotope data points show a negative signature of about -0.5 ‰, already more unradiogenic values were found in more southerly located cores and hence show that they were not bathed by SSW anymore. Between 420 and 415 ka, the Nd isotopic signature decreases slowly from -10.2 to $-11.2\,\varepsilon$-units. During this time, the stable carbon isotopes are still slightly lower (at around +0.3 ‰) than compared to the following stable plateau of ∼+1.0 ‰. Nevertheless, these values are still more positive as one would expect for a water mass of southern origin, which would be expressed in more negative values as seen at DSDP 607 (41°0.1′N, 32°57.5′W, 3427 m water depth) with around -0.8 ‰ [Raymo *et al.*, 1990] or at IODP U1308 (49°52.7′N, 24°14.3′W, 3871 m water depth) with around -0.5 ‰ [Hodell *et al.*, 2008] during MIS 12.

For the LGM, Crocker *et al.* [2016] argue based on the Nd isotopic composition and the reconstructed carbonate ion concentration for the increased influence of overflow waters from the Nordic Seas at the core location. For MIS 12 and beginning of MIS 11, this could also be the case, assuming that the overflow waters mix with water masses from the northeastern Atlantic.

Another possibility, which was also discussed by Crocker *et al.* [2016], is a deepening of Mediterranean Outflow Water and therefore an increased influence of this water

mass at ODP 980. During the last glacial, the Mediterranean Outflow Water (MOW) is assumed to have deepened as it was found at water depths of 1600–2200 m at the Portuguese margin together with an increased flow strength [Schönfeld and Zahn, 2000; Rogerson *et al.*, 2005]. For MIS 12, Sánchez Goñi *et al.* [2016] also found that the lower core of MOW was more enhanced as during interglacials. In a core off Portugal (MD03-2699, 39°2.2′N, 10°39.6′W, 1865 m water depth), the bottom current intensity was strong and warm bottom water temperatures were found, indicating that MOW also settled deeper during MIS 12 [Voelker and Lebreiro, 2010]. In this core however, the bottom water temperatures did not change over the course of the glacial termination and stayed high during the beginning of MIS 11 until about 410 ka [Voelker and Lebreiro, 2010] which hints to a continued influence of MOW. As this pattern resembles the one seen in the Nd isotopes at ODP 980 (despite some inconsistencies in the exact timing), it is plausible that the influence of MOW reached as far north as to the Feni Drift and in a water depth of about 2200 m even during the beginning of the interglacial.

At around 415 ka either the MOW shoaled again or the influence of the Nordic Seas overflows decreased at ODP 980. Afterwards, the core was bathed either by NEADW that gained a more unradiogenic signature than today, or LSW deepened. Today (see Figure 9.4, this water mass is situated in water depths just a little shallower than ODP 980 and exhibits ε_{Nd} values of -13.7 [Dubois-Dauphin *et al.*, 2017]. Therefore, the Nd isotopic values of around -13.5 might represent such a deepening of LSW and subsequent slow shoaling, when the Nd isotopic composition becomes gradually more radiogenic again towards the short cold spell at around 389 ka and thereby increasing the influence of overflow waters again at the core site.

9.1.2 IODP U1304

IODP Site U1304 was chosen to reconstruct the evolution of ISOW over MISs 12–11 as its location on the southern Gardar Drift is directly situated in the flow path of this overflow water mass (see Figure 9.5). In contrast to the other sites studied here, the general trend with more radiogenic water masses during MIS 12 and less radiogenic water masses in the following warm period is reversed. The most unradiogenic values are recorded during MIS 12 with ε_{Nd} values of about -11.3 ± 0.7. This is indicative of the presence of SSW even at the far north Atlantic at 3065 m water depth. The stable carbon isotopes [Xuan *et al.*, 2016; Hodell and Channell, 2016] of the same core support this interpretation. Compared to the LGM [Blaser, 2017], moderately less radiogenic

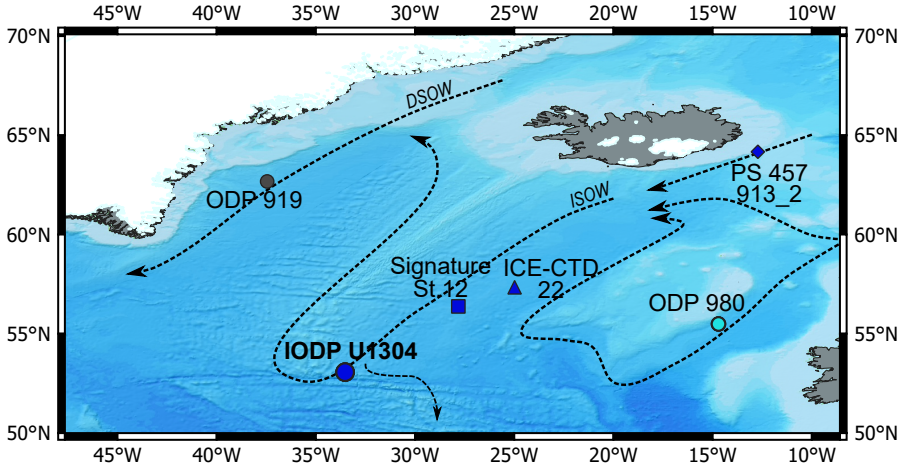

Figure 9.5: Locations of sediment cores and seawater stations discussed in the context of IODP U1304. Dashed arrows depict the schematic flow paths of the overflow water masses. Bathymetry based on ETOPO1 Global Relief Model [Amante and Eakins, 2009].

values are found, but the Nd isotopic composition recorded at the Bermuda Rise is also less radiogenic throughout MIS 12 relative to the LGM. As both IODP U1304 and ODP 1063 record almost the same ε_{Nd} values, both sites are presumably bathed by the same water mass with the same mixing proportions. This also includes that ISOW was either flowing in shallower depths and/or its strength was considerably reduced during the glacial, as no influence is seen at IODP U1304.

This changes in the course of Termination V. A while after the ice volume starts to decrease (as seen by the benthic stable oxygen isotopes [Xuan *et al.*, 2016], Figure 9.6), first the stable carbon isotopes and shortly afterwards, the Nd isotopic composition shifts to less radiogenic values. However, the exact timing and possible lead or lags between ε_{Nd} and $\delta^{13}C$ is hard to determine due to the lower temporal resolution of both records during the termination. Nevertheless, both proxies indicate a change in the water masses. The neodymium isotopes show the presence of pure ISOW at the core location, which has nowadays a Nd isotopic composition of -7.5 ± 0.1 (PS457 913_2, Morrison *et al.* [2019]). Seawater profiles [Lacan and Jeandel, 2004b, 2005a; Dubois-Dauphin *et al.*, 2017] in the vicinity of IODP U1304 (see Figure 9.7) show more radiogenic values in the deeper water than in the overlying water column, indicating the greater admixture of ISOW, however they do not reach such radiogenic values as reported for the pure ISOW. The values become more unradiogenic as North Atlantic water masses get entrained while ISOW sinks down. As this offset between nearby seawater values and the reconstructed Nd isotopic composition at IODP U1304 is also seen at the core top, Blaser [2017] suggested that possibly a more pristine Nd isotopic

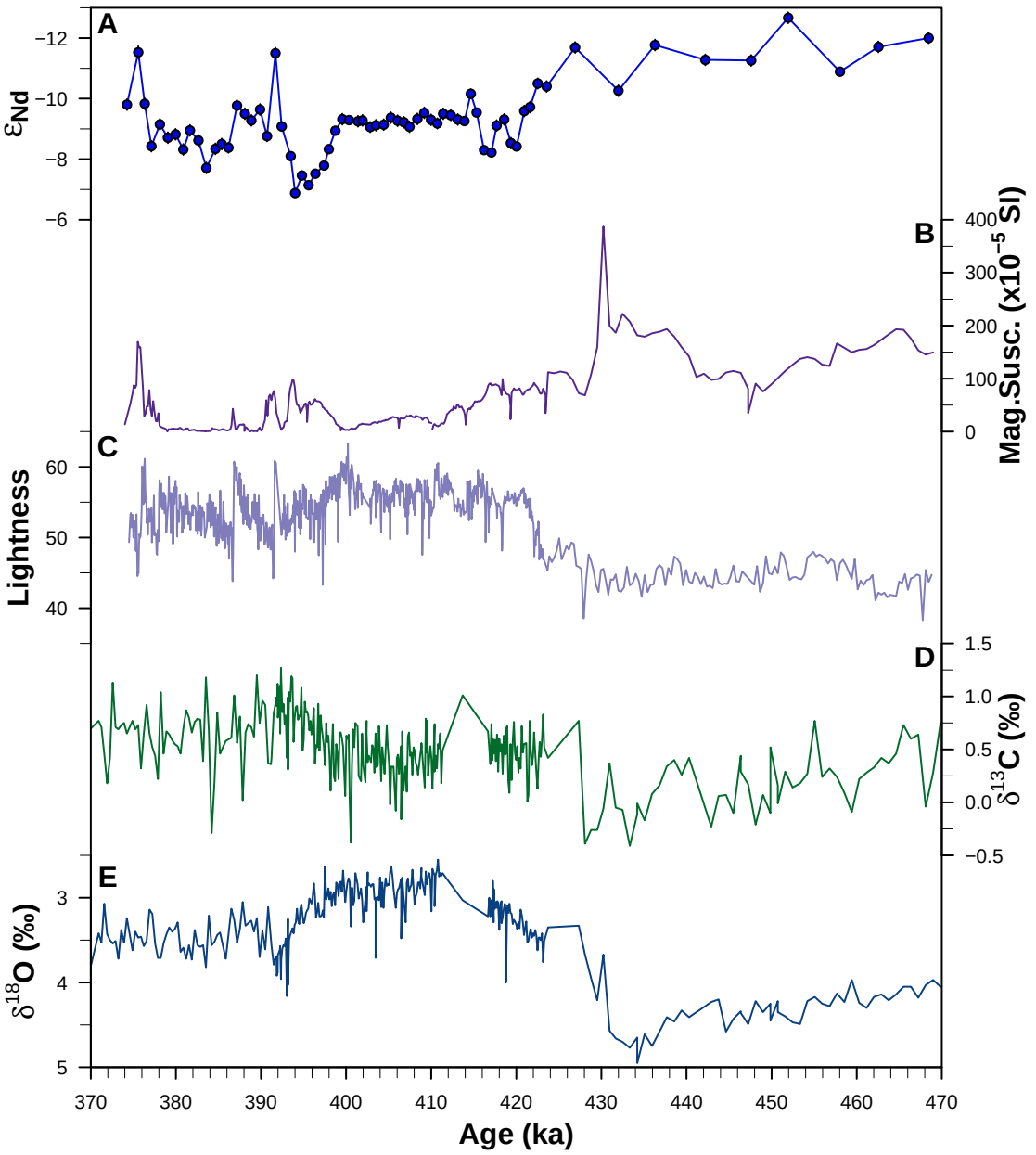

Figure 9.6: Climate records from IODP U1304. (A) Nd isotopic composition. (B) Magnetic susceptibility and (C) lightness (L*) of the sediment [Expedition 303 Scientists, 2006]. (D) Stable carbon and (E) oxygen isotopes of the benthic foraminifera *C. wuellerstorfi* [Xuan *et al.*, 2016; Hodell and Channell, 2016].

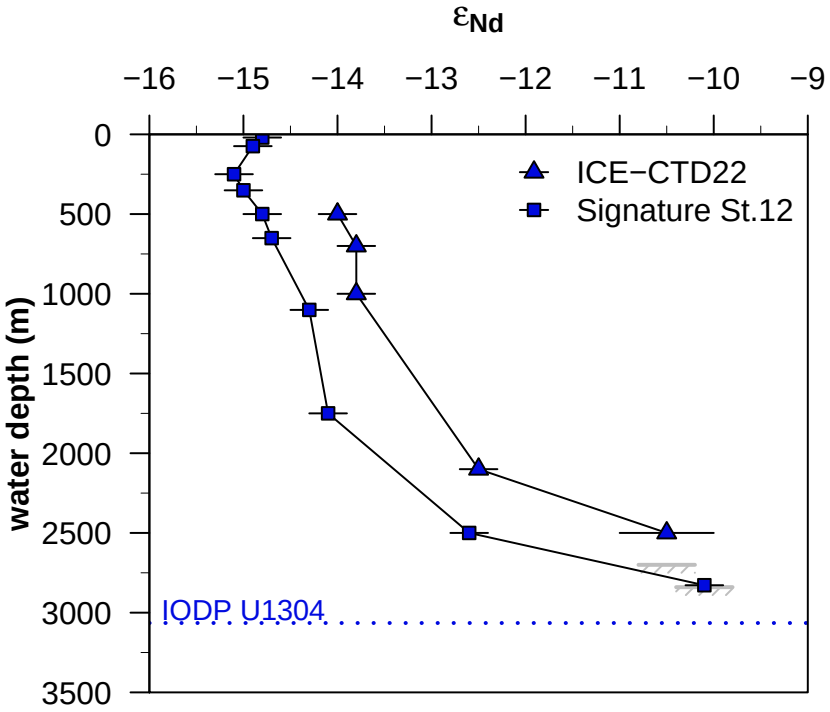

Figure 9.7: Nd isotopic composition of seawater stations in proximity to IODP U1304 in the Iceland Basin. Signature Station 12 [Lacan and Jeandel, 2004c, 2005a] is located about 735 km and ICE-CTD22 [Dubois-Dauphin *et al.*, 2017] 1064 km to the northeast of the cores site, for which its depth is depicted by the dotted line.

signature of the overflow water mass is preserved and transported at the sediment-water interface than several 10s of meters above the seafloor, where the deepest seawater was sampled.

Therefore, I suggest that the ε_{Nd} values of -8.4 from 420 to 416 ka indicate the presence of ISOW, while the following time period between 414 to 398 ka with a very stable Nd isotopic composition shows either a greater entrainment of other North Atlantic water masses into ISOW or a moderate change in the endmember of the overflow water mass. Interestingly, during this phase both the stable isotope records of this core and the ε_{Nd} record of ODP 980 show a plateau-like behavior, suggesting a long-lasting period of stable climatic conditions with only minor fluctuations. This is also seen in other climatic records [e.g. Kandiano *et al.*, 2016]. During the following 7 ka of ice build-up from 398 to 391 ka as seen in the benthic $\delta^{18}O$ [Xuan *et al.*, 2016], the Nd isotopes experience an excursion to even more radiogenic values as previously recorded, with the most extreme value reaching -6.88 ± 0.13. This can be interpreted as an increased influence of the overflows originating from the Iceland-Faroe Ridge. Although the shape of this excursion resembles the concurrent one in the magnetic susceptibility

[Expedition 303 Scientists, 2006], there is no general coherence between both proxies. Therefore a major change in the local inputs of different particles impacting the Nd isotopic composition can be ruled out. This is further supported by the fact that the amount of volcanogenic and lithogenic particles in sediment cores close to IODP U1304 during the past 36 ka do not vary with the Nd isotopic composition [Hodell *et al.*, 2010; Blaser, 2017]. An alternative explanation of these radiogenic values might be that the location of the deep water formation itself shifted further to the south near Iceland into the region where the imprinting of the radiogenic signature happens.

At 391.7 ka a short setback happens, when glacial like ε_{Nd} were found. It seems that there has been a short advance of SSW to the north Atlantic during that period, which though was not long-lasting as the Nd isotopic compositions only thousand years later points again to the enduring presence of ISOW at the core site until 376 ka.

Similarity with ODP 1063

Two sediment cores from the deep northern Atlantic were analyzed which stand out due to their high sedimentation rates and thereby allowing a high temporal resolution of the Nd isotope records. When comparing those records from the western (ODP 1063) and eastern basin (IODP U1304) it is striking that the Nd isotopic composition at both sites show nearly the same evolution, but in opposite directions (see Figure 9.8). While IODP U1304 experiences the most radiogenic bottom water masses, ODP 1063 registers the most unradiogenic values during MIS 11. One can speculate that the communication between the eastern and western basin was not as efficient as it is today. If the eastern deep water masses do not enter the northwestern basin through the Charlie-Gibbs-Fracture Zone, the initial Nd isotopic signature of the water mass passing the southeastern Labrador Sea and the Grand Banks, where boundary exchange and consequently a shift to more unradiogenic values happens today [Lambelet *et al.*, 2016], would be less radiogenic possibly resulting in a more unradiogenic water mass traveling further to the south. On the other hand, as the density layer previously occupied by ISOW would be missing, other water masses, for example LSW, could sink deeper and therefore carry a more unradiogenic signature to the deep ocean. However, at least today, DSOW fills the bottom northern NW Atlantic as the densest water mass. Little is known how DSOW evolved through MIS 11, nevertheless, a decrease in the abundances of benthic foraminifera at ODP Site 919 (62°40.20′N, 37°27.61′W, 2088m water depth) [St. John *et al.*, 2004] points to a decreased presence of DSOW in the

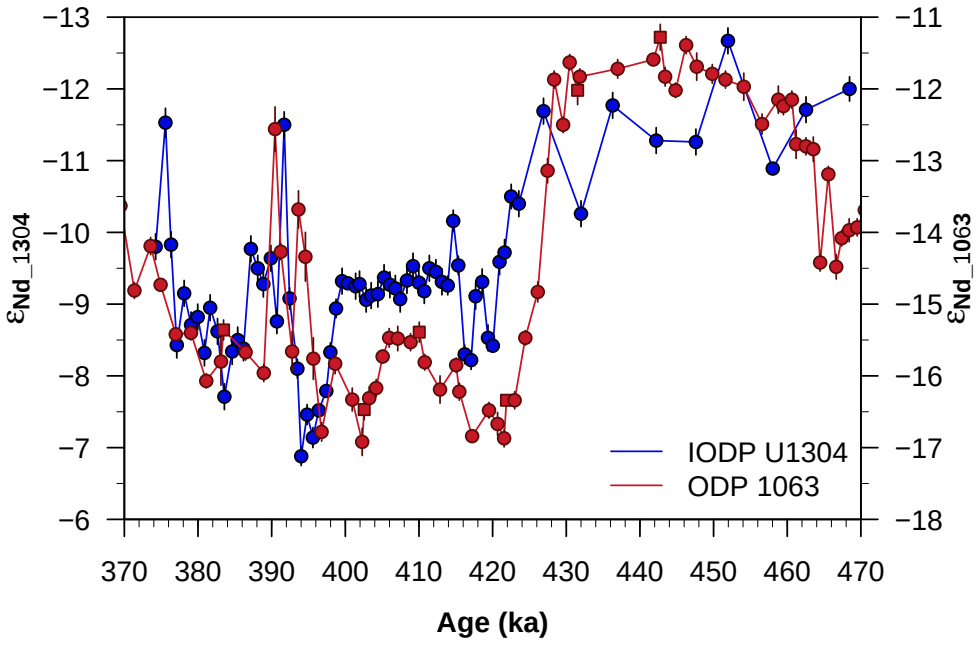

Figure 9.8: Comparison of the Nd isotopic compositions at IODP U1304 (blue, left y-axis) and ODP 1063 (red, right y-axis, circles: this study, squares: Jaume-Seguí *et al.* [2020]) during MISs 12–11. Note that this time. the right y-axis for ODP 1063 is not reversed in contrast to the other graphs in this thesis.

Irminger Sea, thus maybe allowing unradiogenic water masses to sink even deeper.

Modern transport of ISOW from the eastern to the western basin occurs mainly through the Charlie-Gibbs Fracture Zone with about 1.7 ± 0.5 Sv [Bower and Furey, 2017] to 2.4 ± 0.5 Sv [Saunders, 1994; Xu *et al.*, 2018b]. This flow is variable with strong westwards ISOW transport events and weak westwards or even eastwards transport. The latter are associated with a northward meandering of the North Atlantic Current [Bower and Furey, 2017; Xu *et al.*, 2018b]. Instead of passing through the Charlie-Gibbs Fracture Zone, a southward transport along the eastern flank of the Mid-Atlantic Ridge is ascribed to ISOW.

It seems plausible that during MIS 11 the transport of dense, radiogenic waters through the Charlie-Gibbs Fracture Zone was hindered. Hence, a confluence of ISOW (possibly mixed with other deep water masses of the eastern Atlantic) and western deep Atlantic water masses happened at fracture zones further to the south.

9.1.3 ODP 659

Located in the tropical East Atlantic off the African coast, the profile of the Nd isotopic composition at ODP 659 during MISs 12–11 shows a glacial-interglacial variation from

more to less radiogenic values as expected for an associated water mass change. However, compared to the other sites investigated, the timing of the transition is different.

The peak glacial values are recorded from 442 to 432 ka. The values are indicative of a pronounced presence of SSW at the core site. Compared to the other sites, T-V in ε_{Nd} values happens well before the jump in stable benthic oxygen and carbon isotopes (see Figure 9.9). As both stable isotope and Nd samples are from the same core sections, an age model offset can be excluded. Therefore, one can only speculate why the premature glacial termination occurred. The carbonate content also shows an early but gradual increase before the change in the stable isotopes, though not as distinct as the Nd isotope record.

Commonly, this time period is referred to a Heinrich Stadial in many sediment cores, as an enhanced deposition of IRD takes places [Vázquez Riveiros *et al.*, 2013, and references therein]. Simultaneously, at ODP Site 958 (23°59.4′N, 20°0.05′W) about 660 km to the north of ODP 659, an extreme peak of high Fe concentration is recorded, which is interpreted as an increased dust flux from the Southern Sahara and Sahel region [Helmke *et al.*, 2008]. The Nd isotopic signature from material derived from that region is more unradiogenic (<-13 [Grousset *et al.*, 1998]) than what is expected as a seawater source (at around -10 as seen from 442-432 ka). The detrital fraction of a sediment core nearby (MD03-2705, 18°5.8′N, 21°9.2′W) is characterized with ε_{Nd} values between -14.0 to -15.4 during the last glacial [Jullien *et al.*, 2007]. The high amount of iron-stained particles [Helmke *et al.*, 2008] in combination with a more sluggish circulation, which is typical for Heinrich stadials [e.g. Henry *et al.*, 2016], might have reset the Nd isotopic composition of the water column by reversible scavenging.

At around 423 ka a second decrease in Nd isotopes takes place, which is in line with the change in benthic stable carbon and oxygen isotopes [Tiedemann, 1991], and which is expected for T-V. Interpreted as a water mass signal, this would indicate the change from a more southern-sourced water mass to a northern-sourced water mass. The Nd isotope values stay rather constant for the rest of the interglacial at around -12, except for an increase at 412 ka. Unfortunately, the temporal resolution of the other proxies is not as good as for the Nd isotopes, which is why no such event is seen in those records. It is also possible that it rather corresponds to 392 ka, when in the other Northern Hemisphere ε_{Nd} records increases happen. Low sedimentation rates (according to the current age model of Lisiecki and Raymo [2005]) and the low temporal resolution of the benthic stable isotope records leave room for this interpretation. Increasing the temporal resolution and therefore refining the age model in this part of the sediment

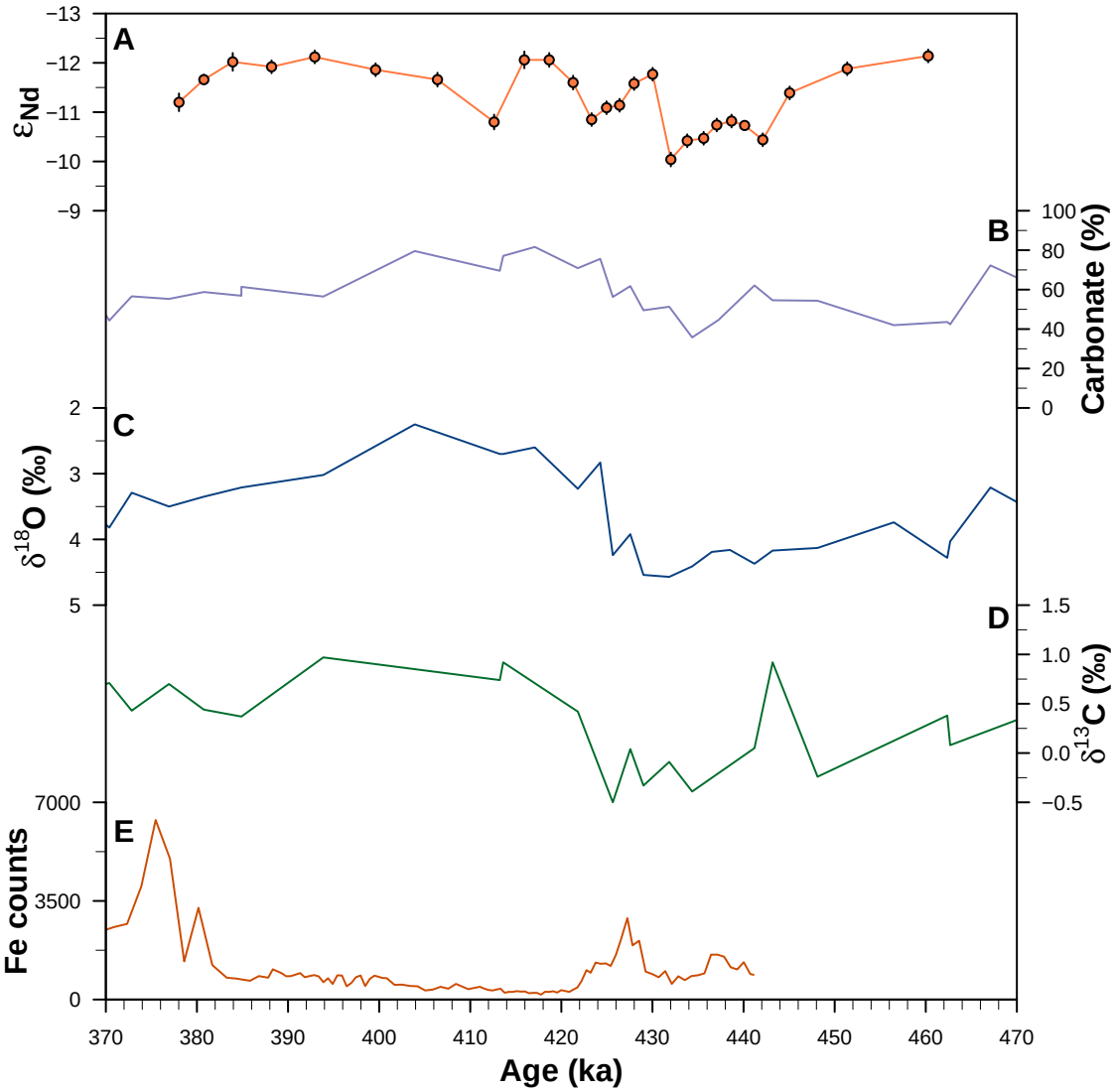

Figure 9.9: Climate records of ODP 659. (A) Nd isotopic composition. (B) Carbonate content of the sediment [Tiedemann, 1991]. (C) Stable oxygen [Tiedemann *et al.*, 1994] and (D) carbon isotopes [Tiedemann, 1991] of the benthic foraminifera *C. wuellerstorfi*. (E) Iron counts of ODP 958 [Helmke *et al.*, 2008]. All age models are based on the LR04 timescale [Lisiecki and Raymo, 2005; Kandiano *et al.*, 2012].

core, could help to define whether this increase in Nd isotopes and associated incursion of more SSW corresponds to the ones seen at the other records in a later part of MIS 11. Nevertheless, the Nd isotopes show a clear dominance of NSW in the deep eastern tropical Atlantic for nearly the full MIS 11.

Howe *et al.* [2017] analyzed planktic foraminifera of time slices of the Holocene and LGM of ODP 659 which resulted in ε_{Nd} values of -12.2 ± 0.13 and -11.2 ± 0.14, respectively. The interglacial values of the Holocene and MIS 11 are similar, where minimum values -12.14 ± 0.13 are reached. However, the glacial values differ, as during MIS 12 up to -10.04 ± 0.14 are recorded and therefore suggest a greater proportion of SSW at the core site compared to the LGM.

9.1.4 ODP 929

After ensuring that the published record of Nd isotopes derived from mixed planktic foraminifera and fish debris [Howe and Piotrowski, 2017] and the here produced ε_{Nd} values from bulk sediment leaching at ODP 929 agree with each other (see Section 8.5), one can merge both data sets. The new data falls in the range for glacials and interglacials during the past 800 ka at the Ceara Rise [Howe and Piotrowski, 2017]. Compared to the other site in the NW Atlantic, ODP 1063, which is located upstream of ODP 929, the Ceara Rise site is generally more radiogenic, especially during the warm phases, when the influence of NSW is dominant. On one hand, this is because of the northern site being located closer to the zone of the influence of unradiogenic signatures to the abyssal depths [Pöppelmeier *et al.*, 2019a], on the other hand because of greater admixture of more radiogenic NSW from the mid-depth Atlantic [Howe *et al.*, 2016b; Howe and Piotrowski, 2017].

The greatest presence of SSW is seen over the course of the glacial maximum of MIS 12 with its maximum at 433 ka. Thereafter, the influence of SSW slightly diminishes during the termination as expressed in the benthic stable oxygen isotopes [Bickert *et al.*, 1997] (see Figure 9.10). Synchronous with the increase in the carbonate content [Curry and Cullen, 1997] and the jump in benthic stable carbon isotopes [Bickert *et al.*, 1997], a marked decrease in Nd isotopes takes place at around 418 ka. Hence, the glacial termination expressed in Nd isotopes is not as sharp as for example at sites ODP 1063 or IODP U1304. The age model though, leaves some room for interpretation due to the poor resolution of the oxygen isotope record (see also Appendix B.1). Therefore, it may well be that the pronounced change in the three proxies mentioned above, occurred

earlier and thereby sharpens the glacial termination.

Nevertheless, what seemed to be a single bulge of more unradiogenic ε_{Nd} values during the entire MIS 11 [Howe and Piotrowski, 2017], turns out to be two separate periods with the enhanced presence of NSW at the core site. They are separated by a period of increased admixture of SSW as seen by more radiogenic ε_{Nd} values at around 395 ka corresponding to MIS 11b. This deterioration was not known before for ODP 929 both from the ε_{Nd} and $\delta^{13}C$ record, but seems to be a common feature in the deep circulation of the Northern Atlantic (see Section 5.3 and Section 9.1.2).

This new data set therefore highlights the need for a high temporal resolution in paleoceanographic reconstructions.

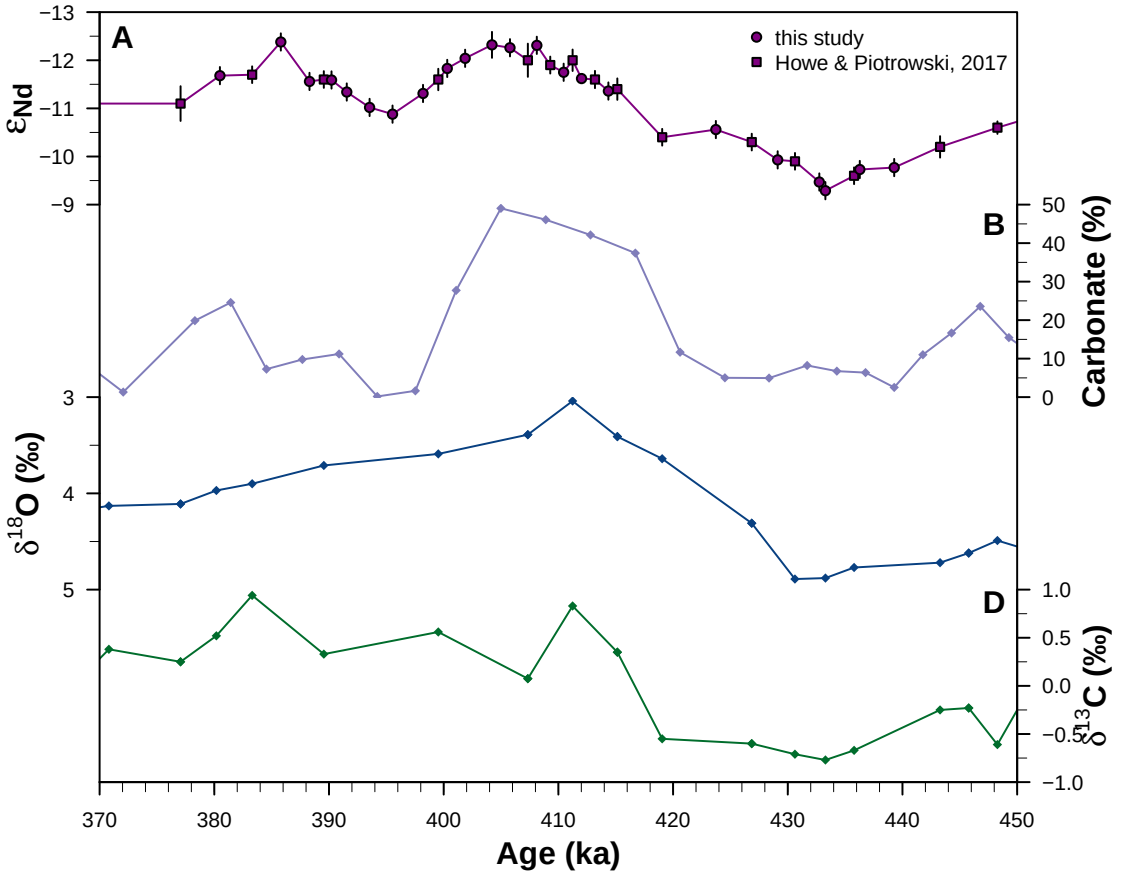

Figure 9.10: Climate records at ODP 929. (A) Neodymium isotopic composition reconstructed via bulk sediment leaching (circles, this thesis) and from planktic foraminifera and fish debris (squares, Howe and Piotrowski [2017]). (B) Carbonate content of the sediment [Curry and Cullen, 1997]. Stable oxygen (C) and carbon (D) isotopes of benthic foraminifera [Bickert *et al.*, 1997].

9.1.5 ODP 1267

The ε_{Nd} record of ODP 1267 on the northern flank of the Walvis Ridge, shows a relatively smooth signal in the course of MISs 12–11. The most radiogenic values, which clearly highlight the enhanced presence of SSW, are seen during the glacial maximum of MIS 12. At the time when the glacial Termination V sets in, the Nd isotopic composition does not change as sharply as the benthic stable isotopes [Bell *et al.*, 2014] (see Figure 9.11) and as the Nd isotopic composition at sites in the North Atlantic. It shows a rather gentle shift to NSW, where its maximum is recorded relatively late during MIS 11 at around 398 ka. Instead of being a purely paleoceanographic feature, it is more reasonable to interpret this smooth transition in the context of the prevailing low sedimentation rate. For MIS 11 it is smaller than 1.3 cm ka^{-1}, therefore bioturbation and diffusion within the sediment column play a role. This is especially true in this core (ODP 1267 A1H), where it is noted in the core description [Shipboard Scientific Party, 2004] that bioturbation is common to moderate and burrows exist, which extend over 10 cm in length. According to Christl [2007], with a bioturbation depth z_b of 10 cm and a sedimentation rate of about 1.25 cm ka^{-1}, the width of the time window t_{bio} within the sedimented signal gets averaged, results in 8 ka.

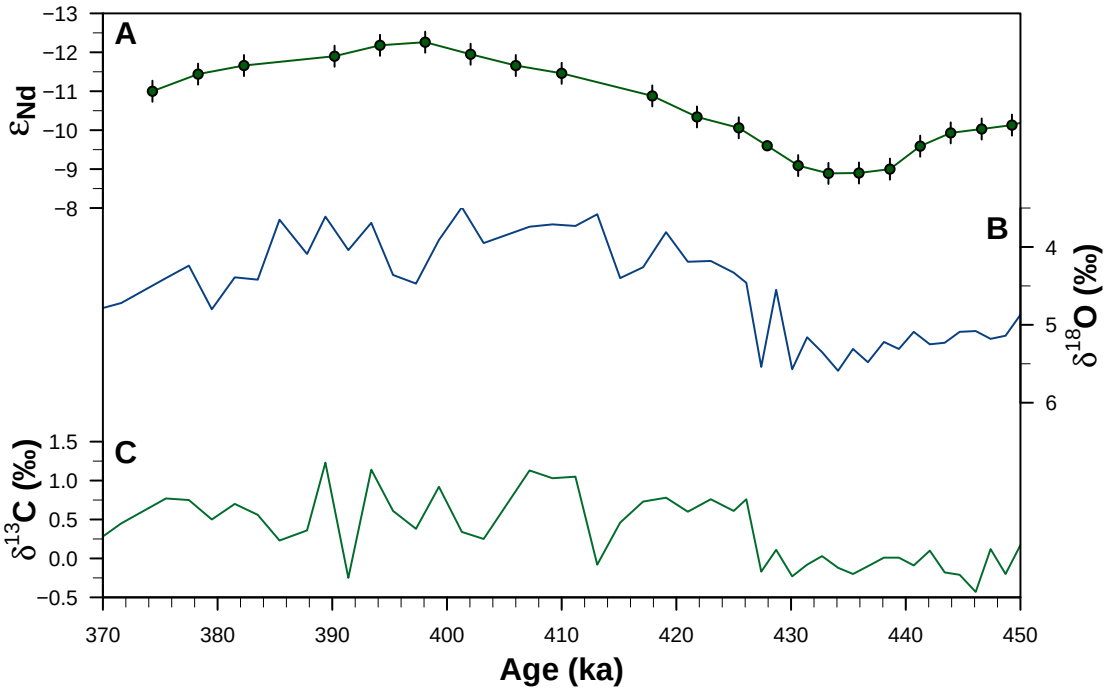

Figure 9.11: Climate records of ODP 1267. (A) Neodymium isotopic composition. Benthic stable oxygen (B) and carbon (C) isotopes [Bell *et al.*, 2014].

Consequently, the most extreme values in the ε_{Nd} record might not even be the most extreme Nd isotopic signature that prevailed at the core site, especially when the duration of the event was short. Thus, the most unradiogenic ε_{Nd} value of -12.26 ± 0.27 is even more outstanding, as it not only reflects nearly the same isotopic composition as it is recorded at the Ceara Rise site, but it also shows that nearly entirely NSW bathed the core site during MIS 11. This is in contrast to previous interglacials, where the Nd isotopic composition ranged between -10.5 and -11.0 for MISs 17, 19, and 21 at ODP 1267 [Farmer *et al.*, 2019]. Assuming that these singular data points really represent the extremes during the interglacials, one can clearly identify a strong advance of NSW into the South Atlantic during MIS 11, which was stronger than during the previous interglacials.

9.1.6 DSDP 517

The interpretation of the Nd isotope record of DSDP 517 is quite challenging, in particular because of the age model whose establishment was not straightforward (see Section 7.1.6). However it provides valuable insights into the paleoceanography of the southwestern Atlantic due to the scarcity of sites of DSDP and its follow-up programs in that region.

The record of the Nd isotopic composition itself is characterized with a radiogenic ε_{Nd} signature of about -8.5 during MIS 12. These values demonstrate the shoaling of SSW even to depths that are today in the core of southwards flowing NSW. During Termination V the values become more unradiogenic and thus indicate the greater proportion of NSW at the core site. One single data point even reached -12.18 ± 0.27, and hence corresponds to 100 % of NSW on the basis of modern sea water data [Jeandel, 1993] (see Figure 9.12). However, this was only a short excursion and the rest of the record reflects a rather stable Nd isotopic composition of -10.3 and therefore less NSW at the site.

Regarding the reliability of the ε_{Nd} values itself, one can be quite confident that they actually correspond to the prevailing water mass. Pöppelmeier *et al.* [2019b] showed that at least for the last 25 ka the detrital signature of a sediment core close by (AII107 65GGC, 32°2.1′N, 36°11.3′W, 2795 m water depth) ranges between -4 and -7 ε_{Nd}-units and is therefore distinctly more radiogenic than the values obtained by leaching. Additionally, the values between the common weak leaching and a stronger leach do not differ and hence confirm the reliability of the leached data.

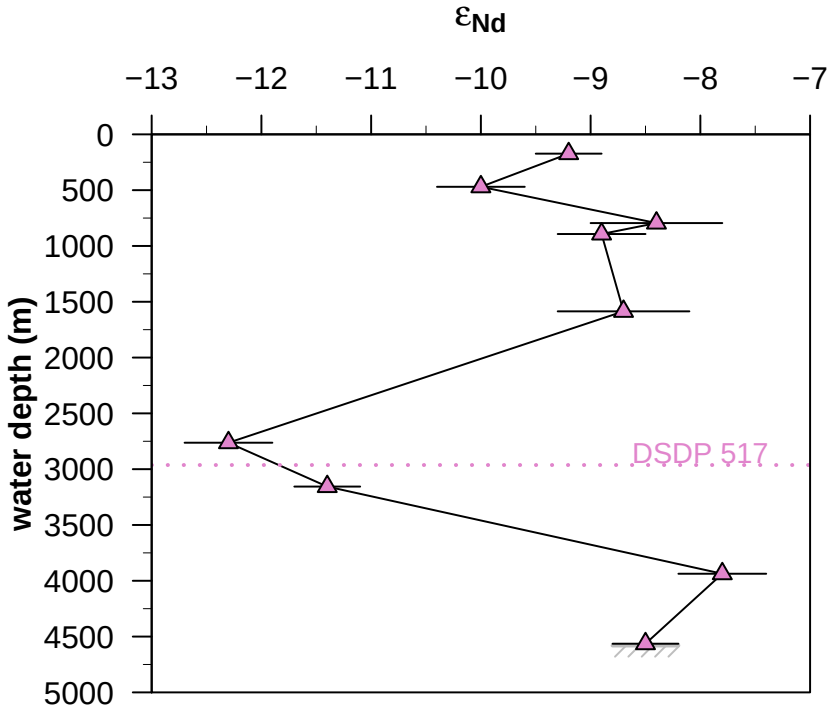

Figure 9.12: Seawater Nd isotopic composition of SAVE St. 302 [Jeandel, 1993] in proximity to DSDP 517. The water depth of the latter is depicted as a dotted line.

Concerning the timing of the water mass changes, there is still room for interpretation though. Especially the timing and the duration of for example the unradiogenic peak is debatable. Looking at the core image [Shipboard Scientific Party, 1983], one can see that this part is considerably more unconsolidated than the adjacent parts of the sediment column and is possibly partly washed out. One can thus speculate, whether these unradiogenic values originally lasted longer than currently preserved in the sediment column of DSDP 517. Otherwise, it might well be that this single peak represents an overshoot of the overturning circulation at the end of Termination V as proposed by Vázquez Riveiros *et al.* [2013].

By comparing the record of Nd isotopes with the profiles of the stable isotopes of benthic foraminifera [Vergnaud Grazzini *et al.*, 1983] (see Figure 9.13) inconsistencies appear. First of all, Termination V in ε_{Nd} happened before the change in $\delta^{18}O$ values was initiated. Additionally, the lowest oxygen isotope values appear very late, in fact clearly after the common interglacial peak at around 399 ± 3 ka [Cheng *et al.*, 2016]. The $\delta^{13}C$ values on the other hand, show an opposing situation with an early peak during Termination V and the ε_{Nd} peak, and a decrease thereafter to glacial-like values while the $\delta^{18}O$ values are still decreasing. One must consider that the stable isotope records

themselves were created by analyzing different genera (*Cibicides, Planulina* and others) that were partly normalized to *Uvigerina* (filled symbols in Figure 9.13 (B) and (C)) and mixed species, that were not corrected (open symbols). Therefore, if one allows for species-effects regarding the part, where only a signal from mixed species was retrieved, the records might resemble each other better. Considering the nearly four decades of analytical advancement since the generation of the stable isotope record, resampling and reanalyzing might help to solve these discrepancies between the records.

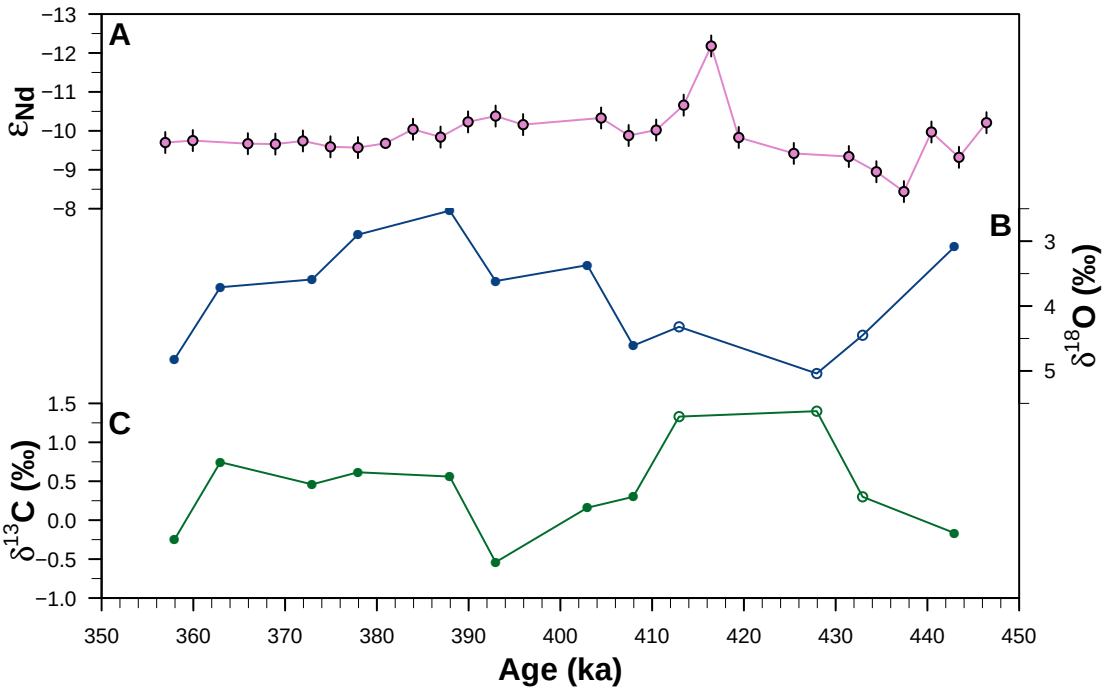

Figure 9.13: Climate records of DSDP 517. (A) Nd isotopic composition. Stable oxygen (B) and carbon (C) isotopes of benthic foraminifera (filled symbols: normalized to *Uvigerina*, open symbols: mixed species, which were not corrected) [Vergnaud Grazzini *et al.*, 1983].

9.2 Atlantic wide circulation pattern

By examining all now available records of Nd isotopes in their entirety, one gets insight into the deep water circulation in the Atlantic from MIS 12 through MIS 11. Strikingly, the records from sites from the Southern Hemisphere and the equatorial Atlantic show virtually the same development on ε_{Nd} values (see Figure 9.14) and therefore that the sites were bathed by the a water mass with the same proportions of NSW vs. SSW. This can be seen in particular during the build-up of the continental ice sheets towards and also over the course of the glacial maximum of MIS 12. The curves of DSDP/ODP Sites

517, 1267, and 929 show the same development with almost the same ε_{Nd} values, where ODP 929 as a site located further to the north records only a slighlty ($\sim 0.4\,\varepsilon$-units) more unradiogenic Nd isotopic composition. From that one can conclude that the entire subtropical South Atlantic in depths below at least about 3000 m and the deep equatorial Atlantic were bathed by a water mass with a high proportion of SSW. In the case of ODP 1267, it means that SSW flowed either all the way north to the Romanche Fracture Zone and from there partly turned eastwards to ultimately flow back to the south and to fill the deep Angola Basin. Alternatively, SSW spilled over the barrier of the Walvis Ridge, which nowadays blocks the Antarctic Bottom Water on its northward flow but which also has some passages that would allow a northward flow of shallower water masses.

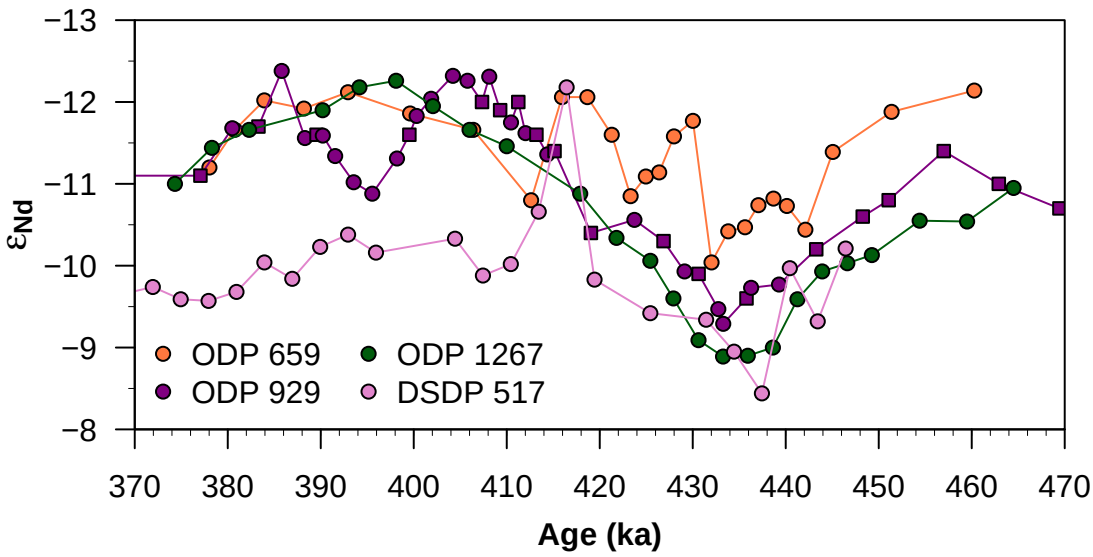

Figure 9.14: Comparison of ε_{Nd} records far away from source regions. For reasons of clarity, the error bars are omitted, but can be seen in the previous section. Squares in the record of ODP 929 represent data from Howe and Piotrowski [2017].

After passing the equator on the way to the north, the fraction of SSW declines. The ε_{Nd} values of ODP 659 are permanently less radiogenic than the ones of ODP 929, 1267, and DSDP 517, which reflects the greater influence of NSW in the North Atlantic even in the glacial. Even in 3069 m water depth at IODP U1304, remains of SSW can be traced during MIS 12. Traditionally, one would suspect a less diluted SSW signal and thus more positive ε_{Nd} values at the Bermuda Rise than at the Gardar Drift site, though the contrary is the case (ε_{Nd} of -11.3 ± 0.7 at IODP U1304 vs. -11.8 ± 0.3 at ODP 1063), even if the difference is quite small. Origin of this discrepancy might well

be the influence of Glacial North Atlantic Bottom Water at the deeper Bermuda Rise site, which was proposed for the LGM both by ε_{Nd} [Pöppelmeier *et al.*, 2018] and by $\delta^{13}C$ as well as $\Delta^{14}C$ [Keigwin and Swift, 2017].

After the glacial maximum of MIS 12, when a large portion of the deep Atlantic was bathed by SSW, glacial Termination V sets in. It is characterized by a massive ice rafting event in the North Atlantic with a reduced deep water formation during this Heinrich Stadial from 430 to 425 ka [Vázquez Riveiros *et al.*, 2013, and references therein]. During this time period, the ε_{Nd} records of the deep North Atlantic sites support this interpretation, as they are still bathed by SSW. Right afterwards, the Nd isotopic signatures of ODP 1063 and IODP U1304 change sharply, indicating the reset of deep water formation as the presence of SSW is replaced by NSW and ISOW, respectively. That also means that the resumption of a deep circulation mode of the AMOC was established already early in the interglacial, even when the deglaciation of the ice sheets (as expressed in benthic $\delta^{18}O$ values [e.g. Lisiecki and Raymo, 2005; Rohling *et al.*, 2010]) was still on-going. Vázquez Riveiros *et al.* [2013] even assumed an AMOC overshoot until 417 ka.

Due to the presence of a cold and fresh surface layer in the Nordic Seas because of the freshwater release from the melting ice sheets [Bauch *et al.*, 2000; Kandiano *et al.*, 2012, 2016; Thibodeau *et al.*, 2017], Kandiano *et al.* [2016] concluded that for the Nordic Seas "it is difficult to decide where and under which circumstances deep convection could have occured during MIS 11." However, the authors also state that the deep water formation might have taken place south of the areas from which records of MIS 11 existed, and Kandiano *et al.* [2017] narrowed it down to the southern part of the Nordic Seas (Norwegian Sea). The record of IODP U1304 clearly supports a deep water formation in the Nordic Seas, as the recorded radiogenic signature indicates a water mass, that must have passed the region around Iceland and the eastward extending Iceland-Scotland Ridge, where (at least today) the overprinting of radiogenic Nd takes place. Furthermore, Doherty and Thibodeau [2018] argue against the meltwater from southern Greenland as a cause for the fresh and cold surface layer. Instead it originated from higher latitudes as enhanced export from the Arctic, elevated runoff from Eurasia, and ice melt from northern Greenland.

Alongside with the deep water formation in the Nordic Seas, deep convection also took place in the Labrador Sea. LSW deepened compared to modern flow patterns at 415 ka and is apparent at ODP 980. At the same time, Dickson *et al.* [2009] report a strengthening of the AMOC based on gradients of stable carbon isotopes between sites

ODP 980 and ODP 1063.

Irrespective of the low sedimentation rates (especially at ODP 1267) and the issue with the correct age-depth relationship (DSDP 517), the subtropical South Atlantic was bathed both in the mid-depth as well as the deep with NSW. Both sites show virtually the same ε_{Nd} values as recorded at ODP 929 (see Figure 9.14), which corresponds to an undiluted signal. That means that there was a strong active upper overturning circulation and the lower overturning cell did not spread out far to the north. In fact, Oppo *et al.* [1990] concluded based on $\delta^{13}C$ gradients that during MIS 11 was the greatest flux of NSW to the Southern Ocean of the past 750 ka.

This overturning was not only active during the interglacial itself (MIS 11c) but also in the rest of the warm stage, albeit with one exception. At ∼395 ka (MIS 11b) the overturning circulation must have weakened drastically and SSW bathed even the deep North Atlantic (glacial-like ε_{Nd} alues at ODP 1063 and IODP U1304). The stable carbon isotope record of ODP 1059 at 2985 m water depth (31°40.46′N, 75°25.13′W) also shows a setback [Haley *et al.*, 2004]. This incursion of SSW is coincident with a major deterioration of the global climate. The sea-level high-stand was over, and the ice-sheets began to build up [Rohling *et al.*, 2010]. The Asian monsoon reached a minimum (dated to 396±3 ka) [Cheng *et al.*, 2016] and SST in the North Atlantic dropped [Martrat *et al.*, 2007].

9.3 Comparison with the Holocene

The data presented here is the first highly-resolved and spatial widespread reconstruction of the deep water flow pattern in the Atlantic for MISs 12–11 using Nd isotopes. To put it in a broader climatological context, it is now compared to the one of the Holocene and LGM, as those time periods were the focus of numerous studies.

On a one-to-one comparison of the individual records, it is intriguing that some records evolve virtually identical. That is especially true for ODP 980 (see Section 9.1.1 and Figure 9.1), where the Nd isotopic composition both of MISs 12–11 and the LGM–Holocene is nearly the same, even in the temporal evolution. The only difference arises in the middle–late Holocene, when the unradiogenic values of the early Holocene rapidly increase to the modern seawater value. During MIS 11, the unradiogenic plateau (interpreted as a deepening of LSW) lasted considerably longer by several thousand years before the ε_{Nd} values gradually increased again. A similar behavior is seen at ODP 1063 (see Section 5.2 and Figure 5.1). During the early Holocene (as well as

during most of the other interglacials) the most unradiogenic ε_{Nd} values are seen, but in contrast to the increase in the middle to late Holocene, these values stay unradiogenic for the whole interglacial.

In order to get an impression about the hydrography, Howe *et al.* [2016a] compiled new and published Nd isotope data for the time slices of the Holocene and LGM in a cross section covering the Atlantic ocean. This compilation provides the basis for the Atlantic-wide comparison of MIS 12 vs. LGM and MIS 11 vs. Holocene (see Figure 9.15). As the MIS 12/11 records of IODP U1304 and ODP 980 should also be displayed and the

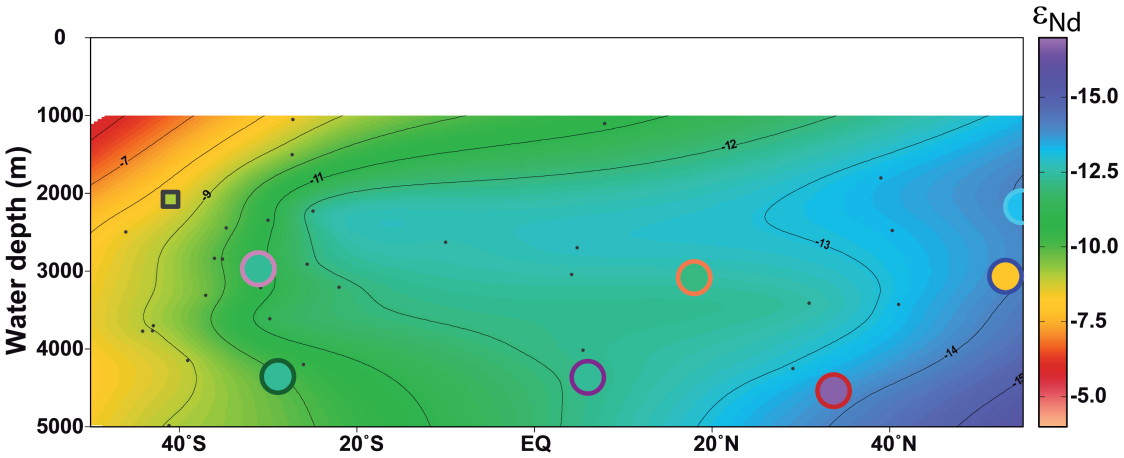

(a) Holocene versus MIS 11.

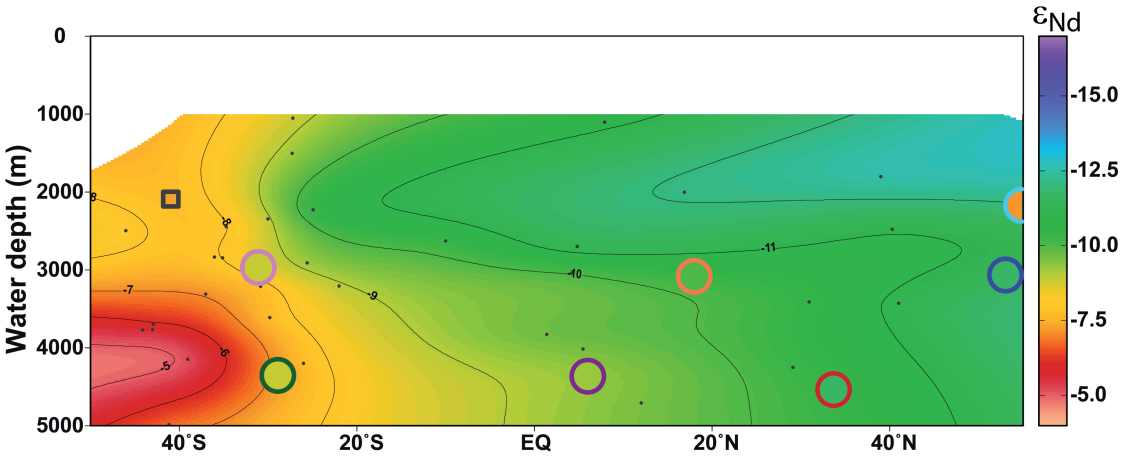

(b) LGM versus MIS 12.

Figure 9.15: Comparisons of the water mass geometry of the Holocene and LGM (background) [after Howe *et al.*, 2016a] and MIS 11 and MIS 12 (circles). The boundary of the circles is colored analog to the site-specific color for Nd isotope records used throughout this chapter, while the filling corresponds to the respective ε_{Nd} value. Also the Nd isotopic composition of ODP 1088 [Dausmann *et al.*, 2017] is included and depicted as a square. Data visualized with ODV software [Schlitzer, 2019].

MIS 11's Nd isotope values for ODP 1063 were outside the scale, the plots were re-done with ODV [Schlitzer, 2019] using the compilation as data input but now spanning 50°S to 55°N and covering a range in ε_{Nd} from -4 down to -17. The fillings of the circles on top the cross section represent the maximum and minimum ε_{Nd} value at the respective sites during MIS 12 and MIS 11 respectively. This ensures that even at the locations with a low sedimentation rate, the glacial and interglacial maximum is represented. The color of the circles' boarder corresponds to the color-code for the individual sites used in the previous sections.

The comparison between the LGM and MIS 12 (see Figure 9.15b) illustrates the accordance of the Nd isotopic composition of the seawater between those time periods. The tongue of SSW penetrated far to the north in the deep and even mid-depth ($\sim$3000 m) Atlantic. However, the north Atlantic is also bathed by a higher amount of NSW compared to the south. Apparent mismatches like the tendentially more unradiogenic values at ODP 1267 are most likely due the averaging across the whole width of the Atlantic. Thus, the signal of the western and eastern basin gets mixed, where in reality, in the eastern basin the Walvis Ridge blocks the advance of SSW. Compared to older glacials like MIS 16 and 22 [Farmer *et al.*, 2019], the signature at this core site is identical and therefore reasonable. The other apparent discrepancy compared to the background is found at ODP 980. Here, the site was not included into the compilation, as studies based on bulk sediment leaching (like [Crocket *et al.*, 2011]) were excluded and the study of Crocker *et al.* [2016] was not published back then. But as aforementioned, the ε_{Nd} values of the LGM and MIS 12 are consistent and therefore also the prevailing circulation patterns.

In contrast, the Nd isotopic composition of MIS 11 differs far more from the one of the Holocene. One of the alleged deviations is seen at IODP U1304 at the Gardar Drift. But here again, the record for the Holocene [Blaser, 2017] was not available up to the time of the publication of the compilation [Howe *et al.*, 2016a]. Additionally, the radiogenic values are expectable as they show the regional feature with pure ISOW flowing along the Reykjanes Ridge.

At ODP 1063, the Nd isotopic signature is much more unradiogenic compared to the Atlantic average at this latitude , which is partly due to the fact that these signatures prevail over the full course of this isotope stage and do not increase to modern values (see also Section 5.3). However, this signal does not get exported toward the south, because the values recorded at ODP 929 are not standing out and match the ones from the Holocene. This means that the Bermuda Rise is more prone to the influence of

unradiogenic Nd originating from the Labrador Sea/NE America region in addition to the climate signal, which it records.

Strikingly, the cores from the Southern Hemisphere exhibit the same Nd isotopic signature as ODP 929 during MIS 11. Thus, they are distinctly more unradiogenic compared to the Holocene and therefore show the enhanced export of NSW into the South Atlantic. Hence, the interpretation of a stronger overturning circulation with enhanced export of NSW gets confirmed.

10 Conclusions

In summary, it emerges that the circulation in the Atlantic during MIS 12 was similar to the one in the LGM. The equatorial and subtropical South Atlantic was bathed by a higher proportion of SSW, whereas in the deep North Atlantic GNABW was presumably present. The deep water formation resumed very early, still in the course of the deglaciaiton, as can be seen for example from the occurrence of ISOW at the Gardar Drift. At around 415 ka, the circulation patterns restructured, and LSW deepened. In the subtropical South Atlantic, the same amount of NSW is recorded as at the equator. Thus, there is a stronger advance of NSW into the South Atlantic during MIS 11 than during the Holocene. Hence, a strong and active overturning circulation prevailed during MIS 11, with a less expanded southern overturning cell compared to the Holocene. The active overturning circulation was not restricted to the interglacial MIS 11c, but also present during substage a. However, during MIS 11b, the overturning circulation drastically changed, as even in the deep North Atlantic glacial-like Nd isotopic compositions prevailed.

The strong AMOC during MIS 11 lead to a large heat transport to the high latitudes, which gave rise to an enhanced mass loss of the Greenland Ice Sheet [Rachmayani *et al.*, 2017] . This mass loss reached rates of up to 0.8 m sea level equivalent (s.l.e.) per thousand years during mid MIS 11c, with on overage 0.4 m s.l.e. per thousand years [Robinson *et al.*, 2017]. If this freshwater input would have had an influence on the deepwater formation during MIS 11, one would have seen it in the Nd data. Instead, for example, a strong presence of ISOW is seen at IODP U1304 during the full interglacial, and the presence of LSW at ODP 980 at the same time as the highest mass loss of the Greenland Ice Sheet [Robinson *et al.*, 2017]. Hence, this study shows that the AMOC was not disturbed by freshwater input from the melting Greenland Ice Sheet during MIS 11.

However, when considering simulations for the future under the RCP 8.5 scenario, a mass loss of up to 9.9 cm s.l.e. for this century is predicted for the southwest and central-west drainage basins of the Greenland Ice Sheet alone [Briner *et al.*, 2020]. Considering the whole Greenland Ice Sheet, this projected rate of mass loss exceeds that of MIS 11,

thus a future influence of meltwater on AMOC (as projected by e.g. Bakker *et al.* [2016]) cannot be precluded based on the paleodata evidence.

11 Concluding Remarks and Outlook

Many paleoceanographic reconstructions rely on the use of nutrient-type tracers like Cd/Ca or $\delta^{13}C$ of benthic foraminifera. However, aggravating effects like for example the thermodynamic fractionation during air-sea gas exchange or species-specific vital effects [Mackensen and Schmiedl, 2019] make the interpretation more challenging. In contrast, Nd isotopes as quasi-conservative tracer allow for the reconstruction of water mass provenance [e.g. Frank, 2002]. In this thesis, two studies were conducted (I) to determine the water mass provenance in the deep Northwest Atlantic during the past one million years and (II) to gain insights into the Atlantic-wide prevailing water mass geometry during the time interval of MISs 12–11. Therefore, the authigenic Nd fraction of deep sea sediments was extracted via bulk sediment leaching.

In Study I a record of authigenic Nd isotopes in the Atlantic that reaches one million years back in time with a millennial-scale temporal resolution was presented. Despite challenging extreme unradiogenic ε_{Nd} values, the record at the Bermuda Rise shows that during most climate conditions, an active deep overturning circulation prevailed in the Atlantic, with NSW bathing the deep Northwest Atlantic most of the time. Only during glacial maxima beginning with the 900 ka event and with the exception of MIS 14, the proportion of NSW got reduced. This 900 ka event is rather a turning point associated with the MPT, when the AMOC reorganized from MIS 24 to 22, than a gradual transition spanning several hundred thousands of years.

Study II showed on the one hand that the extreme unradiogenic Nd isotopic composition recorded at the Bermuda Rise during MIS 11 in Study I did not spread throughout the whole Atlantic. One the other hand, the distribution of water masses showed a similar arrangement as the LGM, and a further advance of NSW into the South Atlantic during MIS 11. Thus, a strong overturning circulation prevailed during a time, when the sea level was elevated and Greenland largely ice-free. Such a detailed analysis of highly resolved Nd records for a specific time interval before the last glacial cycle is unprecedented.

The results presented here, also show the need for a high sampling resolution at sites with a high sedimentation rate when conducting paleoceanographic studies

to capture the full dynamic of the climate system. Only through a high temporal resolution the prevailing variability of the tracer can be assessed. Otherwise the chosen sampling points may not represent the desired time span but rather singular extreme values if the time series is inherently markedly variable. This can be exemplified by the interglacials recorded at ODP 1063. Their typical trend goes from an unradiogenic Nd isotopic composition right after the glacial Termination to a more radiogenic one in the course of the interglacial with an amplitude of several ε-units. Another example is the short setback during MIS 11b recorded at IODP U1304, ODP 1063, and ODP 929. At the here presented temporal resolution, it only encompasses few data points at the different sites and was not seen before in the lower resolved Nd record at ODP 929 of Howe and Piotrowski [2017].

Both studies showed the potential and some limitations of the use of Nd isotopes in paleoceanography. In addition to the new findings mentioned above, this thesis also raises new questions, which could be addressed in future studies. A selection of these are described in more detail below.

Expanding the Bermuda Rise Record

At present, the profile of Nd isotopes at the Bermuda Rise ends at 194.21 mcd (or 181.19 mbsf at Hole B) corresponding to 1026 ka. Therefore, it captures the main part of the Mid-Pleistocene Transition, but not its full span, as it is assumed to start at about 1.4 Ma [Head and Gibbard, 2015] or 1.25 Ma [Clark *et al.*, 2006]. Therefore, it is necessary to see, how the deep water variability behaved when the general climate was dominated by the 41 thousand year cyclicity. Looking at the ε_{Nd} record, the time period before the 900 ka event looks very similar to the time interval of MISs 15-13. Therefore, one can speculate whether the missing advance of SSW to the Northwestern Atlantic during glacials before the 900 ka event was a common feature, that prevailed for a long time, or whether it was simply a feature of the glacials just before the event. The reconstructed glacial Nd isotopic compositions in the South Atlantic reach back to 1043.1 ka (MIS 30, ODP 1090, Pena and Goldstein [2014]) and 1113.1 ka (MIS 34, ODP 1267, Farmer *et al.* [2019]) and suggest no advance of SSW during the glacials. The same picture is also seen at the more shallower site ODP 1088 [Pena and Goldstein, 2014; Dausmann *et al.*, 2017], however this was not the case during glacials between $\sim$ 1.2 and 1.55 Ma.

At ODP 1063, the integrity of the sediment sequences is given down to $\sim$ 232 mcd ($\sim$ 213 mbsf) [Shipboard Scientific Party, 1998]. Based on the last occurrence of the planktic foraminifera *Globigerinoides obliquus* at this specific depth, it can be dated to

1.3 Ma [ibid.]. Thus, one could expand the record of the Bermuda Rise further downcore to resolve whether this transition at around 1.2 Ma as seen at the shallow ODP 1088 [Dausmann *et al.*, 2017], is just a signal in the Southern Hemisphere or expressed more spatially.

Down below $\sim$ 232 mcd, some depths between the drilled holes A and B can be correlated, but no continuous overlap between the cores can be established. So far, the oldest age tie points are the last occurrence of the planktic foraminifer *Dentoglobigerina altispira* at 395 mbsf and the end of the geomagnetic Kaena Subchron at about 387 mbsf both corresponding to $\sim$ 3.12 Ma, and are thus of Pliocene age [Shipboard Scientific Party, 1998]. Despite the constraints regarding the possibly of not recovered depth intervals, by expanding the ε_{Nd} profile, one could gain additional insights into the deep water circulation of the Northwestern Atlantic starting from the intensification of the Northern Hemisphere glaciation [Lang *et al.*, 2016] to the proposed reorganization of the circulation of the Northeastern Atlantic at about 1.6 Ma [Khélifi and Frank, 2014]. The still high overall sedimentation rate of $> 7.4\,\mathrm{cm\,ka^{-1}}$ [Shipboard Scientific Party, 1998] thereby still enables to resolve millennial-scale variations.

How did the circulation look like during MIS 14?

Glacials following the 900 ka event are typically characterized by a build-up of ice-sheets on the continents and associated drop in global mean sea level. However, MIS 14 was one of the mildest glacials of the past 800 ka [Lang and Wolff, 2011] and ice sheets on the Northern Hemisphere were restricted [Hao *et al.*, 2015]. Also the Nd isotopes at the Bermuda Rise do not exhibit common glacial signatures. In comparison with other Nd data from the Ceara Rise [Howe and Piotrowski, 2017] and other circulation proxies, one can assume that the upper overturning cell was still fairly pronounced compared to the other glacials, but that the lower overturning cell presumably occupied also a great proportion in the South Atlantic (see Section 5.4). An asymmetry in the climate of both Hemispheres was attested, with severe glacial conditions in the Southern Hemisphere and not as drastic ones in the Northern Hemisphere [Hao *et al.*, 2015]. Therefore the question arises which role the AMOC played creating or adapting to such an unusual climate pattern. Analogously to the strategy for the reconstruction of the ocean circulation during MIS 11 (see Study II), analyzing the Nd isotopic composition at several sites spanning the Atlantic with a greater focus on the northern low-latitudes to the southern mid-latitudes would enable to decipher the location of the boundary between the overturning cells. In order to compare the MIS 14 ε_{Nd} profiles of the sites

to common glacial periods, the best strategy would be to create respective records spanning from MIS 16a to MIS 12a.

Southern end member

The interpretation of Nd isotopes in terms of changes in the water mass mixing is depending on the knowledge of end member compositions. For SSW, there is currently no temporal highly resolved record available for the past one million years. Ferromanganese crusts do not indicate drastic changes in the Nd isotopic composition in the Southern Ocean [Frank *et al.*, 2002], but recent studies suggest an invasion of Pacific-sourced deep water into the South Atlantic during the last and penultimate glacial maximum [Hallmaier, 2020; Yu *et al.*, 2020] and thus a potential shift in the end members. Therefore, the (in)stability of the southern end member on (sub-)orbital to millennial time scales still needs to be tested.

Processes how seawater gains it Nd isotopic composition

The exact mechanisms how seawater obtains its Nd isotopic composition and how it is altered, is still not sufficiently well-known. Notwithstanding that several processes were proposed (see Section 2.3.1), these face a challenge due to unexpected reconstructed Nd isotopic compositions at several sites and often call for new approaches. At the Bermuda Rise, more unradiogenic ε_{Nd} values than modern seawater are recorded during most parts of the last one million years and several explanations were presented in Section 5.1. In contrast the ε_{Nd} profile of IODP U1304 at the Gardar Drift contains time intervals with more radiogenic than modern signatures see (Section 9.1.2). In order to tackle those challenges, studies of Nd isotopes close to the prospective source regions are required. For example, ε_{Nd} profiles within the Labrador Sea or the Nordic Seas might provide valuable insights in the Nd isotopic composition of the water masses upstream of the analyzed sites. Studies which systematically compare the Nd isotopic composition of different phases in seawater, by measuring the unfiltered and the filtered seawater, as well as the particulate matter, would also help to assess the role of the latter in areas with a high particle load like in the benthic nepheloid layers of the Northwestern Atlantic ocean. Moreover, modeling studies that implement these new diverse mechanisms are crucial for an improved understanding of the Nd cycle.

References

Abbott, A.N., Haley, B.A., McManus, J. (2015a): Bottoms up: Sedimentary control of the deep North Pacific Ocean's ε_{Nd} signature. *Geology* **43**, 1035–1035.

Abbott, A.N., Haley, B.A., McManus, J., Reimers, C.E. (2015b): The sedimentary flux of dissolved rare earth elements to the ocean. *Geochimica et Cosmochimica Acta* **154**, 186–200.

Abbott, A.N., Haley, B.A., McManus, J. (2016): The impact of sedimentary coatings on the diagenetic Nd flux. *Earth and Planetary Science Letters* **449**, 217–227.

Abouchami, W., Goldstein, S.L., Gazer, S.J.G., Eisenhauer, A., Mangini, A. (1997): Secular changes of lead and neodymium in central Pacific seawater recorded by a Fe-Mn crust. *Geochimica et Cosmochimica Acta* **61**, 3957–3974.

Abouchami, W., Galer, S.J.G., Koschinsky, A. (1999): Pb and Nd isotopes in NE Atlantic Fe–Mn crusts: Proxies for trace metal paleosources and paleocean circulation. *Geochimica et Cosmochimica Acta* **63**, 1489–1505.

Abraham, J.P., Baringer, M., Bindoff, N.L., Boyer, T., Cheng, L.J., Church, J.A., Conroy, J.L., Domingues, C.M., Fasullo, J.T., Gilson, J., Goni, G., Good, S.A., Gorman, J.M., Gouretski, V., Ishii, M., Johnson, G.C., Kizu, S., Lyman, J.M., Macdonald, A.M., Minkowycz, W.J., Moffitt, S.E., Palmer, M.D., Piola, A.R., Reseghetti, F., Schuckmann, K., Trenberth, K.E., Velicogna, I., Willis, J.K. (2013): A review of global ocean temperature observations: Implications for ocean heat content estimates and climate change. *Reviews of Geophysics* **51**, 450–483.

Alley, R.B., Clark, P.U. (1999): The deglaciation of the Northern Hemisphere: A Global Perspective. *Annual Review of Earth and Planetary Sciences* **27**, 149–182.

Amante, C., Eakins, B. (2009): ETOPO1 1 Arc-Minute Global Relief Model: Procedures, Data Sources and Analysis. NOAA Technical Memorandum NESDIS NGDC-24.

Anderson, R.F. (2020): GEOTRACES: Accelerating Research on the Marine Biogeochemical Cycles of Trace Elements and Their Isotopes. *Annual Review of Marine Science* **12**, 49–85.

Arhan, M., Mercier, H., Park, Y.H. (2003): On the deep water circulation of the eastern South Atlantic Ocean. *Deep Sea Research Part I: Oceanographic Research Papers* **50**, 889–916.

Arrhenius, G., Bramlette, M.N., Picciotto, E. (1957): Localization of Radioactive and Stable Heavy Nuclides in Ocean Sediments. *Nature* **180**, 85–86.

Arsouze, T., Dutay, J.C., Lacan, F., Jeandel, C. (2009): Reconstructing the Nd oceanic cycle using a coupled dynamical – biogeochemical model. *Biogeosciences* **6**, 2829–2846.

Aschwanden, A., Fahnestock, M.A., Truffer, M., Brinkerhoff, D.J., Hock, R., Khroulev, C., Mottram, R., Khan, S.A. (2019): Contribution of the Greenland Ice Sheet to sea level over the next millennium. *Science Advances* **5**, eaav9396.

Bakker, P., Schmittner, A., Lenaerts, J.T.M., Abe-Ouchi, A., Bi, D., van den Broeke, M.R., Chan, W.L., Hu, A., Beadling, R.L., Marsland, S.J., Mernild, S.H., Saenko, O.A., Swingedouw, D., Sullivan, A., Yin, J. (2016): Fate of the Atlantic Meridional Overturning Circulation: Strong decline under continued warming and Greenland melting. *Geophysical Research Letters* **43**, 12,252–12,260.

Ballini, M., Kissel, C., Colin, C., Richter, T. (2006): Deep-water mass source and dynamic associated with rapid climatic variations during the last glacial stage in the North Atlantic: A multiproxy investigation of the detrital fraction of deep-sea sediments. *Geochemistry, Geophysics, Geosystems* **7**, Q02N01.

Barrat, J., Keller, F., Amossé, J., Taylor, R., Nesbitt, R.W., Hirata, T. (1996): Determination of Rare Earth Elements in sixteen silicate reference samples by ICP-MS after Tm addition and ion exchange separation. *Geostandards Newsletter* **20**, 133–139.

Barth, A.M., Clark, P.U., Bill, N.S., He, F., Pisias, N.G. (2018): Climate evolution across the Mid-Brunhes Transition. *Climate of the Past* **14**, 2071–2087.

Bates, S.L., Siddall, M., Waelbroeck, C. (2014): Hydrographic variations in deep ocean temperature over the mid-Pleistocene transition. *Quaternary Science Reviews* **88**, 147–158.

Bau, M., Koschinsky, A. (2006): Hafnium and neodymium isotopes in seawater and in ferromanganese crusts: The "element perspective". *Earth and Planetary Science Letters* **241**, 952–961.

Bauch, H.A., Erlenkeuser, H., Helmke, J.P., Struck, U. (2000): A paleoclimatic evaluation of marine oxygen isotope stage 11 in the high-northern Atlantic (Nordic seas). *Global and Planetary Change* **24**, 27–39.

Bayon, G., German, C.R., Boella, R.M., Milton, J.A., Taylor, R.N., Nesbitt, R.W. (2002): An improved method for extracting marine sediment fractions and its application to Sr and Nd isotopic analysis. *Chemical Geology* **187**, 179–199.

Bell, D.B., Jung, S.J.A., Kroon, D., Lourens, L.J., Hodell, D.A. (2014): Local and regional trends in Plio-Pleistocene δ^{18}O records from benthic foraminifera. *Geochemistry, Geophysics, Geosystems* **15**, 3304–3321.

Berger, A., Loutre, M.F. (2002): An Exceptionally Long Interglacial Ahead? *Science* **297**, 1287–1288.

Berger, A., Li, X.S., Loutre, M.F. (1999): Modelling northern hemisphere ice volume over the last 3Ma. *Quaternary Science Reviews* **18**, 1–11.

Bianchi, G.G., McCave, I.N. (2000): Hydrography and sedimentation under the deep western boundary current on Björn and Gardar Drifts, Iceland Basin. *Marine Geology* **165**, 137–169.

Bickert, T., Curry, W.B., Wefer, G. (1997): Late Pliocene to Holocene (2.6-0 Ma) western equatorial Atlantic deep-water circulation: Inferences from benthic stable isotopes. In: *Proceedings of the Ocean Drilling Program, Scientific Results*, volume 154, edited by N.J. Shackleton, W.B. Curry, C. Richter, T.J. Bralower, 239–253, Ocean Drilling Program, College Station, TX.

Billups, K., Rabideaux, N., Stoffel, J. (2011): Suborbital-scale surface and deep water records in the subtropical North Atlantic: implications on thermohaline overturn. *Quaternary Science Reviews* **30**, 2976–2987.

Blaser, P. (2017): *The application of radiogenic neodymium isotopes as a palaeo water mass tracer in the subpolar North Atlantic*. Dissertation, Ruperto-Carola University of Heidelberg.

Blaser, P., Lippold, J., Gutjahr, M., Frank, N., Link, J.M., Frank, M. (2016): Extracting foraminiferal seawater Nd isotope signatures from bulk deep sea sediment by chemical leaching. *Chemical Geology* **439**, 189–204.

Blaser, P., Pöppelmeier, F., Schulz, H., Gutjahr, M., Frank, M., Lippold, J., Heinrich, H., Link, J.M., Hoffmann, J., Szidat, S., Frank, N. (2019): The resilience and sensitivity of Northeast Atlantic deep water εNd to overprinting by detrital fluxes over the past 30,000 years. *Geochimica et Cosmochimica Acta* **245**, 79–97.

Böhlke, J.K., de Laeter, J.R., Bièvre, P.D., Hidaka, H., Peiser, H.S., Rosman, K.J.R., Taylor, P.D.P. (2005): Isotopic Compositions of the Elements, 2001. *Journal of Physical and Chemical Reference Data* **34**, 57–67.

Böhm, E., Lippold, J., Gutjahr, M., Frank, M., Blaser, P., Antz, B., Fohlmeister, J., Frank, N., Andersen, M.B., Deininger, M. (2015): Strong and deep Atlantic meridional overturning circulation during the last glacial cycle. *Nature* **517**, 73–76.

Bower, A., Furey, H. (2017): Iceland-Scotland Overflow Water transport variability through the Charlie-Gibbs Fracture Zone and the impact of the North Atlantic Current. *Journal of Geophysical Research: Oceans* **122**, 6989–7012.

Boyer, T.P., Antonov, J.I., Baranova, O.K., Coleman, C., Garcia, H.E., Grodsky, A., Johnson, D.R., Locarnini, R.A., Mishonov, A.V., O'Brien, T.D., Paver, C.R., Reagan, J.R., Seidov, D., Smolyar, I.V., Zweng, M.M. (2013): *World Ocean Database 2013*. NOAA Atlas NESDIS 72, Silver Spring, MD.

Briner, J.P., Cuzzone, J.K., Badgeley, J.A., Young, N.E., Steig, E.J., Morlighem, M., Schlegel, N.J., Hakim, G.J., Schaefer, J.M., Johnson, J.V., Lesnek, A.J., Thomas, E.K., Allan, E., Bennike, O., Cluett, A.A., Csatho, B., de Vernal, A., Downs, J., Larour, E., Nowicki, S. (2020): Rate of mass loss from the Greenland Ice Sheet will exceed Holocene values this century. *Nature* **586**, 70–74.

Broecker, W.S. (1987): The biggest chill : when ocean currents shifted, Europe suddenly got cold; could it happen again? *Natural History* **96**, 74–82.

Broecker, W.S., Peng, T.H. (1982): *Tracers in the Sea*. Lamont-Doherty Geological Observatory, Columbia University, Palisades, New York.

Broecker, W.S., van Donk, J. (1970): Insolation changes, ice volumes, and the O^{18} record in deep-sea cores. *Reviews of Geophysics* **8**, 169–198.

Buckley, M.W., Marshall, J. (2016): Observations, inferences, and mechanisms of the Atlantic Meridional Overturning Circulation: A review. *Reviews of Geophysics* **54**, 5–63.

Burton, K.W., Vance, D. (2000): Glacial–interglacial variations in the neodymium isotope composition of seawater in the Bay of Bengal recorded by planktonic foraminifera. *Earth and Planetary Science Letters* **176**, 425–441.

Burton, K.W., Ling, H.F., O'Nions, R.K. (1997): Closure of the Central American Isthmus and its effect on deep-water formation in the North Atlantic. *Nature* **386**, 382–385.

Byrne, R.H. (2002): Inorganic speciation of dissolved elements in seawater: the influence of pH on concentration ratios. *Geochemical Transactions* **3**, 11–16.

Caesar, L., Rahmstorf, S., Robinson, A., Feulner, G., Saba, V. (2018): Observed fingerprint of a weakening Atlantic Ocean overturning circulation. *Nature* **556**, 191–196.

Candy, I., Schreve, D.C., Sherriff, J., Tye, G.J. (2014): Marine Isotope Stage 11: Palaeoclimates, palaeoenvironments and its role as an analogue for the current interglacial. *Earth-Science Reviews* **128**, 18–51.

Chalk, T.B., Hain, M.P., Foster, G.L., Rohling, E.J., Sexton, P.F., Badger, M.P.S., Cherry, S.G., Hasenfratz, A.P., Haug, G.H., Jaccard, S.L., Martínez-García, A., Pälike, H., Pancost, R.D., Wilson, P.A. (2017): Causes of ice age intensification across the Mid-Pleistocene Transition. *Proceedings of the National Academy of Sciences* **114**, 13114–13119.

Channell, J.E.T., Raymo, M.E. (2003): Paleomagnetic record at ODP Site 980 (Feni Drift, Rockall) for the past 1.2 Myrs. *Geochemistry, Geophysics, Geosystems* **4**, 1033.

Channell, J.E.T., Xuan, C., Hodell, D.A. (2009): Stacking paleointensity and oxygen isotope data for the last 1.5 Myr (PISO-1500). *Earth and Planetary Science Letters* **283**, 14–23.

Channell, J.E.T., Sato, T., Kanamatsu, T., Stein, R., Alvarez Zarikian, C. (2010): Expedition 303/306 synthesis: North Atlantic climate. In: *Proceedings of the Integrated Ocean Drilling Program*, volume 303/306, edited by J.E.T. Channell, T. Kanamatsu, T. Sato, R. Stein, C. Alvarez Zarikian, M. Malone, Expedition 303/306 Scientists, Integrated Ocean Drilling Program Management International, Inc., College Station, TX.

Channell, J.E.T., Hodell, D.A., Curtis, J.H. (2012a): ODP Site 1063 (Bermuda Rise) revisited: Oxygen isotopes, excursions and paleointensity in the Brunhes Chron. *Geochemistry, Geophysics, Geosystems* **13**, Q02001.

Channell, J.E.T., Hodell, D.A., Romero, O., Hillaire-Marcel, C., de Vernal, A., Stoner, J.S., Mazaud, A., Röhl, U. (2012b): A 750-kyr detrital-layer stratigraphy for the North Atlantic (IODP Sites U1302-U1303, Orphan Knoll, Labrador Sea). *Earth and Planetary Science Letters* **317-318**, 218–230.

Chavagnac, V., Saleban Ali, H., Jeandel, C., Leleu, T., Destrigneville, C., Castillo, A., Cotte, L., Waeles, M., Cathalot, C., Laes-Huon, A., Pelleter, E., Nonnotte, P., Sarradin, P.M., Cannat, M. (2018): Sulfate minerals control dissolved rare earth element flux and Nd isotope signature of buoyant hydrothermal plume (EMSO-Azores, 37°N Mid-Atlantic Ridge). *Chemical Geology* **499**, 111–125.

Cheng, H., Edwards, R.L., Sinha, A., Spötl, C., Yi, L., Chen, S., Kelly, M., Kathayat, G., Wang, X., Li, X., Kong, X., Wang, Y., Ning, Y., Zhang, H. (2016): The Asian monsoon over the past 640,000 years and ice age terminations. *Nature* **534**, 640–646.

Chester, R., Hughes, M.J. (1967): A chemical technique for the separation of ferro-manganese minerals, carbonate minerals and adsorbed trace elements from pelagic sediments. *Chemical Geology* **2**, 249–262.

Chevis, D.A., Johannesson, K.H., Burdige, D.J., Cable, J.E., Martin, J.B., Roy, M. (2015): Rare earth element cycling in a sandy subterranean estuary in Florida, USA. *Marine Chemistry* **176**, 34–50.

Christl, M. (2007): Sensitivity and response of beryllium-10 in marine sediments to rapid production changes (geomagnetic events): A box model study. *Geochemistry, Geophysics, Geosystems* **8**, Q09015.

Clark, P.U., Pollard, D. (1998): Origin of the middle Pleistocene transition by ice sheet erosion of regolith. *Paleoceanography* **13**, 1–9.

Clark, P.U., Archer, D., Pollard, D., Blum, J.D., Rial, J.A., Brovkin, V., Mix, A.C., Pisias, N.G., Roy, M. (2006): The middle Pleistocene transition: characteristics, mechanisms, and implications for long-term changes in atmospheric pCO_2. *Quaternary Science Reviews* **25**, 3150–3184.

Cohen, A.S., O'Nions, R.K., Siegenthaler, R., Griffin, W.L. (1988): Chronology of the pressure-temperature history recorded by a granulite terrain. *Contributions to Mineralogy and Petrology* **98**, 303–311.

Cohen, K., Finney, S., Gibbard, P.L., Fan, J.X. (2013; updated): The ICS International Chronostratigraphic Chart. *Episodes* **36**, 119–204.

Cohen, R.S., O'Nions, R.K. (1982): The Lead, Neodymium and Strontium Isotopic Structure of Ocean Ridge Basalts. *Journal of Petrology* **23**, 299–324.

Colin, C., Frank, N., Copard, K., Douville, E. (2010): Neodymium isotopic composition of deep-sea corals from the NE Atlantic: implications for past hydrological changes during the Holocene. *Quaternary Science Reviews* **29**, 2509–2517.

Connary, S.D., Ewing, M. (1974): Penetration of Antarctic bottom water from the Cape Basin into the Angola Basin. *Journal of Geophysical Research* **79**, 463–469.

Copard, K., Colin, C., Douville, E., Freiwald, A., Gudmundsson, G., De Mol, B., Frank, N. (2010): Nd isotopes in deep-sea corals in the North-eastern Atlantic. *Quaternary Science Reviews* **29**, 2499–2508.

Crocker, A.J., Chalk, T.B., Bailey, I., Spencer, M.R., Gutjahr, M., Foster, G.L., Wilson, P.A. (2016): Geochemical response of the mid-depth Northeast Atlantic Ocean to freshwater input during Heinrich events 1 to 4. *Quaternary Science Reviews* **151**, 236–254.

Crocket, K.C., Vance, D., Gutjahr, M., Foster, G.L., Richards, D.A. (2011): Persistent Nordic deep-water overflow to the glacial North Atlantic. *Geology* **39**, 515–518.

Curry, W., Cullen, J.L. (1997): Carbonate production and dissolution in the western equatorial Atlantic during the last 1 M.Y. In: *Proceedings of the Ocean Discovery Program, Scientific Results*, volume 154, edited by N.J. Shackleton, W.B. Curry, C. Richter, T.J. Bralower, 189–199, Ocean Drilling Program, College Station, TX.

Curry, W.B., Oppo, D.W. (2005): Glacial water mass geometry and the distribution of $\delta^{13}C$ of $\sum CO_2$ in the western Atlantic Ocean. *Paleoceanography* **20**, PA1017.

Dausmann, V., Frank, M., Gutjahr, M., Rickli, J. (2017): Glacial reduction of AMOC strength and long-term transition in weathering inputs into the Southern Ocean since the mid-Miocene: Evidence from radiogenic Nd and Hf isotopes. *Paleoceanography* **32**, PA003056.

de Vernal, A., Hillaire-Marcel, C. (2008): Natural Variability of Greenland Climate, Vegetation, and Ice Volume During the Past Million Years. *Science* **320**, 1622–1625.

Deaney, E.L., Barker, S., van de Flierdt, T. (2017): Timing and nature of AMOC recovery across Termination 2 and magnitude of deglacial CO_2 change. *Nature Communications* **8**, 14595.

Denton, G.H. (2000): Does an asymmetric thermohaline–ice-sheet oscillator drive 100 000-yr glacial cycles? *Journal of Quaternary Science* **15**, 301–318.

DePaolo, D.J., Wasserburg, G.J. (1976): Nd isotopic variations and petrogenetic models. *Geophysical Research Letters* **3**, 249–252.

Dickson, A.J., Beer, C.J., Dempsey, C., Maslin, M.A., Bendle, J.A., McClymont, E.L., Pancost, R.D. (2009): Oceanic forcing of the Marine Isotope Stage 11 interglacial. *Nature Geoscience* **2**, 428–433.

Doherty, J.M., Thibodeau, B. (2018): Cold Water in a Warm World: Investigating the Origin of the Nordic Seas' Unique Surface Properties During MIS 11. *Frontiers in Marine Science* **5**, 251.

Dubois-Dauphin, Q., Colin, C., Bonneau, L., Montagna, P., Wu, Q., Van Rooij, D., Reverdin, G., Douville, E., Thil, F., Waldner, A., Frank, N. (2017): Fingerprinting Northeast Atlantic water masses using neodymium isotopes. *Geochimica et Cosmochimica Acta* **210**, 267–288.

Dutton, A., Carlson, A.E., Long, A.J., Milne, G.A., Clark, P.U., DeConto, R., Horton, B.P., Rahmstorf, S., Raymo, M.E. (2015): Sea-level rise due to polar ice-sheet mass loss during past warm periods. *Science* **349**, aaa4019.

Elderfield, H., Ferretti, P., Greaves, M., Crowhurst, S., McCave, I.N., Hodell, D., Piotrowski, A.M. (2012): Evolution of Ocean Temperature and Ice Volume Through the Mid-Pleistocene Climate Transition. *Science* **337**, 704–709.

Elmore, A.C., Piotrowski, A.M., Wright, J.D., Scrivner, A.E. (2011): Testing the extraction of past seawater Nd isotopic composition from North Atlantic deep sea sediments and foraminifera. *Geochemistry, Geophysics, Geosystems* **12**, Q09008.

EPICA Community Members (2004): Eight glacial cycles from an Antarctic ice core. *Nature* **429**, 623–628.

Expedition 303 Scientists (2006): Site 1304. In: *Proceedings of the Integrated Ocean Drilling Program*, volume 303/306, edited by J.E.T. Channell, T. Kanamatsu, T. Sato, R. Stein, C. Alvarez Zarikian, M. Malone, Expedition 303/306 Scientists, Integrated Ocean Drilling Program Management International, Inc., College Station, TX.

Farmer, J.R., Hönisch, B., Haynes, L.L., Kroon, D., Jung, S., Ford, H.L., Raymo, M.E., Jaume-Seguí, M., Bell, D.B., Goldstein, S.L., Pena, L.D., Yehudai, M., Kim, J. (2019): Deep Atlantic Ocean carbon storage and the rise of 100,000-year glacial cycles. *Nature Geoscience* **12**, 355–360.

Ferretti, P., Shackleton, N.J., Rio, D., Hall, M.A. (2005): Early-Middle Pleistocene deep circulation in the western subtropical Atlantic: southern hemisphere modulation of the North Atlantic Ocean. In: *Early–Middle Pleistocene Transitions: The Land–Ocean Evidence*, volume 247 of *Geological Society, London, Special Publications*, edited by M.J. Head, P.L. Gibbard, 131–145.

Filippova, A., Frank, M., Kienast, M., Rickli, J., Hathorne, E., Yashayaev, I.M., Pahnke, K. (2017): Water mass circulation and weathering inputs in the Labrador Sea based on coupled Hf–Nd isotope compositions and rare earth element distributions. *Geochimica et Cosmochimica Acta* **199**, 164–184.

Flanagan, F.J., Gottfried, D. (1980): USGS rock standards, III: Manganese-Nodule Reference Samples USGS-Nod-A-1 and USGS-Nod-P-1. Geological Survey Professional Paper 1155.

Foster, G.L., Vance, D. (2006): In situ Nd isotopic analysis of geological materials by laser ablation MC-ICP-MS. *Journal of Analytical Atomic Spectrometry* **21**, 288–296.

Foster, G.L., Vance, D., Prytulak, J. (2007): No change in the neodymium isotope composition of deep water exported from the North Atlantic on glacial-interglacial time scales. *Geology* **35**, 37–40.

Frajka-Williams, E., Ansorge, I.J., Baehr, J., Bryden, H.L., Chidichimo, M.P., Cunningham, S.A., Danabasoglu, G., Dong, S., Donohue, K.A., Elipot, S., Heimbach, P., Holliday, N.P., Hummels, R., Jackson, L.C., Karstensen, J., Lankhorst, M., Le Bras, I.A., Lozier, M.S., McDonagh, E.L., Meinen, C.S., Mercier, H., Moat, B.I., Perez, R.C., Piecuch, C.G., Rhein, M., Srokosz, M.A., Trenberth, K.E., Bacon, S., Forget, G., Goni, G., Kieke, D., Koelling, J., Lamont, T., McCarthy, G.D., Mertens, C., Send, U., Smeed, D.A., Speich, S., van den Berg, M., Volkov, D., Wilson, C. (2019): Atlantic Meridional Overturning Circulation: Observed Transport and Variability. *Frontiers in Marine Science* **6**, 260.

França, Z.T.M., Tassinari, C.C.G., Cruz, J.V., Aparicio, A.Y., Araña, V., Rodrigues, B.N. (2006): Petrology, geochemistry and Sr–Nd–Pb isotopes of the volcanic rocks from Pico Island—Azores (Portugal). *Journal of Volcanology and Geothermal Research* **156**, 71–89.

Frank, M. (2002): Radiogenic isotopes: Tracers of past ocean circulation and erosional input. *Reviews of Geophysics* **40**, 1–38.

Frank, M., O'Nions, R.K., Hein, J.R., Banakar, V.K. (1999): 60 Myr records of major elements and Pb–Nd isotopes from hydrogenous ferromanganese crusts: reconstruction of seawater paleochemistry. *Geochimica et Cosmochimica Acta* **63**, 1689–1708.

Frank, M., Whiteley, N., Kasten, S., Hein, J.R., O'Nions, K. (2002): North Atlantic Deep Water export to the Southern Ocean over the past 14 Myr: Evidence from Nd and Pb isotopes in ferromanganese crusts. *Paleoceanography* **17**, 1022.

Fröllje, H., Pahnke, K., Schnetger, B., Brumsack, H.J., Dulai, H., Fitzsimmons, J.N. (2016): Hawaiian imprint on dissolved Nd and Ra isotopes and rare earth elements in the central North Pacific: Local survey and seasonal variability. *Geochimica et Cosmochimica Acta* **189**, 110–131.

Garcia-Solsona, E., Jeandel, C., Labatut, M., Lacan, F., Vance, D., Chavagnac, V., Pradoux, C. (2014): Rare earth elements and Nd isotopes tracing water mass mixing and particle-seawater interactions in the SE Atlantic. *Geochimica et Cosmochimica Acta* **125**, 351–372.

Gardner, W.D., Tucholke, B.E., Richardson, M.J., Biscaye, P.E. (2017): Benthic storms, nepheloid layers, and linkage with upper ocean dynamics in the western North Atlantic. *Marine Geology* **385**, 304–327.

Garzoli, S.L., Matano, R. (2011): The South Atlantic and the Atlantic Meridional Overturning Circulation. *Deep Sea Research Part II: Topical Studies in Oceanography* **58**, 1837–1847.

Garzoli, S.L., Dong, S., Fine, R., Meinen, C.S., Perez, R.C., Schmid, C., van Sebille, E., Yao, Q. (2015): The fate of the Deep Western Boundary Current in the South Atlantic. *Deep Sea Research Part I: Oceanographic Research Papers* **103**, 125–136.

Gebbie, G. (2014): How much did Glacial North Atlantic Water shoal? *Paleoceanography* **29**, 190–209.

German, C.R., Klinkhammer, G.P., Edmond, J.M., Mura, A., Elderfield, H. (1990): Hydrothermal scavenging of rare-earth elements in the ocean. *Nature* **345**, 516–518.

Gibbard, P.L., Head, M.J., Walker, M.J.C., the Subcommission on Quaternary Stratigraphy (2010): Formal ratification of the Quaternary System/Period and the Pleistocene Series/Epoch with a base at 2.58 Ma. *Journal of Quaternary Science* **25**, 96–102.

Giosan, L., Flood, R.D., Grützner, J., Franz, S.O., Poli, M.S., Hagen, S. (2001): High-resolution carbonate content estimated from diffuse spectral reflectance for Leg 172 Sites. In: *Proceedings of the Ocean Drilling Program, Scientific Results*, volume 172, edited by L.D. Keigwin, D. Rio, G.D. Acton, E. Arnold, 1–12, Ocean Drilling Program, College Station TX.

Giosan, L., Flood, R.D., Aller, R.C. (2002): Paleoceanographic significance of sediment color on western North Atlantic drifts: I. Origin of color. *Marine Geology* **189**, 25–41.

Goldstein, S.J., Jacobsen, S.B. (1987): The Nd and Sr isotopic systematics of river-water dissolved material: Implications for the sources of Nd and Sr in seawater. *Chemical Geology: Isotope Geoscience section* **66**, 245–272.

Goldstein, S.L., Hemming, S.R. (2003): 6.17 - Long-lived Isotopic Tracers in Oceanography, Paleoceanography, and Ice-sheet Dynamics. In: *Treatise on Geochemistry*, edited by H.D. Holland, K.K. Turekian, 453–489, Pergamon, Oxford.

Grasse, P., Bosse, L., Hathorne, E.C., Böning, P., Pahnke, K., Frank, M. (2017): Short-term variability of dissolved rare earth elements and neodymium isotopes in the entire water column of the Panama Basin. *Earth and Planetary Science Letters* **475**, 242–253.

Grousset, F.E., Parra, M., Bory, A., Martinez, P., Bertrand, P., Shimmield, G., Ellam, R.M. (1998): Saharan wind regimes traced by the Sr-Nd isotopic composition of subtropical Atlantic sediments: Last Glacial Maximum vs today. *Quaternary Science Reviews* **17**, 395–409.

Grousset, F.E., Cortijo, E., Huon, S., Hervé, L., Richter, T., Burdloff, D., Duprat, J., Weber, O. (2001): Zooming in on Heinrich layers. *Paleoceanography* **16**, 240–259.

Grützner, J., Giosan, L., Franz, S.O., Tiedemann, R., Cortijo, E., Chaisson, W.P., Flood, R.D., Hagen, S., Keigwin, L.D., Poli, S., Rio, D., Williams, T. (2002): Astronomical age models for Pleistocene drift sediments from the western North Atlantic (ODP Sites 1055-1063). *Marine Geology* **189**, 5–23.

Gutjahr, M., Lippold, J. (2011): Early arrival of Southern Source Water in the deep North Atlantic prior to Heinrich event 2. *Paleoceanography* **26**, PA2101.

Gutjahr, M., Frank, M., Stirling, C.H., Klemm, V., van de Flierdt, T., Halliday, A.N. (2007): Reliable extraction of a deepwater trace metal isotope signal from Fe–Mn oxyhydroxide coatings of marine sediments. *Chemical Geology* **242**, 351–370.

Gutjahr, M., Hoogakker, B.A.A., Frank, M., McCave, I.N. (2010): Changes in North Atlantic Deep Water strength and bottom water masses during Marine Isotope Stage 3 (45–35 ka BP). *Quaternary Science Reviews* **29**, 2451–2461.

Haley, B.A., Klinkhammer, G.P., McManus, J. (2004): Rare earth elements in pore waters of marine sediments. *Geochimica et Cosmochimica Acta* **68**, 1265–1279.

Haley, B.A., Frank, M., Hathorne, E., Pisias, N. (2014): Biogeochemical implications from dissolved rare earth element and Nd isotope distributions in the Gulf of Alaska. *Geochimica et Cosmochimica Acta* **126**, 455–474.

Haley, B.A., Du, J., Abbott, A.N., McManus, J. (2017): The Impact of Benthic Processes on Rare Earth Element and Neodymium Isotope Distributions in the Oceans. *Frontiers in Marine Science* **4**, 426.

Halliday, A.N., Davidson, J.P., Holden, P., Owen, R.M., Olivarez, A.M. (1992): Metalliferous sediments and the scavenging residence time of Nd near hydrothermal vents. *Geophysical Research Letters* **19**, 761–764.

Hallmaier, M. (2020): *Expansion of Pacific sourced deep water in the South Atlantic during past climate changes*. Bachelor thesis, Heidelberg University.

Hao, Q., Wang, L., Oldfield, F., Guo, Z. (2015): Extra-long interglacial in Northern Hemisphere during MISs 15-13 arising from limited extent of Arctic ice sheets in glacial MIS 14. *Scientific Reports* **5**, 12103.

Head, M.J., Gibbard, P.L. (2015): Early–Middle Pleistocene transitions: Linking terrestrial and marine realms. *Quaternary International* **389**, 7–46.

Helmke, J.P., Bauch, H.A., Röhl, U., Kandiano, E.S. (2008): Uniform climate development between the subtropical and subpolar Northeast Atlantic across marine isotope stage 11. *Climate of the Past* **4**, 181–190.

Henry, L.G., McManus, J.F., Curry, W.B., Roberts, N.L., Piotrowski, A.M., Keigwin, L.D. (2016): North Atlantic ocean circulation and abrupt climate change during the last glaciation. *Science* **353**, 470–474.

Hodell, D.A., Channell, J.E.T. (2016): Mode transitions in Northern Hemisphere glaciation: co-evolution of millennial and orbital variability in Quaternary climate. *Climate of the Past* **12**, 1805–1828.

Hodell, D.A., Venz, K.A., Charles, C.D., Ninnemann, U.S. (2003): Pleistocene vertical carbon isotope and carbonate gradients in the South Atlantic sector of the Southern Ocean. *Geochemistry, Geophysics, Geosystems* **4**, 1–19.

Hodell, D.A., Channell, J.E.T., Curtis, J.H., Romero, O.E., Röhl, U. (2008): Onset of "Hudson Strait" Heinrich events in the eastern North Atlantic at the end of the middle Pleistocene transition (∼640 ka)? *Paleoceanography* **23**, PA4218.

Hodell, D.A., Evans, H.F., Channell, J.E.T., Curtis, J.H. (2010): Phase relationships of North Atlantic ice-rafted debris and surface-deep climate proxies during the last glacial period. *Quaternary Science Reviews* **29**, 3875–3886.

Hongo, Y., Obata, H., Sotto Alibo, D., Nozaki, Y. (2006): Spatial Variations of Rare Earth Elements in North Pacific Surface Water. *Journal of Oceanography* **62**, 441–455.

Hönisch, B., Hemming, N.G., Archer, D., Siddall, M., McManus, J.F. (2009): Atmospheric Carbon Dioxide Concentration Across the Mid-Pleistocene Transition. *Science* **324**, 1551–1554.

Howard, W.R. (1997): A warm future in the past. *Nature* **388**, 418–419.

Howe, J.N.W., Piotrowski, A.M. (2017): Atlantic deep water provenance decoupled from atmospheric CO_2 concentration during the lukewarm interglacials. *Nature Communications* **8**, 2003.

Howe, J.N.W., Piotrowski, A.M., Noble, T.L., Mulitza, S., Chiessi, C.M., Bayon, G. (2016a): North Atlantic Deep Water Production during the Last Glacial Maximum. *Nature Communications* **7**, 11765.

Howe, J.N.W., Piotrowski, A.M., Rennie, V.C.F. (2016b): Abyssal origin for the early Holocene pulse of unradiogenic neodymium isotopes in Atlantic seawater. *Geology* **44**, 831–834.

Howe, J.N.W., Piotrowski, A.M., Hu, R., Bory, A. (2017): Reconstruction of east–west deep water exchange in the low latitude Atlantic Ocean over the past 25,000 years. *Earth and Planetary Science Letters* **458**, 327–336.

Hu, R., Noble, T.L., Piotrowski, A.M., McCave, I.N., Bostock, H.C., Neil, H.L. (2016): Neodymium isotopic evidence for linked changes in Southeast Atlantic and Southwest Pacific circulation over the last 200 kyr. *Earth and Planetary Science Letters* **455**, 106–114.

Huang, K.F., Oppo, D.W., Curry, W.B. (2014): Decreased influence of Antarctic intermediate water in the tropical Atlantic during North Atlantic cold events. *Earth and Planetary Science Letters* **389**, 200–208.

Huck, C.E., van de Flierdt, T., Jiménez-Espejo, F.J., Bohaty, S.M., Röhl, U., Hammond, S.J. (2016): Robustness of fossil fish teeth for seawater neodymium isotope reconstructions under variable redox conditions in an ancient shallow marine setting. *Geochemistry, Geophysics, Geosystems* **17**, 679–698.

Huybers, P. (2009): Pleistocene glacial variability as a chaotic response to obliquity forcing. *Climate of the Past* **5**, 481–488.

Ivanov, V.V., Shapiro, G.I., Huthnance, J.M., Aleynik, D.L., Golovin, P.N. (2004): Cascades of dense water around the world ocean. *Progress in Oceanography* **60**, 47–98.

Ivany, L.C., Van Simaeys, S., Domack, E.W., Samson, S.D. (2006): Evidence for an earliest Oligocene ice sheet on the Antarctic Peninsula. *Geology* **34**, 377–380.

Jacobsen, S.B., Wasserburg, G.J. (1980): Sm-Nd isotopic evolution of chondrites. *Earth and Planetary Science Letters* **50**, 139–155.

James, R.H., Elderfield, H., Palmer, M.R. (1995): The chemistry of hydrothermal fluids from the Broken Spur site, 29°N Mid-Atlantic ridge. *Geochimica et Cosmochimica Acta* **59**, 651–659.

Jansen, E., Raymo, M.E. (1996): Leg 162: New frontiers on past climates. In: *Proceedings of the Ocean Drilling Program, Initial Reports*, volume 162, edited by E. Jansen, M.E. Raymo, P. Blum, et al., 5–20, Ocean Drilling Program, College Station, TX.

Jaume-Seguí, M., Kim, J., Pena, L.D., Goldstein, S.L., Knudson, K.P., Yehudai, M., Hartman, A.E., Bolge, L., Ferretti, P. (2020): Distinguishing Glacial AMOC and Interglacial Non-AMOC Nd Isotopic Signals in the Deep Western Atlantic Over the Last 1 Myr. *Paleoceanography and Paleoclimatology* **36**, e2020PA003877.

Jeandel, C. (1993): Concentration and isotopic composition of Nd in the South Atlantic Ocean. *Earth and Planetary Science Letters* **117**, 581–591.

Jeandel, C. (2016): Overview of the mechanisms that could explain the 'Boundary Exchange' at the land–ocean contact. *Philosophical Transactions of the Royal Society A: Mathematical, Physical and Engineering Sciences* **374**, 20150287.

Jeandel, C., Oelkers, E.H. (2015): The influence of terrigenous particulate material dissolution on ocean chemistry and global element cycles. *Chemical Geology* **395**, 50–66.

Jeandel, C., Arsouze, T., Lacan, F., Techine, P., Dutay, J.C. (2007): Isotopic Nd compositions and concentrations of the lithogenic inputs into the ocean: A compilation, with an emphasis on the margins. *Chemical Geology* **239**, 156–164.

Jickells, T.D., An, Z.S., Andersen, K.K., Baker, A.R., Bergametti, G., Brooks, N., Cao, J.J., Boyd, P.W., Duce, R.A., Hunter, K.A., Kawahata, H., Kubilay, N., laRoche, J., Liss, P.S., Mahowald, N., Prospero, J.M., Ridgwell, A.J., Tegen, I., Torres, R. (2005): Global Iron Connections Between Desert Dust, Ocean Biogeochemistry, and Climate. *Science* **308**, 67–71.

Johannesson, K.H., Burdige, D.J. (2007): Balancing the global oceanic neodymium budget: Evaluating the role of groundwater. *Earth and Planetary Science Letters* **253**, 129–142.

Johannesson, K.H., Palmore, C.D., Fackrell, J., Prouty, N.G., Swarzenski, P.W., Chevis, D.A., Telfeyan, K., White, C.D., Burdige, D.J. (2017): Rare earth element behavior during groundwater–seawater mixing along the Kona Coast of Hawaii. *Geochimica et Cosmochimica Acta* **198**, 229–258.

Johnson, C., Sherwin, T., Smythe-Wright, D., Shimmield, T., Turrell, W. (2010): Wyville Thomson Ridge Overflow Water: Spatial and temporal distribution in the Rockall Trough. *Deep Sea Research Part I: Oceanographic Research Papers* **57**, 1153–1162.

Johnson, D.A. (1983): Regional oceanographic setting of the southwestern Atlantic. In: *Initial Reports of the Deep Sea Drilling Project*, volume 72, edited by P. Barker, R.L. Carlson, D.A. Johnson, 15–35, U.S. Govt. Printing Office, Washington.

Jones, E.J.W., Ewing, M., Ewing, J.I., Eittreim, S.L. (1970): Influences of Norwegian Sea overflow water on sedimentation in the northern North Atlantic and Labrador Sea. *Journal of Geophysical Research* **75**, 1655–1680.

Jullien, E., Grousset, F., Malaizé, B., Duprat, J., Sanchez-Goni, M.F., Eynaud, F., Charlier, K., Schneider, R., Bory, A., Bout, V., Flores, J.A. (2007): Low-latitude "dusty events" vs. high-latitude "icy Heinrich Events". *Quaternary Research* **68**, 379–386.

Kageyama, M., Harrison, S.P., Kapsch, M.L., Löfverström, M., Lora, J.M., Mikolajewicz, U., Sherriff-Tadano, S., Vadsaria, T., Abe-Ouchi, A., Bouttes, N., Chandan, D., LeGrande, A.N., Lhardy, F., Lohmann, G., Morozova, P.A., Ohgaito, R., Peltier, W.R., Quiquet, A., Roche, D.M., Shi, X., Schmittner, A., Tierney, J.E., Volodin, E. (2020): The PMIP4-CMIP6 Last Glacial Maximum experiments: preliminary results and comparison with the PMIP3-CMIP5 simulations. *Climate of the Past Discussions*. **2020**, 1–37.

Kandiano, E.S., Bauch, H.A., Fahl, K., Helmke, J.P., Röhl, U., Pérez-Folgado, M., Cacho, I. (2012): The meridional temperature gradient in the eastern North Atlantic during MIS 11 and its link to the ocean–atmosphere system. *Palaeogeography, Palaeoclimatology, Palaeoecology* **333–334**, 24–39.

Kandiano, E.S., van der Meer, M.T.J., Bauch, H.A., Helmke, J., Sinninghe Damsté, J.S., Schouten, S. (2016): A cold and fresh ocean surface in the Nordic Seas during MIS 11: Significance for the future ocean. *Geophysical Research Letters* **43**, 10929–10937.

Kandiano, E.S., van der Meer, M.T.J., Schouten, S., Fahl, K., Sinninghe Damsté, J.S., Bauch, H.A. (2017): Response of the North Atlantic surface and intermediate ocean structure to climate warming of MIS 11. *Scientific Reports* **7**, 46192.

Keigwin, L.D., Jones, G.A. (1989): Glacial-Holocene stratigraphy, chronology, and paleoceanographic observations on some North Atlantic sediment drifts. *Deep Sea Research Part A. Oceanographic Research Papers* **36**, 845–867.

Keigwin, L.D., Jones, G.A. (1994): Western North Atlantic evidence for millennial-scale changes in ocean circulation and climate. *Journal of Geophysical Research: Oceans* **99**, 12397–12410.

Keigwin, L.D., Swift, S.A. (2017): Carbon isotope evidence for a northern source of deep water in the glacial western North Atlantic. *Proceedings of the National Academy of Sciences* **114**, 2831–2835.

Kender, S., Ravelo, A.C., Worne, S., Swann, G.E.A., Leng, M.J., Asahi, H., Becker, J., Detlef, H., Aiello, I.W., Andreasen, D., Hall, I.R. (2018): Closure of the Bering Strait caused Mid-Pleistocene Transition cooling. *Nature communications* **9**, 5386.

Kenneth, J.P., Cannariato, K.G., Hendy, I.L., Behl, R.J. (2003): *Methane Hydrates in Quaternary Climate Change: The Clathrate Gun Hypothesis*, volume 54. American Geophysical Union, Washington, D.C.

Khélifi, N., Frank, M. (2014): A major change in North Atlantic deep water circulation 1.6 million years ago. *Climate of the Past* **10**, 1441–1451.

Kim, I., Kim, G. (2014): Submarine groundwater discharge as a main source of rare earth elements in coastal waters. *Marine Chemistry* **160**, 11–17.

Kissel, C., Laj, C., Labeyrie, L., Dokken, T., Voelker, A., Blamart, D. (1999): Rapid climatic variations during marine isotopic stage 3: magnetic analysis of sediments from Nordic Seas and North Atlantic. *Earth and Planetary Science Letters* **171**, 489–502.

Klevenz, V., Vance, D., Schmidt, D.N., Mezger, K. (2008): Neodymium isotopes in benthic foraminifera: Core-top systematics and a down-core record from the Neogene south Atlantic. *Earth and Planetary Science Letters* **265**, 571–587.

Koschinsky, A., Halbach, P. (1995): Sequential leaching of marine ferromanganese precipitates: Genetic implications. *Geochimica et Cosmochimica Acta* **59**, 5113–5132.

Kuhlbrodt, T., Griesel, A., Montoya, M., Levermann, A., Hofmann, M., Rahmstorf, S. (2007): On the driving processes of the Atlantic meridional overturning circulation. *Reviews of Geophysics* **45**, 1–32.

Labeyrie, L.D., Duplessy, J.C., Duprat, J., Juillet-Leclerc, A., Moyes, J., Michel, E., Kallel, N., Shackleton, N.J. (1992): Changes in the vertical structure of the North Atlantic Ocean between glacial and modern times. *Quaternary Science Reviews* **11**, 401–413.

Lacan, F., Jeandel, C. (2004a): Denmark Strait water circulation traced by heterogeneity in neodymium isotopic compositions. *Deep Sea Research Part I: Oceanographic Research Papers* **51**, 71–82.

Lacan, F., Jeandel, C. (2004b): Neodymium isotopic composition and rare earth element concentrations in the deep and intermediate Nordic Seas: Constraints on the Iceland Scotland Overflow Water signature. *Geochemistry, Geophysics, Geosystems* **5**, Q11006.

Lacan, F., Jeandel, C. (2004c): Subpolar Mode Water formation traced by neodymium isotopic composition. *Geophysical Research Letters* **31**, L14306.

Lacan, F., Jeandel, C. (2005a): Acquisition of the neodymium isotopic composition of the North Atlantic Deep Water. *Geochemistry, Geophysics, Geosystems* **6**, Q12008.

Lacan, F., Jeandel, C. (2005b): Neodymium isotopes as a new tool for quantifying exchange fluxes at the continent–ocean interface. *Earth and Planetary Science Letters* **232**, 245–257.

Laine, E.P., Hollister, C.D. (1981): Geological effects of the Gulf Stream System on the northern Bermuda Rise. *Marine Geology* **39**, 277–310.

Lambelet, M., van de Flierdt, T., Crocket, K., Rehkämper, M., Kreissig, K., Coles, B., Rijkenberg, M.J.A., Gerringa, L.J.A., de Baar, H.J.W., Steinfeldt, R. (2016): Neodymium isotopic composition and concentration in the western North Atlantic Ocean: Results from the GEOTRACES GA02 section. *Geochimica et Cosmochimica Acta* **177**, 1–29.

Lang, D.C., Bailey, I., Wilson, P.A., Chalk, T.B., Foster, G.L., Gutjahr, M. (2016): Incursions of southern-sourced water into the deep North Atlantic during late Pliocene glacial intensification. *Nature Geoscience* **9**, 375–379.

Lang, N., Wolff, E.W. (2011): Interglacial and glacial variability from the last 800 ka in marine, ice and terrestrial archives. *Climate of the Past* **7**, 361–380.

Laskar, J. (1990): The chaotic motion of the solar system: A numerical estimate of the size of the chaotic zones. *Icarus* **88**, 266–291.

Laskar, J., Robutel, P., Joutel, F., Gastineau, M., Correia, A.C.M., Levrard, B. (2004): A long-term numerical solution for the insolation quantities of the Earth. *Astronomy & Astrophysics* **428**, 261–285.

Laukert, G., Frank, M., Bauch, D., Hathorne, E.C., Gutjahr, M., Janout, M., Hölemann, J. (2017): Transport and transformation of riverine neodymium isotope and rare earth element signatures in high latitude estuaries: A case study from the Laptev Sea. *Earth and Planetary Science Letters* **477**, 205–217.

Lauritzen, S.E., Lundberg, J. (2004): Isotope Stage 11, the "super-Interglacial", from a North Norwegian Speleothem. In: *Studies of Cave Sediments: Physical and Chemical Records of Paleoclimate*, edited by I.D. Sasowsky, J. Mylroie, 257–272, Springer US, Boston, MA.

Lawrence, K.T., Sosdian, S., White, H.E., Rosenthal, Y. (2010): North Atlantic climate evolution through the Plio-Pleistocene climate transitions. *Earth and Planetary Science Letters* **300**, 329–342.

Le Fèvre, B., Pin, C. (2005): A straightforward separation scheme for concomitant Lu–Hf and Sm–Nd isotope ratio and isotope dilution analysis. *Analytica Chimica Acta* **543**, 209–221.

Lenton, T.M., Held, H., Kriegler, E., Hall, J.W., Lucht, W., Rahmstorf, S., Schellnhuber, H.J. (2008): Tipping elements in the Earth's climate system. *Proceedings of the National Academy of Sciences* **105**, 1786–1793.

Ling, H.F., Burton, K.W., O'Nions, R.K., Kamber, B.S., von Blanckenburg, F., Gibb, A.J., Hein, J.R. (1997): Evolution of Nd and Pb isotopes in Central Pacific seawater from ferromanganese crusts. *Earth and Planetary Science Letters* **146**, 1–12.

Link, J.M. (2015): *Rekonstruktion der Ozeanzirkulation im Nordatlantik während ausgewählter glazialer Terminationen der letzten 900 ka anhand von Neodymisotopen*. Master thesis, Heidelberg University.

Lippold, J., Grützner, J., Winter, D., Lahaye, Y., Mangini, A., Christl, M. (2009): Does sedimentary $^{231}Pa/^{230}Th$ from the Bermuda Rise monitor past Atlantic Meridional Overturning Circulation? *Geophysical Research Letters* **36**, L12061.

Lippold, J., Gutjahr, M., Blaser, P., Christner, E., de Carvalho Ferreira, M.L., Mulitza, S., Christl, M., Wombacher, F., Böhm, E., Antz, B., Cartapanis, O., Vogel, H., Jaccard, S.L. (2016): Deep water provenance and dynamics of the (de)glacial Atlantic meridional overturning circulation. *Earth and Planetary Science Letters* **445**, 68–78.

Lippold, J., Pöppelmeier, F., Süfke, F., Gutjahr, M., Goepfert, T.J., Blaser, P., Friedrich, O., Link, J.M., Wacker, L., Rheinberger, S., Jaccard, S.L. (2019): Constraining the Variability of the Atlantic Meridional Overturning Circulation During the Holocene. *Geophysical Research Letters* **46**, 11338–11346.

Lisiecki, L.E., Raymo, M.E. (2005): A Pliocene-Pleistocene stack of 57 globally distributed benthic $\delta^{18}O$ records. *Paleoceanography* **20**, PA1003.

Loutre, M.F., Berger, A. (2003): Marine Isotope Stage 11 as an analogue for the present interglacial. *Global and Planetary Change* **36**, 209–217.

Lugmair, G.W., Marti, K. (1978): Lunar initial $^{143}Nd/^{144}Nd$: Differential evolution of the lunar crust and mantle. *Earth and Planetary Science Letters* **39**, 349–357.

Lumpkin, R., Speer, K. (2007): Global Ocean Meridional Overturning. *Journal of Physical Oceanography* **37**, 2550–2562.

Lüthi, D., Le Floch, M., Bereiter, B., Blunier, T., Barnola, J.M., Siegenthaler, U., Raynaud, D., Jouzel, J., Fischer, H., Kawamura, K., Stocker, T.F. (2008): High-resolution carbon dioxide concentration record 650,000–800,000 years before present. *Nature* **453**, 379–382.

Lynch-Stieglitz, J. (2003): 6.16 - Tracers of Past Ocean Circulation. In: *Treatise on Geochemistry*, edited by H.D. Holland, K.K. Turekian, 433–451, Pergamon, Oxford.

Mackensen, A., Schmiedl, G. (2019): Stable carbon isotopes in paleoceanography: atmosphere, oceans, and sediments. *Earth-Science Reviews* **197**, 102893.

Mackensen, A., Hubberten, H.W., Bickert, T., Fischer, G., Fütterer, D.K. (1993): The δ^{13}C in benthic foraminiferal tests of Fontbotia wuellerstorfi (Schwager) Relative to the δ^{13}C of dissolved inorganic carbon in Southern Ocean Deep Water: Implications for glacial ocean circulation models. *Paleoceanography* **8**, 587–610.

Marchitto, T.M., Broecker, W.S. (2006): Deep water mass geometry in the glacial Atlantic Ocean: A review of constraints from the paleonutrient proxy Cd/Ca. *Geochemistry, Geophysics, Geosystems* **7**, Q12003.

Marshall, J., Speer, K. (2012): Closure of the meridional overturning circulation through Southern Ocean upwelling. *Nature Geoscience* **5**, 171–180.

Martin, E.E., Haley, B.A. (2000): Fossil fish teeth as proxies for seawater Sr and Nd isotopes. *Geochimica et Cosmochimica Acta* **64**, 835–847.

Martrat, B., Grimalt, J.O., Shackleton, N.J., de Abreu, L., Hutterli, M.A., Stocker, T.F. (2007): Four Climate Cycles of Recurring Deep and Surface Water Destabilizations on the Iberian Margin. *Science* **317**, 502–507.

Maslin, M.A., Brierley, C.M. (2015): The role of orbital forcing in the Early Middle Pleistocene Transition. *Quaternary International* **389**, 47–55.

Masson-Delmotte, V., Dreyfus, G., Braconnot, P., Johnsen, S., Jouzel, J., Kageyama, M., Landais, A., Loutre, M.F., Nouet, J., Parrenin, F., Raynaud, D., Stenni, B., Tuenter, E. (2006): Past temperature reconstructions from deep ice cores: relevance for future climate change. *Climate of the Past* **2**, 145–165.

Matsumoto, K. (2017): Tantalizing evidence for the glacial North Atlantic bottom water. *Proceedings of the National Academy of Sciences* **114**, 2794–2796.

McClymont, E.L., Sosdian, S.M., Rosell-Melé, A., Rosenthal, Y. (2013): Pleistocene sea-surface temperature evolution: Early cooling, delayed glacial intensification, and implications for the mid-Pleistocene climate transition. *Earth-Science Reviews* **123**, 173–193.

McManus, J.F., Oppo, D.W., Cullen, J.L. (1999): A 0.5-Million-Year Record of Millennial-Scale Climate Variability in the North Atlantic. *Science* **283**, 971–975.

McManus, J.F., Francois, R., Gherardi, J.M., Keigwin, L.D., Brown-Leger, S. (2004): Collapse and rapid resumption of Atlantic meridional circulation linked to deglacial climate changes. *Nature* **428**, 834–837.

Meland, M.Y., Dokken, T.M., Jansen, E., Hevrøy, K. (2008): Water mass properties and exchange between the Nordic seas and the northern North Atlantic during the period 23–6 ka: Benthic oxygen isotopic evidence. *Paleoceanography* **23**, PA1210.

Melles, M., Brigham-Grette, J., Minyuk, P.S., Nowaczyk, N.R., Wennrich, V., DeConto, R.M., Anderson, P.M., Andreev, A.A., Coletti, A., Cook, T.L., Haltia-Hovi, E., Kukkonen, M., Lozhkin, A.V., Rosén, P., Tarasov, P., Vogel, H., Wagner, B. (2012): 2.8

Million Years of Arctic Climate Change from Lake El'gygytgyn, NE Russia. *Science* **337**, 315–320.

Mercier, H., Weatherly, G.L., Arhan, M. (2000): Bottom water throughflows at the Rio de Janeiro and Rio Grande Fracture Zones. *Geophysical Research Letters* **27**, 1503–1506.

Meyers, S.R. (2014): Astrochron: An R Package for Astrochronology. https://cran.r-project.org/package=astrochron.

Michard, A., Albarède, F., Michard, G., Minster, J.F., Charlou, J.L. (1983): Rare-earth elements and uranium in high-temperature solutions from East Pacific Rise hydrothermal vent field (13 °N). *Nature* **303**, 795–797.

Milker, Y., Rachmayani, R., Weinkauf, M.F.G., Prange, M., Raitzsch, M., Schulz, M., Kučera, M. (2015): Global Synthesis of Sea-Surface Temperature Trends During Marine Isotope Stage 11. In: *Integrated Analysis of Interglacial Climate Dynamics (INTERDYNAMIC)*, edited by M. Schulz, A. Paul, SpringerBriefs in Earth System Sciences, 13–18, Springer International Publishing, Heidelberg [u.a.].

Miller, K.G., Wright, J.D., Fairbanks, R.G. (1991): Unlocking the Ice House: Oligocene-Miocene oxygen isotopes, eustasy, and margin erosion. *Journal of Geophysical Research: Solid Earth* **96**, 6829–6848.

Monnin, E., Indermühle, A., Dällenbach, A., Flückiger, J., Stauffer, B., Stocker, T.F., Raynaud, D., Barnola, J.M. (2001): Atmospheric CO_2 Concentrations over the Last Glacial Termination. *Science* **291**, 112–114.

Morrison, R., Waldner, A., Hathorne, E.C., Rahlf, P., Zieringer, M., Montagna, P., Colin, C., Frank, N., Frank, M. (2019): Limited influence of basalt weathering inputs on the seawater neodymium isotope composition of the northern Iceland Basin. *Chemical Geology* **511**, 358–370.

Mudelsee, M., Raymo, M.E. (2005): Slow dynamics of the Northern Hemisphere glaciation. *Paleoceanography* **20**, PA4022.

Müller, P. (2019): *Untersuchung und Rekonstruktion der atlantisch-meridionalen Ozeanzirkulation (AMOC) im interglazialen Stadium MIS-11 durch Neodymisotopie-Messungen*. Bachelor thesis, Heidelberg University.

New, A.L., Smythe-Wright, D. (2001): Aspects of the circulation in the Rockall Trough. *Continental Shelf Research* **21**, 777–810.

North Greenland Ice Core Project members (2004): High-resolution record of Northern Hemisphere climate extending into the last interglacial period. *Nature* **431**, 147–151.

O'Nions, R.K., Carter, S.R., Evensen, N.M., Hamilton, P.J. (1979): Geochemical and Cosmochemical Applications of Nd Isotope Analysis. *Annual Review of Earth and Planetary Sciences* **7**, 11–38.

O'Nions, R.K., Frank, M., von Blanckenburg, F., Ling, H.F. (1998): Secular variation of Nd and Pb isotopes in ferromanganese crusts from the Atlantic, Indian and Pacific Oceans. *Earth and Planetary Science Letters* **155**, 15–28.

Oppo, D.W., Lehman, S.J. (1993): Mid-Depth Circulation of the Subpolar North Atlantic During the Last Glacial Maximum. *Science* **259**, 1148–1152.

Oppo, D.W., Fairbanks, R.G., Gordon, A.L., Shackleton, N.J. (1990): Late Pleistocene Southern Ocean δ^{13}C variability. *Paleoceanography* **5**, 43–54.

Oppo, D.W., McManus, J.F., Cullen, J.L. (1998): Abrupt Climate Events 500,000 to 340,000 Years Ago: Evidence from Subpolar North Atlantic Sediments. *Science* **279**, 1335–1338.

Ortiz, J., Mix, A., Harris, S., O'Connell, S. (1999): Diffuse spectral reflectance as a proxy for percent carbonate content in North Atlantic sediments. *Paleoceanography* **14**, 171–186.

Osborne, A.H., Newkirk, D.R., Groeneveld, J., Martin, E.E., Tiedemann, R., Frank, M. (2014): The seawater neodymium and lead isotope record of the final stages of Central American Seaway closure. *Paleoceanography* **29**, 715–729.

Paillard, D., Labeyrie, L., Yiou, P. (1996): Macintosh Program performs time-series analysis. *Eos, Transactions American Geophysical Union* **77**, 379–379.

Palmer, M.R. (1985): Rare earth elements in foraminifera tests. *Earth and Planetary Science Letters* **73**, 285–298.

Palmer, M.R., Elderfield, H. (1986): Rare earth elements and neodymium isotopes in ferromanganese oxide coatings of Cenozoic foraminifera from the Atlantic Ocean. *Geochimica et Cosmochimica Acta* **50**, 409–417.

Past Interglacials Working Group of PAGES (2016): Interglacials of the last 800,000 years. *Reviews of Geophysics* **54**, 162–219.

Pearce, C.R., Jones, M.T., Oelkers, E.H., Pradoux, C., Jeandel, C. (2013): The effect of particulate dissolution on the neodymium (Nd) isotope and Rare Earth Element (REE) composition of seawater. *Earth and Planetary Science Letters* **369-370**, 138–147.

Pena, L.D., Goldstein, S.L. (2014): Thermohaline circulation crisis and impacts during the mid-Pleistocene transition. *Science* **345**, 318–322.

Pena, L.D., Goldstein, S.L., Hemming, S.R., Jones, K.M., Calvo, E., Pelejero, C., Cacho, I. (2013): Rapid changes in meridional advection of Southern Ocean intermediate waters to the tropical Pacific during the last 30kyr. *Earth and Planetary Science Letters* **368**, 20–32.

Pépin, L., Raynaud, D., Barnola, J.M., Loutre, M.F. (2001): Hemispheric roles of climate forcings during glacial-interglacial transitions as deduced from the Vostok record and LLN-2D model experiments. *Journal of Geophysical Research: Atmospheres* **106**, 31885–31892.

Petit, J.R., Jouzel, J., Raynaud, D., Barkov, N.I., Barnola, J.M., Basile, I., Bender, M., Chappellaz, J., Davis, M., Delaygue, G., Delmotte, M., Kotlyakov, V.M., Legrand, M., Lipenkov, V.Y., Lorius, C., Pepin, L., Ritz, C., Saltzman, E., Stievenard, M. (1999): Climate and atmospheric history of the past 420,000 years from the Vostok ice core, Antarctica. *Nature* **399**, 429–436.

Peucker-Ehrenbrink, B. (2009): Land2Sea database of river drainage basin sizes, annual water discharges, and suspended sediment fluxes. *Geochemistry, Geophysics, Geosystems* **10**, Q06014.

Piepgras, D.J., Wasserburg, G.J. (1980): Neodymium isotopic variations in seawater. *Earth and Planetary Science Letters* **50**, 128–138.

Piepgras, D.J., Wasserburg, G.J. (1987): Rare earth element transport in the western North Atlantic inferred from Nd isotopic observations. *Geochimica et Cosmochimica Acta* **51**, 1257–1271.

Piepgras, D.J., Wasserburg, G.J., Dasch, E.J. (1979): The isotopic composition of Nd in different ocean masses. *Earth and Planetary Science Letters* **45**, 223–236.

Pin, C., Briot, D., Bassin, C., Poitrasson, F. (1994): Concomitant separation of strontium and samarium-neodymium for isotopic analysis in silicate samples, based on specific extraction chromatography. *Analytica Chimica Acta* **298**, 209–217.

Piotrowski, A.M., Goldstein, S.L., Hemming, S.R., Fairbanks, R.G. (2004): Intensification and variability of ocean thermohaline circulation through the last deglaciation. *Earth and Planetary Science Letters* **225**, 205–220.

Piotrowski, A.M., Goldstein, S.L., Hemming, S.R., Fairbanks, R.G., Zylberberg, D.R. (2008): Oscillating glacial northern and southern deep water formation from combined neodymium and carbon isotopes. *Earth and Planetary Science Letters* **272**, 394–405.

Poirier, R.K., Billups, K. (2014): The intensification of northern component deepwater formation during the mid-Pleistocene climate transition. *Paleoceanography* **29**, 1046–1061.

Poli, M.S., Thunell, R.C., Rio, D. (2000): Millennial-scale changes in North Atlantic Deep Water circulation during marine isotope stages 11 and 12: Linkage to Antarctic climate. *Geology* **28**, 807–810.

Pöppelmeier, F., Gutjahr, M., Blaser, P., Keigwin, L.D., Lippold, J. (2018): Origin of Abyssal NW Atlantic Water Masses Since the Last Glacial Maximum. *Paleoceanography and Paleoclimatology* **33**, 530–543.

Pöppelmeier, F., Blaser, P., Gutjahr, M., Süfke, F., Thornalley, D.J.R., Grützner, J., Jakob, K.A., Link, J.M., Szidat, S., Lippold, J. (2019a): Influence of Ocean Circulation and Benthic Exchange on Deep Northwest Atlantic Nd Isotope Records During the Past 30,000 Years. *Geochemistry, Geophysics, Geosystems* **20**, 4457–4469.

Pöppelmeier, F., Gutjahr, M., Blaser, P., Oppo, D.W., Jaccard, S.L., Regelous, M., Huang, K.F., Süfke, F., Lippold, J. (2019b): Water mass gradients of the mid-depth Southwest Atlantic during the past 25,000 years. *Earth and Planetary Science Letters* 115963.

Puig, P., de Madron, X.D., Salat, J., Schroeder, K., Martín, J., Karageorgis, A.P., Palanques, A., Roullier, F., Lopez-Jurado, J.L., Emelianov, M., Moutin, T., Houpert, L. (2013a): Thick bottom nepheloid layers in the western Mediterranean generated by deep dense shelf water cascading. *Progress in Oceanography* **111**, 1–23.

Puig, P., Greenan, B.J.W., Li, M.Z., Prescott, R.H., Piper, D.J.W. (2013b): Sediment transport processes at the head of Halibut Canyon, eastern Canada margin: An interplay between internal tides and dense shelf-water cascading. *Marine Geology* **341**, 14–28.

Rachmayani, R., Prange, M., Lunt, D.J., Stone, E.J., Schulz, M. (2017): Sensitivity of the Greenland Ice Sheet to Interglacial Climate Forcing: MIS 5e Versus MIS 11. *Paleoceanography* **32**, 1089–1101.

Rahlf, P., Hathorne, E., Laukert, G., Gutjahr, M., Weldeab, S., Frank, M. (2020): Tracing water mass mixing and continental inputs in the southeastern Atlantic Ocean with dissolved neodymium isotopes. *Earth and Planetary Science Letters* **530**, 115944.

Rahmstorf, S. (2002): Ocean circulation and climate during the past 120,000 years. *Nature* **419**, 207–214.

Rahmstorf, S. (2006): Thermohaline Circulation. In: *Encyclopedia of Quaternary Sciences*, edited by S.A. Elias, 1–10, Elsevier, Amsterdam.

Railsback, L.B., Gibbard, P.L., Head, M.J., Voarintsoa, N.R.G., Toucanne, S. (2015): An optimized scheme of lettered marine isotope substages for the last 1.0 million years, and the climatostratigraphic nature of isotope stages and substages. *Quaternary Science Reviews* **111**, 94–106.

Ravelo, A.C., Hillaire-Marcel, C. (2007): The Use of Oxygen and Carbon Isotopes of Foraminifera in Paleoceanography. In: *Proxies in Late Cenozoic Paleoceanography*, volume 1 of *Developments in Marine Geology*, edited by C. Hillaire–Marcel, A. de Vernal, 735 – 764, Elsevier.

Raymo, M.E., Mitrovica, J.X. (2012): Collapse of polar ice sheets during the stage 11 interglacial. *Nature* **483**, 453–456.

Raymo, M.E., Ruddiman, W.F., Froelich, P.N. (1988): Influence of late Cenozoic mountain building on ocean geochemical cycles. *Geology* **16**, 649–653.

Raymo, M.E., Ruddiman, W.F., Shackleton, N.J., Oppo, D.W. (1990): Evolution of Atlantic-Pacific δ^{13}C gradients over the last 2.5 m.y. *Earth and Planetary Science Letters* **97**, 353–368.

Raymo, M.E., Oppo, D.W., Curry, W. (1997): The mid-Pleistocene climate transition: A deep sea carbon isotopic perspective. *Paleoceanography* **12**, 546–559.

Raymo, M.E., Lisiecki, L.E., Nisancioglu, K.H. (2006): Plio-Pleistocene Ice Volume, Antarctic Climate, and the Global δ^{18}O Record. *Science* **313**, 492–495.

Raynaud, D., Barnola, J.M., Souchez, R., Lorrain, R., Petit, J.R., Duval, P., Lipenkov, V.Y. (2005): The record for marine isotopic stage 11. *Nature* **436**, 39–40.

Rehfeld, K., Marwan, N., Heitzig, J., Kurths, J. (2011): Comparison of correlation analysis techniques for irregularly sampled time series. *Nonlinear Processes in Geophysics* **18**, 389–404.

Rempfer, J., Stocker, T.F., Joos, F., Dutay, J.C., Siddall, M. (2011): Modelling Nd-isotopes with a coarse resolution ocean circulation model: Sensitivities to model parameters and source/sink distributions. *Geochimica et Cosmochimica Acta* **75**, 5927–5950.

Reyes, A.V., Carlson, A.E., Beard, B.L., Hatfield, R.G., Stoner, J.S., Winsor, K., Welke, B., Ullman, D.J. (2014): South Greenland ice-sheet collapse during Marine Isotope Stage 11. *Nature* **510**, 525–528.

Reynolds, B.C., Frank, M., O'Nions, R.K. (1999): Nd- and Pb-isotope time series from Atlantic ferromanganese crusts: implications for changes in provenance and paleocirculation over the last 8 Myr. *Earth and Planetary Science Letters* **173**, 381–396.

Rhein, M., Kieke, D., Steinfeldt, R. (2015): Advection of North Atlantic Deep Water from the Labrador Sea to the southern hemisphere. *Journal of Geophysical Research: Oceans* **120**, 2471–2487.

Rial, J.A., Oh, J., Reischmann, E. (2013): Synchronization of the climate system to eccentricity forcing and the 100,000-year problem. *Nature Geoscience* **6**, 289–293.

Rickli, J., Frank, M., Halliday, A.N. (2009): The hafnium–neodymium isotopic composition of Atlantic seawater. *Earth and Planetary Science Letters* **280**, 118–127.

Rickli, J., Frank, M., Baker, A.R., Aciego, S., de Souza, G., Georg, R.B., Halliday, A.N. (2010): Hafnium and neodymium isotopes in surface waters of the eastern Atlantic Ocean: Implications for sources and inputs of trace metals to the ocean. *Geochimica et Cosmochimica Acta* **74**, 540–557.

Riser, S.C., Freeland, H.J., Roemmich, D., Wijffels, S., Troisi, A., Belbéoch, M., Gilbert, D., Xu, J., Pouliquen, S., Thresher, A., Le Traon, P.Y., Maze, G., Klein, B., Ravichandran, M., Grant, F., Poulain, P.M., Suga, T., Lim, B., Sterl, A., Sutton, P., Mork, K.A., Vélez-Belchí, P.J., Ansorge, I., King, B., Turton, J., Baringer, M., Jayne, S.R. (2016): Fifteen years of ocean observations with the global Argo array. *Nature Climate Change* **6**, 145–153.

Roberts, N.L., Piotrowski, A.M. (2015): Radiogenic Nd isotope labeling of the northern NE Atlantic during MIS 2. *Earth and Planetary Science Letters* **423**, 125–133.

Roberts, N.L., Piotrowski, A.M., McManus, J.F., Keigwin, L.D. (2010): Synchronous deglacial overturning and water mass source changes. *Science* **327**, 75–78.

Roberts, N.L., Piotrowski, A.M., Elderfield, H., Eglinton, T.I., Lomas, M.W. (2012): Rare earth element association with foraminifera. *Geochimica et Cosmochimica Acta* **94**, 57–71.

Robinson, A., Alvarez-Solas, J., Calov, R., Ganopolski, A., Montoya, M. (2017): MIS-11 duration key to disappearance of the Greenland ice sheet. *Nature Communications* **8**, 16008.

Robinson, S., Ivanovic, R., van de Flierdt, T., Blanchet, C.L., Tachikawa, K., Martin, E.E., Cook, C.P., Williams, T., Gregoire, L., Plancherel, Y., Jeandel, C., Arsouze, T. (2021): Global continental and marine detrital ε_{Nd}: An updated compilation for use in understanding marine Nd cycling. *Chemical Geology* **567**, 120119.

Robinson, S.G. (1986): The late Pleistocene palaeoclimatic record of North Atlantic deep-sea sediments revealed by mineral-magnetic measurements. *Physics of the Earth and Planetary Interiors* **42**, 22–47.

Robinson, S.G., McCave, I.N. (1994): Orbital forcing of bottom-current enhanced sedimentation on Feni Drift, NE Atlantic, during the mid-Pleistocene. *Paleoceanography* **9**, 943–972.

Rogerson, M., Rohling, E.J., Weaver, P.P.E., Murray, J.W. (2005): Glacial to interglacial changes in the settling depth of the Mediterranean Outflow plume. *Paleoceanography* **20**, PA3007.

Rohling, E.J., Braun, K., Grant, K., Kucera, M., Roberts, A.P., Siddall, M., Trommer, G. (2010): Comparison between Holocene and Marine Isotope Stage-11 sea-level histories. *Earth and Planetary Science Letters* **291**, 97–105.

Rousseau, T.C.C., Sonke, J.E., Chmeleff, J., van Beek, P., Souhaut, M., Boaventura, G., Seyler, P., Jeandel, C. (2015): Rapid neodymium release to marine waters from lithogenic sediments in the Amazon estuary. *Nature Communications* **6**, 7592.

Ruddiman, W.F. (2006): Orbital changes and climate. *Quaternary Science Reviews* **25**, 3092–3112.

Ruddiman, W.F., Raymo, M., McIntyre, A. (1986): Matuyama 41,000-year cycles: North Atlantic Ocean and northern hemisphere ice sheets. *Earth and Planetary Science Letters* **80**, 117–129.

Ruddiman, W.F., Raymo, M.E., Martinson, D.G., Clement, B.M., Backman, J. (1989): Pleistocene evolution: Northern hemisphere ice sheets and North Atlantic Ocean. *Paleoceanography* **4**, 353–412.

Rutberg, R.L., Hemming, S.R., Goldstein, S.L. (2000): Reduced North Atlantic Deep Water flux to the glacial Southern Ocean inferred from neodymium isotope ratios. *Nature* **405**, 935–938.

Sánchez Goñi, M.F., Llave, E., Oliveira, D., Naughton, F., Desprat, S., Ducassou, E., Hodell, D.A., Hernández-Molina, F.J. (2016): Climate changes in south western Iberia and Mediterranean Outflow variations during two contrasting cycles of the last 1 Myrs: MIS 31–MIS 30 and MIS 12–MIS 11. *Global and Planetary Change* **136**, 18–29.

Sarnthein, M., Tetzlaff, G., Koopmann, B., Wolter, K., Pflaumann, U. (1981): Glacial and interglacial wind regimes over the eastern subtropical Atlantic and North-West Africa. *Nature* **293**, 193–196.

Sarnthein, M., Winn, K., Jung, S.J.A., Duplessy, J.C., Labeyrie, L., Erlenkeuser, H., Ganssen, G. (1994): Changes in East Atlantic Deepwater Circulation over the last 30,000 years: Eight time slice reconstructions. *Paleoceanography* **9**, 209–267.

Saunders, P.M. (1994): The flux of overflow water through the Charlie-Gibbs Fracture Zone. *Journal of Geophysical Research: Oceans* **99**, 12343–12355.

Schlitzer, R. (2019): Ocean Data View. https://odv.awi.de.

Schmitz, W.J., McCartney, M.S. (1993): On the North Atlantic Circulation. *Reviews of Geophysics* **31**, 29–49.

Schönfeld, J., Zahn, R. (2000): Late Glacial to Holocene history of the Mediterranean Outflow. Evidence from benthic foraminiferal assemblages and stable isotopes at the Portuguese margin. *Palaeogeography, Palaeoclimatology, Palaeoecology* **159**, 85–111.

SCOR Working Group (2007): GEOTRACES – An international study of the global marine biogeochemical cycles of trace elements and their isotopes. *Geochemistry* **67**, 85–131.

Shackleton, N.J., Hall, M.A. (1984): Oxygen and carbon isotope stratigraphy of Deep Sea Drilling Project Hole 552A: Plio-Pleistocene Glacial History. In: *Initial Reports of the Deep Sea Drilling Project*, volume 81, edited by D.G. Roberts, D. Schnitker, B. Jan, J.G. Baldauf, A. Desprairies, R. Homrighausen, P. Huddlestun, A.J. Kaltenback, K.A.O. Krumsiek, A.C. Morton, J.W. Murray, J. Westberg-Smith, H.B. Zimmerman, 599–609, U.S. Government Printing Office, Washington D.C.

Shapiro, G.I., Huthnance, J.M., Ivanov, V.V. (2003): Dense water cascading off the continental shelf. *Journal of Geophysical Research: Oceans* **108**, 3390.

Shaw, H.F., Wasserburg, G.J. (1985): Sm-Nd in marine carbonates and phosphates: Implications for Nd isotopes in seawater and crustal ages. *Geochimica et Cosmochimica Acta* **49**, 503–518.

Shipboard Scientific Party (1983): Site 517: West Flank, Rio Grande Rise. In: *Initial Reports of the Deep Sea Drilling Project*, volume 72, edited by P.F. Barker, R.L. Carlson, D.A. Johnson, 339–356, U.S. Govt. Printing Office, Washington.

Shipboard Scientific Party (1988): Site 659. In: *Proceedings of the Ocean Drilling Program, Initial Reports*, volume 108, edited by W.F. Ruddiman, M. Sarnthein, J. Baldauf, J. Backman, J. Bloemendal, W. Curry, P. Farrimond, J.C. Faugeres, T. Janacek, Y. Katsura, H. Manivit, J. Mazzullo, J. Mienert, E. Pokras, M.E. Raymo, P. Schultheiss, R. Stein, L. Tauxe, J.P. Valet, P. Weaver, H. Yasuda, 221–325, Ocean Drilling Program, College Station, TX.

Shipboard Scientific Party (1995): Site 929. In: *Proceedings of the Ocean Discovery Program, Initial Reports*, volume 154, edited by W.B. Curry, N.J. Shackleton, C. Richter, J.E. Backman, F. Bassinot, T. Bickert, W.P. Chaisson, J.L. Cullen, P. deMenocal, D. McCullough Dobson, L. Ewert, J. Grützner, T. King Hagelberg, G. Hampt, S.E. Harris, T.D. Herbert, K. Moran, M. Murayama, D.W. Murray, P.N. Pearson, I. Raffi, D.A. Schneider, R. Tiedemann, J.P. Valet, G.P. Weedon, H. Yasuda, J.C. Zachos, 337–417, Ocean Drilling Program, College Station, TX.

Shipboard Scientific Party (1996): Sites 980/981. In: *Proceedings of Ocean Drilling Program, Initial Reports*, volume 162, edited by E. Jansen, M.E. Raymo, P. Blum, E.S. Andersen, W.E. Austin, K.H. Baumann, V. Bout-Roumazeilles, S.J. Carter, J.E.T. Channell, J.L. Cullen, B. Flower, S. Higgins, D.A. Hodell, J.A. Hood, S.M. Hyun, M. Ikehara, T. King, R. Larter, B. Lehman, S. Locker, K. McIntyre, J. McManus, L.B. Meng, S. O'Connell, J.D. Ortiz, F.R. Rack, A. Solheim, W. Wei, 49–90, Ocean Drilling Program, College Station, TX.

Shipboard Scientific Party (1998): Bermuda Rise and Sohm Abyssal Plain, Sites 1063 and 1064. In: *Proceedings of the Ocean Drilling Program, Initial Reports*, volume 172, edited by L.D. Keigwin, D. Rio, G.D. Acton, G.G. Bianchi, W. Borowski, N. Catagay, W.P. Chaisson, B.M. Clement, E. Cortijo, G.B. Dunbar, R.D. Flood, S.O. Franz, L. Giosan, J. Grützner, S. Hagen, B. Haskell, M.J. Horowitz, E.P. Laine, S.P. Lund, M. Okada, M.S. Poli, I. Raddi, M.K. Reuer, Y.G. Ternois, T. Williams, D.M. Winter, M.E. Yokokawa, book section 6, 251–308, Ocean Drilling Program, College Station, TX.

Shipboard Scientific Party (2004): Site 1267. In: *Proceedings of the Ocean Discovery Program, Initial Reports*, volume 208, edited by J.C. Zachos, D. Kroon, P. Blum, J. Bowles, P. Gaillot, T. Hasegawa, E.C. Hathorne, D.A. Hodell, D.C. Kelly, J.H. Jung, S.M. Keller, Y.S. Lee, D.C. Leuschner, Z. Liu, K.C. Lohmann, L.J. Lourens, S. Monechi, M. Nicolo, I. Raffi, C. Riesselman, U. Röhl, S.A. Schellenberg, D. Schmidt, A. Sluijs, D. Thomas, E. Thomas, H. Vallius, 1–77, Ocean Drilling Program, College STation, TX.

Siddall, M., Khatiwala, S., van de Flierdt, T., Jones, K., Goldstein, S.L., Hemming, S., Anderson, R.F. (2008): Towards explaining the Nd paradox using reversible scavenging in an ocean general circulation model. *Earth and Planetary Science Letters* **274**, 448–461.

Siegenthaler, U., Stocker, T.F., Monnin, E., Lüthi, D., Schwander, J., Stauffer, B., Raynaud,

D., Barnola, J.M., Fischer, H., Masson-Delmotte, V., Jouzel, J. (2005): Stable Carbon Cycle-Climate Relationship During the Late Pleistocene. *Science* **310**, 1313–1317.

Speich, S., Blanke, B., Cai, W. (2007): Atlantic meridional overturning circulation and the Southern Hemisphere supergyre. *Geophysical Research Letters* **34**, L23614.

Spratt, R.M., Lisiecki, L.E. (2016): A Late Pleistocene sea level stack. *Climate of the Past* **12**, 1079–1092.

St. John, K., Flower, B.P., Krissek, L. (2004): Evolution of iceberg melting, biological productivity, and the record of Icelandic volcanism in the Irminger basin since 630 ka. *Marine Geology* **212**, 133–152.

Staudigel, H., Doyle, P., Zindler, A. (1985): Sr and Nd isotope systematics in fish teeth. *Earth and Planetary Science Letters* **76**, 45–56.

Stewart, R.H. (2008): *Introduction to Physical Oceanography*. R. H. Stewart. http://hdl.handle.net/1969.1/160216.

Stichel, T., Frank, M., Rickli, J., Haley, B.A. (2012): The hafnium and neodymium isotope composition of seawater in the Atlantic sector of the Southern Ocean. *Earth and Planetary Science Letters* **317–318**, 282–294.

Stichel, T., Hartman, A.E., Duggan, B., Goldstein, S.L., Scher, H., Pahnke, K. (2015): Separating biogeochemical cycling of neodymium from water mass mixing in the Eastern North Atlantic. *Earth and Planetary Science Letters* **412**, 245–260.

Stichel, T., Pahnke, K., Duggan, B., Goldstein, S.L., Hartman, A.E., Paffrath, R., Scher, H.D. (2018): TAG Plume: Revisiting the Hydrothermal Neodymium Contribution to Seawater. *Frontiers in Marine Science* **5**, 96.

Stordal, M.C., Wasserburg, G.J. (1986): Neodymium isotopic study of Baffin Bay water: sources of REE from very old terranes. *Earth and Planetary Science Letters* **77**, 259–272.

Stramma, L., England, M. (1999): On the water masses and mean circulation of the South Atlantic Ocean. *Journal of Geophysical Research: Oceans* **104**, 20863–20883.

Struve, T., van de Flierdt, T., Burke, A., Robinson, L.F., Hammond, S.J., Crocket, K.C., Bradtmiller, L.I., Auro, M.E., Mohamed, K.J., White, N.J. (2017): Neodymium isotopes and concentrations in aragonitic scleractinian cold-water coral skeletons - Modern calibration and evaluation of palaeo-applications. *Chemical Geology* **453**, 146–168.

Struve, T., Roberts, N.L., Frank, M., Piotrowski, A.M., Spielhagen, R.F., Gutjahr, M., Teschner, C., Bauch, H.A. (2019): Ice-sheet driven weathering input and water mass mixing in the Nordic Seas during the last 25,000 years. *Earth and Planetary Science Letters* **514**, 108–118.

Sutter, J., Fischer, H., Grosfeld, K., Karlsson, N.B., Kleiner, T., Van Liefferinge, B., Eisen, O. (2019): Modelling the Antarctic Ice Sheet across the mid-Pleistocene transition – implications for Oldest Ice. *The Cryosphere* **13**, 2023–2041.

Tachikawa, K., Jeandel, C., Roy-Barman, M. (1999): A new approach to the Nd residence time in the ocean: the role of atmospheric inputs. *Earth and Planetary Science Letters* **170**, 433–446.

Tachikawa, K., Athias, V., Jeandel, C. (2003): Neodymium budget in the modern ocean and paleo-oceanographic implications. *Journal of Geophysical Research: Oceans* **108**, 3254.

Tachikawa, K., Toyofuku, T., Basile-Doelsch, I., Delhaye, T. (2013): Microscale neodymium distribution in sedimentary planktonic foraminiferal tests and associated mineral phases. *Geochimica et Cosmochimica Acta* **100**, 11–23.

Tachikawa, K., Piotrowski, A.M., Bayon, G. (2014): Neodymium associated with foraminiferal carbonate as a recorder of seawater isotopic signatures. *Quaternary Science Reviews* **88**, 1–13.

Tachikawa, K., Arsouze, T., Bayon, G., Bory, A., Colin, C., Dutay, J.C., Frank, N., Giraud, X., Gourlan, A.T., Jeandel, C., Lacan, F., Meynadier, L., Montagna, P., Piotrowski, A.M., Plancherel, Y., Pucéat, E., Roy-Barman, M., Waelbroeck, C. (2017): The large-scale evolution of neodymium isotopic composition in the global modern and Holocene ocean revealed from seawater and archive data. *Chemical Geology* **457**, 131–148.

Tachikawa, K., Rapuc, W., Vidal, L., Dubois-Dauphin, Q., Westerhold, T., Guihou, A., Bickert, T., Pérez-Asensio, J.N., Deschamps, P., Skonieczny, C. (2021): Eastern Atlantic deep-water circulation and carbon storage inferred from neodymium and carbon isotopic compositions over the past 1.1 million years. *Quaternary Science Reviews* **252**, 106752.

Tanaka, T., Togashi, S., Kamioka, H., Amakawa, H., Kagami, H., Hamamoto, T., Yuhara, M., Orihashi, Y., Yoneda, S., Shimizu, H., Kunimaru, T., Takahashi, K., Yanagi, T., Nakano, T., Fujimaki, H., Shinjo, R., Asahara, Y., Tanimizu, M., Dragusanu, C. (2000): JNdi-1: a neodymium isotopic reference in consistency with LaJolla neodymium. *Chemical Geology* **168**, 279–281.

Teal, L.R., Bulling, M.T., Parker, E.R., Solan, M. (2008): Global patterns of bioturbation intensity and mixed depth of marine soft sediments. *Aquatic Biology* **2**, 207–218.

Thibodeau, B., Bauch, H.A., Pedersen, T.F. (2017): Stratification-induced variations in nutrient utilization in the Polar North Atlantic during past interglacials. *Earth and Planetary Science Letters* **457**, 127–135.

Thomas, D.J., Lyle, M., Moore, T.C., Rea, D.K. (2008): Paleogene deepwater mass composition of the tropical Pacific and implications for thermohaline circulation in a greenhouse world. *Geochemistry, Geophysics, Geosystems* **9**, Q02002.

Thornalley, D.J.R., Bauch, H.A., Gebbie, G., Guo, W., Ziegler, M., Bernasconi, S.M., Barker, S., Skinner, L.C., Yu, J. (2015): A warm and poorly ventilated deep Arctic Mediterranean during the last glacial period. *Science* **349**, 706–710.

Thornalley, D.J.R., Oppo, D.W., Ortega, P., Robson, J.I., Brierley, C.M., Davis, R., Hall, I.R., Moffa-Sanchez, P., Rose, N.L., Spooner, P.T., Yashayaev, I., Keigwin, L.D. (2018): Anomalously weak Labrador Sea convection and Atlantic overturning during the past 150 years. *Nature* **556**, 227–230.

Tiedemann, R. (1991): *Acht Millionen Jahre Klimageschichte von Nordwest Afrika und Paläo-Ozeanographie des angrenzenden Atlantiks: Hochauflösende Zeitreihen von ODP-Sites 658-661*. Number 46 in Berichte - Reports, Geol.-Paläont. Inst. Univ. Kiel.

Tiedemann, R., Sarnthein, M., Shackleton, N.J. (1994): Astronomic timescale for the Pliocene Atlantic δ^{18}O and dust flux records of Ocean Drilling Program site 659. *Paleoceanography* **9**, 619–638.

Trauth, M.H., Sarnthein, M., Arnold, M. (1997): Bioturbational mixing depth and carbon flux at the seafloor. *Paleoceanography* **12**, 517–526.

Tripati, A.K., Roberts, C.D., Eagle, R.A., Li, G. (2011): A 20 million year record of planktic foraminiferal B/Ca ratios: Systematics and uncertainties in pCO_2 reconstructions. *Geochimica et Cosmochimica Acta* **75**, 2582–2610.

van Aken, H.M., de Boer, C.J. (1995): On the synoptic hydrography of intermediate and deep water masses in the Iceland Basin. *Deep Sea Research Part I: Oceanographic Research Papers* **42**, 165–189.

van de Flierdt, T., Frank, M., Lee, D.C., Halliday, A.N., Reynolds, B.C., Hein, J.R. (2004): New constraints on the sources and behavior of neodymium and hafnium in seawater from Pacific Ocean ferromanganese crusts. *Geochimica et Cosmochimica Acta* **68**, 3827–3843.

van de Flierdt, T., Robinson, L.F., Adkins, J.F., Hemming, S.R., Goldstein, S.L. (2006): Temporal stability of the neodymium isotope signature of the Holocene to glacial North Atlantic. *Paleoceanography* **21**, PA4102.

van de Flierdt, T., Robinson, L.F., Adkins, J.F. (2010): Deep-sea coral aragonite as a recorder for the neodymium isotopic composition of seawater. *Geochimica et Cosmochimica Acta* **74**, 6014–6032.

van de Flierdt, T., Griffiths, A.M., Lambelet, M., Little, S.H., Stichel, T., Wilson, D.J. (2016): Neodymium in the oceans: a global database, a regional comparison and implications for palaeoceanographic research. *Philosophical Transactions of the Royal Society A: Mathematical, Physical and Engineering Sciences* **374**, 20150293.

Vance, D., Burton, K. (1999): Neodymium isotopes in planktonic foraminifera: a record of the response of continental weathering and ocean circulation rates to climate change. *Earth and Planetary Science Letters* **173**, 365–379.

Vance, D., Scrivner, A.E., Beney, P., Staubwasser, M., Henderson, G.M., Slowey, N.C. (2004): The use of foraminifera as a record of the past neodymium isotope composition of seawater. *Paleoceanography* **19**, PA2009.

Vance, D., Teagle, D.A.H., Foster, G.L. (2009): Variable Quaternary chemical weathering fluxes and imbalances in marine geochemical budgets. *Nature* **458**, 493–496.

Vázquez Riveiros, N., Waelbroeck, C., Skinner, L., Duplessy, J.C., McManus, J.F., Kandiano, E.S., Bauch, H.A. (2013): The "MIS 11 paradox" and ocean circulation: Role of millennial scale events. *Earth and Planetary Science Letters* **371–372**, 258–268.

Vergnaud Grazzini, C., Grably, M., Pujol, C., Duprat, J. (1983): Oxygen isotope stratigraphy and paleoclimatology of southwestern Atlantic Quaternary sediments (Rio Grande Rise) at Deep Sea Drilling Project Site 517. In: *Initial Reports of the Deep Sea Drilling Project*, volume 72, edited by P. Barker, R.L. Carlson, D.A. Johnson, 871–884, U.S. Govt. Printing Office, Washington.

Voelker, A.H.L., Lebreiro, S. (2010): Millennial-scale changes in deep water properties at the mid-depth western Iberian margin linked to Mediterranean Outflow Water activity. *Geo-Temas* **7**, 175–176.

Vogt-Vincent, N., Lippold, J., Kaboth-Bahr, S., Blaser, P. (2020): Ice-rafted debris as a source of non-conservative behaviour for the εNd palaeotracer: insights from a simple model. *Geo-Marine Letters* **40**, 325–340.

von Blanckenburg, F., Nägler, T.F. (2001): Weathering versus circulation-controlled changes in radiogenic isotope tracer composition of the Labrador Sea and North Atlantic Deep Water. *Paleoceanography* **16**, 424–434.

Walling, D.E. (2006): Human impact on land–ocean sediment transfer by the world's rivers. *Geomorphology* **79**, 192–216.

Wefing, A.M., Arps, J., Blaser, P., Wienberg, C., Hebbeln, D., Frank, N. (2017): High precision U-series dating of scleractinian cold-water corals using an automated chromatographic U and Th extraction. *Chemical Geology* **475**, 140–148.

Wilkens, R.H., Westerhold, T., Drury, A.J., Lyle, M., Gorgas, T., Tian, J. (2017): Revisiting the Ceara Rise, equatorial Atlantic Ocean: isotope stratigraphy of ODP Leg 154 from 0 to 5 Ma. *Climate of the Past* **13**, 779–793.

Willeit, M., Ganopolski, A., Calov, R., Brovkin, V. (2019): Mid-Pleistocene transition in glacial cycles explained by declining CO_2 and regolith removal. *Science Advances* **5**, eaav7337.

Wilson, D.J., Piotrowski, A.M., Galy, A., Clegg, J.A. (2013): Reactivity of neodymium carriers in deep sea sediments: Implications for boundary exchange and paleoceanography. *Geochimica et Cosmochimica Acta* **109**, 197–221.

Wilson, D.J., Crocket, K.C., van de Flierdt, T., Robinson, L.F., Adkins, J.F. (2014): Dynamic intermediate ocean circulation in the North Atlantic during Heinrich Stadial 1: A radiocarbon and neodymium isotope perspective. *Paleoceanography* **29**, 1072–1093.

Winckler, G., Anderson, R.F., Fleisher, M.Q., McGee, D., Mahowald, N. (2008): Covariant Glacial-Interglacial Dust Fluxes in the Equatorial Pacific and Antarctica. *Science* **320**, 93–96.

Xu, L., Yang, J., Ni, Q., Yang, Y., Hu, Z., Liu, Y., Wu, Y., Luo, T., Hu, S. (2018a): Determination of Sm-Nd Isotopic Compositions in Fifteen Geological Materials Using Laser Ablation MC-ICP-MS and Application to Monazite Geochronology of Metasedimentary Rock in the North China Craton. *Geostandards and Geoanalytical Research* **42**, 379–394.

Xu, X., Bower, A., Furey, H., Chassignet, E.P. (2018b): Variability of the Iceland-Scotland Overflow Water Transport Through the Charlie-Gibbs Fracture Zone: Results From an Eddying Simulation and Observations. *Journal of Geophysical Research: Oceans* **123**, 5808–5823.

Xuan, C., Channell, J.E.T., Hodell, D.A. (2016): Quaternary magnetic and oxygen isotope stratigraphy in diatom-rich sediments of the southern Gardar Drift (IODP Site U1304, North Atlantic). *Quaternary Science Reviews* **142**, 74–89.

Yu, J., Menviel, L., Jin, Z.D., Anderson, R.F., Jian, Z., Piotrowski, A.M., Ma, X., Rohling, E.J., Zhang, F., Marino, G., McManus, J.F. (2020): Last glacial atmospheric CO_2 decline due to widespread Pacific deep-water expansion. *Nature Geoscience* **13**, 628–633.

Zachos, J., Pagani, M., Sloan, L., Thomas, E., Billups, K. (2001): Trends, Rhythms, and Aberrations in Global Climate 65 Ma to Present. *Science* **292**, 686–693.

Zachos, J.C., Dickens, G.R., Zeebe, R.E. (2008): An early Cenozoic perspective on greenhouse warming and carbon-cycle dynamics. *Nature* **451**, 279–283.

Zieringer, M., Frank, M., Stumpf, R., Hathorne, E.C. (2019): The distribution of neodymium isotopes and concentrations in the eastern tropical North Atlantic. *Chemical Geology* **511**, 265–278.

A Supplementary material for Study I

A.1 Depth alignment to the splice

Due to the fact that the samples for ε_{Nd} measurements were not always from the shipboard splice, their depths needed to be adjusted. Therefore, the cores were aligned to the splice (see Section 3.2.2). The results of this adjustment are shown in Figures A.1 to A.5. Here, the lightness or magnetic susceptibility data of the splice in blue and the individual holes are shown before the alignment (red) and afterwards (green). The marks at the bottom of the top panel show the tuning points. In the bottom panel, the depth of the shifted core is given as adjusted mcd (amcd). An overview of all tuned cores and the tie points is given in Table A.1.

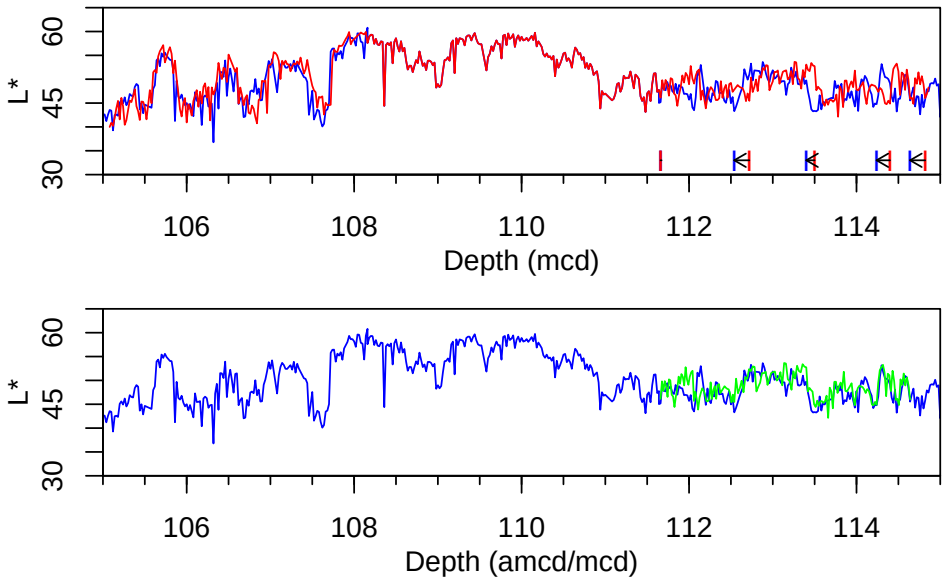

Figure A.1: Core C12 before (red, upper panel) and after (green, bottom panel) tuning to the lightness data of the splice (blue).

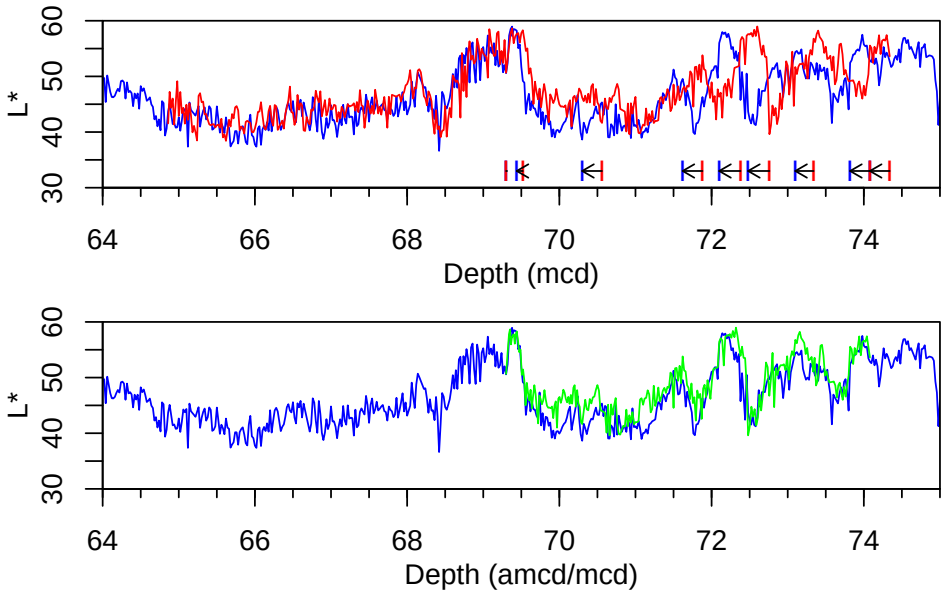

Figure A.2: Core D08 before (red, upper panel) and after (green, bottom panel) tuning to the lightness data of the splice (blue).

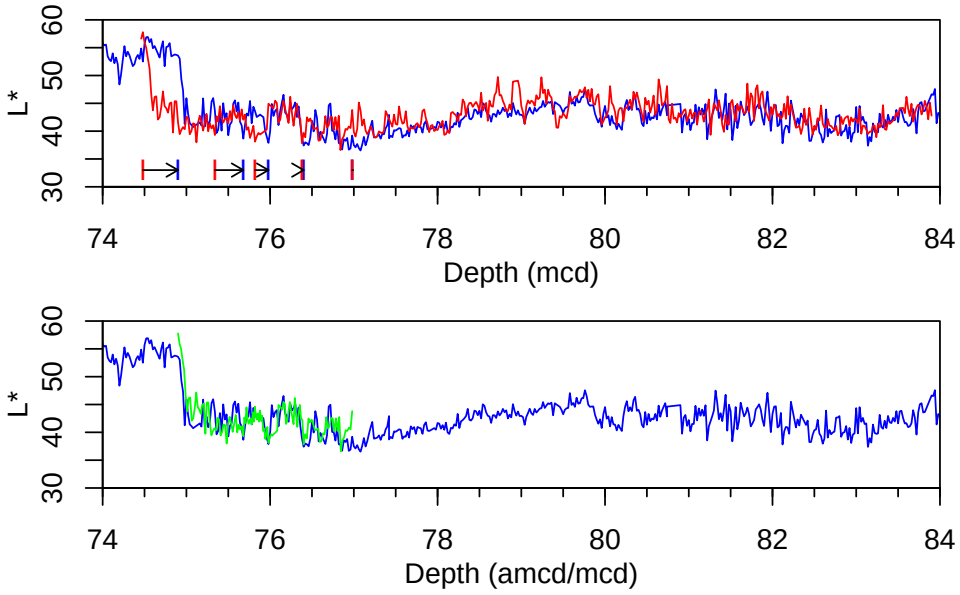

Figure A.3: Core D09 before (red, upper panel) and after (green, bottom panel) tuning to the lightness data of the splice (blue).

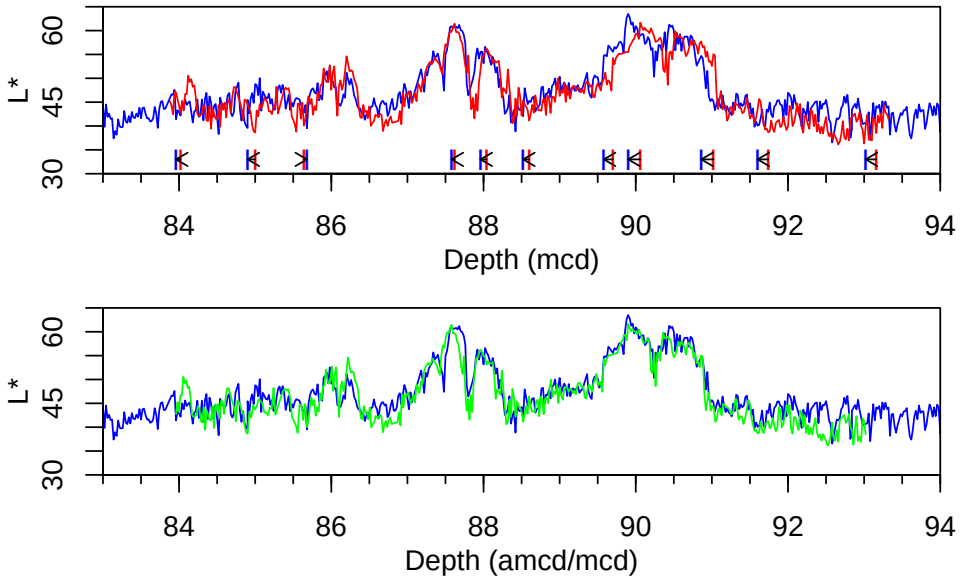

Figure A.4: Core D10 before (red, upper panel) and after (green, bottom panel) tuning to the lightness data of the splice (blue).

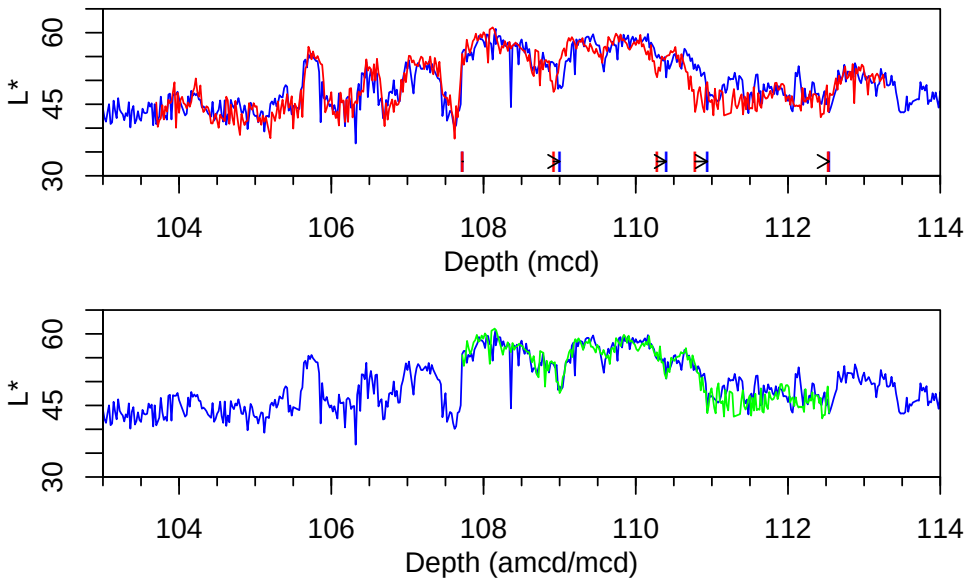

Figure A.5: Core D12 before (red, upper panel) and after (green, bottom panel) tuning to the lightness data of the splice (blue).

Table A.1: Tie points used for the depth alignment of ODP 1063 cores to the splice.

Core	mcd	amcd
C12	111.66	111.66
C12	112.72	112.54
C12	113.50	113.40
C12	114.40	114.24
C12	114.82	114.64
D08	69.30	69.30
D08	69.52	69.44
D08	70.56	70.30
D08	71.88	71.62
D08	72.38	72.10
D08	72.76	72.48
D08	73.34	73.10
D08	74.08	73.82
D08	74.34	74.08
D09	74.48	74.90
D09	75.34	75.68
D09	75.82	75.98
D09	76.38	76.40
D09	76.98	76.98

Core	mcd	amcd
D10	84.02	83.96
D10	85.00	84.90
D10	85.64	85.68
D10	87.62	87.58
D10	88.04	87.96
D10	88.60	88.52
D10	89.70	89.58
D10	90.06	89.90
D10	91.02	90.86
D10	91.74	91.60
D10	93.16	93.02
D12	107.72	107.72
D12	108.92	109.00
D12	110.28	110.40
D12	110.78	110.94
D12	112.53	112.54

B Supplementary material for Study II

B.1 Elaboration on the age model of ODP 929

Several age models exist for ODP 929 spanning MISs 12–11. These include the one of Lisiecki and Raymo [2005], who created a global mean stack of stable oxygen isotopes of benthic foraminifera (the LR04, gray curve in Figure B.1 A). The δ^{18}O record of ODP 929 [Bickert *et al.*, 1997] was incorporated in the establishment of the LR04 and thereby an age-depth relationship got defined [Lisiecki and Raymo, 2005] (blue curve in Figure B.1 A). The age model of Howe and Piotrowski [2017] closed gaps in the δ^{18}O record of Bickert *et al.* [1997] spanning the transition of MISs 11/10 and MIS 13 and tied this composite record again to the LR04 (green curve in Figure B.1). Wilkens *et al.* [2017] took a different approach. These authors created a common depth scale for the Ceara Rise sites (ODP 925–929). The individual sites were tied to the depth scale of ODP 926 based on physical properties data and core images. For this reference site, an age model was generated by tuning the physical properties data and core images to the orbital solution of Laskar *et al.* [2004]. The resulting age model for site ODP 929 is shown in the rosy curve in Figure B.1.

The choice of applying the age model of Lisiecki and Raymo [2005] in this thesis for ODP 929 is based on the apparent better agreement of the δ^{18}O curve with the LR04 compared to the other age models. The regional difference in the δ^{18}O records of the Ceara Rise to the LR04 of 0.2 ‰[Wilkens *et al.*, 2017] is also reflected. Furthermore, the age models of the other sites (with the exception of DSDP 517) also use the LR04 as a reference curve. For this reason, the comparability of the different ε_{Nd} records is given.

The different age models lead to deviations in the ages of the Nd samples of up to 9.5 ka during MIS 11 (see Figure B.1 B). This mainly affects the interpretation of the dip in ε_{Nd} around 395 ka (Lisiecki-age model), which is currently ascribed to MIS 11b. If the other age models were used, this dip would occur earlier and could possibly match to the mid-MIS 11c dip, which is seen in the sediment core ODP 1063. In order to reduce the uncertainty regarding the age models, the temporal resolution of the δ^{18}O record could be increased with additional samples. Thereby, the determination of the

tie points to the LR04 stack becomes more unambiguous.

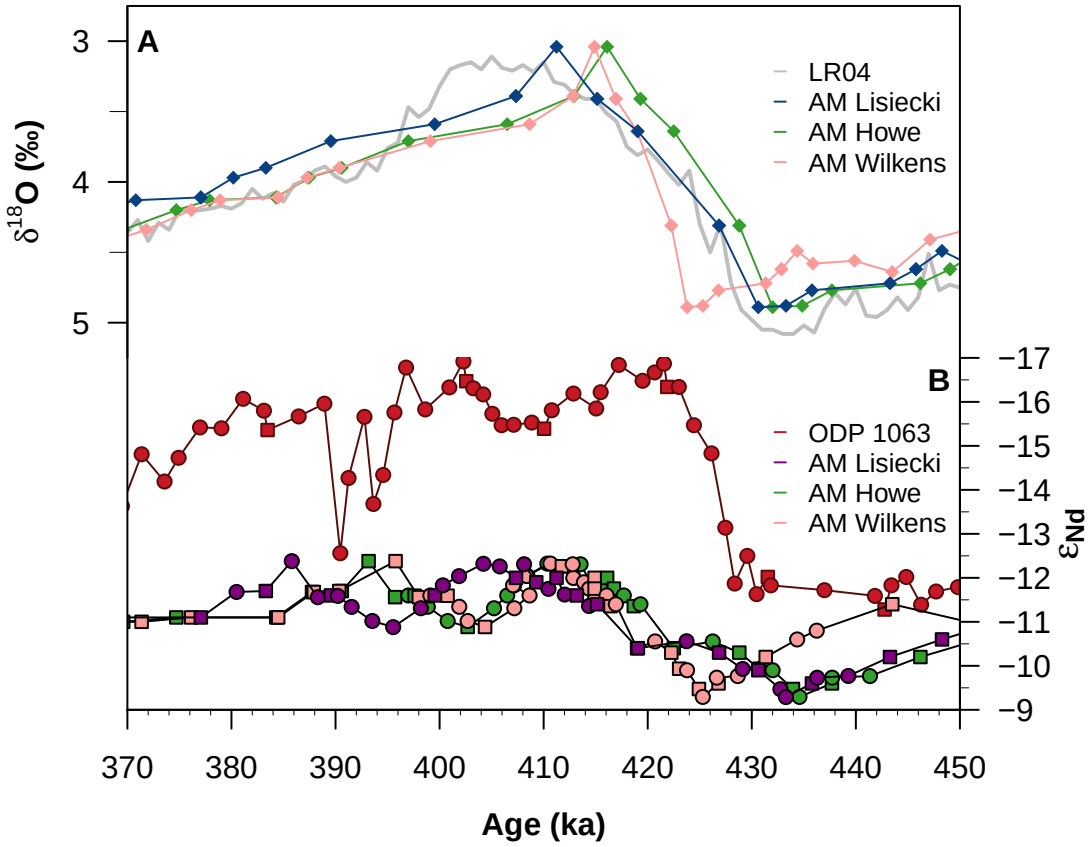

Figure B.1: Different age models of ODP 929. (A) Stable oxygen record of benthic foraminifera compared to the global stack LR04 in gray [Lisiecki and Raymo, 2005]. The age model of the blue curve is originally established by the LR04 [Lisiecki and Raymo, 2005] and is the one used throughout this thesis. The age model of the green curve was established by Howe and Piotrowski [2017] and the rosy one by Wilkens *et al.* [2017]. (B) Nd isotopic composition of ODP 929 compared to the one of ODP 1063 in red. Data points analyzed in this thesis are shown as circles, and the published ones by Howe and Piotrowski [2017] for ODP 929 and Jaume-Seguí *et al.* [2020] for ODP 1063 as squares. The purple curve is based on the age model by Lisiecki and Raymo [2005] , the green one based on Howe and Piotrowski [2017], and the rosy one based on Wilkens *et al.* [2017].

C Data from Study I

Table C.1: Authigenic Nd isotopic composition of ODP 1063 by bulk sediment leaching. Samples labeled with * are from Link [2015].

Site	Label	Top (cm)	Bottom (cm)	Depth (mcd)	Depth (amcd)	Age (ka)	Sample #	ε_{Nd}	Int. 2 SEM	Ext. 2 SD	W. Mean ε_{Nd}	2 SEM
ODP 1063	B5H4W	55	57	44.89		149.1	3577	-11.11	0.16	0.19		
ODP 1063	B5H4W	95	97	45.29		150.0	4039	-11.47	0.13	0.28		
ODP 1063	B5H4W	144	146	45.78		151.1	4054	-11.40	0.13	0.28		
ODP 1063	B5H5W	22	24	46.06		151.7	3614	-12.23	0.18	0.19		
ODP 1063	B5H5W	50	52	46.34		152.3	3592	-11.86	0.15	0.19		
ODP 1063	B5H5W	70	72	46.54		152.8	4048	-11.40	0.16	0.28		
ODP 1063	B5H5W	110	112	46.94		153.7	4036	-11.94	0.14	0.28		
ODP 1063	B5H5W	140	142	47.24		154.3	3608	-12.66	0.13	0.19		
ODP 1063	B5H6W	20	22	47.54		155.0	3609	-13.11	0.15	0.19		
ODP 1063	B5H6W	38	40	47.72		155.9	4052	-12.80	0.15	0.28		
ODP 1063	D6H3W	59	61	47.89		156.8	3579	-12.62	0.17	0.19		
ODP 1063	D6H3W	77	79	48.07		157.8	4263	-12.88	0.10	0.24		
ODP 1063	D6H3W	101	103	48.31		159.0	4274	-14.64	0.10	0.24		
ODP 1063	D6H3W	125	127	48.55		160.2	4266	-13.39	0.11	0.24		
ODP 1063	D6H3W	148	150	48.78		161.4	3568	-13.19	0.17	0.19		
ODP 1063	D6H4W	23	25	49.03		162.7	4269	-14.49	0.08	0.24		
ODP 1063	D6H4W	47	49	49.27		164.0	4293	-14.30	0.10	0.24		
ODP 1063	D6H4W	71	73	49.51		165.2	3574	-14.58	0.18	0.19		
ODP 1063	D6H4W	95	97	49.75		166.5	4313	-14.22	0.07	0.24		
ODP 1063	D6H4W	119	121	49.99		167.7	4281	-13.98	0.11	0.24		
ODP 1063	D6H4W	143	145	50.23		169.0	4259	-14.48	0.14	0.24		

Site	Label	Top (cm)	Bottom (cm)	Depth (mcd)	Depth (amcd)	Age (ka)	Sample #	ε_{Nd}	Int. 2 SEM	Ext. 2 SD	W. Mean ε_{Nd}	2 SEM
ODP 1063	D6H5W	17	19	50.47		170.2	3619	-13.41	0.15	0.19		
ODP 1063	D6H5W	35	37	50.65		171.2	4006	-12.51	0.14	0.28		
ODP 1063	D6H5W	52	54	50.82		172.0	4009	-12.43	0.13	0.28		
ODP 1063	D6H5W	70	72	51.00		173.0	4306	-14.23	0.07	0.24		
ODP 1063	D6H5W	89	91	51.19		174.0	4046	-12.43	0.15	0.28		
ODP 1063	D6H5W	98	100	51.28		174.4	3602	-12.53	0.13	0.19		
ODP 1063	D6H5W	108	110	51.38		175.0	4010	-12.51	0.15	0.28		
ODP 1063	D6H5W	127	129	51.57		175.9	4056	-12.84	0.14	0.28		
ODP 1063	D6H6W	32	34	52.12		178.8	3584	-14.35	0.17	0.19		
ODP 1063	D6H6W	60	62	52.40		180.3	4297	-15.79	0.08	0.24		
ODP 1063	D6H6W	87	89	52.67		181.7	4033	-13.74	0.13	0.28		
ODP 1063	D6H6W	114	116	52.94		183.1	4271	-13.69	0.08	0.24		
ODP 1063	D6H6W	127	129	53.07		183.7	3621	-14.21	0.17	0.19		
ODP 1063	D6H6W	145	147	53.25		184.7	4267	-14.07	0.10	0.24		
ODP 1063	B6H2W	109	111	53.47		185.8	4035	-13.75	0.12	0.28		
ODP 1063	D6H7W	29	31	53.59		186.4	4286	-13.66	0.09	0.24		
ODP 1063	B6H2W	129	131	53.67		186.9	3589	-13.66	0.14	0.19		
ODP 1063	B6H3W	0	4	53.88		187.9	4031	-13.55	0.13	0.28		
ODP 1063	B6H3W	18	20	54.06		189.2	4294	-13.38	0.09	0.24		
ODP 1063	B6H3W	39	42	54.27		190.6	3597	-14.76	0.18	0.19		
ODP 1063	B6H3W	59	61	54.47		191.9	4005	-15.84	0.12	0.28		
ODP 1063	B6H3W	68	70	54.56		192.6	4295	-15.65	0.09	0.24		
ODP 1063	B6H3W	80	82	54.68		193.4	4254	-13.98	0.12	0.24		

Site	Label	Top (cm)	Bottom (cm)	Depth (mcd)	Depth (amcd)	Age (ka)	Sample #	ε_{Nd}	Int. 2 SEM	Ext. 2 SD	W. Mean ε_{Nd}	2 SEM
ODP 1063	B6H3W	100	102	54.88		194.7	3583	-12.98	0.15	0.19	-12.91	0.15
ODP 1063	B6H3W	100	102	54.88		194.7	4303	-12.89	0.08	0.24		
ODP 1063	C7H1W	32	34	55.38		198.1	4050	-16.22	0.15	0.28		
ODP 1063	C7H1W	35	37	55.41		198.3	3603	-15.02	0.15	0.19		
ODP 1063	C7H1W	54	56	55.60		199.6	4262	-16.20	0.11	0.24		
ODP 1063	C7H1W	74	76	55.80		201.0	3572	-16.22	0.16	0.19		
ODP 1063	C7H1W	93	95	55.99		203.3	4025	-14.42	0.14	0.28		
ODP 1063	C7H1W	118	120	56.24		206.3	3618	-14.71	0.15	0.19		
ODP 1063	C7H1W	145	147	56.51		209.5	4305	-14.84	0.08	0.24		
ODP 1063	C7H2W	17	19	56.73		212.1	3598	-16.16	0.14	0.19		
ODP 1063	C7H2W	35	37	56.91		214.3	3578	-18.37	0.13	0.19	-18.32	0.08
ODP 1063	C7H2W	35	37	56.91		214.3	4280	-18.30	0.09	0.24		
ODP 1063	C7H2W	38	40	56.94		214.6	4253	-18.19	0.10	0.24		
ODP 1063	C7H2W	58	60	57.14		217.0	3570	-14.34	0.17	0.19		
ODP 1063	C7H2W	75	77	57.31		219.1	3617	-12.39	0.16	0.19		
ODP 1063	C7H2W	98	100	57.54		222.0	3606	-11.73	0.17	0.19		
ODP 1063	C7H2W	116	118	57.72		222.7	3580	-12.68	0.15	0.19		
ODP 1063	C7H2W	118	120	57.74		222.8	3600	-12.73	0.16	0.19		
ODP 1063	C7H2W	138	140	57.94		223.6	3573	-13.68	0.18	0.19		
ODP 1063	C7H3W	28	30	58.34		225.2	3616	-14.50	0.14	0.19		
ODP 1063	C7H3W	51	53	58.57		226.1	4276	-11.99	0.10	0.24		
ODP 1063	C7H3W	74	76	58.80		227.0	3596	-13.73	0.15	0.19		
ODP 1063	C7H3W	97	99	59.03		229.6	3610	-13.36	0.16	0.19		

Site	Label	Top (cm)	Bottom (cm)	Depth (mcd)	Depth (amcd)	Age (ka)	Sample #	ε_{Nd}	Int. 2 SEM	Ext. 2 SD	W. Mean ε_{Nd}	2 SEM
ODP 1063	C7H3W	120	122	59.26		232.3	3605	-14.02	0.14	0.19		
ODP 1063	C7H3W	143	145	59.49		234.9	3590	-14.21	0.17	0.19		
ODP 1063	C7H4W	16	18	59.72		237.6	3622	-16.09	0.17	0.19		
ODP 1063	C7H4W	37	39	59.93		240.0	3566	-16.03	0.17	0.19		
ODP 1063	C7H4W	62	64	60.18		243.3	3599	-12.80	0.17	0.19	-12.67	0.09
ODP 1063	C7H4W	62	64	60.18		243.3	4291	-12.62	0.10	0.24		
ODP 1063	C7H4W	82	84	60.38		246.0	3612	-15.31	0.16	0.19		
ODP 1063	C7H4W	85	87	60.41		246.1	3588	-15.55	0.14	0.19		
ODP 1063	C7H4W	108	110	60.64		247.1	3613	-13.42	0.19	0.19		
ODP 1063	C7H4W	132	134	60.88		248.1	3581	-12.28	0.15	0.19		
ODP 1063	C7H5W	3	5	61.09		249.0	3585	-14.59	0.15	0.19		
ODP 1063	C7H5W	28	30	61.34		250.1	3571	-13.96	0.16	0.19		
ODP 1063	C7H5W	48	50	61.54		250.9	3607	-13.05	0.17	0.19		
ODP 1063	C7H5W	70	72	61.76		251.8	3575	-14.28	0.16	0.19	-14.29	0.12
ODP 1063	C7H5W	70	72	61.76		251.8	3611	-14.30	0.19	0.19		
ODP 1063	C7H5W	72	74	61.78		251.9	3567	-14.12	0.19	0.19		
ODP 1063	C7H5W	93	95	61.99		252.8	3565	-13.64	0.17	0.19		
ODP 1063	C7H5W	114	116	62.20		253.7	4296	-13.50	0.10	0.24		
ODP 1063	C7H5W	138	140	62.44		254.7	3569	-13.05	0.16	0.19		
ODP 1063	C7H6W	9	11	62.65		255.6	4302	-15.17	0.07	0.24		
ODP 1063	C7H6W	32	34	62.88		256.6	3561	-14.45	0.14	0.19		
ODP 1063	C7H6W	54	56	63.10		257.5	4260	-16.08	0.12	0.24		
ODP 1063	C7H6W	72	74	63.28		258.3	3586	-13.53	0.14	0.19		

Site	Label	Top (cm)	Bottom (cm)	Depth (mcd)	Depth (amcd)	Age (ka)	Sample #	ε_{Nd}	Int. 2 SEM	Ext. 2 SD	W. Mean ε_{Nd}	2 SEM
ODP 1063	D7H7W	2	4	63.40		258.8	3267	-13.28	0.09	0.16		
ODP 1063	D7H7W	32	34	63.70		260.2	3278	-13.55	0.14	0.16		
ODP 1063	B7H3W	32	34	64.00		264.6	3285	-12.93	0.12	0.16		
ODP 1063	B7H3W	62	64	64.30		267.7	3941	-13.62	0.17	0.16	-13.66	0.12
ODP 1063	B7H3W	62	64	64.30		267.7	3947	-13.70	0.18	0.16		
ODP 1063	B7H3W	92	94	64.60		269.5	3274	-12.25	0.12	0.16		
ODP 1063	D8H1W	8	10	64.90		271.0	4011	-12.48	0.15	0.28		
ODP 1063	D8H1W	38	40	65.20		272.4	3301	-12.38	0.13	0.16		
ODP 1063	D8H1W	68	70	65.50		273.7	3258	-12.52	0.11	0.16		
ODP 1063	D8H1W	98	100	65.80		274.9	3945	-13.99	0.17	0.16	-13.79	0.08
ODP 1063	D8H1W	98	100	65.80		274.9	4270	-13.74	0.09	0.24		
ODP 1063	D8H1W	128	130	66.10		276.1	3303	-12.57	0.11	0.16		
ODP 1063	D8H2W	8	10	66.40		277.0	3260	-12.89	0.12	0.16		
ODP 1063	D8H2W	68	70	67.00		277.7	4258	-13.24	0.10	0.24		
ODP 1063	D8H2W	98	100	67.30		278.6	3263	-15.29	0.09	0.16		
ODP 1063	D8H2W	100	102	67.32		278.7	4022	-15.01	0.13	0.28		
ODP 1063	D8H2W	128	130	67.60		279.5	3946	-14.57	0.17	0.16		
ODP 1063	D8H3W	8	10	67.90		280.6	3275	-14.41	0.12	0.16		
ODP 1063	D8H3W	69	71	68.51		281.8	3248	-13.23	0.10	0.16	-13.19	0.07
ODP 1063	D8H3W	69	71	68.51		281.8	3256	-13.15	0.11	0.16		
ODP 1063	D8H3W	94	96	68.76		282.3	4265	-15.22	0.10	0.24		
ODP 1063	D8H3W	128	130	69.10		282.8	3255	-15.87	0.15	0.16		
ODP 1063	D8H4A	8	10	69.40	69.36	283.3	3277	-16.29	0.13	0.16		

Site	Label	Top (cm)	Bottom (cm)	Depth (mcd)	Depth (amcd)	Age (ka)	Sample #	ε_{Nd}	Int. 2 SEM	Ext. 2 SD	W. Mean ε_{Nd}	2 SEM
ODP 1063	D8H4A	38	40	69.70	69.59	285.0	3969	-12.42	0.17	0.16		
ODP 1063	D8H4A	68	70	70.00	69.84	286.8	4019	-12.76	0.15	0.28		
ODP 1063	D8H4W	86	88	70.18	69.99	287.6	3279	-12.53	0.12	0.16		
ODP 1063	D8H4A	128	130	70.60	70.34	289.6	3259	-13.69	0.13	0.16		
ODP 1063	D8H5W	8	10	70.90	70.64	291.4	2382	-13.22	0.16	0.16		
ODP 1063	D8H5W	38	40	71.20	70.94	293.0	2411	-13.58	0.18	0.27		
ODP 1063	D8H5W	70	72	71.52	71.26	294.4	2391	-14.43	0.14	0.14		
ODP 1063	D8H5W	98	100	71.80	71.54	295.5	2372	-15.90	0.12	0.14		
ODP 1063	D8H5W	128	130	72.10	71.83	297.7	2386	-13.72	0.15	0.15	-13.82	0.10
ODP 1063	D8H5W	128	130	72.10	71.83	297.7	2428	-13.90	0.15	0.27		
ODP 1063	D8H5W	138	140	72.20	71.93	298.5	3993	-13.40	0.18	0.16		
ODP 1063	D8H6W	8	10	72.40	72.12	299.9	2388	-16.01	0.13	0.14		
ODP 1063	D8H6W	38	40	72.70	72.42	302.2	2421	-16.92	0.13	0.27		
*ODP 1063	D8H6W	68	70	73.00	72.74	304.6	1062	-15.37	0.30	0.37		
ODP 1063	D8H6W	84	86	73.16	72.91	306.6	2420	-14.40	0.13	0.27		
*ODP 1063	D8H6W	98	100	73.30	73.06	308.6	1096	-13.19	0.25	0.37		
ODP 1063	D8H6W	110	112	73.42	73.18	310.1	2387	-14.06	0.15	0.15		
*ODP 1063	D8H6W	128	130	73.60	73.35	312.3	1056	-14.77	0.38	0.37		
ODP 1063	D8H6W	143	145	73.75	73.50	314.2	2412	-13.89	0.19	0.27		
*ODP 1063	D8H7W	8	10	73.90	73.64	316.1	1113	-12.69	0.35	0.37		
ODP 1063	B8H3W	14	16	73.76		317.5	2418	-12.50	0.15	0.27		
*ODP 1063	D8H7W	38	40	74.20	73.94	319.8	1071	-13.87	0.36	0.37	-13.52	0.22
*ODP 1063	D8H7W	38	40	74.20	73.94	319.8	1086	-13.33	0.27	0.37		

Site	Label	Top (cm)	Bottom (cm)	Depth (mcd)	Depth (amcd)	Age (ka)	Sample #	ε_{Nd}	Int. 2 SEM	Ext. 2 SD	W. Mean ε_{Nd}	2 SEM
ODP 1063	B8H3W	34	36	73.96		320.2	2088	-13.29	0.08	0.09		
ODP 1063	B8H3W	54	56	74.16		323.6	2080	-14.34	0.11	0.09		
ODP 1063	B8H3W	64	66	74.26		325.3	2425	-14.79	0.16	0.27		
ODP 1063	B8H3W	79	81	74.41		327.7	2075	-15.04	0.08	0.09		
ODP 1063	B8H3W	94	96	74.56		330.0	2430	-15.57	0.16	0.27		
ODP 1063	B8H3W	104	106	74.66		331.5	2086	-16.39	0.09	0.09		
ODP 1063	B8H3W	114	116	74.76		333.2	2410	-16.83	0.18	0.27		
ODP 1063	B8H3W	123	125	74.85		334.6	2101	-14.82	0.10	0.12		
*ODP 1063	D9H1W	8	10	74.50	74.92	335.2	1067	-14.54	0.30	0.37		
ODP 1063	D9H1W	38	40	74.80	75.19	336.8	4311	-11.56	0.07	0.24		
*ODP 1063	D9H1W	40	42	74.82	75.21	336.9	1105	-11.71	0.31	0.37		
*ODP 1063	D9H1W	68	70	75.10	75.46	337.9	1085	-11.25	0.24	0.37		
*ODP 1063	D9H1W	98	100	75.40	75.72	338.4	1074	-11.04	0.34	0.37		
*ODP 1063	D9H1W	128	130	75.70	75.91	338.8	1110	-11.67	0.33	0.37		
*ODP 1063	D9H2W	8	10	76.00	76.12	339.3	1066	-11.81	0.30	0.37		
*ODP 1063	D9H2W	38	40	76.30	76.34	339.8	1054	-11.35	0.35	0.37		
*ODP 1063	D9H2W	68	70	76.60	76.61	340.4	1079	-11.95	0.31	0.37		
ODP 1063	D9H2W	98	100	76.90	76.90	341.1	2399	-11.78	0.11	0.16		
ODP 1063	D9H2W	128	130	77.20		341.7	4018	-12.78	0.11	0.28		
ODP 1063	D9H3W	8	10	77.50		342.5	2402	-11.98	0.15	0.16		
ODP 1063	D9H3W	38	40	77.80		343.2	2407	-11.74	0.16	0.27		
ODP 1063	D9H3W	98	100	78.40		344.6	2393	-11.65	0.11	0.14		
ODP 1063	D9H3W	128	130	78.70		345.3	3994	-12.06	0.18	0.16		

Site	Label	Top (cm)	Bottom (cm)	Depth (mcd)	Depth (amcd)	Age (ka)	Sample #	ε_{Nd}	Int. 2 SEM	Ext. 2 SD	W. Mean ε_{Nd}	2 SEM
ODP 1063	D9H4W	8	10	79.00		346.0	2371	-13.52	0.11	0.14		
ODP 1063	D9H4W	8	10	79.00		346.0	2374	-13.25	0.15	0.15	-13.43	0.09
ODP 1063	D9H4W	38	40	79.30		346.9	2395	-12.58	0.15	0.16		
ODP 1063	D9H4W	70	72	79.62		348.0	2380	-11.80	0.13	0.14		
ODP 1063	D9H4W	98	100	79.90		349.0	2417	-12.95	0.14	0.27		
ODP 1063	D9H4W	128	130	80.20		349.9	2376	-12.55	0.11	0.14		
ODP 1063	D9H5W	38	40	80.80		350.7	3107	-12.86	0.10	0.24		
ODP 1063	D9H5W	104	106	81.46		351.6	3952	-13.34	0.18	0.16		
ODP 1063	D9H6W	8	10	82.00		352.4	3146	-15.10	0.12	0.24	-14.96	0.09
ODP 1063	D9H6W	8	10	82.00		352.4	4053	-14.78	0.13	0.28		
ODP 1063	D9H6W	70	72	82.62		353.2	3564	-14.41	0.16	0.19		
ODP 1063	D9H7W	8	10	83.50		354.5	3111	-15.29	0.13	0.24		
ODP 1063	D10H1W	26	28	84.10	84.04	355.2	3956	-14.10	0.17	0.16		
ODP 1063	D10H1W	86	88	84.70	84.61	356.3	3129	-13.64	0.10	0.24	-13.59	0.08
ODP 1063	D10H1W	86	88	84.70	84.61	356.3	3164	-13.52	0.11	0.24		
ODP 1063	D10H1W	116	118	85.00	84.90	357.2	3161	-13.09	0.11	0.24		
ODP 1063	D10H1W	146	148	85.30	85.27	360.3	3154	-13.55	0.11	0.24		
ODP 1063	D10H2W	26	28	85.60	85.63	363.6	3110	-13.05	0.11	0.24		
ODP 1063	D10H2W	36	38	85.70	85.74	364.6	3149	-13.81	0.13	0.24		
ODP 1063	D10H2W	56	58	85.90	85.93	366.4	3136	-15.45	0.11	0.24		
ODP 1063	D10H2W	86	88	86.20	86.22	368.0	3143	-15.95	0.10	0.24	-16.00	0.09
ODP 1063	D10H2W	86	88	86.20	86.22	368.0	3968	-16.15	0.17	0.16		
ODP 1063	D10H2W	116	118	86.50	86.51	369.5	3118	-13.63	0.13	0.24		

Site	Label	Top (cm)	Bottom (cm)	Depth (mcd)	Depth (amcd)	Age (ka)	Sample #	ε_{Nd}	Int. 2 SEM	Ext. 2 SD	W. Mean ε_{Nd}	2 SEM
ODP 1063	D10H2W	146	148	86.80	86.79	371.4	3117	-14.81	0.12	0.24		
ODP 1063	D10H3W	16	18	87.00	86.99	373.6	3135	-14.19	0.11	0.24		
ODP 1063	D10H3W	26	28	87.10	87.08	374.9	3123	-14.73	0.12	0.24		
ODP 1063	D10H3W	41	43	87.25	87.22	377.0	3140	-15.42	0.13	0.24		
ODP 1063	D10H3W	56	58	87.40	87.37	379.0	3137	-15.40	0.10	0.24		
ODP 1063	D10H3W	71	73	87.55	87.51	381.1	3102	-16.07	0.13	0.24		
ODP 1063	D10H3W	86	88	87.70	87.65	383.1	3126	-15.80	0.09	0.24		
ODP 1063	D10H3W	116	118	88.00	87.92	386.5	4051	-15.67	0.14	0.28		
ODP 1063	D10H3W	146	148	88.30	88.22	388.9	4014	-15.96	0.13	0.28		
ODP 1063	D10H4W	16	18	88.50	88.42	390.5	4040	-12.56	0.13	0.28		
ODP 1063	D10H4W	26	28	88.60	88.52	391.3	2095	-14.27	0.10	0.12		
ODP 1063	D10H4W	46	48	88.80	88.71	392.8	2097	-15.66	0.11	0.12		
*ODP 1063	D10H4W	57	59	88.91	88.82	393.6	1057	-13.68	0.37	0.37		
ODP 1063	D10H4W	66	68	89.00	88.91	394.6	2083	-14.34	0.09	0.09		
ODP 1063	D10H4W	76	78	89.10	89.00	395.7	2091	-15.76	0.11	0.12		
*ODP 1063	D10H4W	86	88	89.20	89.10	396.8	1073	-16.78	0.33	0.37		
ODP 1063	D10H4W	96	98	89.30	89.19	398.6	2085	-15.83	0.09	0.09		
ODP 1063	D10H4W	106	108	89.40	89.29	400.9	2102	-16.33	0.10	0.12		
*ODP 1063	D10H4W	116	118	89.50	89.39	402.3	1089	-16.92	0.33	0.37		
ODP 1063	D10H4W	126	128	89.60	89.48	403.2	2087	-16.31	0.09	0.09		
ODP 1063	D10H4W	136	138	89.70	89.58	404.2	2079	-16.17	0.10	0.09		
*ODP 1063	D10H4W	146	148	89.80	89.67	405.1	1075	-15.73	0.33	0.37		
ODP 1063	D10H5W	6	8	89.90	89.76	406.0	2089	-15.47	0.08	0.09		

Site	Label	Top (cm)	Bottom (cm)	Depth (mcd)	Depth (amcd)	Age (ka)	Sample #	ε_{Nd}	Int. 2 SEM	Ext. 2 SD	W. Mean ε_{Nd}	2 SEM
ODP 1063	D10H5W	16	18	90.00	89.85	407.1	2424	-15.48	0.12	0.27		
*ODP 1063	D10H5W	26	28	90.10	89.94	408.9	1109	-15.53	0.31	0.37		
ODP 1063	D10H5W	36	38	90.20	90.04	410.8	2077	-15.81	0.09	0.09		
ODP 1063	D10H5W	46	48	90.30	90.14	412.9	2078	-16.19	0.10	0.09		
*ODP 1063	D10H5W	56	58	90.40	90.24	415.0	1092	-15.85	0.29	0.37		
ODP 1063	D10H5W	58	59	90.42	90.26	415.5	2096	-16.22	0.12	0.12		
ODP 1063	D10H5W	66	68	90.50	90.34	417.2	2100	-16.84	0.11	0.12		
ODP 1063	D10H5W	76	78	90.60	90.44	419.5	2074	-16.48	0.12	0.09		
ODP 1063	D10H5W	81	82	90.65	90.49	420.7	2073	-16.77	0.09	0.09	-16.67	0.07
ODP 1063	D10H5W	81	82	90.65	90.49	420.7	2076	-16.54	0.10	0.09		
*ODP 1063	D10H5W	86	88	90.70	90.54	421.6	1082	-16.85	0.31	0.37	-16.87	0.08
ODP 1063	D10H5W	86	88	90.70	90.54	421.6	2090	-16.87	0.10	0.09		
ODP 1063	D10H5W	86	88	90.70	90.54	421.6	2802	-16.89	0.12	0.17		
ODP 1063	D10H5W	96	98	90.80	90.64	423.0	2092	-16.34	0.10	0.12		
ODP 1063	D10H5W	106	108	90.90	90.74	424.4	2084	-15.47	0.10	0.09		
*ODP 1063	D10H5W	116	118	91.00	90.84	426.1	1114	-14.83	0.33	0.37		
ODP 1063	D10H5W	122	124	91.06	90.90	427.5	2434	-13.14	0.14	0.27		
ODP 1063	D10H5W	126	128	91.10	90.94	428.4	2081	-11.87	0.11	0.09		
ODP 1063	D10H5W	136	138	91.20	91.05	429.6	2098	-12.50	0.12	0.12		
*ODP 1063	D10H5W	146	148	91.30	91.15	430.5	1095	-11.63	0.31	0.37		
ODP 1063	D10H6W	6	8	91.40	91.25	431.8	2082	-11.83	0.11	0.09		
*ODP 1063	D10H6W	26	28	91.60	91.46	437.0	1068	-11.72	0.28	0.37		
*ODP 1063	D10H6W	56	58	91.90	91.76	441.8	1060	-11.59	0.26	0.37		

Site	Label	Top (cm)	Bottom (cm)	Depth (mcd)	Depth (amcd)	Age (ka)	Sample #	ε_{Nd}	Int. 2 SEM	Ext. 2 SD	W. Mean ε_{Nd}	2 SEM
*ODP 1063	D10H6W	86	88	92.20	92.06	443.4	1078	-11.83	0.34	0.37		
*ODP 1063	D10H6W	116	118	92.50	92.36	444.8	1112	-12.02	0.29	0.37		
ODP 1063	D10H6W	146	148	92.80	92.66	446.3	2409	-11.39	0.13	0.27		
ODP 1063	D10H7W	26	28	93.10	92.96	447.7	2405	-11.69	0.14	0.27		
ODP 1063	D11H1W	10	12	93.40		449.8	2403	-11.79	0.16	0.27		
ODP 1063	D11H1W	40	42	93.70		451.6	3988	-11.87	0.19	0.16		
ODP 1063	D11H1W	70	72	94.00		454.1	3130	-11.97	0.14	0.24		
ODP 1063	D11H1W	100	102	94.30		456.6	3937	-12.49	0.16	0.16		
ODP 1063	D11H1W	130	132	94.60		458.8	3127	-12.15	0.12	0.24		
ODP 1063	D11H2W	10	12	94.90		459.5	4292	-12.24	0.09	0.24		
ODP 1063	D11H2W	70	72	95.50		460.6	3112	-12.15	0.13	0.24		
ODP 1063	D11H2W	100	102	95.80		461.2	3943	-12.77	0.17	0.16		
ODP 1063	D11H3W	20	22	96.50		462.5	3109	-12.80	0.12	0.24		
ODP 1063	D11H3W	72	74	97.02		463.5	4003	-12.84	0.14	0.28		
ODP 1063	D11H3W	130	132	97.60		464.5	3121	-14.42	0.11	0.24		
ODP 1063	D11H4W	70	72	98.50		465.6	3963	-13.19	0.19	0.16		
ODP 1063	D11H5W	10	12	99.40		466.7	3142	-14.48	0.10	0.24		
ODP 1063	D11H5W	72	74	100.02		467.4	3105	-14.08	0.12	0.24		
ODP 1063	D11H5W	100	102	100.30		468.4	4308	-13.97	0.08	0.24		
ODP 1063	D11H5W	130	132	100.60		469.5	3160	-13.93	0.11	0.24		
ODP 1063	D11H6W	10	12	100.90		470.5	4043	-13.69	0.16	0.28		
ODP 1063	D11H6W	70	72	101.50		471.4	3138	-15.34	0.12	0.24		

Site	Label	Top (cm)	Bottom (cm)	Depth (mcd)	Depth (amcd)	Age (ka)	Sample #	ε_{Nd}	Int. 2 SEM	Ext. 2 SD	W. Mean ε_{Nd}	2 SEM
ODP 1063	C11H6W	24	26	102.42		472.6	3252	-16.68	0.12	0.16	-16.55	0.07
ODP 1063	C11H6W	24	26	102.42		472.6	4285	-16.47	0.09	0.24		
ODP 1063	C11H6W	110	112	103.28		474.0	3139	-15.04	0.12	0.24		
ODP 1063	D12H1W	54	56	104.20		475.7	3153	-15.50	0.10	0.24		
ODP 1063	D12H1W	114	116	104.80		476.8	3106	-13.43	0.14	0.24		
ODP 1063	D12H2W	24	26	105.40		477.9	3978	-14.68	0.17	0.16		
ODP 1063	D12H2W	58	60	105.74		478.9	4064	-16.72	0.12	0.28		
ODP 1063	D12H2W	84	86	106.00		479.9	3124	-14.18	0.11	0.24		
ODP 1063	D12H2W	114	116	106.30		480.9	3125	-14.04	0.11	0.24		
ODP 1063	D12H2W	144	146	106.60		482.0	3982	-15.59	0.20	0.16		
ODP 1063	D12H3W	24	26	106.90		483.1	4032	-15.23	0.11	0.28		
ODP 1063	D12H3W	54	56	107.20		484.4	3152	-17.32	0.13	0.24		
ODP 1063	D12H3W	84	86	107.50		489.7	3162	-21.46	0.11	0.24	-21.22	0.06
ODP 1063	D12H3W	84	86	107.50		489.7	4057	-21.05	0.14	0.28		
ODP 1063	D12H3W	84	86	107.50		489.7	4283	-21.13	0.09	0.24		
ODP 1063	D12H3W	114	116	107.80	107.81	493.2	3148	-15.68	0.18	0.24		
ODP 1063	D12H3W	144	146	108.10	108.13	496.6	3145	-15.46	0.13	0.24		
ODP 1063	D12H4W	24	26	108.40	108.45	500.3	3134	-17.23	0.10	0.24		
ODP 1063	D12H4W	54	56	108.70	108.77	505.0	3158	-17.48	0.12	0.24		
ODP 1063	D12H4W	84	86	109.00	109.08	508.0	3974	-15.57	0.19	0.16		
ODP 1063	D12H4W	114	116	109.30	109.39	510.6	3122	-15.89	0.13	0.24		
ODP 1063	D12H4W	144	146	109.60	109.70	516.6	3163	-15.98	0.12	0.24		
ODP 1063	D12H5W	24	26	109.90	110.01	519.2	3953	-17.25	0.19	0.16		

Site	Label	Top (cm)	Bottom (cm)	Depth (mcd)	Depth (amcd)	Age (ka)	Sample #	ε_{Nd}	Int. 2 SEM	Ext. 2 SD	W. Mean ε_{Nd}	2 SEM
ODP 1063	D12H5W	54	56	110.20	110.32	521.8	3133	-17.50	0.14	0.24		
ODP 1063	D12H5W	84	86	110.50	110.64	523.6	3973	-18.31	0.19	0.16		
ODP 1063	D12H5W	114	116	110.80	110.96	526.8	3120	-16.12	0.12	0.24		
ODP 1063	D12H5W	144	146	111.10	111.23	529.0	3150	-15.62	0.12	0.24		
ODP 1063	D12H6W	19	21	111.40	111.51	531.0	3992	-16.04	0.20	0.16		
ODP 1063	D12H6W	49	51	111.70	111.78	532.9	3155	-15.93	0.12	0.24		
ODP 1063	D12H6W	79	81	112.00	112.06	534.9	3972	-15.09	0.17	0.16		
ODP 1063	D12H6W	109	111	112.30	112.33	536.9	3157	-15.83	0.12	0.24		
ODP 1063	D12H6W	139	141	112.60		539.2	3156	-15.95	0.11	0.24		
ODP 1063	D12H7W	19	21	112.90		542.0	3977	-16.61	0.17	0.16		
ODP 1063	D12H7W	50	52	113.21		544.2	3104	-16.53	0.11	0.24		
ODP 1063	C12H6W	96	98	113.50	113.40	545.2	3981	-16.13	0.16	0.16		
ODP 1063	C12H6W	126	128	113.80	113.68	546.9	3101	-14.33	0.12	0.24		
ODP 1063	C12H7W	6	8	114.10	113.96	550.4	3114	-14.94	0.11	0.24		
ODP 1063	D13H1W	29	31	114.40		552.3	4029	-13.89	0.13	0.28		
ODP 1063	D13H1W	59	61	114.70		553.2	3949	-14.90	0.17	0.16		
ODP 1063	D13H1W	89	91	115.00		554.6	3119	-15.57	0.10	0.24		
ODP 1063	D13H1W	119	121	115.30		559.4	3103	-14.76	0.10	0.24	-14.74	0.08
ODP 1063	D13H1W	119	121	115.30		559.4	3147	-14.73	0.13	0.24		
ODP 1063	D13H2W	24	26	115.60		561.9	3132	-16.23	0.11	0.24		
ODP 1063	D13H2W	54	56	115.90		564.0	3979	-12.66	0.18	0.16	-12.75	0.07
ODP 1063	D13H2W	54	56	115.90		564.0	4304	-12.77	0.08	0.24		
ODP 1063	D13H2W	84	86	116.20		566.6	3141	-15.27	0.12	0.24		

Site	Label	Top (cm)	Bottom (cm)	Depth (mcd)	Depth (amcd)	Age (ka)	Sample #	ε_{Nd}	Int. 2 SEM	Ext. 2 SD	W. Mean ε_{Nd}	2 SEM
ODP 1063	D13H2W	114	116	116.50		575.3	3115	-16.37	0.11	0.24		
ODP 1063	D13H3W	24	26	117.10		580.6	2373	-15.22	0.11	0.14		
ODP 1063	D13H3W	54	56	117.40		583.2	2398	-13.21	0.17	0.17		
ODP 1063	D13H3W	84	86	117.70		585.5	2433	-13.99	0.14	0.27		
ODP 1063	D13H3W	114	116	118.00		587.4	2397	-13.30	0.14	0.16		
ODP 1063	D13H3W	144	146	118.30		589.0	2423	-17.34	0.13	0.27		
ODP 1063	D13H3W	144	146	118.30		589.0	4034	-16.90	0.15	0.28	-17.31	0.07
ODP 1063	D13H3W	144	146	118.30		589.0	4481	-17.43	0.09	0.12		
ODP 1063	D13H4W	24	26	118.60		590.9	2378	-13.06	0.14	0.14		
ODP 1063	D13H4W	54	56	118.90		593.1	2415	-15.75	0.13	0.27		
*ODP 1063	D13H4W	84	86	119.20		596.3	1065	-13.05	0.33	0.37		
ODP 1063	D13H4W	99	101	119.35		597.9	2432	-14.77	0.14	0.27		
*ODP 1063	D13H4W	114	116	119.50		599.6	1064	-14.51	0.31	0.37		
*ODP 1063	D13H4W	144	146	119.80		602.9	1107	-14.45	0.26	0.37		
ODP 1063	D13H5W	9	11	119.95		604.6	2413	-14.36	0.14	0.27		
*ODP 1063	D13H5W	24	26	120.10		607.5	1088	-14.55	0.35	0.37		
ODP 1063	D13H5W	34	36	120.20		609.9	2406	-14.47	0.14	0.27		
ODP 1063	D13H5W	44	46	120.30		612.2	2422	-15.94	0.13	0.27		
*ODP 1063	D13H5W	54	56	120.40		614.4	1051	-15.31	0.31	0.37		
ODP 1063	D13H5W	66	68	120.52		616.7	2416	-15.35	0.12	0.27		
ODP 1063	D13H5W	74	76	120.60		618.0	2427	-14.22	0.13	0.27		
*ODP 1063	D13H5W	84	86	120.70		619.6	1093	-13.63	0.32	0.37		
ODP 1063	D13H5W	99	101	120.85		621.2	2419	-10.97	0.12	0.27		

Site	Label	Top (cm)	Bottom (cm)	Depth (mcd)	Depth (amcd)	Age (ka)	Sample #	ε_{Nd}	Int. 2 SEM	Ext. 2 SD	W. Mean ε_{Nd}	2 SEM
*ODP 1063	D13H5W	114	116	121.00		622.2	1053	-11.74	0.35	0.37		
*ODP 1063	D13H5W	144	146	121.30		626.1	1106	-11.34	0.32	0.37		
*ODP 1063	D13H5W	144	146	121.30		626.1	1108	-11.84	0.37	0.37		
ODP 1063	D13H5W	144	146	121.30		626.1	2072	-11.68	0.09	0.09		
ODP 1063	D13H5W	144	146	121.30		626.1	2408	-11.63	0.15	0.27		
ODP 1063	D13H5W	144	146	121.30		626.1	2765	-11.66	0.06	0.31		
ODP 1063	D13H5W	144	146	121.30		626.1	2987	-11.65	0.08	0.20		
ODP 1063	D13H5W	144	146	121.30		626.1	3116	-11.54	0.12	0.24		
ODP 1063	D13H5W	144	146	121.30		626.1	3273	-11.78	0.15	0.16		
ODP 1063	D13H5W	144	146	121.30		626.1	3576	-11.76	0.17	0.19	-11.68	0.03
ODP 1063	D13H5W	144	146	121.30		626.1	3967	-11.91	0.17	0.16		
ODP 1063	D13H5W	144	146	121.30		626.1	4062	-11.42	0.12	0.28		
ODP 1063	D13H5W	144	146	121.30		626.1	4307	-11.69	0.08	0.24		
ODP 1063	D13H5W	144	146	121.30		626.1	4496	-11.76	0.09	0.12		
ODP 1063	D13H5W	144	146	121.30		626.1	4792	-11.77	0.08	0.18		
ODP 1063	D13H5W	144	146	121.30		626.1	5027	-11.70	0.10	0.13		
ODP 1063	D13H5W	144	146	121.30		626.1	5080	-11.53	0.12	0.18		
ODP 1063	D13H5W	144	146	121.30		626.1	5141	-11.71	0.17	0.27		
*ODP 1063	D13H6W	24	26	121.60		627.7	1081	-11.41	0.27	0.37		
*ODP 1063	D13H6W	54	56	121.90		628.6	1101	-11.45	0.26	0.37		
*ODP 1063	D13H6W	84	86	122.20		628.9	1061	-11.58	0.31	0.37		
*ODP 1063	D13H6W	114	116	122.50		629.3	1100	-11.97	0.38	0.37		
*ODP 1063	D13H6W	144	146	122.80		629.7	1098	-11.75	0.31	0.37		

Site	Label	Top (cm)	Bottom (cm)	Depth (mcd)	Depth (amcd)	Age (ka)	Sample #	ε_{Nd}	Int. 2 SEM	Ext. 2 SD	W. Mean ε_{Nd}	2 SEM
ODP 1063	C13H6W	140	142	123.70		630.6	2377	-11.47	0.14	0.14		
ODP 1063	D14H1W	14	16	124.30		631.0	2392	-11.63	0.11	0.14		
ODP 1063	D14H1W	104	106	125.20		631.7	2383	-11.51	0.13	0.14		
ODP 1063	D14H1W	134	136	125.50		632.6	2381	-11.42	0.14	0.14		
ODP 1063	D14H2W	14	16	125.80		634.0	2389	-12.05	0.14	0.14		
ODP 1063	D14H2W	44	46	126.10		635.1	2401	-12.52	0.14	0.16		
ODP 1063	D14H2W	74	76	126.40		635.9	2375	-12.09	0.12	0.14		
ODP 1063	D14H2W	104	106	126.70		636.6	2429	-11.89	0.14	0.27		
ODP 1063	D14H2W	134	136	127.00		637.1	2431	-11.81	0.14	0.27		
ODP 1063	D14H3W	44	46	127.60		638.1	2414	-12.03	0.17	0.27		
ODP 1063	D14H3W	74	76	127.90		639.3	2384	-11.89	0.13	0.14		
ODP 1063	D14H3W	104	106	128.20		641.1	3286	-12.73	0.14	0.16		
ODP 1063	D14H3W	134	136	128.50		642.8	3270	-13.59	0.12	0.16		
ODP 1063	D14H4W	14	16	128.80		644.4	3268	-13.32	0.14	0.16		
ODP 1063	D14H4W	44	46	129.10		646.0	3261	-13.00	0.11	0.16		
ODP 1063	D14H4W	74	76	129.40		647.6	3287	-13.90	0.12	0.16		
ODP 1063	D14H4W	104	106	129.70		649.3	3280	-12.73	0.10	0.16		
ODP 1063	D14H4W	134	136	130.00		652.2	3294	-13.21	0.09	0.16		
ODP 1063	D14H5W	14	16	130.30		655.9	3290	-13.63	0.13	0.16		
ODP 1063	D14H5W	44	46	130.60		658.1	3281	-13.07	0.09	0.16		
ODP 1063	D14H5W	74	76	130.90		661.0	3253	-12.80	0.12	0.16		
ODP 1063	D14H5W	104	106	131.20		664.2	3282	-13.59	0.12	0.16		
ODP 1063	D14H5W	134	136	131.50		666.0	3249	-13.02	0.12	0.16		

Site	Label	Top (cm)	Bottom (cm)	Depth (mcd)	Depth (amcd)	Age (ka)	Sample #	ε_{Nd}	Int. 2 SEM	Ext. 2 SD	W. Mean ε_{Nd}	2 SEM
ODP 1063	D14H6W	14	16	131.80		668.0	3271	-13.19	0.09	0.16		
ODP 1063	D14H6W	44	46	132.10		669.9	3262	-14.30	0.11	0.16		
ODP 1063	D14H6W	74	76	132.40		672.0	3283	-13.66	0.13	0.16	-13.57	0.08
ODP 1063	D14H6W	74	76	132.40		672.0	3297	-13.50	0.11	0.16		
ODP 1063	D14H6W	104	106	132.70		673.5	3241	-14.72	0.14	0.16		
ODP 1063	D14H6W	134	136	133.00		674.7	4008	-13.10	0.15	0.28	-13.03	0.10
ODP 1063	D14H6W	134	136	133.00		674.7	4015	-12.96	0.15	0.28		
ODP 1063	D14H7W	14	16	133.30		676.2	3265	-14.96	0.12	0.16		
ODP 1063	D14H7W	44	46	133.60		677.6	3276	-13.46	0.12	0.16		
ODP 1063	C14H6W	23	25	133.89		678.5	4298	-15.41	0.08	0.24		
ODP 1063	C14H6W	53	55	134.19		679.7	3244	-15.32	0.10	0.16		
ODP 1063	C14H6W	83	85	134.49		681.7	3020	-14.25	0.11	0.12		
ODP 1063	C14H6W	113	115	134.79		683.7	4257	-14.53	0.13	0.24		
ODP 1063	D15H1W	2	4	135.10		684.9	3257	-13.38	0.11	0.16		
ODP 1063	D15H1W	62	64	135.70		686.4	3002	-14.47	0.14	0.12		
ODP 1063	D15H1W	92	94	136.00		687.1	4058	-13.60	0.12	0.28		
ODP 1063	D15H2W	32	34	136.90		688.3	3284	-15.32	0.13	0.16		
ODP 1063	D15H2W	62	64	137.20		689.2	4023	-12.96	0.15	0.28		
ODP 1063	D15H2W	92	94	137.50		690.0	3024	-13.45	0.10	0.12	-13.45	0.06
ODP 1063	D15H2W	92	94	137.50		690.0	4310	-13.44	0.08	0.24		
ODP 1063	D15H2W	122	124	137.80		693.3	3247	-19.23	0.13	0.16	-19.00	0.08
ODP 1063	D15H2W	122	124	137.80		693.3	4273	-18.87	0.10	0.24		
ODP 1063	D15H3W	2	4	138.10		695.4	2970	-17.49	0.12	0.20		

Site	Label	Top (cm)	Bottom (cm)	Depth (mcd)	Depth (amcd)	Age (ka)	Sample #	ε_{Nd}	Int. 2 SEM	Ext. 2 SD	W. Mean ε_{Nd}	2 SEM
ODP 1063	D15H3W	32	34	138.40		703.4	2980	-16.58	0.08	0.20		
ODP 1063	D15H3W	62	64	138.70		711.9	2988	-14.52	0.11	0.20		
ODP 1063	D15H3W	92	94	139.00		715.1	2977	-12.15	0.09	0.20		
ODP 1063	D15H3W	122	124	139.30		716.6	4268	-11.84	0.12	0.24		
ODP 1063	D15H4W	2	4	139.60		717.9	3007	-12.25	0.10	0.12		
ODP 1063	D15H4W	32	34	139.90		719.3	3298	-12.08	0.09	0.16		
ODP 1063	D15H4W	62	64	140.20		720.4	3004	-12.06	0.11	0.12		
ODP 1063	D15H4W	92	94	140.50		721.6	3954	-12.08	0.17	0.16		
ODP 1063	D15H4W	122	124	140.80		722.4	4063	-12.34	0.15	0.28		
ODP 1063	D15H5W	2	4	141.10		723.1	3017	-12.70	0.12	0.12		
ODP 1063	D15H5W	62	64	141.70		724.2	4002	-12.09	0.13	0.28		
ODP 1063	D15H5W	92	94	142.00		724.8	3254	-13.11	0.12	0.16		
ODP 1063	D15H6W	2	4	142.60		725.9	2998	-14.71	0.11	0.20		
ODP 1063	D15H6W	32	34	142.90		727.9	2962	-16.15	0.11	0.20		
ODP 1063	D15H6W	62	64	143.20		730.2	3005	-15.99	0.12	0.12		
ODP 1063	D15H6W	92	94	143.50		733.0	2961	-15.68	0.14	0.20		
ODP 1063	D15H6W	122	124	143.80		736.6	3006	-16.02	0.11	0.12		
ODP 1063	D15H7W	2	4	144.10		740.3	2978	-13.80	0.10	0.20		
ODP 1063	D15H7W	32	34	144.40		741.9	3245	-13.49	0.11	0.16		
ODP 1063	D15H7W	62	64	144.70		743.2	3009	-14.14	0.11	0.12		
ODP 1063	B15H3W	4	6	145.00		744.5	3011	-14.21	0.13	0.12		
ODP 1063	B15H3W	34	36	145.30		745.9	2994	-14.40	0.08	0.20		

Site	Label	Top (cm)	Bottom (cm)	Depth (mcd)	Depth (amcd)	Age (ka)	Sample #	ε_{Nd}	Int. 2 SEM	Ext. 2 SD	W. Mean ε_{Nd}	2 SEM
ODP 1063	B15H3W	64	66	145.60		747.4	4004	-13.73	0.12	0.28	-13.65	0.08
ODP 1063	B15H3W	64	66	145.60		747.4	4012	-13.57	0.12	0.28		
ODP 1063	B15H3W	94	96	145.90		748.9	3015	-13.13	0.11	0.12		
ODP 1063	D16H1W	16	18	146.20		750.6	3292	-13.22	0.12	0.16		
ODP 1063	D16H1W	76	78	146.80		752.6	3243	-13.55	0.11	0.16		
ODP 1063	D16H1W	106	108	147.10		753.3	4024	-14.01	0.14	0.28		
ODP 1063	D16H1W	136	138	147.40		754.0	3299	-13.78	0.10	0.16		
ODP 1063	D16H2W	16	18	147.70		754.7	4016	-14.18	0.14	0.28		
ODP 1063	D16H2W	46	48	148.00		756.4	3295	-14.79	0.11	0.16		
ODP 1063	D16H2W	76	78	148.30		758.6	3289	-14.83	0.11	0.16		
ODP 1063	D16H2W	106	108	148.60		760.2	3272	-12.61	0.12	0.16		
ODP 1063	D16H2W	136	138	148.90		761.8	3934	-15.43	0.16	0.16	-15.22	0.09
ODP 1063	D16H2W	136	138	148.90		761.8	4261	-15.12	0.11	0.24		
ODP 1063	D16H3W	16	18	149.20		763.4	3266	-12.96	0.10	0.16	-12.88	0.06
ODP 1063	D16H3W	16	18	149.20		763.4	3958	-13.16	0.18	0.16		
ODP 1063	D16H3W	16	18	149.20		763.4	4288	-12.75	0.09	0.24		
ODP 1063	D16H3W	46	48	149.50		765.2	3964	-16.08	0.18	0.16	-15.99	0.07
ODP 1063	D16H3W	46	48	149.50		765.2	4279	-15.97	0.08	0.24		
ODP 1063	D16H3W	76	78	149.80		768.6	3291	-13.35	0.12	0.16	-13.40	0.10
ODP 1063	D16H3W	76	78	149.80		768.6	3957	-13.54	0.21	0.16		
ODP 1063	D16H3W	106	108	150.10		773.2	2973	-14.55	0.15	0.20	-14.61	0.07
ODP 1063	D16H3W	106	108	150.10		773.2	3013	-14.63	0.09	0.12		
ODP 1063	D16H3W	136	138	150.40		777.8	2992	-16.30	0.10	0.20		

Site	Label	Top (cm)	Bottom (cm)	Depth (mcd)	Depth (amcd)	Age (ka)	Sample #	ε_{Nd}	Int. 2 SEM	Ext. 2 SD	W. Mean ε_{Nd}	2 SEM
ODP 1063	D16H4W	16	18	150.70		783.6	3000	-16.89	0.13	0.20		
ODP 1063	D16H4W	46	48	151.00		785.8	4314	-11.79	0.10	0.24		
ODP 1063	D16H4W	76	78	151.30		786.3	2993	-11.49	0.12	0.20		
ODP 1063	D16H4W	106	108	151.60		786.7	4001	-10.76	0.11	0.28		
ODP 1063	D16H4W	136	138	151.90		787.1	3959	-11.49	0.17	0.16		
ODP 1063	D16H5W	16	18	152.20		787.7	4028	-11.05	0.13	0.28		
ODP 1063	D16H5W	46	48	152.50		789.3	2975	-11.73	0.14	0.20	-11.58	0.11
ODP 1063	D16H5W	46	48	152.50		789.3	3563	-11.37	0.18	0.19		
ODP 1063	D16H5W	76	78	152.80		791.0	2983	-11.59	0.12	0.20		
ODP 1063	D16H5W	106	108	153.10		794.2	3966	-11.71	0.15	0.16		
ODP 1063	D16H5W	136	138	153.40		795.1	2965	-12.12	0.10	0.20		
ODP 1063	D16H6W	106	108	154.60		796.1	3021	-13.16	0.12	0.12	-12.91	0.07
ODP 1063	D16H6W	106	108	154.60		796.1	4041	-12.72	0.13	0.28		
ODP 1063	D16H6W	106	108	154.60		796.1	4049	-12.83	0.12	0.28		
ODP 1063	C17H1W	56	58	155.20		797.6	4290	-14.31	0.10	0.24		
ODP 1063	C17H1W	86	88	155.50		798.3	3010	-13.84	0.13	0.12		
ODP 1063	D17H1W	58	60	156.10		799.7	4055	-13.82	0.13	0.28		
ODP 1063	D17H1W	88	90	156.40		800.4	3264	-13.59	0.12	0.16		
ODP 1063	D17H1W	118	120	156.70		801.0	4255	-13.59	0.12	0.24		
ODP 1063	D17H1W	148	150	157.00		804.2	3246	-13.34	0.11	0.16		
ODP 1063	D17H2W	29	31	157.31		811.4	3250	-13.75	0.29	0.16	-13.79	0.13
ODP 1063	D17H2W	29	31	157.31		811.4	3591	-13.80	0.15	0.19		
ODP 1063	D17H2W	58	60	157.60		815.0	2799	-15.15	0.11	0.17		

Site	Label	Top (cm)	Bottom (cm)	Depth (mcd)	Depth (amcd)	Age (ka)	Sample #	ε_{Nd}	Int. 2 SEM	Ext. 2 SD	W. Mean ε_{Nd}	2 SEM
ODP 1063	D17H2W	88	90	157.90		816.7	3976	-15.18	0.21	0.16		
ODP 1063	D17H2W	118	120	158.20		818.7	3936	-14.23	0.18	0.16		
ODP 1063	D17H2W	147	149	158.49		824.3	2808	-13.04	0.10	0.17		
ODP 1063	D17H3W	28	30	158.80		834.3	2805	-15.81	0.09	0.17		
ODP 1063	D17H3W	58	60	159.10		847.2	2796	-16.31	0.10	0.17		
ODP 1063	D17H3W	88	90	159.40		850.7	3008	-14.01	0.10	0.12		
ODP 1063	D17H3W	118	120	159.70		851.6	4256	-12.70	0.11	0.24		
ODP 1063	D17H3W	148	150	160.00		852.4	2999	-14.40	0.12	0.20		
ODP 1063	D17H4W	28	30	160.30		853.3	4312	-15.00	0.09	0.24		
*ODP 1063	D17H4W	118	120	161.20		855.0	1076	-13.24	0.31	0.37		
*ODP 1063	D17H4W	148	150	161.50		855.4	1069	-13.86	0.33	0.37		
ODP 1063	C17H5W	86	88	161.50		855.4	2755	-13.96	0.12	0.12	-14.01	0.07
ODP 1063	C17H5W	86	88	161.50		855.4	2761	-14.05	0.08	0.31		
ODP 1063	C17H5W	116	118	161.80		856.2	2806	-13.87	0.09	0.17		
ODP 1063	C17H5W	146	148	162.10		859.6	2801	-14.72	0.10	0.17		
ODP 1063	A17H3W	6	8	162.40		866.5	2772	-11.45	0.07	0.31		
ODP 1063	A17H3W	37	39	162.71		869.6	2779	-11.06	0.15	0.12		
ODP 1063	A17H3W	64	66	162.98		869.9	2783	-10.82	0.09	0.18		
ODP 1063	A17H3W	95	97	163.29		870.2	2769	-11.00	0.08	0.31		
*ODP 1063	D17H6W	28	30	163.30		870.2	1097	-10.65	0.27	0.37		
*ODP 1063	D17H6W	58	60	163.60		870.4	1077	-11.76	0.30	0.37		
*ODP 1063	D17H6W	88	90	163.90		870.6	1102	-11.20	0.27	0.37		
*ODP 1063	D17H6W	118	120	164.20		870.9	1087	-10.87	0.37	0.37		

Site	Label	Top (cm)	Bottom (cm)	Depth (mcd)	Depth (amcd)	Age (ka)	Sample #	ε_{Nd}	Int. 2 SEM	Ext. 2 SD	W. Mean ε_{Nd}	2 SEM
*ODP 1063	D17H6W	148	150	164.50		871.1	1072	-10.88	0.45	0.37		
ODP 1063	D18H1W	38	40	165.10		872.1	2757	-11.22	0.15	0.12		
ODP 1063	D18H1W	68	70	165.40		873.1	2751	-11.28	0.14	0.12		
ODP 1063	D18H1W	98	100	165.70		874.1	4013	-10.69	0.12	0.28		
ODP 1063	D18H1W	128	130	166.00		875.1	3986	-11.26	0.17	0.16		
ODP 1063	D18H2W	8	10	166.30		876.4	2809	-10.81	0.10	0.17		
ODP 1063	D18H2W	38	40	166.60		878.2	4061	-11.91	0.17	0.28		
ODP 1063	D18H2W	68	70	166.90		879.3	3300	-10.07	0.11	0.16		
ODP 1063	D18H3W	8	10	167.80		880.1	4287	-10.44	0.09	0.24		
ODP 1063	C18H3W	70	72	168.40		880.7	2810	-10.64	0.10	0.17		
ODP 1063	C18H3W	100	102	168.70		881.0	3984	-11.22	0.31	0.16		
ODP 1063	C18H4W	10	12	169.30		881.7	3293	-11.01	0.11	0.16		
ODP 1063	C18H4W	40	42	169.60		882.9	3938	-10.85	0.16	0.16		
ODP 1063	C18H4W	70	72	169.90		884.5	2797	-11.10	0.10	0.17		
ODP 1063	C18H4W	100	102	170.20		886.1	3990	-11.03	0.21	0.16		
ODP 1063	C18H4W	130	132	170.50		887.8	4045	-11.10	0.13	0.28		
ODP 1063	C18H5W	10	12	170.80		889.4	2778	-11.87	0.15	0.12		
ODP 1063	C18H5W	40	42	171.10		891.0	3948	-12.08	0.17	0.16		
ODP 1063	C18H5W	70	72	171.40		892.7	4059	-12.74	0.11	0.28		
ODP 1063	C18H5W	100	102	171.70		894.2	2752	-13.52	0.14	0.12		
ODP 1063	C18H5W	130	132	172.00		895.6	3960	-13.97	0.16	0.16		
ODP 1063	C18H6W	10	12	172.30		899.1	2760	-13.85	0.15	0.12		
ODP 1063	C18H6W	40	42	172.60		902.5	2964	-14.52	0.10	0.20		

Site	Label	Top (cm)	Bottom (cm)	Depth (mcd)	Depth (amcd)	Age (ka)	Sample #	ε_{Nd}	Int. 2 SEM	Ext. 2 SD	W. Mean ε_{Nd}	2 SEM
ODP 1063	B18H2W	56	58	172.90		904.5	2773	-14.40	0.07	0.31		
ODP 1063	B18H2W	86	88	173.20		905.5	2985	-15.25	0.14	0.20		
ODP 1063	B18H2W	116	118	173.50		906.6	2971	-15.95	0.11	0.20		
ODP 1063	B18H2W	146	148	173.80		907.7	2767	-15.92	0.07	0.31		
ODP 1063	B18H3W	26	28	174.10		909.0	2982	-14.99	0.13	0.20		
ODP 1063	B18H3W	56	58	174.40		910.4	3019	-13.93	0.11	0.12		
ODP 1063	B18H3W	86	88	174.70		911.8	3931	-15.18	0.17	0.16	-15.16	0.12
ODP 1063	B18H3W	86	88	174.70		911.8	3935	-15.15	0.17	0.16		
ODP 1063	B18H3W	116	118	175.00		913.1	2781	-16.55	0.09	0.18	-16.50	0.07
ODP 1063	B18H3W	116	118	175.00		913.1	2990	-16.44	0.10	0.20		
ODP 1063	B18H3W	146	148	175.30		914.5	2995	-14.24	0.10	0.20		
ODP 1063	B18H4W	26	28	175.60		915.3	4020	-13.68	0.16	0.28		
ODP 1063	B18H4W	86	88	176.20		916.4	2803	-13.84	0.11	0.17		
ODP 1063	B18H4W	146	148	176.80		917.4	2968	-14.02	0.11	0.20		
ODP 1063	B18H5W	26	28	177.10		917.8	3016	-14.08	0.12	0.12		
ODP 1063	B18H5W	86	88	177.70		918.8	2979	-14.19	0.11	0.20		
ODP 1063	B18H5W	146	148	178.30		919.8	2813	-14.56	0.11	0.17		
ODP 1063	B18H6W	26	28	178.60		920.7	2972	-15.30	0.12	0.20		
ODP 1063	B18H6W	56	58	178.90		923.5	2811	-13.21	0.09	0.17		
ODP 1063	B18H6W	86	88	179.20		926.3	2996	-14.82	0.09	0.20		
ODP 1063	C19H4W	88	90	179.50		929.1	2775	-16.41	0.22	0.12	-16.13	0.11
ODP 1063	C19H4W	88	90	179.50		929.1	4027	-16.03	0.13	0.28		
ODP 1063	C19H4W	118	120	179.80		931.9	3932	-16.14	0.14	0.16		

Site	Label	Top (cm)	Bottom (cm)	Depth (mcd)	Depth (amcd)	Age (ka)	Sample #	ε_{Nd}	Int. 2 SEM	Ext. 2 SD	W. Mean ε_{Nd}	2 SEM
ODP 1063	C19H4W	148	150	180.10		934.4	2814	-13.22	0.11	0.17		
ODP 1063	C19H5W	58	60	180.70		937.2	2758	-13.85	0.14	0.12		
ODP 1063	C19H5W	88	90	181.00		938.5	4278	-15.07	0.11	0.24		
ODP 1063	C19H5W	118	120	181.30		939.9	3989	-14.63	0.19	0.16		
ODP 1063	C19H5W	148	150	181.60		941.2	2770	-16.13	0.07	0.31		
ODP 1063	C19H6W	58	60	182.20		943.9	3933	-17.40	0.17	0.16		
ODP 1063	C19H6W	88	90	182.50		945.2	2768	-16.70	0.08	0.31	-16.64	0.07
ODP 1063	C19H6W	88	90	182.50		945.2	4277	-16.54	0.11	0.24		
ODP 1063	C19H6W	118	120	182.80		946.5	3965	-18.16	0.18	0.16		
ODP 1063	B19H2W	70	72	183.10		947.8	3944	-18.37	0.19	0.16		
ODP 1063	B19H2W	100	102	183.40		949.1	2787	-17.12	0.11	0.18		
ODP 1063	B19H2W	130	132	183.70		950.9	2791	-18.93	0.11	0.17		
ODP 1063	B19H3W	10	12	184.00		953.3	2753	-19.68	0.14	0.12	-19.66	0.10
ODP 1063	B19H3W	10	12	184.00		953.3	3296	-19.63	0.14	0.16		
ODP 1063	B19H3W	40	42	184.30		955.3	2780	-18.73	0.12	0.12		
ODP 1063	B19H3W	70	72	184.60		957.2	2782	-17.92	0.10	0.18	-17.94	0.07
ODP 1063	B19H3W	70	72	184.60		957.2	2784	-17.97	0.10	0.18		
ODP 1063	B19H3W	100	102	184.90		959.2	3242	-14.43	0.15	0.16	-14.45	0.10
ODP 1063	B19H3W	100	102	184.90		959.2	3624	-14.48	0.15	0.19		
ODP 1063	B19H3W	130	132	185.20		961.4	2795	-14.01	0.12	0.17		
ODP 1063	B19H4W	10	12	185.50		964.2	2788	-15.37	0.11	0.18		
ODP 1063	B19H4W	40	42	185.80		965.4	4038	-16.26	0.13	0.28		
ODP 1063	B19H4W	70	72	186.10		966.6	2764	-16.81	0.07	0.31		

Site	Label	Top (cm)	Bottom (cm)	Depth (mcd)	Depth (amcd)	Age (ka)	Sample #	ε_{Nd}	Int. 2 SEM	Ext. 2 SD	W. Mean ε_{Nd}	2 SEM
ODP 1063	B19H4W	100	102	186.40		970.0	2759	-16.98	0.15	0.12		
ODP 1063	B19H4W	130	132	186.70		976.3	2771	-15.69	0.08	0.31	-15.64	0.07
ODP 1063	B19H4W	130	132	186.70		976.3	4017	-15.49	0.14	0.28		
ODP 1063	B19H5W	40	42	187.30		977.7	4047	-17.12	0.14	0.28		
ODP 1063	B19H5W	70	72	187.60		980.4	2763	-15.83	0.09	0.31		
ODP 1063	B19H5W	100	102	187.90		985.7	2798	-15.13	0.11	0.17		
ODP 1063	B19H6W	10	12	188.50		989.0	2792	-18.02	0.08	0.17		
ODP 1063	B19H6W	40	42	188.80		990.8	4044	-14.93	0.13	0.28		
ODP 1063	B19H6W	70	72	189.10		992.9	2789	-17.04	0.11	0.17		
ODP 1063	B19H6W	97	99	189.37		994.8	3940	-16.98	0.17	0.16		
ODP 1063	C20H6W	84	86	189.70		997.2	2762	-18.27	0.07	0.31		
ODP 1063	C20H6W	114	116	190.00		999.4	4301	-15.97	0.08	0.24		
ODP 1063	C20H6W	144	146	190.30		1001.6	2777	-16.08	0.11	0.12	-16.05	0.08
ODP 1063	C20H6W	144	146	190.30		1001.6	3113	-16.02	0.13	0.24		
ODP 1063	C20H7W	24	26	190.60		1003.8	2804	-14.75	0.09	0.17		
ODP 1063	C20H7W	54	56	190.90		1006.0	2800	-17.19	0.10	0.17		
ODP 1063	C20H7W	84	86	191.20		1008.1	3971	-16.97	0.16	0.16		
ODP 1063	C20H7W	114	116	191.50		1010.3	2756	-14.35	0.14	0.12	-14.09	0.09
ODP 1063	C20H7W	114	116	191.50		1010.3	4272	-13.95	0.11	0.24		
ODP 1063	C20H7W	144	146	191.80		1012.5	3987	-16.79	0.17	0.16		
ODP 1063	C20H8W	24	26	192.10		1014.7	2786	-14.77	0.13	0.18		
ODP 1063	C20H8W	54	56	192.40		1016.9	3951	-17.11	0.19	0.16		
ODP 1063	B20H2W	88	90	192.70		1018.8	2766	-17.11	0.09	0.31		

Site	Label	Top (cm)	Bottom (cm)	Depth (mcd)	Depth (amcd)	Age (ka)	Sample #	ε_{Nd}	Int. 2 SEM	Ext. 2 SD	W. Mean ε_{Nd}	2 SEM
ODP 1063	B20H2W	117	119	192.99		1020.0	4299	-14.60	0.08	0.24		
ODP 1063	B20H2W	147	149	193.29		1021.2	4030	-15.08	0.14	0.28		
ODP 1063	B20H3W	28	30	193.60		1022.5	2790	-17.29	0.09	0.17		
ODP 1063	B20H3W	58	60	193.90		1024.1	3961	-19.30	0.18	0.16		
ODP 1063	B20H3W	89	91	194.21		1026.2	2793	-18.35	0.11	0.17		

Table C.2: Nd Isotopic composition of mixed planktic foraminifera of ODP 1063. In cases, where foraminifera were scarce, two samples from the same depth range were combined (see Section 3.4.2 for further details).

Site	Label	Top (cm)	Bottom (cm)	Depth (mcd)	Depth (amcd)	Age (ka)	sample #	ε_{Nd}	Int. 2 SEM	Ext. 2 SD
ODP 1063	D9H1A	8	10	74.50	74.92	335.2	1307	-15.36	0.10	0.12
ODP 1063	D10H3A	146	148	88.30	88.22	388.9	1302	-15.70	0.13	0.12
ODP 1063	A10H1W	100	102	88.30		389.5				
ODP 1063	D10H4A	26	28	88.60	88.52	391.3	1305	-13.90	0.10	0.12
ODP 1063	A10H1W	130	132	88.60		391.9				
ODP 1063	D10H5A	86	88	90.70	90.54	421.6	1306	-16.75	0.13	0.12
ODP 1063	D10H5A	88	90	90.72	90.56	421.9	1318	-16.76	0.10	0.12
ODP 1063	D10H5A	116	118	91.00	90.84	426.1	1317	-14.65	0.13	0.12
ODP 1063	D10H5A	118	120	91.02	90.86	426.6	1304	-14.47	0.12	0.12
ODP 1063	A13H2W	110	112	120.40		614.4	1310	-15.25	0.10	0.12
ODP 1063	D13H5A	54	56	120.40		614.4				

Table C.3: Stable oxygen and carbon isotopes of benthic foraminifera in ODP 1063. When available, *Cibicidoides wuellerstorfi* was used for equilibrium values by adding a species-specific offset of +0.64 ‰for δ^{18}O [Shackleton and Hall, 1984] and no adjustment factor for δ^{13}C. In cases where only *Oridorsalis umbonatus* was present, the values were first corrected to *C. wuellerstorfi* by -0.43 ‰ for δ^{18}O and +1.42 ‰ for δ^{13}C (respective mean of the differences of 45 paired measurements of both species) and afterwards adjusted to the equilibrium value by +0.64 ‰ for δ^{18}O [Shackleton and Hall, 1984] and no further adjustment for δ^{13}C.

Site	Label	Top (cm)	Bottom (cm)	Depth (mcd)	Age (ka)	Species	δ^{18}O (‰VPDB)	δ^{18}O $_{eq}$ (‰ VPDB)	δ^{13}C (‰ VPDB)	δ^{13}C $_{eq}$ (‰ VPDB)
ODP 1063	B5H4W	35	37	44.69	148.7	*O. umb.*	3.80		-1.69	
ODP 1063	B5H4W	35	37	44.69	148.7	*C. wuell.*	4.30	4.94	-0.40	-0.40
ODP 1063	B5H4W	55	57	44.89	149.1	*C. wuell.*	4.29	4.93	-0.40	-0.40
ODP 1063	B5H4W	75	77	45.09	149.6	*O. umb.*	4.63		-1.83	
ODP 1063	B5H4W	75	77	45.09	149.6	*C. wuell.*	4.34	4.98	-1.18	-1.18
ODP 1063	B5H4W	95	97	45.29	150.0	*O. umb.*	4.61		-2.24	
ODP 1063	B5H4W	95	97	45.29	150.0	*C. wuell.*	4.27	4.91	-0.93	-0.93
ODP 1063	B5H4W	115	117	45.49	150.4	*O. umb.*	4.38	4.59	-0.36	1.06
ODP 1063	B5H4W	144	146	45.78	151.1	*C. wuell.*	4.90	5.54	-1.94	-1.94
ODP 1063	B5H5W	36	38	46.20	152.0	*O. umb.*	4.95	5.16	-1.89	-0.47
ODP 1063	B5H5W	70	72	46.54	152.8	*O. umb.*	4.94	5.14	-1.89	-0.47
ODP 1063	B5H5W	110	112	46.94	153.7	*O. umb.*	4.80	5.01	-1.98	-0.56
ODP 1063	B5H6W	20	22	47.54	155.0	*O. umb.*	3.55	3.76	-1.33	0.09
ODP 1063	D6H3W	59	61	47.89	156.8	*C. wuell.*	4.24	4.88	-1.02	-1.02
ODP 1063	D6H3W	77	79	48.07	157.8	*O. umb.*	4.74		-2.23	
ODP 1063	D6H3W	77	79	48.07	157.8	*C. wuell.*	4.24	4.88	-1.42	-1.42
ODP 1063	D6H3W	101	103	48.31	159.0	*C. wuell.*	4.23	4.87	0.24	0.24
ODP 1063	D6H4W	23	25	49.03	162.7	*O. umb.*	3.53		-2.05	

Site	Label	Top (cm)	Bottom (cm)	Depth (mcd)	Age (ka)	Species	$\delta^{18}O$ (‰VPDB)	$\delta^{18}O_{eq}$ (‰ VPDB)	$\delta^{13}C$ (‰ VPDB)	$\delta^{13}C_{eq}$ (‰ VPDB)
ODP 1063	D6H4W	23	25	49.03	162.7	*C. wuell.*	3.88	4.52	-0.58	-0.58
ODP 1063	D6H4W	50	52	49.30	164.1	*O. umb.*	4.36		-2.18	
ODP 1063	D6H4W	50	52	49.30	164.1	*C. wuell.*	4.24	4.88	-1.08	-1.08
ODP 1063	D6H4W	71	73	49.51	165.2	*O. umb.*	4.88	5.09	-1.97	-0.55
ODP 1063	D6H4W	95	97	49.75	166.5	*C. wuell.*	4.02	4.66	-0.45	-0.45
ODP 1063	D6H4W	117	119	49.97	167.6	*O. umb.*	3.87		-2.14	
ODP 1063	D6H4W	117	119	49.97	167.6	*C. wuell.*	3.79	4.43	-0.04	-0.04
ODP 1063	D6H4W	143	145	50.23	169.0	*O. umb.*	4.45		-1.47	
ODP 1063	D6H4W	143	145	50.23	169.0	*C. wuell.*	4.06	4.70	0.01	0.01
ODP 1063	D6H5W	17	19	50.47	170.2	*O. umb.*	4.54	4.74	-1.95	-0.53
ODP 1063	D6H5W	35	37	50.65	171.2	*O. umb.*	4.08	4.29	-1.96	-0.54
ODP 1063	D6H5W	52	54	50.82	172.0	*O. umb.*	4.51		-2.15	
ODP 1063	D6H5W	52	54	50.82	172.0	*C. wuell.*	3.69	4.33	-0.76	-0.76
ODP 1063	D6H5W	70	72	51.00	173.0	*O. umb.*	4.45	4.66	-1.72	-0.30
ODP 1063	D6H5W	89	91	51.19	174.0	*O. umb.*	4.46	4.67	-2.10	-0.68
ODP 1063	D6H5W	108	110	51.38	175.0	*O. umb.*	4.60	4.81	-1.81	-0.39
ODP 1063	D6H5W	127	129	51.57	176.0	*O. umb.*	4.60		-1.85	
ODP 1063	D6H5W	127	129	51.57	176.0	*C. wuell.*	4.04	4.68	-0.29	-0.29
ODP 1063	D6H5W	145	147	51.75	176.9	*O. umb.*	4.73		-2.02	
ODP 1063	D6H5W	145	147	51.75	176.9	*C. wuell.*	4.15	4.79	-0.77	-0.77
ODP 1063	D6H6W	13	15	51.93	177.8	*O. umb.*	4.63		-1.81	
ODP 1063	D6H6W	13	15	51.93	177.8	*C. wuell.*	3.81	4.45	-1.30	-1.30
ODP 1063	D6H6W	32	34	52.12	178.8	*O. umb.*	4.72		-1.65	

Site	Label	Top (cm)	Bottom (cm)	Depth (mcd)	Age (ka)	Species	$\delta^{18}O$ (‰VPDB)	$\delta^{18}O_{eq}$ (‰ VPDB)	$\delta^{13}C$ (‰ VPDB)	$\delta^{13}C_{eq}$ (‰ VPDB)
ODP 1063	D6H6W	32	34	52.12	178.8	*C. wuell.*	4.10	4.74	-0.59	-0.59
ODP 1063	D6H6W	50	52	52.30	179.7	*O. umb.*	4.72	4.93	-1.25	0.17
ODP 1063	D6H6W	70	72	52.50	180.8	*O. umb.*	4.46		-1.56	
ODP 1063	D6H6W	70	72	52.50	180.8	*C. wuell.*	3.89	4.53	-0.26	-0.26
ODP 1063	D6H6W	87	89	52.67	181.7	*O. umb.*	4.42		-2.10	
ODP 1063	D6H6W	87	89	52.67	181.7	*C. wuell.*	4.00	4.64	-0.75	-0.75
ODP 1063	D6H6W	109	111	52.89	182.8	*O. umb.*	3.84	4.04	-2.92	-1.50
ODP 1063	D6H6W	127	129	53.07	183.7	*O. umb.*	4.60		-2.13	
ODP 1063	D6H6W	127	129	53.07	183.7	*C. wuell.*	4.17	4.81	-0.82	-0.82
ODP 1063	B6H2W	89	91	53.27	184.8	*O. umb.*	4.74		-1.70	
ODP 1063	B6H2W	89	91	53.27	184.8	*C. wuell.*	3.83	4.47	-0.66	-0.66
ODP 1063	B6H2W	109	111	53.47	185.8	*C. wuell.*	3.92	4.56	-0.67	-0.67
ODP 1063	B6H2W	129	131	53.67	186.9	*C. wuell.*	3.94	4.58	-0.34	-0.34
ODP 1063	B6H3W	0	4	53.89	188.0	*O. umb.*	4.58	4.79	-1.37	0.05
ODP 1063	B6H3W	18	20	54.06	189.2	*O. umb.*	4.45		-1.74	
ODP 1063	B6H3W	18	20	54.06	189.2	*C. wuell.*	3.95	4.59	-0.38	-0.38
ODP 1063	B6H3W	39	42	54.275	190.6	*O. umb.*	4.41		-1.48	
ODP 1063	B6H3W	39	42	54.275	190.6	*C. wuell.*	3.72	4.36	-0.15	-0.15
ODP 1063	B6H3W	59	61	54.47	191.9	*O. umb.*	3.88		-1.91	
ODP 1063	B6H3W	59	61	54.47	191.9	*C. wuell.*	3.64	4.28	0.07	0.07
ODP 1063	B6H3W	80	82	54.68	193.4	*O. umb.*	3.55	3.76	-2.63	-1.21
ODP 1063	C7H1W	1	3	55.07	196.0	*O. umb.*	4.42		-1.48	
ODP 1063	C7H1W	1	3	55.07	196.0	*C. wuell.*	3.89	4.53	-1.01	-1.01

Site	Label	Top (cm)	Bottom (cm)	Depth (mcd)	Age (ka)	Species	$\delta^{18}O$ (‰VPDB)	$\delta^{18}O_{eq}$ (‰ VPDB)	$\delta^{13}C$ (‰ VPDB)	$\delta^{13}C_{eq}$ (‰ VPDB)
ODP 1063	C7H1W	32	34	55.38	198.1	*O. umb.*	3.89		-1.53	
ODP 1063	C7H1W	32	34	55.38	198.1	*C. wuell.*	3.53	4.17	-0.04	-0.04
ODP 1063	C7H1W	54	56	55.60	199.6	*O. umb.*	3.45		-1.36	
ODP 1063	C7H1W	54	56	55.60	199.6	*C. wuell.*	3.15	3.79	0.29	0.29
ODP 1063	C7H1W	74	76	55.80	201.0	*O. umb.*	3.38		-1.65	
ODP 1063	C7H1W	74	76	55.80	201.0	*C. wuell.*	2.99	3.63	-0.97	-0.97
ODP 1063	C7H1W	93	95	55.99	203.3	*O. umb.*	3.49		-1.11	
ODP 1063	C7H1W	93	95	55.99	203.3	*C. wuell.*	3.13	3.77	-0.04	-0.04
ODP 1063	C7H1W	118	120	56.24	206.3	*O. umb.*	3.87		-0.93	
ODP 1063	C7H1W	118	120	56.24	206.3	*C. wuell.*	3.32	3.96	-1.05	-1.05
ODP 1063	C7H1W	143	145	56.49	209.2	*C. wuell.*	3.30	3.94	0.09	0.09
ODP 1063	C7H2W	17	19	56.73	212.1	*C. wuell.*	3.42	4.06	-1.11	-1.11
ODP 1063	C7H2W	35	37	56.91	214.3	*O. umb.*	3.26		-0.84	
ODP 1063	C7H2W	35	37	56.91	214.3	*C. wuell.*	2.85	3.49	0.29	0.29
ODP 1063	C7H2W	58	60	57.14	217.0	*O. umb.*	3.32	3.52	-1.31	0.11
ODP 1063	C7H2W	75	77	57.31	219.1	*O. umb.*	3.90		-1.56	
ODP 1063	C7H2W	75	77	57.31	219.1	*C. wuell.*	3.63	4.27	-0.15	-0.15
ODP 1063	C7H2W	98	100	57.54	222.0	*O. umb.*	4.49		-2.14	
ODP 1063	C7H2W	98	100	57.54	222.0	*C. wuell.*	4.09	4.73	-0.68	-0.68
ODP 1063	C7H2W	116	118	57.72	222.7	*O. umb.*	4.77		-1.89	
ODP 1063	C7H2W	116	118	57.72	222.7	*C. wuell.*	4.11	4.75	-0.79	-0.79
ODP 1063	C7H2W	138	140	57.94	223.6	*O. umb.*	4.15	4.36	-1.81	-0.39
ODP 1063	C7H3W	9	11	58.15	224.4	*O. umb.*	4.44		-1.23	

Site	Label	Top (cm)	Bottom (cm)	Depth (mcd)	Age (ka)	Species	$\delta^{18}O$ (‰VPDB)	$\delta^{18}O_{eq}$ (‰ VPDB)	$\delta^{13}C$ (‰ VPDB)	$\delta^{13}C_{eq}$ (‰ VPDB)
ODP 1063	C7H3W	9	11	58.15	224.4	*C. wuell.*	3.94	4.58	0.18	0.18
ODP 1063	C7H3W	28	30	58.34	225.2	*C. wuell.*	3.94	4.58	-0.89	-0.89
ODP 1063	C7H3W	74	76	58.8	227.0	*O. umb.*	4.31	4.52	-1.99	-0.57
ODP 1063	C7H3W	95	97	59.01	229.4	*O. umb.*	4.13	4.34	-1.63	-0.21
ODP 1063	C7H3W	120	122	59.26	232.3	*O. umb.*	4.22		-1.62	
ODP 1063	C7H3W	120	122	59.26	232.3	*C. wuell.*	3.41	4.05	0.58	0.58
ODP 1063	C7H3W	141	143	59.47	234.7	*O. umb.*	3.66		-1.56	
ODP 1063	C7H3W	141	143	59.47	234.7	*C. wuell.*	3.54	4.18	0.20	0.20
ODP 1063	C7H4W	16	18	59.72	237.6	*O. umb.*	3.46	3.66	-0.88	0.54
ODP 1063	C7H4W	37	39	59.93	240.0	*O. umb.*	3.08		-0.80	
ODP 1063	C7H4W	37	39	59.93	240.0	*C. wuell.*	2.68	3.32	0.00	0.00
ODP 1063	C7H4W	62	64	60.18	243.3	*O. umb.*	4.20		-1.74	
ODP 1063	C7H4W	62	64	60.18	243.3	*C. wuell.*	3.34	3.98	-0.40	-0.40
ODP 1063	C7H4W	82	84	60.38	246.0	*O. umb.*	4.50		-1.77	
ODP 1063	C7H4W	82	84	60.38	246.0	*C. wuell.*	4.05	4.69	0.38	0.38
ODP 1063	C7H4W	108	110	60.64	247.1	*O. umb.*	4.38	4.58	-2.19	-0.77
ODP 1063	C7H4W	132	134	60.88	248.1	*O. umb.*	4.54		-2.28	
ODP 1063	C7H4W	132	134	60.88	248.1	*C. wuell.*	3.41	4.05	-1.11	-1.11
ODP 1063	C7H5W	3	5	61.09	249.0	*O. umb.*	4.55		-2.61	
ODP 1063	C7H5W	3	5	61.09	249.0	*C. wuell.*	4.24	4.88	0.51	0.51
ODP 1063	C7H5W	28	30	61.34	250.1	*O. umb.*	3.85	4.06	-2.90	-1.48
ODP 1063	C7H5W	48	50	61.54	250.9	*O. umb.*	3.87		-1.99	
ODP 1063	C7H5W	48	50	61.54	250.9	*C. wuell.*	4.10	4.74	-0.08	-0.08

Site	Label	Top (cm)	Bottom (cm)	Depth (mcd)	Age (ka)	Species	$\delta^{18}O$ (‰VPDB)	$\delta^{18}O_{eq}$ (‰ VPDB)	$\delta^{13}C$ (‰ VPDB)	$\delta^{13}C_{eq}$ (‰ VPDB)
ODP 1063	C7H5W	72	74	61.78	251.9	*O. umb.*	4.62		-2.40	
ODP 1063	C7H5W	72	74	61.78	251.9	*C. wuell.*	3.14	3.78	0.00	0.00
ODP 1063	C7H5W	93	95	61.99	252.8	*O. umb.*	3.71		-0.55	
ODP 1063	C7H5W	93	95	61.99	252.8	*C. wuell.*	4.27	4.91	-0.07	-0.07
ODP 1063	C7H5W	138	140	62.44	254.7	*C. wuell.*	4.19	4.83	-0.05	-0.05
ODP 1063	C7H6W	13	15	62.69	255.8	*O. umb.*	4.64		-1.92	
ODP 1063	C7H6W	13	15	62.69	255.8	*C. wuell.*	4.29	4.93	-0.35	-0.35
ODP 1063	C7H6W	32	34	62.88	256.6	*O. umb.*	4.56		-2.49	
ODP 1063	C7H6W	32	34	62.88	256.6	*C. wuell.*	4.11	4.75	0.16	0.16
ODP 1063	C7H6W	51	53	63.07	257.4	*O. umb.*	4.47	4.68	-1.83	-0.41
ODP 1063	C7H6W	72	74	63.28	258.3	*O. umb.*	3.59	3.80	-3.10	-1.68
ODP 1063	C7H6W	92	94	63.48	259.1	*O. umb.*	4.60		-2.45	
ODP 1063	C7H6W	92	94	63.48	259.1	*C. wuell.*	4.09	4.73	0.11	0.11
ODP 1063	C7H6W	113	115	63.69	260.0	*O. umb.*	4.59		-2.31	
ODP 1063	C7H6W	113	115	63.69	260.0	*C. wuell.*	4.05	4.69	0.06	0.06

Table C.4: Nd isotopic composition of USGS standard Nod-A-1.

sample #	$\varepsilon_{\mathbf{Nd}}$	$\mathbf{2}\sigma$
1070	-9.64	0.37
3604	-9.50	0.19
3975	-9.39	0.17
4026	-9.39	0.28
4289	-9.41	0.24
4836	-9.60	0.13
5038	-9.40	0.13
5095	-9.76	0.18
5149	-9.50	0.27

Table C.5: Nd isotopic composition of replicates from Böhm *et al.* [2015] (B2015).

Site	Label	Top (cm)	Bottom (cm)	ε_{Nd} this study	Int. 2 SEM	Ext. 2 SD	ε_{Nd} B2015 leach	2 SD	ε_{Nd} B2015 foram	2 SD
ODP 1063	B1H4W	130	132	-11.03	0.19	0.16	-10.88	0.36		
ODP 1063	D3H2W	74	76	-11.98	0.29	0.37	-12.12	0.20		
ODP 1063	D3H6W	40	42	-14.72	0.31	0.37	-15.02	0.20		
ODP 1063	C4H4W	140	141	-18.62	0.34	0.37	-18.03	0.20	-18.58	0.57

D Data from Study II

Table D.1: Authigenic Nd isotopic composition of ODP 980.

Site	Label	Top (cm)	Bottom (cm)	Depth (mcd)	Age (ka)	Sample #	ε_{Nd}	Int. 2 SEM	Ext. 2 SD	W. Mean ε_{Nd}	2 SEM
ODP 980	B6H2W	67	68	50.02	384.8	4823	-11.35	0.12	0.13	-11.40	0.08
ODP 980	B6H2W	67	68	50.02	384.8	4835	-11.45	0.12	0.13		
ODP 980	B6H2W	97	98	50.32	386.7	4842	-11.46	0.12	0.13		
ODP 980	B6H2W	127	128	50.62	388.7	4479	-10.36	0.07	0.12		
ODP 980	B6H3W	7	8	50.92	390.7	4464	-10.74	0.11	0.17		
ODP 980	B6H3W	37	38	51.22	392.8	4470	-11.25	0.09	0.17		
ODP 980	B6H3W	67	68	51.52	394.6	4513	-11.68	0.09	0.12		
ODP 980	B6H3W	97	98	51.82	395.9	4477	-11.93	0.09	0.17		
ODP 980	B6H3W	127	128	52.12	397.4	4511	-12.20	0.08	0.12		
ODP 980	B6H4W	7	8	52.42	399.5	4520	-12.61	0.08	0.12		
ODP 980	B6H4W	37	38	52.72	401.9	4522	-12.96	0.07	0.12		
ODP 980	B6H4W	67	68	53.02	404.4	4517	-13.29	0.10	0.12		
ODP 980	B6H4W	97	98	53.32	406.8	4503	-13.41	0.11	0.12		
ODP 980	B6H4W	127	128	53.62	409.3	4492	-13.52	0.10	0.12		
ODP 980	B6H5W	7	8	53.92	411.3	4475	-12.87	0.24	0.17		
ODP 980	B6H5W	42	43	54.27	412.8	4516	-13.22	0.09	0.12		
ODP 980	B6H5W	67	68	54.52	414.0	4498	-13.15	0.09	0.12		
ODP 980	B6H5W	97	98	54.82	415.3	4494	-11.17	0.09	0.12		
ODP 980	B6H5W	127	128	55.12	416.6	4501	-11.14	0.10	0.12		
ODP 980	B6H6W	7	8	55.42	417.9	4468	-10.63	0.15	0.17	-10.60	0.10
ODP 980	B6H6W	7	8	55.42	417.9	4832	-10.59	0.13	0.13		

Site	Label	Top (cm)	Bottom (cm)	Depth (mcd)	Age (ka)	Sample #	ε_{Nd}	Int. 2 SEM	Ext. 2 SD	W. Mean ε_{Nd}	2 SEM
ODP 980	B6H6W	37	38	55.72	419.3	4512	-10.37	0.09	0.12		
ODP 980	B6H6W	69	70	56.04	420.7	4510	-10.19	0.09	0.12		
ODP 980	B6H6W	97	98	56.32	421.9	4461	-8.48	0.15	0.17		
ODP 980	B6H6W	127	128	56.62	423.2	4506	-9.70	0.10	0.12	-9.73	0.06
ODP 980	B6H6W	127	128	56.62	423.2	4508	-9.75	0.08	0.12		
ODP 980	B6H7W	9	10	56.94	424.5	4486	-9.77	0.07	0.12		
ODP 980	C7H3W	11	12	57.22	425.7	4497	-9.68	0.09	0.12		
ODP 980	C7H3W	38	39	57.49	426.8	4490	-9.51	0.08	0.12		
ODP 980	C7H3W	71	72	57.82	428.5	4480	-8.26	0.08	0.12		
ODP 980	C7H3W	101	102	58.12	430.4	4489	-7.82	0.10	0.12		
ODP 980	C7H3W	131	132	58.42	432.6	4471	-7.20	0.09	0.17		
ODP 980	C7H4W	11	12	58.72	434.8	4811	-7.67	0.11	0.13		
ODP 980	C7H4W	35	36	58.96	436.9	4812	-9.29	0.10	0.13		
ODP 980	B7H1W	86	87	59.34	440.3	4483	-9.32	0.09	0.12		
ODP 980	B7H1W	112	113	59.6	442.5	4523	-7.55	0.10	0.12		
ODP 980	B7H1W	142	143	59.9	444.7	4474	-10.62	0.10	0.17		

Table D.2: Authigenic Nd isotopic composition of IODP U1304.

Site	Label	Top (cm)	Bottom (cm)	Depth (mcd)	Age (ka)	Sample #	ε_{Nd}	Int. 2 SEM	Ext. 2 SD	W. Mean ε_{Nd}	2 SEM
IODP U1304	B6H3W	2	3	54.11	374.3	4779	-9.80	0.08	0.18		
IODP U1304	B6H3W	37	38	54.46	375.6	4790	-11.53	0.20	0.18		
IODP U1304	B6H3W	62	63	54.71	376.3	4757	-9.83	0.11	0.18		
IODP U1304	B6H3W	88	89	54.97	377.1	4753	-8.43	0.13	0.18		
IODP U1304	B6H3W	121	122	55.3	378.1	4763	-9.15	0.11	0.18		
IODP U1304	B6H4W	2	3	55.61	379.1	4746	-8.71	0.09	0.18		
IODP U1304	B6H4W	32	33	55.91	380.0	4758	-8.82	0.09	0.18		
IODP U1304	B6H4W	62	63	56.21	380.9	4741	-8.32	0.13	0.18		
IODP U1304	B6H4W	88	89	56.47	381.7	4774	-8.95	0.08	0.18		
IODP U1304	B6H4W	121	122	56.8	382.7	4751	-8.62	0.07	0.18		
IODP U1304	B6H5W	2	3	57.11	383.6	4796	-7.71	0.08	0.18		
IODP U1304	B6H5W	37	38	57.46	384.6	4789	-8.34	0.10	0.18		
IODP U1304	B6H5W	62	63	57.71	385.4	4745	-8.50	0.10	0.18		
IODP U1304	B6H5W	88	89	57.97	386.2	4799	-8.38	0.08	0.17		
IODP U1304	B6H5W	121	122	58.3	387.2	4769	-9.77	0.08	0.18		
IODP U1304	B6H6W	2	3	58.61	388.1	4772	-9.50	0.07	0.18		
IODP U1304	B6H6W	27	28	58.86	388.9	4766	-9.28	0.09	0.18		
IODP U1304	B6H6W	61	62	59.2	389.9	4793	-9.64	0.07	0.18		
IODP U1304	B6H6W	88	89	59.47	390.7	4800	-8.76	0.09	0.17		
IODP U1304	B6H6W	121	122	59.8	391.7	4765	-11.50	0.07	0.18		
IODP U1304	A6H3W	37	38	60.07	392.4	4819	-9.08	0.15	0.13		

Site	Label	Top (cm)	Bottom (cm)	Depth (mcd)	Age (ka)	Sample #	ε_{Nd}	Int. 2 SEM	Ext. 2 SD	W. Mean ε_{Nd}	2 SEM
IODP U1304	A6H3W	77	78	60.47	393.5	4816	-8.10	0.11	0.13		
IODP U1304	A6H3W	97	98	60.67	394.0	4828	-6.88	0.13	0.13		
IODP U1304	A6H3W	127	128	60.97	394.8	4831	-7.46	0.14	0.13		
IODP U1304	A6H4W	7	8	61.27	395.6	4840	-7.14	0.14	0.13		
IODP U1304	A6H4W	37	38	61.57	396.4	4820	-7.50	0.13	0.13	-7.52	0.09
IODP U1304	A6H4W	37	38	61.57	396.4	4834	-7.53	0.11	0.13		
IODP U1304	A6H4W	76	77	61.96	397.4	4822	-7.89	0.12	0.13	-7.79	0.08
IODP U1304	A6H4W	76	77	61.96	397.4	5053	-7.72	0.11	0.13		
IODP U1304	A6H4W	97	98	62.17	398.0	4829	-8.33	0.12	0.13		
IODP U1304	A6H4W	126	127	62.46	398.7	4841	-8.94	0.11	0.13		
IODP U1304	A6H5W	7	8	62.77	399.6	4780	-9.32	0.08	0.18		
IODP U1304	A6H5W	37	38	63.07	400.4	4777	-9.37	0.08	0.18	-9.29	0.06
IODP U1304	A6H5W	37	38	63.07	400.4	4783	-9.21	0.08	0.18		
IODP U1304	A6H5W	77	78	63.47	401.4	4786	-9.25	0.09	0.18		
IODP U1304	A6H5W	97	98	63.67	401.9	4794	-9.28	0.10	0.18		
IODP U1304	B7H3W	21	22	64.01	402.8	4798	-9.06	0.08	0.17		
IODP U1304	B7H3W	47	48	64.27	403.5	4748	-9.12	0.09	0.18		
IODP U1304	B7H3W	81	82	64.61	404.4	4764	-9.14	0.09	0.18		
IODP U1304	B7H3W	113	114	64.93	405.3	4754	-9.37	0.08	0.18		
IODP U1304	B7H3W	143	144	65.23	406.0	4742	-9.27	0.10	0.18		
IODP U1304	B7H4W	22	23	65.51	406.8	4778	-9.22	0.08	0.18		
IODP U1304	B7H4W	47	48	65.76	407.4	4770	-9.07	0.11	0.18		
IODP U1304	B7H4W	82	83	66.11	408.4	4749	-9.33	0.09	0.18		

Site	Label	Top (cm)	Bottom (cm)	Depth (mcd)	Age (ka)	Sample #	ε_{Nd}	Int. 2 SEM	Ext. 2 SD	W. Mean ε_{Nd}	2 SEM
IODP U1304	B7H4W	113	114	66.42	409.2	4785	-9.53	0.09	0.18		
IODP U1304	B7H4W	143	144	66.72	410.0	4797	-9.30	0.08	0.18		
IODP U1304	B7H5W	22	23	67	410.7	4803	-9.18	0.09	0.17		
IODP U1304	B7H5W	48	49	67.26	411.4	4776	-9.50	0.07	0.18		
IODP U1304	B7H5W	82	83	67.6	412.3	4804	-9.45	0.07	0.17		
IODP U1304	B7H5W	113	114	67.91	413.1	4761	-9.31	0.08	0.18		
IODP U1304	B7H5W	143	144	68.21	413.9	4824	-9.26	0.13	0.13		
IODP U1304	B7H6W	22	23	68.49	414.7	4839	-10.16	0.15	0.13		
IODP U1304	B7H6W	48	49	68.75	415.3	4818	-9.54	0.12	0.13		
IODP U1304	B7H6W	81	82	69.08	416.2	4814	-8.30	0.11	0.13		
IODP U1304	B7H6W	114	115	69.41	417.1	4813	-8.22	0.12	0.13		
IODP U1304	A7H1W	88	89	69.64	417.7	4768	-9.11	0.11	0.18		
IODP U1304	A7H1W	122	123	69.98	418.6	4795	-9.31	0.08	0.18		
IODP U1304	A7H2W	2	3	70.28	419.4	4775	-8.53	0.08	0.18		
IODP U1304	A7H2W	27	28	70.53	420.0	4755	-8.45	0.09	0.18	-8.42	0.07
IODP U1304	A7H2W	27	28	70.53	420.0	5000	-8.38	0.11	0.13		
IODP U1304	A7H2W	61	62	70.87	420.9	4773	-9.59	0.08	0.18		
IODP U1304	A7H2W	87	88	71.13	421.6	4752	-9.72	0.08	0.18		
IODP U1304	A7H2W	121	122	71.47	422.5	4802	-10.50	0.09	0.17		
IODP U1304	A7H3W	2	3	71.78	423.6	4747	-10.40	0.10	0.18		
IODP U1304	A7H3W	27	28	72.03	426.9	4788	-11.69	0.09	0.18		
IODP U1304	A7H3W	62	63	72.38	432.0	4756	-10.26	0.09	0.18		
IODP U1304	A7H3W	87	88	72.63	436.3	4787	-11.77	0.07	0.18		

Site	Label	Top (cm)	Bottom (cm)	Depth (mcd)	Age (ka)	Sample #	ε_{Nd}	Int. 2 SEM	Ext. 2 SD	W. Mean ε_{Nd}	2 SEM
IODP U1304	A7H3W	121	122	72.97	442.2	4759	-11.28	0.10	0.18		
IODP U1304	A7H4W	2	3	73.28	447.6	4762	-11.26	0.06	0.18		
IODP U1304	A7H4W	27	28	73.53	451.9	4782	-12.67	0.08	0.18		
IODP U1304	A7H4W	62	63	73.88	458.0	4760	-10.87	0.09	0.18	-10.89	0.05
IODP U1304	A7H4W	62	63	73.88	458.0	4771	-10.90	0.07	0.18		
IODP U1304	A7H4W	88	89	74.14	462.6	4784	-11.71	0.09	0.18		
IODP U1304	A7H4W	122	123	74.48	468.5	4801	-12.00	0.07	0.17		

Table D.3: Authigenic Nd isotopic composition of ODP 659.

Site	Label	Top (cm)	Bottom (cm)	Depth (amcd)	Age (ka)	Sample #	ε_{Nd}	Int. 2 SEM	Ext. 2 SD	W. Mean ε_{Nd}	2 SEM
ODP 659	C2H2W	118	120	12.68	378.03	5120	-11.20	0.14	0.18		
ODP 659	C2H2W	128	130	12.78	380.76	5066	-11.67	0.14	0.18	-11.66	0.10
ODP 659	C2H2W	128	130	12.78	380.76	5163	-11.66	0.15	0.27		
ODP 659	C2H2W	138	140	12.88	383.93	5118	-12.02	0.15	0.18		
ODP 659	C2H2W	148	150	12.98	388.19	5049	-11.92	0.11	0.13		
ODP 659	C2H3W	8	10	13.08	392.93	5039	-12.12	0.10	0.13		
ODP 659	C2H3W	18	20	13.18	399.61	5013	-11.86	0.11	0.13		
ODP 659	C2H3W	28	30	13.28	406.40	5033	-11.66	0.14	0.13		
ODP 659	C2H3W	38	40	13.38	412.62	4998	-10.80	0.15	0.13		
ODP 659	C2H3W	48	50	13.48	415.94	5008	-12.06	0.17	0.13		
ODP 659	C2H3W	58	60	13.58	418.67	5018	-12.06	0.14	0.13		
ODP 659	C2H3W	68	70	13.68	421.29	5031	-11.60	0.14	0.13		
ODP 659	C2H3W	78	80	13.78	423.32	4991	-10.85	0.13	0.13		
ODP 659	C2H3W	88	90	13.88	424.96	4992	-11.09	0.10	0.13		
ODP 659	C2H3W	98	100	13.98	426.39	5011	-11.14	0.12	0.13		
ODP 659	C2H3W	108	110	14.08	427.98	5037	-11.58	0.13	0.13		
ODP 659	C2H3W	118	120	14.18	430.02	5052	-11.77	0.13	0.13		
ODP 659	C2H3W	128	130	14.28	432.02	5012	-10.04	0.14	0.13		
ODP 659	C2H3W	138	140	14.38	433.82	5003	-10.42	0.11	0.13		
ODP 659	C2H3W	148	150	14.48	435.62	5026	-10.47	0.11	0.13		
ODP 659	C2H4W	6	8	14.56	437.06	5014	-10.74	0.11	0.13		

Site	Label	Top (cm)	Bottom (cm)	Depth (amcd)	Age (ka)	Sample #	ε_{Nd}	Int. 2 SEM	Ext. 2 SD	W. Mean ε_{Nd}	2 SEM
ODP 659	C2H4W	15	17	14.65	438.68	5051	-10.82	0.13	0.13		
ODP 659	C2H4W	23	25	14.73	440.12	4994	-10.75	0.13	0.13	-10.73	0.08
ODP 659	C2H4W	23	25	14.73	440.12	5005	-10.72	0.11	0.13		
ODP 659	C2H4W	34	36	14.84	442.11	5041	-10.44	0.11	0.13		
ODP 659	C2H4W	48	50	14.98	445.06	5046	-11.39	0.12	0.13		
ODP 659	C2H4W	68	70	15.18	451.38	5045	-11.88	0.11	0.13		
ODP 659	C2H4W	88	90	15.38	460.27	5020	-12.14	0.12	0.13		

Table D.4: Authigenic Nd isotopic composition of ODP 929.

Site	Label	Top (cm)	Bottom (cm)	Depth (mcd)	Age (ka)	Sample #	ε_{Nd}	Int. 2 SEM	Ext. 2 SD	W. Mean ε_{Nd}	2 SEM
ODP 929	B2H5W	16.84	72	74	380.5	5092	-11.68	0.11	0.18		
ODP 929	B2H5W	17.01	89	90	385.8	5113	-12.38	0.13	0.18		
ODP 929	B2H5W	17.09	97	98	388.3	5091	-11.56	0.13	0.18		
ODP 929	B2H5W	17.15	103	104	390.2	5075	-11.59	0.13	0.18		
ODP 929	B2H5W	17.19	107	108	391.5	5086	-11.34	0.12	0.18		
ODP 929	B2H5W	17.25	113	114	393.5	5076	-11.02	0.12	0.18		
ODP 929	B2H5W	17.31	119	120	395.5	5088	-10.88	0.13	0.18		
ODP 929	B2H5W	17.39	127	128	398.2	5073	-11.31	0.12	0.18		
ODP 929	B2H5W	17.45	133	134	400.3	5104	-11.83	0.16	0.18		
ODP 929	B2H5W	17.49	137	138	401.9	5090	-12.04	0.15	0.18		
ODP 929	B2H5W	17.55	143	144	404.2	5097	-12.32	0.27	0.18		
ODP 929	B2H5W	17.59	147	148	405.8	5064	-12.26	0.12	0.18		
ODP 929	B2H6W	17.65	3	4	408.1	5078	-12.31	0.12	0.18		
ODP 929	B2H6W	17.71	9	10	410.5	5124	-11.75	0.12	0.18		
ODP 929	B2H6W	17.75	13	14	412.0	5068	-11.50	0.13	0.18	-11.62	0.09
ODP 929	B2H6W	17.75	13	14	412.0	5112	-11.76	0.14	0.18		
ODP 929	B2H6W	17.81	19	20	414.4	5069	-11.36	0.13	0.18		
ODP 929	B2H6W	18.05	43	44	423.7	5106	-10.56	0.15	0.18		
ODP 929	B2H6W	18.19	57	58	429.1	5065	-9.93	0.15	0.18		
ODP 929	B2H6W	18.31	69	70	432.8	5061	-9.47	0.14	0.18		
ODP 929	B2H6W	18.33	71	72	433.3	5083	-9.29	0.14	0.18		

Site	Label	Top (cm)	Bottom (cm)	Depth (mcd)	Age (ka)	Sample #	ε_{Nd}	Int. 2 SEM	Ext. 2 SD	W. Mean ε_{Nd}	2 SEM
ODP 929	B2H6W	18.45	83	84	436.3	5070	-9.73	0.15	0.18		
ODP 929	B2H6W	18.57	95	96	439.3	5111	-9.77	0.15	0.18		

Table D.5: Authigenic Nd isotopic composition of ODP 1267.

Site	Label	Top (cm)	Bottom (cm)	Depth (mcd)	Age (ka)	Sample #	ε_{Nd}	Int. 2 SEM	Ext. 2 SD	W. Mean ε_{Nd}	2 SEM
ODP 1267	A1H3W	35	36	3.38	374.3	5147	-11.00	0.14	0.27		
ODP 1267	A1H3W	40	41	3.43	378.3	5132	-11.44	0.16	0.27		
ODP 1267	A1H3W	45	46	3.48	382.3	5166	-11.66	0.15	0.27		
ODP 1267	A1H3W	55	56	3.58	390.2	5176	-11.90	0.15	0.27		
ODP 1267	A1H3W	60	61	3.63	394.2	5154	-12.18	0.20	0.27		
ODP 1267	A1H3W	65	66	3.68	398.1	5193	-12.26	0.15	0.27		
ODP 1267	A1H3W	70	71	3.73	402.1	5183	-11.95	0.20	0.27		
ODP 1267	A1H3W	75	76	3.78	406.0	5184	-11.66	0.15	0.27		
ODP 1267	A1H3W	80	81	3.83	410.0	5177	-11.46	0.16	0.27		
ODP 1267	A1H3W	90	91	3.93	417.9	5142	-10.88	0.16	0.27		
ODP 1267	A1H3W	95	96	3.98	421.8	5164	-10.34	0.18	0.27		
ODP 1267	A1H3W	100	101	4.03	425.4	5145	-10.06	0.17	0.27		
ODP 1267	A1H3W	105	106	4.08	427.9	5146	-9.60	0.15	0.27	-9.55	0.11
ODP 1267	A1H3W	105	106	4.08	427.9	5152	-9.47	0.18	0.27		
ODP 1267	A1H3W	110	111	4.13	430.6	5161	-9.09	0.17	0.27		
ODP 1267	A1H3W	115	116	4.18	433.3	5148	-8.89	0.14	0.27		
ODP 1267	A1H3W	120	121	4.23	435.9	5156	-8.90	0.16	0.27		
ODP 1267	A1H3W	125	126	4.28	438.6	5139	-9.00	0.15	0.27		
ODP 1267	A1H3W	130	131	4.33	441.3	5172	-9.59	0.16	0.27		
ODP 1267	A1H3W	135	136	4.38	443.9	5140	-9.93	0.14	0.27		
ODP 1267	A1H3W	140	141	4.43	446.6	5170	-10.03	0.14	0.27		

Site	Label	Top (cm)	Bottom (cm)	Depth (mcd)	Age (ka)	Sample #	ε_{Nd}	Int. 2 SEM	Ext. 2 SD	W. Mean ε_{Nd}	2 SEM
ODP 1267	A1H3W	145	146	4.48	449.3	5158	-10.13	0.15	0.27		
ODP 1267	A1H4W	2	3	4.55	454.4	5175	-10.55	0.14	0.27		
ODP 1267	A1H4W	7	8	4.6	459.5	5190	-10.54	0.14	0.27		
ODP 1267	A1H4W	12	13	4.65	464.5	5192	-10.95	0.17	0.27		

Table D.6: Authigenic Nd isotopic composition of DSDP 517.

Site	Label	Top (cm)	Bottom (cm)	Depth (mbsf)	Age (ka)	Sample #	ε_{Nd}	Int. 2 SEM	Ext. 2 SD	W. Mean ε_{Nd}	2 SEM
DSDP 517	Z2H1W	68	70	3.18	356.9	5189	-9.70	0.15	0.27		
DSDP 517	Z2H1W	74	76	3.24	359.9	5133	-9.75	0.21	0.27		
DSDP 517	Z2H1W	86	88	3.36	365.9	5165	-9.67	0.17	0.27		
DSDP 517	Z2H1W	92	94	3.42	368.9	5150	-9.66	0.18	0.27		
DSDP 517	Z2H1W	98	100	3.48	371.9	5162	-9.74	0.15	0.27		
DSDP 517	Z2H1W	104	106	3.54	374.9	5185	-9.59	0.15	0.27		
DSDP 517	Z2H1W	110	112	3.6	377.9	5131	-9.57	0.18	0.27		
DSDP 517	Z2H1W	116	118	3.66	380.9	5160	-9.71	0.16	0.27	-9.68	0.11
DSDP 517	Z2H1W	116	118	3.66	380.9	5167	-9.65	0.14	0.27		
DSDP 517	Z2H1W	122	124	3.72	383.9	5168	-10.04	0.17	0.27		
DSDP 517	Z2H1W	128	130	3.78	386.9	5138	-9.84	0.20	0.27		
DSDP 517	Z2H1W	134	136	3.84	389.9	5178	-10.23	0.14	0.27		
DSDP 517	Z2H1W	140	142	3.9	392.9	5151	-10.38	0.17	0.27		
DSDP 517	Z2H1W	146	148	3.96	395.9	5173	-10.16	0.15	0.27		
DSDP 517	Z2H2W	13	15	4.13	404.4	5169	-10.33	0.16	0.27		
DSDP 517	Z2H2W	19	21	4.19	407.4	5188	-9.88	0.15	0.27		
DSDP 517	Z2H2W	25	27	4.25	410.4	5174	-10.02	0.18	0.27		
DSDP 517	Z2H2W	31	33	4.31	413.4	5135	-10.66	0.18	0.27		
DSDP 517	Z2H2W	37	39	4.37	416.4	5159	-12.18	0.14	0.27		
DSDP 517	Z2H2W	43	45	4.43	419.4	5143	-9.83	0.11	0.27		
DSDP 517	Z2H2W	55	57	4.55	425.4	5181	-9.42	0.16	0.27		

Site	Label	Top (cm)	Bottom (cm)	Depth (mbsf)	Age (ka)	Sample #	ε_{Nd}	Int. 2 SEM	Ext. 2 SD	W. Mean ε_{Nd}	2 SEM
DSDP 517	Z2H2W	67	69	4.67	431.4	5186	-9.34	0.17	0.27		
DSDP 517	Z2H2W	73	75	4.73	434.4	5194	-8.95	0.15	0.27		
DSDP 517	Z2H2W	79	81	4.79	437.4	5144	-8.44	0.14	0.27		
DSDP 517	Z2H2W	85	87	4.85	440.4	5180	-9.97	0.20	0.27		
DSDP 517	Z2H2W	91	93	4.91	443.4	5157	-9.32	0.17	0.27		
DSDP 517	Z2H2W	97	99	4.97	446.4	5191	-10.21	0.16	0.27		

Acknowledgements

„Leider läßt sich eine wahrhafte Dankbarkeit mit Worten nicht ausdrücken."
Johann Wolfgang von Goethe, Brief an die Fürstin Gallitzin, 6. Februar 1797

Trotzdem möchte ich es versuchen und all denjenigen meinen Dank aussprechen, die mich auf dem langen Weg zur Erstellung dieser Doktorarbeit unterstützt haben:

Allen voran gilt mein größter Dank meinem Doktorvater **Norbert Frank**, der mir die Möglichkeit gab dieses Promotionsprojekt durchzuführen. Dadurch konnte ich die Tiefen der Paläozeanographie frei erkunden und dabei jederzeit auf deinen Rat zählen. Danke für die gemeinsamen Diskussionen, aus denen viele neue Denkanstöße und Ideen für Projekte hervorgegangen sind. Vielen Dank auch an das entgegengebrachte Vertrauen mich in diese Projekte von Beginn an einzubinden. Durch deine stetige Förderung führte mich meine Reise nicht nur mit dem Schiff mitten auf den Atlantik, sondern durch zahlreiche Konferenzen und Workshops auch rund um die Welt. Ich fand immer eine offene Tür vor für Gespräche rund um sowie abseits der Wissenschaft und konnte immer auf deine Unterstützung und Zuspruch vertrauen, auch in manchen für mich nicht so leichten Zeiten. Herzlichen Dank!

Oliver Friedrich sei gedankt für die Übernahme der Zweitkorrektur dieser Arbeit.

Die Vielzahl an bearbeiteten Proben wäre niemals ohne Unterstützung zustande gekommen. Vielen Dank für die Hilfe bei der Aufbereitung an **Thomas Krengel**, **Evan Border**, **Paul Müller** und vor allem **Elvira Beisel**. Ohne deine gewissenhafte, sorgfältige und vorausschauende Arbeit wären die Datentabellen deutlich kürzer ausgefallen! Ich möchte mich auch für das Messen bei **Marcus Gutjahr**, **Patrick Blaser**, **Frerk Pöppelmeier** und **Julius Förstel** bedanken. Genauso gilt mein Dank **Anne Osborne** für die Hilfe bei der Aufbereitung und das Messen der Nd Isotope an Foraminiferen. Vielen Dank an **Kim Jakob** für die Produktion der stabilen Sauerstoff- und Kohlenstoffisotopendaten am ODP 1063.

Ohne die Idee von **Patrick Blaser** am ODP 1063 weiter zu arbeiten und das Nd Profil zu erweitern, wäre dieses Projekt gar nicht erst beantragt worden. Schon zu meinen Hiwi-Zeiten hast du mich in die Künste der Nd Chemie eingeführt und dann während des Projekts weiter unterstützt. Vielen Dank dafür! Ebenso gilt mein Dank **Jörg Lippold**, der mich damals überhaupt erst als Hiwi aufgenommen und in den darauffolgenden Jahren beim 1063er Projekt begleitet hat. Vielen Dank auch an **Martin Frank**, der es mir ermöglichte in Kiel die Foraminiferen-Proben zu bearbeiten und

seitdem immer mit Interesse dabei ist.

Ein herzliches Dankeschön an sowohl die aktuellen wie auch ehemaligen **PUAs** – ihr seid die beste Gruppe, die man sich wünschen kann! Es macht nicht nur Spaß an euren wissenschaftlichen Themen teilzuhaben und so immer etwas Neues dazu zu lernen, ebenso bin ich auch dankbar für eure Ideen, Diskussionen und Hilfe was meine eigenen Projekte anging. Aber vor allem möchte ich mich bedanken für die tolle Atmosphäre und den vielen Spaß, den wir auch neben der Wissenschaft während der letzten Jahre gemeinsam hatten. Ganz besonderer Dank gilt dabei Marleen Lausecker und Andrea Schröder-Ritzrau, die mich durch all die Tiefen und Höhen der letzten Jahre begleitet haben. Bedanken möchte ich mich auch bei den aktuellen **Neodymis** Moritz Hallmaier, Eva Rückert und Laura Lütkes. Gemeinsam mit euch an euren Neodym-Projekten zu arbeiten, bereitet mir viel Freude.

Lieben Dank auch an meinen „Doktoropa“**Augusto Mangini** – für dein Interesse an meiner Arbeit sowie für unsere Gespräche über alte Anekdoten, Italien und die Musik. Grazie mille!

Mit **Nicole Aeschbach** begann bereits während des Bachelorstudiums meine Reise in die Paläoklimatologie und ans IUP. Danke für deine stete Begleitung und dass ich auch nach dem Ende der offiziellen Betreuung immer noch auf deinen Rat bei einem Stück Kuchen zählen kann.

Auch mein privates Umfeld hatte einen großen Einfluss auf die Entstehung dieser Arbeit. Daher möchte ich all meinen **Freunden** danken für die Unterstützung, Motivation und manchmal notwendige Ablenkung während der letzten Jahre. Mein allergrößter Dank geht an meine **Familie**, insbesondere an meine Eltern und meine Schwester - danke für euren liebevollen Rückhalt und eure unentwegte Unterstützung. Gerade die letzten Jahre haben gezeigt, dass wir als Familie uns immer auf uns verlassen können, egal was wieder in den Rucksack gepackt wurde!

This research used samples provided by the Deep Sea Drilling Project (DSDP), the Ocean Drilling Program (ODP), and Integrated Ocean Drilling Program (IODP). Funding for this research was provided by the German Research Foundation (DFG) in the framework of the Priority Program SPP 527 through grants FR1341-5 and FR1341-13/1. I am also grateful for travel support provided by PAGES to attend the PAGES 5^{th} OSM in Zaragoza in 2017.

NATURWISSENSCHAFTLICH-MATHEMATISCHE GESAMTFAKULTÄT

COMBINED FACULTY OF NATURAL SCIENCES AND MATHEMATICS

RUPRECHT-KARLS-
UNIVERSITÄT
HEIDELBERG

Eidesstattliche Versicherung gemäß § 8 der Promotionsordnung für die Naturwissenschaftlich-Mathematische Gesamtfakultät der Universität Heidelberg / Sworn Affidavit according to § 8 of the doctoral degree regulations of the Combined Faculty of Natural Sciences and Mathematics

1. Bei der eingereichten Dissertation zu dem Thema / The thesis I have submitted entitled

   ……

   ……

   handelt es sich um meine eigenständig erbrachte Leistung / is my own work.

2. Ich habe nur die angegebenen Quellen und Hilfsmittel benutzt und mich keiner unzulässigen Hilfe Dritter bedient. Insbesondere habe ich wörtlich oder sinngemäß aus anderen Werken übernommene Inhalte als solche kenntlich gemacht. / I have only used the sources indicated and have not made unauthorised use of services of a third party. Where the work of others has been quoted or reproduced, the source is always given.

3. Die Arbeit oder Teile davon habe ich wie folgt/bislang nicht[1)] an einer Hochschule des In- oder Auslands als Bestandteil einer Prüfungs- oder Qualifikationsleistung vorgelegt. / I have not yet/have already[1)] presented this thesis or parts thereof to a university as part of an examination or degree.

   Titel der Arbeit / Title of the thesis: ……

   Hochschule und Jahr / University and year: ……..……..

   Art der Prüfungs- oder Qualifikationsleistung / Type of examination or degree: ……

4. Die Richtigkeit der vorstehenden Erklärungen bestätige ich. / I confirm that the declarations made above are correct.

5. Die Bedeutung der eidesstattlichen Versicherung und die strafrechtlichen Folgen einer unrichtigen oder unvollständigen eidesstattlichen Versicherung sind mir bekannt. / I am aware of the importance of a sworn affidavit and the criminal prosecution in case of a false or incomplete affidavit.

Ich versichere an Eides statt, dass ich nach bestem Wissen die reine Wahrheit erklärt und nichts verschwiegen habe. / I affirm that the above is the absolute truth to the best of my knowledge and that I have not concealed anything.

…….. ……..……..

Ort und Datum / Place and date — Unterschrift / Signature

[1)] Nicht Zutreffendes streichen. Bei Bejahung sind anzugeben: der Titel der andernorts vorgelegten Arbeit, die Hochschule, das Jahr der Vorlage und die Art der Prüfungs- oder Qualifikationsleistung. / Please cross out what is not applicable. If applicable, please provide: the title of the thesis that was presented elsewhere, the name of the university, the year of presentation and the type of examination or degree.

The German text is legally binding.